Change of Roughness and Mobility upon Coarse-Graining Molecular-Dynamics Models

Veränderung von Rauheit und Mobilität bei Vergröberung molekulardynamischer Modelle
Zur Erlangung des Grades eines Doktors der Naturwissenschaften (Dr. rer. nat.)
Genehmigte Dissertation im Fachbereich Chemie von Melissa K. Meinel aus Offenbach
Tag der Einreichung: 7. Mai 2024, Tag der Prüfung: 01. Juli 2024

1. Gutachten: Prof. Dr. Florian Müller-Plathe
2. Gutachten: Prof. Dr. Nico van der Vegt
Darmstadt, Technische Universität Darmstadt

TECHNISCHE UNIVERSITÄT DARMSTADT

Chemistry Department
Eduard-Zintl-Institute for Inorganic and Physical Chemistry
Theoretical Physical Chemistry

Change of Roughness and Mobility upon Coarse-Graining Molecular-Dynamics Models
Veränderung von Rauheit und Mobilität bei Vergröberung molekulardynamischer Modelle

Accepted doctoral thesis in the department of Chemistry by Melissa K. Meinel

Date of submission: 7. Mai 2024
Date of thesis defense: 01. Juli 2024

Darmstadt, Technische Universität Darmstadt

Bitte zitieren Sie dieses Dokument als:
URN: urn:nbn:de:tuda-tuprints-277853
URL: https://tuprints.ulb.tu-darmstadt.de/27785
Jahr der Veröffentlichung auf TUprints: 2024

Dieses Dokument wird bereitgestellt von tuprints,
E-Publishing-Service der TU Darmstadt
https://tuprints.ulb.tu-darmstadt.de
tuprints@ulb.tu-darmstadt.de

Meinen Eltern.

Erklärungen laut Promotionsordnung

§8 Abs. 1 lit. c PromO

Ich versichere hiermit, dass die elektronische Version meiner Dissertation mit der schriftlichen Version übereinstimmt.

§8 Abs. 1 lit. d PromO

Ich versichere hiermit, dass zu einem vorherigen Zeitpunkt noch keine Promotion versucht wurde. In diesem Fall sind nähere Angaben über Zeitpunkt, Hochschule, Dissertationsthema und Ergebnis dieses Versuchs mitzuteilen.

§9 Abs. 1 PromO

Ich versichere hiermit, dass die vorliegende Dissertation selbstständig und nur unter Verwendung der angegebenen Quellen verfasst wurde.

§9 Abs. 2 PromO

Die Arbeit hat bisher noch nicht zu Prüfungszwecken gedient.

Darmstadt, 7. Mai 2024

M. K. Meinel

Die vorliegende Dissertation wurde unter der Leitung von Herrn Prof. Dr. Florian Müller-Plathe in der Zeit vom 2. Mai 2019 bis zum 7. Mai 2024 im Fachbereich Chemie der Technischen Universität Darmstadt durchgeführt.

Teile dieser Arbeit sind bereits veröffentlicht:

- M. K. Meinel, F. Müller-Plathe, *Loss of Molecular Roughness upon Coarse-Graining Predicts the Artificially Accelerated Mobility of Coarse-Grained Molecular Simulation Models*, J. Chem. Theory Comput. **16**, 1411-1419 (2020)
- M. K. Meinel, F. Müller-Plathe, *Roughness volumes: An improved RoughMob concept for predicting the increase of molecular mobility upon coarse-graining*, J. Phys. Chem. B **126**, 3737-3747 (2022)
- M. K. Meinel, F. Müller-Plathe, *Predicting the artificial dynamical acceleration of binary hydrocarbon mixtures upon coarse-graining with roughness volumes and simple averaging rules*, J. Chem. Phys. **160**, 174108 (2024)

In dieser Dissertation nicht enthalten, aber im gleichen Zeitraum entstanden sind:

- J. Schneider, M. K. Meinel, H. Dittmar, F. Müller-Plathe, *Different Stages of Polymer-Chain Collapse Following Solvent Quenching–Scaling Relations from Dissipative Particle Dynamics Simulations*, Macromolecules **53**, 20, 8889–8900 (2020)
- S. Das, M. K. Meinel, Z. Wu, F. Müller-Plathe, *The role of the envelope protein in the stability of a coronavirus model membrane against an ethanolic disinfectant*, J. Chem. Phys. **154**, 245101 (2021)
- S. Bag, M. K. Meinel, F. Müller-Plathe, *Toward a Mobility-Preserving Coarse-Grained Model: A Data-Driven Approach*, J. Chem. Theory Comput. **18**, 12, 7108–7120 (2022)
- S. Bag, M. K. Meinel, F. Müller-Plathe, *Synthetic Force-Field Database for Training Machine Learning Models to Predict Mobility-Preserving Coarse-Grained Molecular-Simulation Potentials*, J. Chem. Theory Comput. **20**, 8, 3046–3060 (2024)

Acknowledgements

First of all, I wholeheartedly want to thank my supervisor Florian Müller-Plathe for his guidance, his support and his trust. His door is always open and I equally value his professional knowledge, expertise and wit as I appreciate the close-knit and empathetic workplace culture he creates.

I want to express my gratitude to Nico van der Vegt for examining this thesis and for all interactions with him and his group in- and outside of our shared group seminar. Further, I'm grateful to Vera Krewald and Markus Biesalski for kindly accepting to be part of my evaluation committee.

Of course, I want to dearly thank all friends and colleagues I was lucky to meet in the Müller-Plathe group: Eva, Manisha, Saeed M., Xinxin, Dejian, Soham, Kamonthira, Hossein, Donatas, Susana, Vikram, Kenkoh, Saurav, Hari, Shubhadip, Eunsang, Danna, Jeffrey, Yunfeng, Hongyang, Ananya and Hans-Jürgen. I sincerely miss the discussions, the cultural exchange and many shared laughs. Special thanks to Andreas, Jurek, Yash, Tobias, Simon, Saeed N., Zhenghao, Tianhang, Saientan and Gustavo - for their company, their support and the joy they brought me.

The group would be a different place without Dana, who not only smooths the path by removing all bureaucratic obstacles but also never ceases to brighten the mood of everyone around her with her warm kindness. I am profoundly grateful that I had the chance to meet Michael Böhm, whom I will always remember for his genuine interest in the people around him, their work and their well-being as well as for his great sense of humor.

I am incredibly thankful for the people in- and outside of the university that travelled with me along the way — be it as supportive and understanding friends or as dedicated project partners. Thank you to Annabella, Max, Amanda, Janik, Tobias, Stefan, Marieke, Michael, Han, Kilian and Miriam. I sincerely thank Aaron for accompanying me through most of my journey — starting from our joined bachelor studies and even now being ready to proofread whenever needed.

My deepest gratitude goes to my family. I grew up in the most loving household possible, providing me with the confidence and endurance needed to pursue my studies. My parents have been and are incredible supportive, always putting the needs of my sister and me first. My sister has been my closest confidant from the very start — developing our scientific curiosity together, we conducted our first secret experiments in the attic. I am profoundly grateful to Maxim — for being patient and understanding, when things do not work out as expected, for making me laugh when I need it, for constantly tickling my brain and for his unwavering support and love.

Zusammenfassung

All-Atom-Molekulardynamiksimulationen liefern detaillierte Einblicke in molekulare Strukturen und Verhaltensweisen. Das Simulieren großer Systeme oder langer Zeitskalen bleibt jedoch mit einer hohen Rechenintensität behaftet. Vergröberte Modelle reduzieren die Komplexität, indem sie mehrere Atome zu einzelnen Einheiten, sogenannten Beads, zusammenfassen und sich auf die wichtigsten Aspekte des Systems konzentrieren, während unnötige Freiheitsgrade entfernt werden. Dieser Ansatz ermöglicht es, größere Systeme über längere Zeiten zu betrachten, beschleunigt jedoch auch die dynamischen Eigenschaften im Vergleich zu ihrem atomistischen Referenzmodell. Diese Beschleunigung der Dynamik, beispielsweise gemessen als das Verhältnis der Selbstdiffusionskoeffizienten beider Modelle, kann zwischen einer und drei Größenordnungen variieren und macht daher den Einsatz vergröberter Modelle zur Bestimmung genauer dynamischer Eigenschaften praktisch unmöglich.

Diese Dissertation präsentiert einen neuartigen Ansatz zur Vorhersage der beobachteten Beschleunigung dynamischer Eigenschaften in vergröberten Modellen im Vergleich zu ihren atomistischen Gegenstücken, indem die bei der Vergröberung verlorene geometrische Information quantifiziert wird. Mehrere Atome verschmelzen in die kugelförmige Oberfläche eines Beads, wodurch die Oberfläche geglättet und Reibung reduziert wird. Die verringerte Rauheit ermöglicht es den Molekülen, müheloser aneinander vorbeizugleiten — und damit schneller. Der Schlüsselparameter der Methode ist die *molekulare Rauheitsdifferenz* (engl. *molecular roughness difference*), eine Metrik, die aus einem numerischen Vergleich zwischen den molekularen Oberflächen des atomistischen und des vergröberten Modells abgeleitet wird. Diese Metrik wird durch vier *Rauheitsvolumen* ergänzt, die Bereiche beschreiben, in denen sich die Rauheit ändert und Bereiche, in denen dies nicht der Fall ist. Der Anwendungsbereich der RoughMob Methode (*Rough*ness=Rauheit und *Mob*ility=Beweglichkeit) wird systematisch ausgeweitet. Ursprünglich entwickelt mit einer kleinen Gruppe von sieben einfachen Kohlenwasserstoffflüssigkeiten, die sechs bis acht Kohlenstoffatome pro Molekül enthalten und jeweils durch ein einzelnes vergröbertes Bead repräsentiert werden, wird die Methode erweitert, um Moleküle im Bereich von fünf bis 13 Kohlenstoffatomen einzuschließen. Diese breitere Palette umfasst auch asphärischere atomistische Modelle und führt verschiedene Mapping-Schemata ein. Der verfeinerte Ansatz wird anschließend auf binäre Mischungen bei verschiedenen Zusammensetzungen und Konzentrationen von Molekülen innerhalb dieses erweiterten Größenbereichs angewendet und angepasst.

Die einfachen vergröberten Modelle mit einem Bead pro Molekül werden mithilfe der strukturbasierten iterativen Boltzmann-Inversion entwickelt, die die radialen Verteilungsfunktionen des vergröberten Modells an das atomistische Modell durch iterative Anpassungen angleicht. Die geometrischen Informationen werden aus der strukturell äquilibrierten atomistischen Trajektorie und den Nichtbindungspotentialen der Modelle abgeleitet. Die festgestellte Korrelation zwischen den Rauheitsparametern und dem Beschleunigungsfaktor ermöglicht eine a priori Vorhersage des Beschleunigungsfaktors. Dies ermöglicht es, dynamische Eigenschaften, wie den Selbstdiffusionskoeffizienten, aus der kostengünstigen vergröberten Simulation zu berechnen und diesen anschließend so zu skalieren, dass er dem atomistischen Diffusionskoeffizienten entspricht. Für binäre Mischungen kann die Beschleunigung vorhergesagt werden, indem die Rauheitsparameter aus denen der

reinen Komponenten mithilfe einfacher Mittelungsregeln berechnet werden, ergänzt durch einen quadratischen Korrekturterm in der Konzentration, ohne dass zusätzliche Berechnungen an den Trajektorien der Mischungen selbst erforderlich sind.

Die Studie ist derzeit auf kleine, unpolare Kohlenwasserstoffflüssigkeiten beschränkt, die bei einem Zustandspunkt simuliert werden. Die Ergebnisse sind jedoch vielversprechend für eine weitere Entwicklung. Von besonderem Interesse ist die Erweiterung auf Polymersysteme, bei denen typischerweise eine Monomereinheit einem oder zwei Beads entspricht — passend zum Grad der Vergröberung, der für die Kohlenwasserstoffe in dieser Forschung verwendet wurde.

Abstract

All-atom molecular dynamics simulations provide detailed insights into molecular structures and behaviors. However, simulating large systems or long processes remains computationally intense. Coarse-grained models reduce the complexity by combining multiple atoms into single units called beads, focusing on the most crucial aspects of the system and removing unnecessary degrees of freedom. This approach enables studying bigger systems over longer times but also accelerates the dynamics when compared to their all-atom reference model. This acceleration of dynamics, e.g. measured as the ratio between the self-diffusion coefficients in both representations, can vary between one and three orders of magnitude and thus practically precludes the use of coarse-grained models for determining accurate dynamical properties.

This thesis presents a novel approach designed to predict the dynamical acceleration observed in coarse-grained models relative to their atomistic counterparts by quantifying the lost geometric information upon coarse-graining. Several atoms merge into the spherical surface of one bead, thereby smoothening the surface and reducing the friction. The reduced roughness allows the molecules to glide past each other more effortlessly, thus faster. The key parameter of the method is the *molecular roughness difference*, a metric derived from a numerical comparison between the all-atom and coarse-grained molecular surfaces. This metric is expanded upon with four *roughness volumes*, which introduce the concept of specific areas where roughness changes occur and areas where they do not. The application scope of the RoughMob (*Rough*ness and *Mob*ility) method is systematically expanded. Starting from the development with a small set of seven simple hydrocarbon liquids containing six to eight carbon atoms, each represented by a single coarse-grained bead, the method is extended to include molecules ranging from five to 13 carbon atoms. This broader range also includes more aspherical all-atom models and introduces different mapping schemes. The refined approach is subsequently applied and adapted to binary mixtures at various compositions and concentrations of molecules within this expanded size range. The simple one-bead coarse-grained models are developed using structure-based iterative Boltzmann inversion, which matches the radial distribution functions of the coarse-grained model to the all-atom model through iterative adjustments. The geometrical information used for calculating the changes in roughness is derived from the structurally equilibrated atomistic trajectory and the nonbonded potentials of the models. The found connection between the roughness parameters and the acceleration factor enables an a priori prediction of the acceleration factor. Dynamical properties, such as the self-diffusion coefficient, can then be calculated from the cost-effective coarse-grained simulation and scaled to match the atomistic diffusion coefficient. For binary mixtures, the acceleration can be predicted by calculating the roughness parameters from those of pure components using simple averaging rules, supplemented by a correction term quadratic in the concentration, without the need for any additional calculations on the trajectories of the mixtures themselves.

The study is currently limited to small, nonpolar hydrocarbon liquids simulated at a single state point. However, the results are promising for further development. Of particular interest is the expansion to polymeric systems, where typically one monomer unit corresponds to one or two coarse-grained beads — matching the degree of coarse-graining employed for hydrocarbons in this research.

Contents

1 Introduction

All atoms are moving. Whether they are bonded or not — they interact with their surroundings, resulting in a change of their movements and positions and ultimately causing manifold different macroscopic properties. This simple interplay is exploited by molecular dynamics (MD) simulations. "All" that is needed, is a model describing the interactions and the configuration of a system with initial positions and velocities. Once a system is initialized, forces acting on each atom or particle are calculated and Newton's equation of motion is solved for each atom or particle simultaneously. Thereupon, positions and velocities of each particle are updated and saved in a trajectory. This capturing and storing of the positions and velocities of each particle at every point in a certain time interval is hardly ever possible in experiments, and it enables to obtain detailed information on a molecular level of both structure and dynamics. This makes MD simulations an indispensable tool when experiments are expensive, difficult or hazardous. Molecular dynamics calculations thereby not only allow the detailed analysis of phenomena and properties observed in nature or laboratories but also the investigation of materials not yet synthesized. Furthermore, the conditions under which a simulation takes place are precisely controllable. [1]

Thus, the use of MD simulations has continuously grown over the past decades across a diverse array of fields ranging from material science and chemistry to nanotechnology, biology and neuroscience. [2–9] Increased computational power and improved software enables MD simulations to span longer timeframes and larger length scales on a fully atomistic detail level. [10, 11] Despite these advancements, limitations persist, confining all-atom (AA) MD simulations to system sizes of hundreds of nanometers and timescales of only a few microseconds. [12] This is a notable disadvantage when large or complex systems such as biological cells or polymer melts or other soft matter systems are to be studied. [13–15] In these cases, some relaxation times can exceed the accessible simulation durations. [16–18] This prevents the use of such simulation methods for studying self-assembly or phase transition phenomena in large systems or simply calculating the diffusion coefficient in polymer melts or solutions.

Coarse-grained (CG) approaches try to find a balance between computational efficiency and accuracy. Coarse-graining simplifies molecular systems by keeping only the details that are needed to simulate certain target properties. Instead of simulating each atom individually, several atoms are grouped together in a so-called CG bead. They are then presented as a single interaction site. The number of atoms grouped into one bead can vary significantly. In united-atom models, hydrogen atoms are grouped together with their directly bonded carbon atom. In simulations involving water, each water molecule might be represented by one CG bead [19], or alternatively, several water molecules can be grouped into a single CG bead [20, 21] to further simplify the

model. At the more extreme end of coarse-graining, entire polymer chains may be represented by a single CG bead. [22] The simple hydrocarbons presented in this work range from 5 to 13 carbon atoms that are coarse-grained into one bead per molecule. This fits to a degree of coarse-graining, where a polymer would be represented with one or two CG beads per monomer. [23–26]

When systems are coarse-grained systematically from a more detailed (e.g. all-atom) reference system, a set of target properties is selected that the CG model should reproduce. Depending on the target properties and the choice and parameterization of the CG model, the capability of the CG model to represent different properties can differ widely. [12–14, 27] Properties targeted by different methods include structural properties [28], forces acting on the sites [29, 30], free energies [31, 32], or entropies [33]. Some thermodynamic properties, such as pressure or compressibility, can be added. [28, 34–37] Degrees of freedom (DOFs) which are assumed to be unnecessary for the desired analysis or target properties are averaged out. This reduction of DOFs greatly increases the size and time range that is accessible. [38, 39] The reduced number of interaction sites that have to be simulated already directly decreases the computational load. Additionally, the potential energy surface is smoothed, allowing larger integration time steps to be used within the simulation[14]. The smoother potential energy surface also removes molecular friction between the molecules, which leads to faster dynamics and thus faster equilibration. [22, 26, 40] This acceleration of dynamics upon coarse-graining further increases the computational efficiency. It, however, prevents the use of coarse-grained simulations for the quantitative analysis of dynamical and transport properties. This is especially problematic when polymer melts and other soft matter materials are considered. Here, the artificial acceleration of dynamics upon coarse-graining practically excludes MD simulations from capturing quantitative material-specific dynamical properties. All-atom simulations are computationally too insufficient to even calculate e.g. the diffusion coefficient in a polymer melt. Coarse-grained simulations are technically able to access the dynamics. They are, however, accelerated unpredictably between one and three orders of magnitude. [22, 41]
A robust approach for an a priori prediction of the expected dynamical acceleration factor α is therefore highly desirable. A common definition of the acceleration (or scaling) factor α is the ratio of the all-atom (D_{AA}) and the coarse-grained (D_{CG}) self-diffusion coefficients. [22, 42–44]

$$\alpha = \frac{D_{\mathrm{CG}}}{D_{\mathrm{AA}}} \tag{1.1}$$

When the acceleration factor is known or experimental or atomistic dynamical properties are available, the dynamics can be included in the coarse-graining process. This approach aims to directly reproduce the correct dynamics with CG models and account for the physical reasons behind the acceleration. [45–58] This, however, poses the risk of worsening other structural and thermodynamic properties and to some extent reducing the computational gain. A second approach, which is followed in this study, starts posterior to the CG simulation. It aims to either directly rescale the dynamical properties (e.g. $D_{\mathrm{AA}} = D_{\mathrm{CG}}/\alpha$) or to rescale the time ($\Delta t_{\mathrm{AA}} = \alpha \Delta t_{\mathrm{CG}}$). [22–26, 38, 59–62] This implies the assumption, that the same acceleration factor is valid for different dynamical properties as has been shown for systems of moderate size. [63, 64] Several

methods for the a priori estimation of the acceleration upon coarse-graining have been proposed. These range from using relative entropy or excess entropy scaling [33, 65–67], over solving memory functions [68, 69] to using big databases and automated decomposition of molecules into CG beads [70]. More examples are given at the beginning of the result sections 4.1, 4.2 and 4.3 and in Ref. [71].

1.1 A mechanical approach

The studies that are part of this work focus on the development of an entirely new scheme to predict the acceleration of dynamics upon coarse-graining. The loss of friction that results from the smoother potential energy surface is interpreted as a “mechanical” friction. Molecules are considered to have actual hard surfaces. Upon coarse-graining, the surface of the all-atom molecule loses some of its roughness as several atoms are merged into one smoother CG bead. Figure 1.1 shows the cross-section of three molecules (2,3-dimethylbutane) in the AA representation (a) and in the CG representation (b) as a single bead. In the CG model, the smoother beads glide past each other more effortlessly than the rougher AA molecules. Throughout this research, this fundamental concept has been developed into a comprehensive framework we called RoughMob (*Rough*ness and *Mob*ility) method.

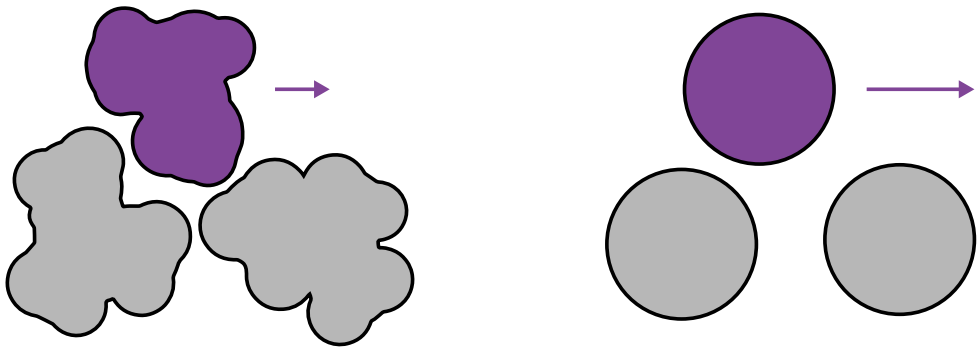

Figure 1.1: Cross-section of three molecules in their all-atom representation (a) with a rough surface and their coarse-grained representation (b) with a smoother surface.

The RoughMob method is developed starting from a set of seven neat aliphatic and aromatic liquid systems with six (C6) or eight (C8) carbon atoms that are coarse-grained into one CG bead per molecule. [41] The application range is further extended to a different mapping scheme and an enlarged size and shape range with five (C5) to 13 (C13) carbon atoms per molecule [72], before binary mixtures are considered [73]. Starting the method development with simple hydocarbons has several advantages:

- The dynamical properties are accessible in the AA and CG representation and with that the acceleration factor. This is essential for the validation of the developed quantities.

- Factors that can interfere with the dynamical acceleration are limited. This includes the use of ambient conditions for all simulations, absence of polar interactions, and minimizing overlapping relaxation processes (e.g., no bond relaxations).
- The single CG bead represents an easy geometrical structure — a sphere — simplifying any related numerical calculations.
- Previous studies have shown that the acceleration factor varies with the molar mass [43] and the degree of coarse-graining [25, 74]. In this work, we find that the acceleration factors for two different C8 isomers can vary by as much as a factor of three, illustrating a much more nuanced differentiation in the method.
- The selected size and shape range is intended to match the degree of coarse-graining used in polymers. Ethylbenzene and Benzene, which can be considered as basic structures for polystyrene, are part of the first test set.
- This approach allows for a systematic development of the RoughMob method: Start as simple as possible — add complexity where it is needed.

The key quantity, we called the *molecular roughness difference*, is calculated through a numerical comparison of the molecular surfaces in both the all-atom and coarse-grained representations. To accommodate a broader range of sizes and shapes, the method is augmented by adding the concept of where the roughness acts (and where not). Four so-called *roughness volumes* are introduced, each derived based on the *molecular roughness difference*. Attending to binary mixtures of hydrocarbons with six to 13 carbon atoms, the same *roughness volumes* prove effective as basis for predicting the acceleration of both self-diffusion coefficients and mutual diffusion coefficients in these mixtures.

1.2 Structure of this thesis

The thesis is structured as follows: Chapter 2 reviews the most relevant methods employed for the MD simulations and analysis of dynamics. Chapter 3 gives an overview over the most important quantities and stages in the development of the RoughMob method. The main results are presented in Chapter 4 in form of the published journal articles. Here, specifics on the numerical definitions and calculations are provided and the method is tested and validated empirically for the respective ranges of application. The last Chapter (5) provides, besides the summarized conclusion of the studies presented in Chapter 4, an outlook on future investigations. This includes considerations for algorithmic refinements and expanding the method's application scope.

2 Methods

This chapter outlines the methodologies used in this thesis. The first section introduces MD simulations and force fields, with a focus on AA and CG types essential to this work, including the specific coarse-graining processes employed. The second section provides a brief introduction on the dynamical acceleration upon coarse-graining.

2.1 Molecular Dynamics Simulation

Molecular dynamics simulations require a set of initial positions $\mathbf{r}^N = \{\mathbf{r}_1, \mathbf{r}_2, ..., \mathbf{r}_N\}$, a set of initial velocities $\mathbf{v}^N = \{\mathbf{v}_1, \mathbf{v}_2, ..., \mathbf{v}_N\}$ (or momenta $\mathbf{p} = m\mathbf{v}$, with the mass m) and a model describing the interactions. The latter provides the potential energy $U = U(\mathbf{r}^N)$ of the system which is dependent on the positions $\mathbf{r}^N$. The set of parameters and/or the functional form that defines the potential energy in MD simulations is commonly referred to as force field. With that at hand, Newton's equation of motion

$$\mathbf{F}_i = -\frac{\partial U}{\partial \mathbf{r}_i} = m_i \frac{\partial^2 \mathbf{r}_i}{\partial t^2} \tag{2.1}$$

with the mass m_i of particle i and the force acting on that particle $\mathbf{F}_i$ is integrated step-wise for each particle simultaneously to derive the positions and velocities at time t. [75] This is often achieved via a numerical step-by-step integration with Verlet's algorithm. [76] For systems with small molecules, the initial positions can e.g. be generated by evenly distributing the molecules on a cubic lattice and including a randomization step into the simulation protocol. Initial velocities can be assigned to each particle e.g. via an uniform distribution or more commonly via a Maxwell-Boltzmann distribution. [77] They are usually chosen so that they correspond to the desired simulation temperature T according to the average kinetic energy E_{kin}

$$E_{kin} = \langle \frac{1}{2} \sum_i m_i \mathbf{v}_i^2 \rangle = \frac{3}{2} N k_B T \tag{2.2}$$

with the number of atoms or particles N and the Boltzmann constant k_B. The potential energy U is separated into nonbonded and bonded interactions. [1]

$$U = U_{\text{bonded}} + U_{\text{nonbonded}} \tag{2.3}$$

The nonbonded interactions act between different molecules (intermolecular) or within a molecule (intramolecular) provided the particles are not close neighbors in the same molecule. Many-body potentials can be used or added [78–80], but can make the simulation computationally impractical. Nonbonded interactions may be short- or long-ranged. Ideally, the potentials decay to zero as the distance increases and start with a very repulsive character (high potential) at short distances, effectively ensuring that the particles cannot cross. Bonded interactions only consist of intramolecular interactions. They conserve the molecular geometry and include 2-body (bonds), 3-body (angles) and 4-body (dihedral torsion, improper angles) terms. Depending on the model and its resolution, not all interaction terms are required. The coarse-grained models employed in this work only use nonbonded interactions.

2.1.1 All-atom representation

The most common all-atom force fields, like the OPLS-AA force field [81] that is used in this work, split the nonbonded interactions into short- and long-ranged contributions. The short-range van der Waals interactions are thereby modelled with an 12-6 Lennard-Jones potential

$$U_{\text{LJ},ij} = 4\epsilon_{ij}\left(\left(\frac{\sigma_{ij}}{r_{ij}}\right)^{12} - \left(\frac{\sigma_{ij}}{r_{ij}}\right)^{6}\right) \tag{2.4}$$

with the interaction parameters σ_{ij} and ϵ_{ij} and the distance r_{ij} between two particles i and j. The parameter ϵ_{ij} describes the depth of the potential, thus takes the negative value at the minimum of the potential and is also referred to as energy parameter. The parameter σ_{ij} is the distance at which the positive potential changes into a negative potential and can thus be interpreted as the size (diameter) of the particle. The nonbonded size σ_{ij} and energy ϵ_{ij} parameters are derived by combination rules for interactions between different species — in the case of OPLS-AA geometric combination rules are used for both parameters.

$$\sigma_{ij} = \sqrt{\sigma_{\text{i}}\sigma_{\text{j}}}\,, \qquad \epsilon_{ij} = \sqrt{\epsilon_{\text{i}}\epsilon_{\text{j}}} \tag{2.5}$$

When (partial) charges are present, the long-ranged electrostatics are modelled with a Coulomb potential.

A basic example for the modelling of a bonded interaction is shown in Eq. 2.6. The bond stretching between the directly connected particles i and j is described by a harmonic potential with the equilibration bond length r_{eq} and the force constant $K_{r,ij}$ that determines the stiffness of the bond.

$$U_{\text{bond},ij} = K_{r,ij}(r_{ij} - r_{\text{eq}})^2 \tag{2.6}$$

2.1.2 Coarse-grained representation

The CG molecules in this work consist of one CG bead. Consequently, only nonbonded interactions are needed. Contrary to the all-atom representation, the interactions are not described by a set of functions and parameters. Instead, the nonbonded CG potentials are tabulated. Here, the potential energies (and usually forces) are listed in a file as a function of the distance. Potentials for distances that are not listed in the table are interpolated. In this work, a linear interpolation between the two closest surrounding values is used. If the potential possesses an attractive part, the distance where $U(r) = 0$ for the first time can by interpreted as the size of the CG bead and is also referred to as effective hard-sphere diameter. This is similar to the interpretation of the size parameter σ in the AA representation and illustrated in Fig. 2.1.

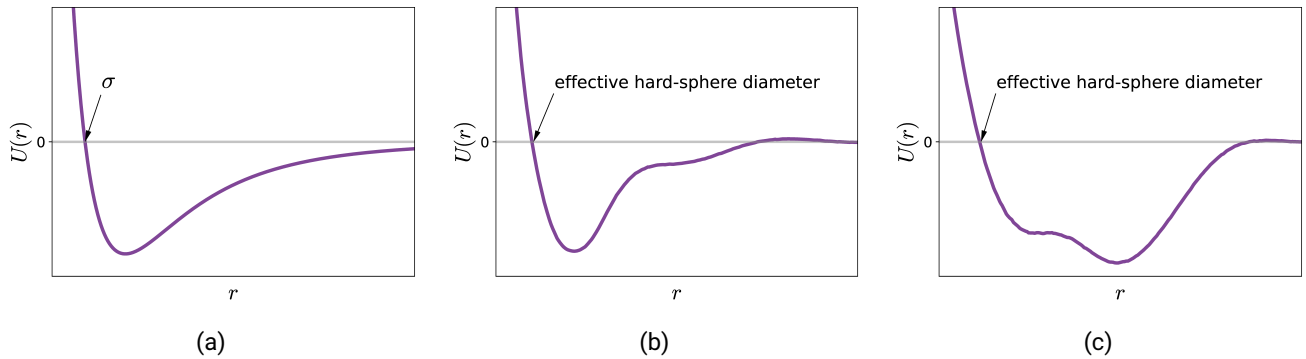

Figure 2.1: Illustration of a Lennard-Jones potential with the size parameter σ (a), and two examples of tabulated nonbonded coarse-grained potentials with their effective hard-sphere diameters: 2,3-dimethylbutane (b) and ethylbenzene (c).

2.1.3 Coarse-graining

A tabulated force-field as described above is usually the result of a bottom-up coarse-graining approach. The CG potentials are derived systematically in order to match target properties of the underlying reference AA simulations (or any more detailed representation). [36, 82] Top-down approaches use function based force-fields that are parameterized so that the CG model matches macroscopic, often experimental observables, or are able to study phenomenological problems. [30, 83] However, compared to bottom-up approaches, they lack information on chemical specificity which is needed in the scope of this work. In accordance with the geometric approach of the RoughMob method, a structure-based bottom-up method, the iterative Boltzmann inversion, is applied. Structure-based methods use, as the name suggests, structural information of the AA system as target properties. For nonbonded interactions this target property is commonly the radial distribution function (RDF). The CG potential is thus constructed so that the RDF of the CG model matches the RDF of the mapped target AA system.

Radial distribution function

The radial distribution function (RDF) describes the local structure of a liquid and is a measurement of the packing or organization of the molecules or particles around one another. It is defined as the average local number density $\rho(r)$ of particles at a distance r from a central particle in ratio to the bulk (number) density $\rho = N/V$. [84]

Practically, the RDF is calculated by counting the number of particles $N(r, \Delta r)$ in a small spherical shell at radius r and of the thickness Δr divided by the approximated spherical shell volume $\Delta V_r \approx 4\pi r^2 \Delta r$, the particle number N and the bulk density ρ.

$$RDF(r) = \frac{N(r, \Delta r)}{4\pi r^2 \Delta r N \rho} \tag{2.7}$$

Figure 2.2 illustrates the *RDF*. The first and second solvation shells are highlighted in blue and green. In those areas, the local density $\rho(r)$ is higher than the average bulk density ρ, the *RDF* thus has a value larger than 1.

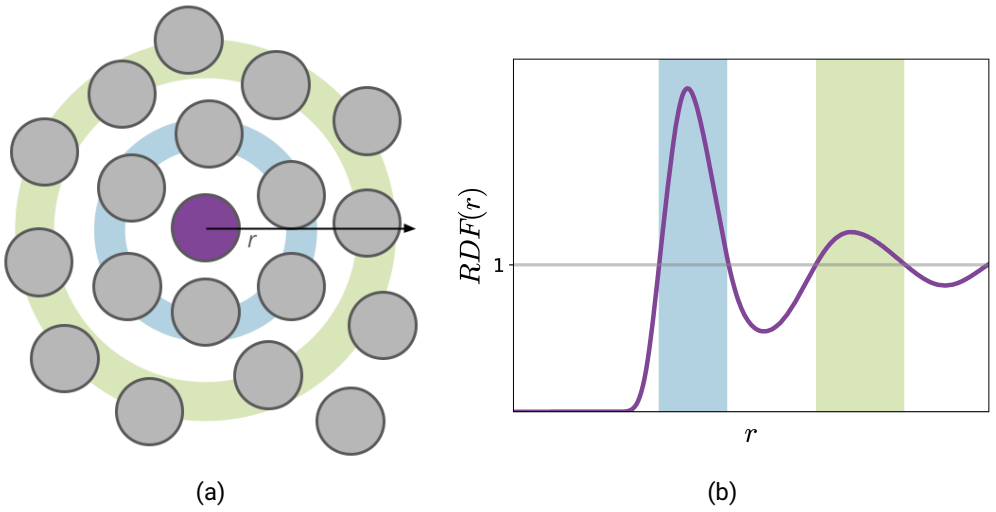

Figure 2.2: Illustration of (a) the radial distribution of particles around a central particle (*purple*) in two dimensions with (b) the resulting radial distribution function; the first and second solvation shell and the corresponding peaks are highlighted in *blue* and *green*.

Iterative Boltzmann inversion

The iterative Boltzmann inversion is one of the most commonly used structure-based coarse-graining methods. It follows a simple scheme that updates the CG potential iteratively until the radial distribution function of the CG model matches the target distribution function of the more detailed (all-atom) model. [35] The steps are described below and illustrated in Figure 2.3.

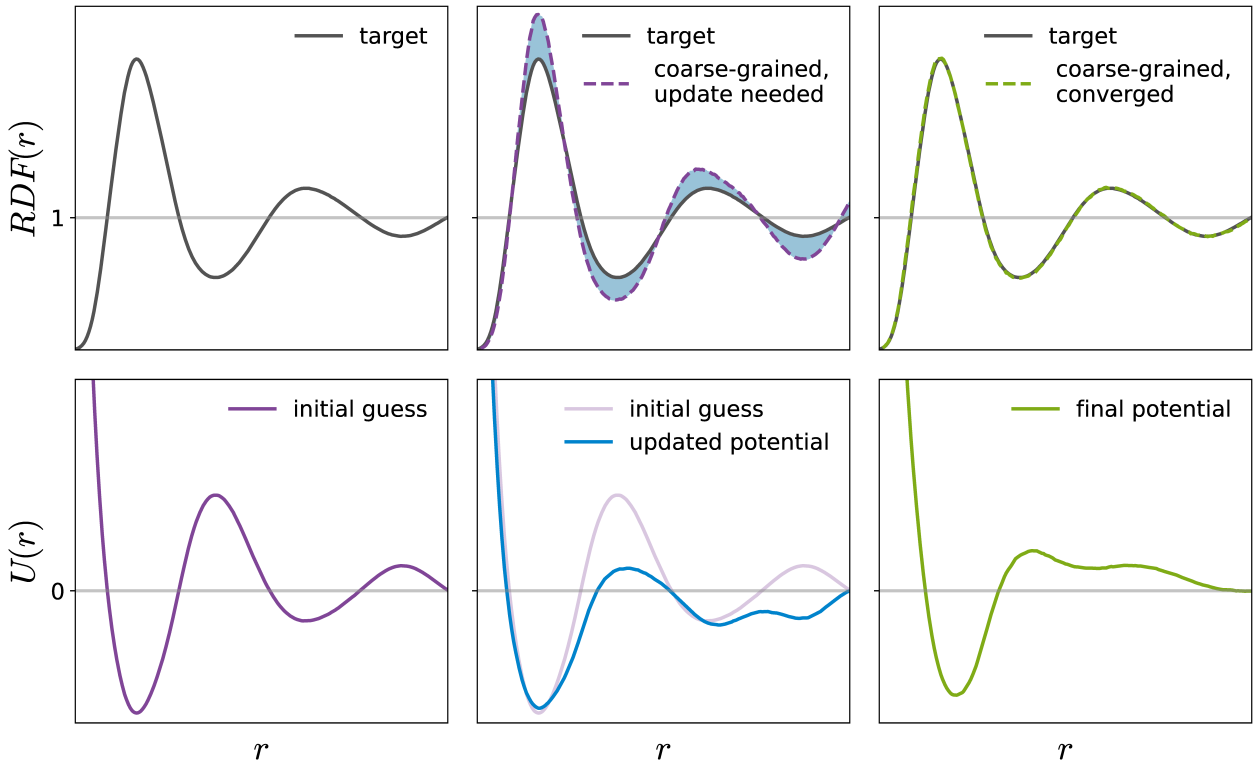

Figure 2.3: Illustration of the radial distribution functions (*RDF*) of the target all-atom and the coarse-grained simulation (upper row) and the coarse-grained potential (lower row) at different steps in the iterative Boltzmann inversion scheme. The first column illustrates the target *RDF* and the initial guess (steps 1. and 2.), the second column illustrates the comparison of *RDF*s and update of CG potentials (steps 3. and 4.) which are repeated iteratively until convergence is reached (last column).

1. A short AA production run is needed to calculate the target RDF. The target RDF is calculated from the mapped AA trajectory. In most cases, a center of mass mapping is applied. This means, the distance from particle i to particle j is measured according to the distances of their respective centers of mass. However, the mapping scheme is mostly decided intuitively by the researchers. Other options are e.g. the geometric center of the molecule or one specific atom of the molecule or monomer.

2. An initial CG potential is needed. This initial guess is usually derived by a simple Boltzmann inversion of the target distribution RDF_{tgt}.
$$U_0 = -k_B T \ln RDF_{tgt}(r) \tag{2.8}$$

3. The CG potential is used for a short equilibration and production run. The RDF_k of the k^{th} CG simulation is calculated and RDF_k is compared to RDF_{tgt}.

4. If RDF_k matches RDF_{tgt} within a given tolerance, convergence is reached. Otherwise, the the CG potential is updated with a correction term calculated based on the mismatch between the two distribution

functions.

$$U_{k+1}(r) = U_k(r) + \lambda k_B T \ln\left(\frac{RDF_k(r)}{RDF_{tgt}(r)}\right) \tag{2.9}$$

If $RDF_k(r)$ is larger than $RDF_{tgt}(r)$, the logarithm returns a positive value and the value of $U(r)$ is increased for the next iteration. The numerical factor λ is a positive value ≤ 1 that prevents the scheme from oscillating around the target RDF when large correction terms are needed.

5. Steps 3 and 4 are repeated iteratively, until convergence is reached. Convergence is reached when RDF_k matches RDF_{tgt}, which can be assessed e.g. by an error function [39] or visually.

2.2 Acceleration of dynamics upon coarse-graining

To quantify the acceleration of dynamics upon coarse-graining, we use the ratio of self-diffusion coefficients in the AA and the CG representation (Eq. 1.1) in all presented studies. For the mixtures used in Section 4.1, a binary diffusion coefficient is calculated additionally to the two self-diffusion coefficients of both components. The introduction here is limited to the self-diffusion coefficient as a general means to illustrate the acceleration of dynamics. As MD simulations track the movement of each particle at every time step, the self-diffusion coefficient can easily be calculated according to Einstein's equation from the slope of the mean squared displacement (MSD):

$$D = \lim_{t\to\infty} \frac{1}{6t} \left\langle \frac{1}{N} \sum_{i=1}^{N} |\mathbf{r}_{\mathrm{COM},i}(t) - \mathbf{r}_{\mathrm{COM},i}(0)|^2 \right\rangle \tag{2.10}$$

with the center of mass position $\mathbf{r}_{\mathrm{COM}}, i$ of molecule i. The calculation requires a linear scaling of the MSD with the time. The simple fluids used in the presented studies reach this diffusive regime very fast after ten to 100 picoseconds. The MSD of the atoms in the diffusive regime would provide the same self-diffusion coefficient as the MSD of the molecules' centers of mass in the diffusive regime. The mapped AA trajectory is used to enable the direct comparison between coarse-grained and all-atom representations.

Plotting the MSD against the time (Figure 2.4) illustrates the importance of proper equilibration and sufficiently long simulation times for the extraction of dynamical properties. The Figure shows a comparison of the all-atom-MSD and the coarse-grained-MSD of 2,3-dimethylbutane plotted against the time in a logarithmic scale. The inset shows the time of the CG simulation scaled with the acceleration factor ($t_{scaled} = \alpha t_{\mathrm{CG}}$).

For a very short time (in the femtosecond scale), the MSD is identical for the mapped AA and the unscaled CG system. Here, the systems are in the ballistic regime, where the movement of the particles is unhindered by the surrounding particles and thus only depends on the kinetic energy in the system (Eq. 2.2). In other words, their MSD scales with the time as t^2 since the molecule's ability to travel only depends on its velocity. Differences start, as soon as the particles start to interact with their surroundings.

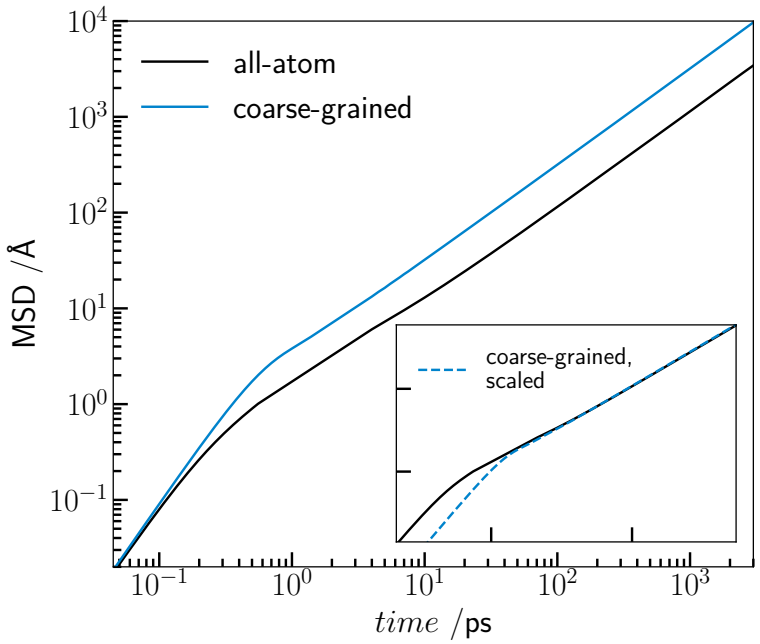

Figure 2.4: Logarithmic mean squared displacement of 2,3-diemthylbutane plotted against the logarithmic time of a all-atom simulation (*black line*) an unscaled coarse-grained simulation (*blue line*) and a scaled coarse-grained simulation (*blue dashed line, inset*).

A simple time scaling of the CG simulation (as shown in the inset of Figure 2.4) can therefore not yield a match of the MSDs at all times.

3 Roughness and Mobility

This chapter aims to provide a comprehensive overview of the key quantities and stages in the development of the RoughMob method. The first section introduces the key quantities of the RoughMob method: the *molecular roughness difference* and the *roughness volumes* derived from it. This chapter primarily focuses on the conceptual definitions of these terms. Details on their numerical determination are provided in Chapter 4. The second section offers a walkthrough of the development stages of the RoughMob method. It explains which key quantities introduced in Section 3.1 and augmentations to the method were required by each targeted application range.

3.1 Molecular Roughness Difference and Roughness Volumes

The use of a geometrical or rather mechanical approach requires for all molecules — in both AA and CG representation — the definition of an actual hard surface. Ideally, this definition can be applied analogously in both representations. The definition used here has already been introduced in the Sections 2.1.1 and 2.1.2. We use the size parameter of the AA force field σ and the effective hard-sphere diameter (or radius) of the tabulated CG potentials (cf. Figure 2.1). Other definitions have not yet been tested but are possible and valid and might even be necessary e.g. if the CG potential does not have a negative range. The molecular surfaces are described as numerical grids with n_{grid} points. Each grid point i on the CG surface has a counterpart on the AA surface. Their distances to the center of the molecule are of the length $r_{\mathrm{CG}}^{(i)}$ and $r_{\mathrm{AA}}^{(i)}$.

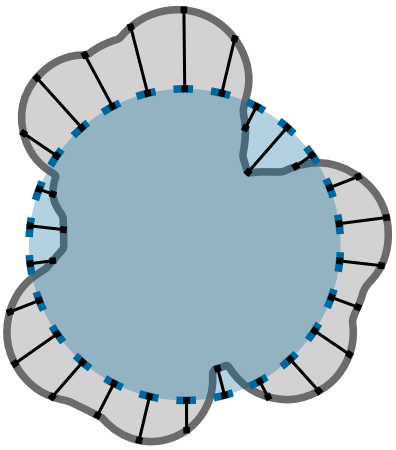

Figure 3.1: Scheme of the *molecular roughness difference* ΔR: All-atom (*grey solid)* and coarse-grained (*blue dashed*) surface; *black line segments*: deviation between AA and CG surface, the average is ΔR.

Molecular roughness difference The key parameter used in the RoughMob method is the *molecular roughness difference* ΔR (denoted as ΔR_a in Section 4.1). It only exists as a comparative quantity between the AA representation and the CG representation. Its calculation is illustrated in Figure 3.1. As indicated in its name ("*difference*"), the deviation between the AA and the CG surface is determined via a simple subtraction. The absolute distance between the AA and the CG surface is calculated at evenly distributed points on the surfaces and averaged over all points on the molecule.

$$\Delta R = \frac{1}{n_{grid}} \sum_{i=1}^{n_{grid}} |r_{\mathrm{AA}}^{(i)} - r_{\mathrm{CG}}^{(i)}| \tag{3.1}$$

No difference is made between peaks, where the AA surface overtowers the CG surface, and valleys, where the CG surface overtowers the AA surface. The size of the surface has no direct impact on the value of ΔR which is an average over all points that describe the surfaces. In consequence ΔR only slowly increases with the size of a molecule as a result of e.g. more possibilities for more pronounced peaks and valleys if more (or less) branches in the molecule are present.

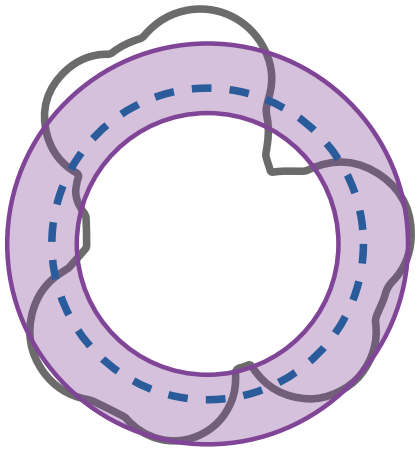

Figure 3.2: Scheme of the shell volume (*purple*); All-atom (*grey solid)* and coarse-grained (*blue dashed*) surface; thickness of the shell is twice the *molecular roughness difference*.

Shell volume The *shell volume* V_{shell} defines the volume where most of the change of the roughness takes place. It is illustrated in Figure 3.2. The thickness of the shell is directly related to the *molecular roughness difference*. The thickness takes twice the value of ΔR. Contrary to the *molecular roughness difference*, the size of the surface directly impacts the value of V_{shell} as a larger molecule will have a larger surface on which the change of roughness takes place. The *shell volume* is thus a quantity, that takes the space needed for the change of roughness into account. The concept of volumes instead of a simple difference also takes into account the positioning of the molecules within the system. We consider not only how much space the change requires but also where it takes place — and where not. This leads to the definition of four so-called *roughness volumes*.

Roughness volumes — active and passive The *roughness volumes* are divided into active and passive volumes. The shell volume is the basis of what we called *active volumes* — the region where the change acts. It is only augmented by the overlap volume — the area where the shell volumes of different molecules overlap (Figure 3.3 (a)). We found that the size of the regions that are *not* directly affected by the change of the

surface roughness can be equally important. They are characterized in so-called *passive volumes*, which are further divided into the inner passive volume (Figure 3.3 (b)) and outer passive volume (Figure 3.3 (c)). A large shell volume, a large overlap volume and a large inner passive volume all increase the acceleration factor. The first two are similar to the *molecular roughness difference* in their interpretation: A large change in roughness results in a large change in mobility. The latter accounts for an increasing size (or degree of coarse-graining) that is not yet properly accounted for by the shell volume. A larger outer passive volume decreases the acceleration factor. Molecules with more space between one another are less affected when the surface roughness changes.

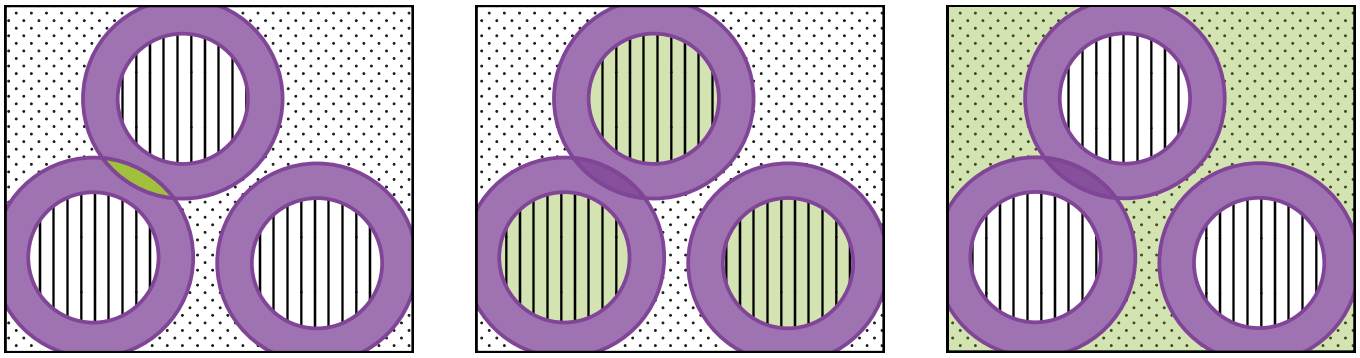

Figure 3.3: Schematic of active roughness volumes (*purple*) and passive roughness volumes (*white with patterns*). Highlighted in *green* (a) overlap volume, (b) inner passive volume, and (c) outer passive volume.

Form of the prediction equations Although establishing a functional form that combines the key quantities to predict the acceleration factor is crucial, details are omitted here for two reasons. First, this information is quite detailed, not suited for a brief and still comprehensive overview and will be revisited in Chapter 4 containing the results. Second, the fit functions employed are phenomenological descriptions of observed behaviors and should be treated as such. These functions are designed around a concept, that has shown success in its application. Their validation is carried out through testing — an important part of this research. As the application range expands, the method will need further adjustments, refinements and augmentation as it already did during the development outlined in the next section.

3.2 Application range

The studies in Sections 4.1 and 4.2 deal with single component systems and show the evolution from using ΔR to the augmentation of the RoughMob method with *roughness volumes*. The first test set, the “original set”, contains seven aliphatic and aromatic neat liquids with six or eight carbon atoms. The acceleration factor of the original set scales linearly with the *molecular roughness difference* as illustrated in Figure 3.4 (a). The relation remains valid, when a different mapping for coarse-graining some of the same systems is

added, as can be seen in Figure 3.4 (b) (*purple triangles*). Here the extended application range from a center of mass mapping to a mapping scheme based on a specific atom of the AA structure does not require any methodological enhancements. Systems represented by *purple circles* are from the same application range as the original set and fit well. The systems represented by the *blue diamonds* extend the application range by adding a very aspherical molecule and three system of an extended size range (C5, C11 and C13).

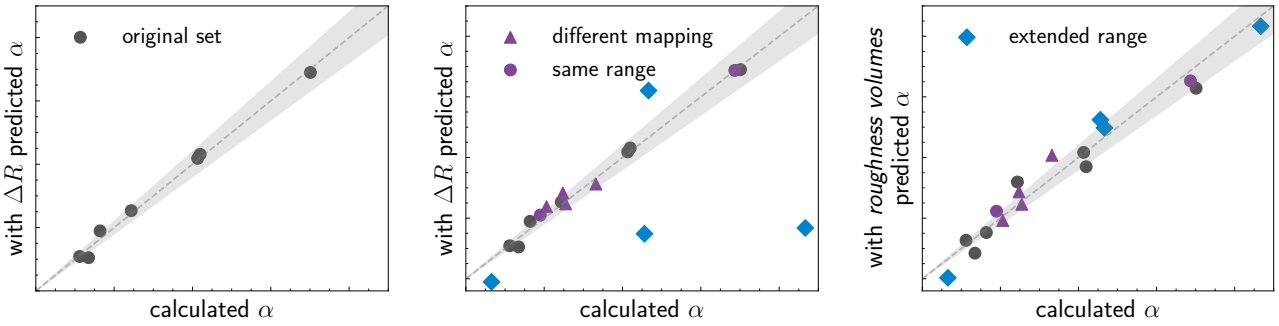

Figure 3.4: Predicted acceleration factor α plotted against the acceleration factor as calculated from the diffusion coefficients of the simulations; *grey dashed line* represents a perfect prediction; *grey area* illustrates a 10 % error margin.

This extension requires the introduction of the concept of the *roughness volumes*. Once three fitting parameters have been determined via least square fit and with a training set of acceleration factors α and *roughness volumes*, all systems can be predicted using the same equation (Figure 3.4 (c)). It, however, has to be noted, that the precision is slightly decreased. The grey area illustrates a 10 % error margin. For molecules with a low acceleration factor, it is harder to match this precision.

The study in Section 4.3 expands the application range to binary mixtures of the same liquids that have been used in the previous studies. For simplicity, here, only the mixture average acceleration of the self-diffusion coefficients is shown. Both the determination of the individual acceleration factors of the two self-diffusion coefficients and the acceleration factor of the binary diffusion coefficient use this number-weighted averaged acceleration factor as basis. Figure 3.5 (a) shows the quality of prediction using *exactly the same* equation and fitting parameters as derived for the previously discussed application on neat liquids within a range of five to 13 carbon atoms. The *roughness volumes* for the mixtures are estimated as a simple number-weighted average of the neat components' *roughness volumes*. The mixtures that are only composed of molecules that did not rely on *roughness volumes* (*grey circles*) are already predicted very well without the need for any adjustment. As soon as the mixture includes a molecule from the extended range (*blue diamonds*) that relies on the use of *roughness volumes*, a refinement of the method is needed. This can be achieved by adding a correction in form of a cross-term quadratic in the concentration (Figure 3.5 (b)). However, this cross-term purely uses quantities from the neat components. No additional calculations or fittings are required. More refinements introduced for the differentiation between the two self-diffusion coefficients and the binary diffusion coefficient will be

discussed in Section 4.3.

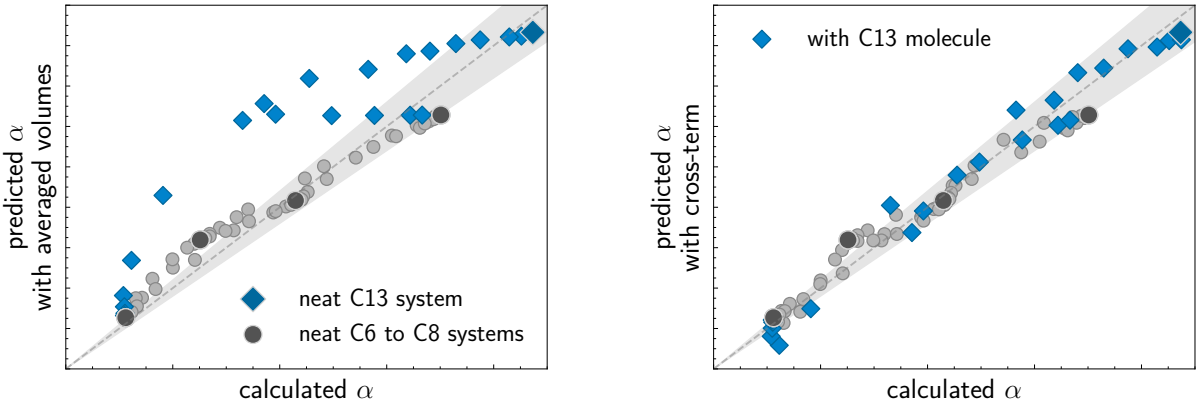

Figure 3.5: Predicted acceleration factor α (average of the mixture) plotted against the acceleration factor as calculated from the diffusion coefficients of the simulations; *grey dashed line* represents a perfect prediction; *grey area* illustrates a 10 % error margin.

4 Results

4.1 Loss of Molecular Roughness upon Coarse-Graining Predicts the Artificially Accelerated Mobility of Coarse-Grained Molecular Simulation Models

Correction The subsection 3.5 states:

> The offset in ΔR_a by 0.43 Å means that no significant acceleration of dynamics upon coarse-graining should occur for small molecules with a ΔR_a below 0.43 Å.

and refers to Equation 19. This is not true. A value of $\Delta R_a = 0.43$ Å would, based on the provided Equation 19, result in $\alpha = 0$ which is not a physically realistic value. No significant acceleration is observed, when $\alpha = 1$ which would occur for $\Delta R_a = 0.46$ Å.

JCTC Journal of Chemical Theory and Computation

pubs.acs.org/JCTC Article

Loss of Molecular Roughness upon Coarse-Graining Predicts the Artificially Accelerated Mobility of Coarse-Grained Molecular Simulation Models

Melissa K. Meinel* and Florian Müller-Plathe*

Cite This: J. Chem. Theory Comput. 2020, 16, 1411−1419 Read Online

ACCESS | Metrics & More | Article Recommendations | Supporting Information

ABSTRACT: Coarse-grained models include only the most important degrees of freedom to match certain target properties and thus reduce the computational costs. The dynamics of these models is usually accelerated compared to those of the parent atomistic models. We propose a new approach to predict this acceleration on the basis of the loss of geometric information upon coarse-graining. To this end, the molecular roughness difference is calculated by a numerical comparison of the molecular surfaces of both the atomistic and the coarse-grained systems. Seven homogeneous hydrocarbon liquids are coarse-grained using the structure-based iterative Boltzmann inversion. An acceleration factor is calculated as the ratio of diffusion coefficients of the coarse-grained and atomistic simulation. The molecular roughness difference and the acceleration factor of the seven test systems reach a very good linear correlation.

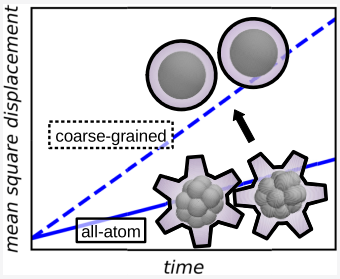

1. INTRODUCTION

All-atom (AA) molecular dynamics (MD) simulations represent each atom as a single point particle and provide reliable information about molecular and intermolecular structure, transport, and movement. Even though computational power increases, MD simulations of large systems or on long time scales, such as simulations of a variety of polymers,[1,2] surfactants[3,4] and proteins,[5,6] can be too demanding to be carried out by atomistic simulations. One way to reduce the computational cost is to use coarse-grained (CG) models,[7−12] which include in the computation only the most important degrees of freedom (DOFs) that are necessary to match a certain target property or a set of target properties. These CG models combine several atoms into one group, hereafter called a CG bead. Fewer particles, short-range or simpler potentials, and the possibility to use larger integration time steps significantly reduce the computational cost.[13]

In the top-down approach, interaction forces or potentials of the CG beads are modeled with functional forms that are parameterized to match macroscopic thermodynamic properties or other experimental observables.[7,8] In the bottom-up approach, the target properties are derived from underlying reference AA or united-atom (UA) simulations.[9,10,14] Hybrid models that combine both the bottom-up and the top-down approaches[11] as well as the AA-CG hybrid models have also been developed.[12]

Depending on the choice of the approach and the CG model, the model's ability to represent the structural, thermodynamic, and dynamic properties of the studied system can differ widely. Generally, the reduction of the number of degrees of freedom by coarse-graining results in faster dynamics compared to that of atomistic models. This acceleration upon coarse-graining has been observed quite universally,[15−19] and different concepts have been used to explain it. In this contribution, we follow a "mechanical" picture: on the outside, a molecule composed of several atoms presents itself as an aggregate of overlapping spheres, causing the surface to become rough, which, in turn, causes friction. When the same molecule is coarse-grained into a single spherical CG bead, some of the surface structure is lost and the friction is concomitantly reduced.

Some effort has been directed toward the development of dynamic CG models[20−29] that accurately describe dynamical properties, such as the diffusion coefficient, by including them as targets in the parametrization, thus enforcing correct dynamical behavior within the coarse-graining process. Our own experience shows that, very often, this has the undesirable side effect of worsening the reproduction of other structural or thermodynamic properties.

This work focuses on the prediction of the acceleration factor of the dynamics. As a definition of the time scaling or acceleration factor α, we use the ratio of diffusion coefficients of the CG and AA simulation.

$$\alpha = \frac{D_{CG}}{D_{AA}} \tag{1}$$

Received: September 24, 2019
Published: January 30, 2020

https://dx.doi.org/10.1021/acs.jctc.9b00943
J. Chem. Theory Comput. 2020, 16, 1411−1419

While the calculation, and ultimately the prediction, of an acceleration factor does not explain the physical reasons of the dynamical differences, it opens up the possibility to simulate on longer time scales and thereby sample a larger portion of the conformational space. The acceleration of the dynamics thus plays a crucial role in increasing computational efficiency.[18,30]

The acceleration factor α can be calculated from the diffusion coefficients or other dynamic properties such as viscosities, reorientation times, etc. of both the coarse-grained and the atomistic models. For systems, which (unlike the small molecules of this contribution) show slow dynamics, the necessary atomistic MD calculation can be computationally extremely challenging or even completely infeasible. It would, therefore, be much more useful to a priori predict α at the time of coarse-graining. This would open a way to estimate, say, the atomistic diffusion coefficient D_{AA} using only the much more affordable coarse-grained calculations as $D_{AA} = 1/\alpha \cdot D_{CG}$.

Efforts have been made to predict α via relative entropy[14,31] or a bias potential.[15,32] These methods take the pair potential functions into account by combining them with a weighting function and integrating the resulting functions over their domain or a subset. Following an energy renormalization strategy, the CG dynamics is rescaled by correcting the activation free energy of the CG model.[33−35] Moreover, an approximate analytical solution of the rescaling formalism is derived by solving the memory functions of the CG and atomistic representation to derive expressions for the friction coefficients.[16,36] Various studies suggest that the acceleration factor can be correlated with the molar mass (in the case of alkanes),[37] the degree of coarse-graining,[19,38] or the monomeric friction coefficient of unentangled polymers according to the Rouse model.[2,39,40] Besides the efforts that have been made to derive α from or correlate it to physical properties, there are also approaches based on big databases and automated decomposition of molecules into the CG beads.[41,42]

However, α has been shown to be independent of the chain length of polyethylene[19,38] and to some degree of highly coarse-grained polymers, where one polymer chain is represented by one to ten CG beads.[30] It does depend on the mapping scheme[43] and the temperature. The acceleration factor typically decreases as the temperature increases since the roughness of the free-energy landscape loses importance when k_BT rises.[19,26,44] As a consequence, the recalibration of CG potential models is a known requirement as one changes the state point.[45−47]

In this work, an entirely different scheme for the prediction of the acceleration upon coarse-graining is presented and applied to systems at, for the time being, one state point defined by the temperature and pressure. Contrary to the available methods for the prediction of the acceleration factor,[17] ours is motivated by mechanical considerations. It is based on the correlation of the loss of geometrical information upon coarse-graining and the acceleration of dynamics. The parameter that we found to be suitable for this purpose has some analogy with the surface roughness of solids often analyzed in materials science.[48−57] Therefore, hard molecular surfaces are defined. The difference in molecular roughness is calculated numerically by comparing the AA and CG molecular surfaces. The correlation between this change and the acceleration factor is examined for several fluids of C6 and C8 molecules as a first step.

This is the typical number of atoms collected into one coarse-grained bead by bottom-up coarse-graining procedures such as iterative Boltzmann inversion.[1,58] Since the present study is done with the view of applying it to polymer simulations, we opt for this level of coarse-graining. In this contribution, we also restrict the study to uncharged, nonpolar species.

2. METHODS

2.1. Simulation Details. Seven homogeneous hydrocarbon liquids, five of them branched alkanes and two of them aromatic molecules, are simulated (see Figure 1) at ambient conditions.

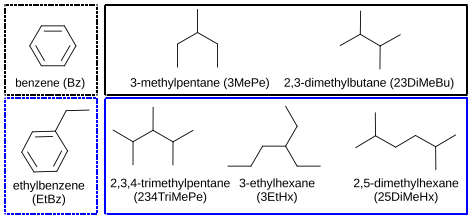

Figure 1. Simulated molecules, their abbreviated names, chemical type, and the number of carbon atoms: black dashed: C6 aromatic; black dotted: C6 alkane; blue dashed: C8 aromatic; blue dotted: C8 alkane.

Molecular dynamics simulations are performed using the large-scale atomic/molecular massively parallel simulator (LAMMPS).[59] The initial AA configurations are created using the following protocol: using Moltemplate,[60] 1000 molecules are distributed in a cubic simulation box with a side length of 100 Å. The system is energy-minimized using a conjugate gradient algorithm. Molecular orientations and conformations are randomized by Brownian dynamics at 900 K for 0.2 ns, followed by *NVT* dynamics with a Nosé−Hoover thermostat for 0.5 ns (coupling time $\tau_t = 50$ fs). Using two simulations of 0.5 ns each under *NPT* conditions with a Nosé−Hoover thermostat ($\tau_t = 50$ fs) and Nosé−Hoover barostat ($\tau_p = 500$ fs), the system is cooled down to 298.15 K at 500 atm and the pressure is decreased to 1 atm.

All AA-MD and CG-MD equilibration and production simulations are carried out under isothermal−isobaric (*NPT*) conditions at 1 atm and 298.18 K with both the Nosé−Hoover thermostat ($\tau_t = 50$ fs) and the barostat ($\tau_p = 500$ fs) and a velocity-Verlet integrator. Periodic boundary conditions are applied in all three dimensions. All of the systems are equilibrated (self-diffusion coefficients of two successive 2 ns time intervals differ by less than 10%) for 10 ns with a time step of $\Delta t = 0.5$ fs, followed by production runs of 10 ns using the same time step.

2.2. All-Atom Model. All-atom (AA) interactions are modeled with the fully flexible OPLS-AA force field. The nonbonded parameters are given in Table 1. The bonded OPLS-AA parameters are given in the Supporting Information. Both

Table 1. OPLS-AA Force-Field Nonbonded Energy Parameters[62]

atom type	description	ϵ/kcal mol^{-1}	σ/Å	q/e
CT_{CH3}	aliphatic carbon (CH_3)	0.066	3.5	−0.18
CT_{CH2}	aliphatic carbon (CH_2)	0.066	3.5	−0.12
CT_{CH}	aliphatic carbon (CH)	0.066	3.5	−0.06
CT_{CA}	aliphatic carbon bonded to aromatic carbon	0.066	3.5	−0.005
HC	aliphatic hydrogen	0.030	2.5	0.06
CA	aromatic carbon	0.070	3.55	−0.115
HA	aromatic hydrogen	0.030	2.42	0.115

https://dx.doi.org/10.1021/acs.jctc.9b00943
J. Chem. Theory Comput. 2020, 16, 1411−1419

the nonbonded size σ and the nonbonded energy ϵ parameters are described with geometric combination rules for interactions between different species.

$$\sigma_{ij} = \sqrt{\sigma_i \sigma_j} \tag{2}$$

$$\epsilon_{ij} = \sqrt{\epsilon_i \epsilon_j} \tag{3}$$

Standard long-range van der Waals corrections are added to the energy and pressure during the simulations.[61] All nonbonded interactions are treated with a spherical cutoff with a cutoff distance of 11 Å. Intramolecular nonbonded interactions are evaluated for atom pairs separated by three or more bonds with the normal nonbonded potentials; for 1,4-intramolecular interactions, the potential is scaled down by half.

2.3. Coarse-Grained Model. Each molecule is mapped into a single CG bead positioned at the center of mass of the AA molecule. Only nonbonded interactions are needed for the CG simulation. The tabulated numerical CG potential is derived by iterative Boltzmann inversion, where the CG-pair potential functions $U^{CG}(r)$ are updated iteratively until the radial distribution function of the CG model $g_i^{CG}(r)$ matches the target radial distribution function $g^{target}(r)$, which is calculated from the atomistic reference simulation.[1,58] An initial guess $U_0^{CG}(r)$ is derived by Boltzmann-inverting $g^{target}(r)$. A pressure correction[58] is applied during the iterative process. The cutoff radii r_{cut} used for the iterative Boltzmann inversion and the CG simulation, as well as CG-pair potentials $U^{CG}(r)$, are shown in Table 2 and Figure 2, respectively. The cutoff radius is chosen to

Table 2. Cutoff Radii for the Iterative Boltzmann Inversion and CG Simulations

	r_{cut}/Å
benzene	14.3
3-methylpentane	15.3
2,3-dimethylbutane	15.5
ethylbenzene	14.9
2,3,4-trimethylpentane	16.5
3-ethylhexane	15.1
2,5-dimethylhexane	15.2

satisfy the condition $g^{target}(r_{cut}) = 1$ between the second minimum and the third maximum of $g^{target}(r)$. The resulting numerical CG potentials are represented as tables ($\Delta r = 1 \times 10^{-3}$ Å) with linear interpolations between the points. The tabulated potentials are provided in the Supporting Information. The CG simulations run, on average, about 50 times faster than the parent AA simulations.

2.4. Molecular Surfaces. Our method uses the difference between the molecular surface of the parent atomistic model (AA) and the coarse-grained (CG) model derived from it by iterative Boltzmann inversion. Therefore, the molecular surface must be defined and then evaluated. To simplify the analysis, description, and calculation of each atomistic molecule's surface, two steps are required. First, the center of mass of each molecule is placed at the origin of the coordinate system. Second, the unweighted atomic positions of both C and H atoms are used to calculate the molecular gyration tensor. The principal axis belonging to its largest eigenvalue is aligned with the x-axis. Molecular surfaces for both AA and CG models are described as numerical point grids on the basis of the spherical Fibonacci grid that provides approximately evenly distributed points on a sphere. The spherical Fibonacci grid uses the golden ratio

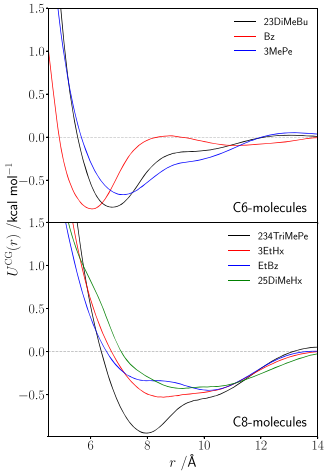

Figure 2. Nonbonded pair potentials between beads of the coarse-grained model obtained from iterative Boltzmann inversion. The coarse-grained bead is positioned at the center of mass of the atomistic model.

$\Phi = (1 + \sqrt{5})/2$ to generate a spherical grid evenly spaced in $\sin(\theta)$ with the latitude θ and the longitude φ.[63]

$$\varphi_l = 2\pi l \Phi^{-1} \tag{4}$$

$$\sin(\theta_l) = \frac{2l}{n_{grid}} \tag{5}$$

The integer l ranges from $-n$ to n and $n_{grid} = 2n + 1$ is the number of grid points. The elevation angle θ ranges from $-\pi/2$ to $+\pi/2$ as the latitudes on earth. This affects the transformation from the spherical to the Cartesian coordinate system $((\theta, \varphi, r) \rightarrow (x, y, z):(r\cos(\theta)\sin(\varphi), r\cos(\theta)\cos(\varphi), r\sin(\theta)))$.

Both AA and CG molecular surfaces use the same ray directions $\mathcal{R}_{dir}$ generated with the spherical Fibonacci grid algorithm with $n_{grid} = 2501$ and $r = 1$.

$$\mathcal{R}_{dir} = \{(\theta_i, \varphi_i, 1) \in \mathbb{R}^3 | i = 1, ..., n_{grid}\} \tag{6}$$

For the AA molecular surfaces, the set $\mathcal{M}$ of ray−sphere intersections $\mathbf{p}$ is calculated between all rays and all-atom spheres. An atom sphere $S_{r_k}(\mathbf{a}_k) = S_k$ of an atom k is placed at the position of the atom $\mathbf{a}_k$ and has the radius r_k.

$$S_k = \{\mathbf{x} \in \mathbb{R}^3 | \|\mathbf{x} - \mathbf{a}_k\|_2 = r_k\} \tag{7}$$

The radius is chosen to be half its nonbonded Lennard-Jones size parameter $r_k = 0.5\sigma_k$.

$$\mathcal{M} = \{\mathbf{p} \in S_k \cap r \cdot \mathcal{R}_{dir} | \forall\, k;\, r \in \mathbb{R}^+\} \tag{8}$$

Since each ray can intersect more than one atom sphere and each one up to two times, the AA molecular surface $\mathcal{R}_{AA}$ is the set of all intersection points with the highest radius for each ray.

$$\mathcal{R}_{AA} = \{\mathbf{v} \in \mathbb{R}^3 | \|\mathbf{v}\|_2 = \max_{\substack{(\theta_i, \varphi_i, r) \in M \\ i = 1, ..., n_{grid}}} r\} \tag{9}$$

The principal axis with the largest eigenvalue of the molecule has been aligned with the x-axis using unweighted positions of atoms. The length along the x-axis, considering the molecular surface, is defined as follows

https://dx.doi.org/10.1021/acs.jctc.9b00943
J. Chem. Theory Comput. 2020, 16, 1411−1419

$$L_x = \max_{(x,y,z)\in\mathcal{R}_{AA}}(x) + |\min_{(x,y,z)\in\mathcal{R}_{AA}}(x)| \quad (10)$$

For the CG model, the calculation of the surface is simpler, as there is only one bead, i.e., only one sphere. The radius of the sphere is chosen to be half of the radius where $U^{CG} = 0$ (Figure 2), thus the effective hard-sphere radius of the CG beads (see Table 3). This is done in analogy to the AA atom radius, which is taken as half of the value where the Lennard-Jones potential is zero.

Table 3. L_x (Equation 10) and the Effective Hard-Sphere Radius of CG Beads

	L_x/Å	r_{CG}/Å
2,3-dimethylbutane	7.96	2.77
benzene	7.20	2.45
3-methylpentane	8.73	2.84
2,3,4-trimethylpentane	9.06	3.19
3-ethylhexane	9.78	3.37
ethylbenzene	9.65	3.28
2,5-dimethylhexane	10.36	3.54

$$r_{CG} = \frac{1}{2}\min\{r \in [0, r_{cut}] | U^{CG}(r) = 0\} \quad (11)$$

The CG molecular surface grid $\mathcal{R}_{CG}$ uses the same ray directions as the AA surface.

$$\mathcal{R}_{CG} = r_{CG}\cdot\mathcal{R}_{dir} \quad (12)$$

2.5. Molecular Roughness Difference. Surface roughness is defined as the deviation of a surface profile from a reference surface. Positive deviations are denoted as peaks, with R_p being the maximum peak height, and negative deviations as valleys (Figure 3). To describe the loss in surface roughness upon coarse-graining, the surface profile is taken to be the AA molecular surface and the reference surface as the surface of the (spherical) CG bead. The arithmetic mean of the absolute surface profile height h is, therefore, a comparative quantity that describes the molecular roughness difference ΔR_a.

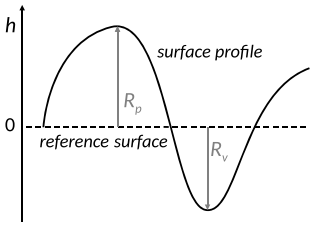

Figure 3. Schematic view of a surface profile (solid) and its reference line (dashed) with the maximum peak height (R_p) and maximum valley depth (R_v).

$$h_i = r_{AA}^{(i)} - r_{CG}^{(i)}$$
$$\forall\ (\varphi_i, \theta_i, r_{AA})^{(i)} \in \mathcal{R}_{AA}$$
$$(\varphi_i, \theta_i, r_{CG})^{(i)} \in \mathcal{R}_{CG} \quad (13)$$

$$\Delta R_a = \frac{1}{n_{grid}}\sum_{i=1}^{n_{grid}} |h_i| \quad (14)$$

For a more detailed analysis, we also calculate the higher moments of the distribution of h_i. The skewness R_{sk} measures the asymmetry of the density curve of peaks and valleys, with a positive value meaning that peaks dominate the roughness difference, while a negative value indicates that the contribution of the valleys to the roughness difference is higher.

$$R_{sk} = \frac{1}{n_{grid}R_q^3}\sum_{i=1}^{n_{grid}} h_i^3 \quad (15)$$

$$R_q = \sqrt{\frac{1}{n_{grid}}\sum_{i=1}^{n_{grid}} h_i^2} \quad (16)$$

The kurtosis R_{ku} expresses the sharpness of the density curve, with a low value indicating that there are fewer but higher peaks and/or fewer but deeper valleys.

$$R_{ku} = \frac{1}{n_{grid}R_q^4}\sum_{i=1}^{n_{grid}} h_i^4 \quad (17)$$

As a fully flexible AA model is used, the molecular roughness difference is different for each molecule within a system. Thus, for each system, the parameters ΔR_a, R_{sk}, and R_{ku} are averaged over 200 molecules. Atomic positions are taken from the last frame of the production run. Error bars are determined by the standard deviation.

3. RESULTS AND DISCUSSION

3.1. Coarse-Grained Potentials and Bead Radius. The nonbonded CG pair potentials are displayed in Figure 2. Not all of the potentials have a global minimum that directly follows the monotonic decrease of the repulsive part. Since all of the potentials exhibit a repulsive and an attractive part, they allow the determination of the effective hard-sphere radius of the CG bead r_{CG} as one half of its first pass through zero. We note that for a longer L_x, the radius of the CG bead becomes larger (Table 3).

3.2. Liquid Structure. The structure is characterized by the radial distribution function $g(r)$. To make the radial distribution functions of the CG model and the AA model comparable, the distribution functions of the center of mass are used (Figure 4). For the calculation of $g(r)$, the configuration of every 1000th time step (every 0.5 ps) is used and averaged over 10 ns. All of the molecules show a difference of less than 1% between $g^{CG}(r)$ and $g^{AA}(r)$ as characterized by the error function[26]

$$\delta g = \frac{\int_0^{r_{cut}} |g^{CG}(r) - g^{AA}(r)| dr}{\int_0^{r_{cut}} g^{AA}(r) dr} \quad (18)$$

where r_{cut} is the cutoff radius used in the CG model. This is no surprise, as the CG potentials are constructed to reproduce the atomistic $g(r)$. The mass densities ρ of the CG and AA simulations are in good agreement (Table 4). They differ by at most 3% from the experimental values. This agreement is of no relevance to the present paper, which makes comparisons only between coarse-grained models and their parent atomistic models, but it reflects the quality of the AA model.

3.3. Dynamic Properties. The dynamics is characterized by the center-of-mass self-diffusion coefficient of the molecules D. It is calculated from their center-of-mass mean square displacement (MSD) according to the Einstein relation. The averaged center-of-mass MSD is calculated using every 1000th

https://dx.doi.org/10.1021/acs.jctc.9b00943
J. Chem. Theory Comput. 2020, 16, 1411−1419

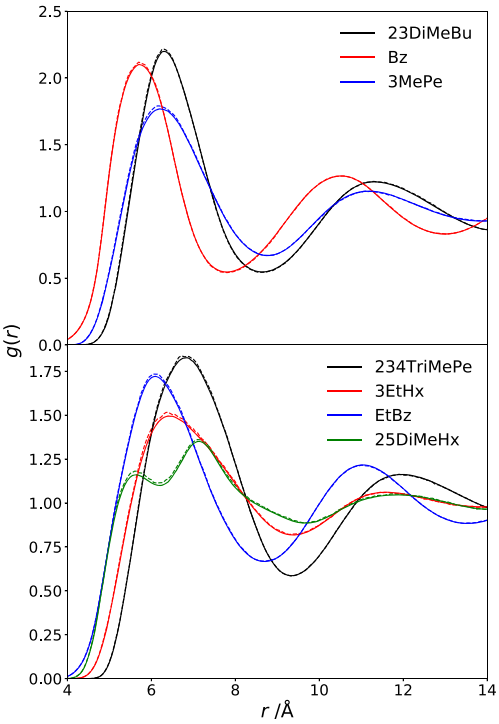

Figure 4. Comparison of center-of-mass radial distribution function obtained from atomistic (solid lines) and coarse-grained (dashed lines) simulations.

Table 4. Deviation between Atomistic and Coarse-Grained Radial Distribution Functions, Densities of All-Atom Simulation, Coarse-Grained Simulation and Experimental Densities

	δg/%	ρ_{AA}/g cm^{-3}	ρ_{CG}/g cm^{-3}	$\rho_{exp.}$/g cm^{-3}
benzene	0.35	0.874	0.874	0.873[a]
3-methylpentane	0.57	0.665	0.664	0.660[a]
2,3-dimethylbutane	0.50	0.680	0.675	0.658[a]
ethylbenzene	0.37	0.869	0.869	0.864[b]
2,3,4-trimethylpentane	0.34	0.730	0.730	0.716[a]
3-ethylhexane	0.57	0.705	0.704	0.710[a]
2,5-dimethylhexane	0.71	0.705	0.704	0.690[a]

[a]Value from ref 64. [b]Value from ref 65.

time step from a 10 ns trajectory (Figure 5). Diffusion coefficients are calculated by fitting the MSD versus time, with a linear function up to 7.5 ns. Table 5 lists the self-diffusion coefficients and the acceleration factor $\alpha = D_{CG}/D_{AA}$. Figure 6 uses 2,5-dimethylhexane as an example to show that the MSD of the all-atom and scaled coarse-grained simulation coincide above 0.15 ns and are in the diffusive regime. Only in the picosecond time scale, the scaled diffusion lies behind the atomistic diffusion. This might be due to the molecular rotational and conformational freedom, which only the AA model possesses.

3.4. Coarse-Graining and the Molecular Roughness Difference. The molecular roughness difference ΔR_a of the molecules ranges from 0.512 Å (Bz) to 0.969 Å (25DiMeHx). Aliphatic and aromatic molecules follow the same trend. The surfaces of 2,3-dimethylbutane and 2,5-dimethylhexane are

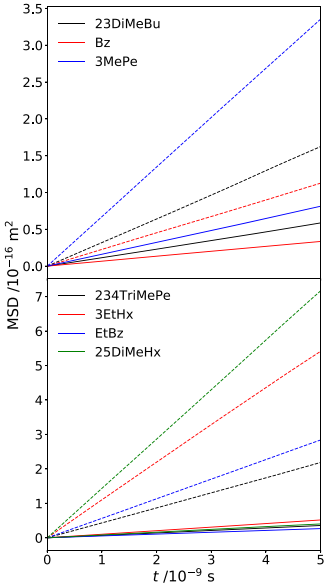

Figure 5. Comparison of the center-of-mass mean square displacement of all-atom (solid lines) and coarse-grained (dashed lines) simulations.

Table 5. Self-Diffusion Coefficients in 10^{-9} m^2 s^{-1} and Acceleration Factor α[a]

	D_{AA}	D_{CG}	α
2,3-dimethylbutane	1.96 (0.04)	5.46 (0.08)	2.78 (0.09)
benzene	1.12 (0.08)	3.77 (0.16)	3.37 (0.38)
3-methylpentane	2.74 (0.18)	11.21 (0.63)	4.10 (0.49)
2,3,4-trimethylpentane	1.20 (0.05)	7.29 (0.09)	6.09 (0.34)
3-ethylhexane	1.72 (0.12)	17.79 (1.01)	10.33 (1.32)
ethylbenzene	0.90 (0.03)	9.47 (0.35)	10.49 (0.72)
2,5-dimethylhexane	1.35 (0.02)	23.82 (1.24)	17.67 (1.23)

[a]Standard deviations between the individual Cartesian components are shown in parentheses.

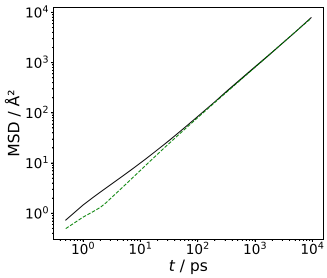

Figure 6. Comparison of center-of-mass mean square displacement of all-atom (solid line) and the scaled coarse-grained (dashed line) simulations of 2,5-dimethylhexane.

shown as examples in Figure 7. They show similarities in their structural formulas, with isopropyl structures on both sides, yet their ΔR_a values (0.515 Å for 23DiMeBu) differ by a factor of almost 1.9. The difference is that 2,5-dimethylhexane shows both a high *x*-elongation and low *y*- and *z*-values close to the center of mass of the molecule, which increases the roughness difference, while 2,3-dimethylbutane is rather spherical (Table 6).

https://dx.doi.org/10.1021/acs.jctc.9b00943
J. Chem. Theory Comput. 2020, 16, 1411−1419

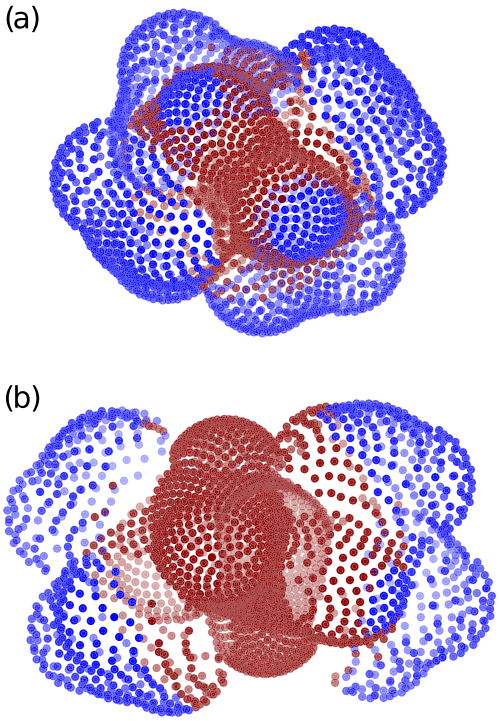

Figure 7. Grid of the all-atom molecular surface of 2,3-dimethylbutane (a) and 2,5-dimethylhexane (b) with 2501 grid points; the *x*-axis is horizontal and the *y*-axis is vertical; blue: peaks; red: valleys.

Table 6. Molecular Roughness Difference, Skewness, and Kurtosis Averaged over 200 Molecules for Each System[a]

	ΔR_a/Å	R_{sk}	R_{ku}
2,3-dimethylbutane	0.515 (0.031)	0.54 (0.12)	2.17 (0.15)
benzene	0.512 (0.006)	0.64 (0.02)	2.25 (0.01)
3-methylpentane	0.578 (0.031)	0.40 (0.12)	2.46 (0.19)
2,3,4-trimethylpentane	0.608 (0.031)	−0.20 (0.08)	2.31 (0.15)
3-ethylhexane	0.757 (0.036)	−0.46 (0.10)	2.19 (0.12)
ethylbenzene	0.767 (0.015)	−1.00 (0.06)	2.21 (0.11)
2,5-dimethylhexane	0.969 (0.042)	−0.87 (0.06)	1.77 (0.13)

[a]Standard deviations are shown in parentheses.

This influence of the molecular shape on ΔR_a is illustrated in Figure 8. The CG bead is a sphere, and hence the reference surface is a sphere, too. This geometry necessarily leads to certain features of the molecular roughness difference. The principal axis belonging to the largest eigenvalue is aligned with the *x*-axis. The remaining two principal axes thus point in the direction of *y*- and *z*-axis. Under the condition that $L_x/2 > r_{CG}$, which is true for all molecules analyzed, there will always be peaks in the directions of the *x*-component. Two structural characteristics, that highly influence ΔR_a can be identified:

1. *x*-Elongation: The elongation of the surface profile, the AA molecular surface, increases ΔR_a (Figure 8a→b).
2. *yz*-Arrangement: Assuming that the structure of the molecule is approximately determined by the arrangement of volume elements of a fixed size, the atoms, an arrangement with the lowest *y*- and *z*-values close to $x = 0$ leads to higher ΔR_a (Figure 8a→c).

We have also studied how the size of the reference sphere would change the roughness difference. It is noticeable in the change of sign of R_{sk}. An increase of r_{CG} can both increase and decrease ΔR_a. If the number of profile height points h_i with a negative sign is larger than the number of positive profile height points, ΔR_a is increased. However, an increase of r_{CG} always lowers R_{sk} as the distribution is shifted toward the valleys (Figure 8a→d). For all C6 molecules, the distribution is skewed toward the peaks; for all C8 molecules, it is skewed toward the valleys. Two alternative ways of defining the reference geometry, showing the sensitivity toward the choice of r_{CG}, are given in the Supporting Information.

The kurtosis of a normal distribution is 3. Thus, all of the molecules are platykurtic. 25DiMeHx has a lower kurtosis, with $R_{ku} = 1.77$, than that of all other molecules, with $R_{ku} = 2.32 \pm 0.15$. The kurtosis is affected by small deviations, caused by the H atoms, and large peaks and valleys due to different atomic arrangements caused by different bonding patterns and different number of atoms. While the small deviations are similar for all molecules, 2,5-dimethylhexane, being the molecule with the highest ΔR_a, has a very distinct valley (*yz*-Arrangement; Figure 7b), causing the reduction of R_{ku}.

3.5. Smoothening of the Molecular Surface and Mobility Acceleration upon Coarse-Graining. We now have the data in place to investigate the relation between the molecular roughness difference ΔR_a and the acceleration of the molecular mobility α, both introduced by coarse-graining. For the set of small hydrocarbon solvents of similar sizes but varied shapes, the relation between α and ΔR_a is close to being linear (correlation coefficient $R^2 = 0.996$; Figure 9).

$$\alpha = 32\ \text{Å}^{-1}\,(\Delta R_a - 0.43\ \text{Å}) \tag{19}$$

Generally, C6 molecules have lower ΔR_a and α values than C8 molecules, even though the values of 2,3,4-trimethylpentane are closer to those of 3-methylpentane than to those of other C8 molecules. It is to be expected that different C7 molecules can have both lower α than C6 molecules and higher α than C8 molecules. Even though ΔR_a does not even double, when the lowest and highest values are compared, α more than sextupled from a value of 2.78 (23DiMeBu) to 17.67 (25DiMeHx), showing that the acceleration factor is very sensitive to small changes in the roughness difference. The offset in ΔR_a by 0.43 Å means that no significant acceleration of dynamics upon coarse-graining should occur for small molecules with a ΔR_a below 0.43 Å. Unfortunately, we have not been able to find such a molecule. The roughness differences between fully atomistic (all-atom) and united-atom models, however, often fall into this range, and the self-diffusion coefficients for liquids are often very similar when simulated by both models.

As there is no physical observable "molecular surface", it must be subjectively defined. Different choices are possible and valid, and hence also the roughness difference can be quantified by different measures. We have experimented with a few other measures but have found ΔR_a, the average absolute surface deviation, to provide the best correlation with the acceleration of dynamics α. Other surface measures are included in the Supporting Information for reference but are not further discussed here.

4. CONCLUSIONS

In this work, a method to link the acceleration of the dynamics of a liquid system, as one moves from an atomistic to a coarse-

https://dx.doi.org/10.1021/acs.jctc.9b00943
J. Chem. Theory Comput. 2020, 16, 1411−1419

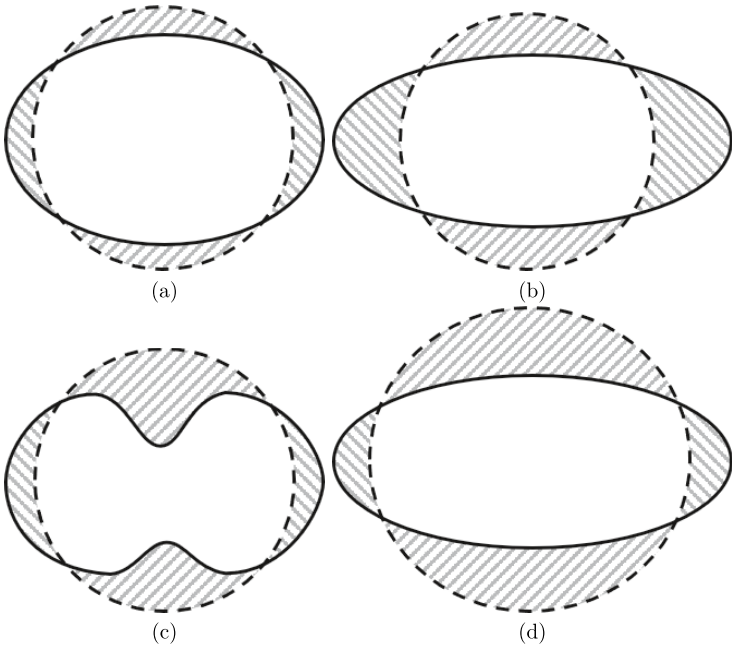

Figure 8. Schematic of the influence of molecular shape on molecular roughness descriptors: (a) solid: atomistic surface profile, dashed: reference (coarse-grained) surface, hatched: area of interest for molecular roughness calculation. (b) Effect of elongation: roughness difference increases. (c) Effect of increasing valley depths in directions orthogonal to the longest component: roughness difference increases, kurtosis decreases. (d) Effect of increasing radius of reference sphere: skewness decreases.

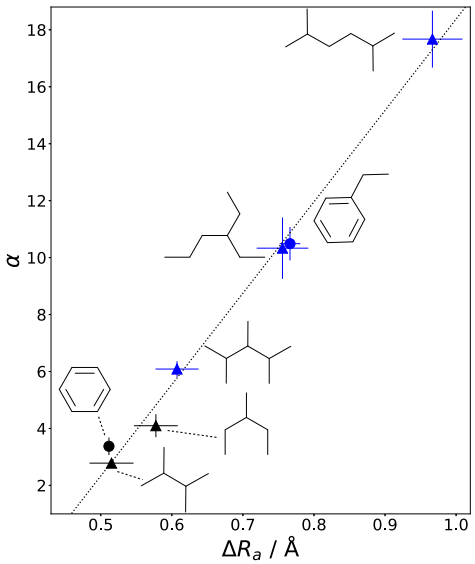

Figure 9. Acceleration factor against molecular roughness difference; error bars for the molecular roughness difference represent the standard deviation from averaging over the conformation of 200 molecules for each system; error bars for the acceleration factor are added up relative standard deviations between the individual Cartesian components. The line is the linear fit of eq 19.

grained model, to geometrical differences between the two models is developed. We found that the acceleration α, defined as the ratio of the self-diffusion coefficients of both models, is linearly related to the molecular roughness difference ΔR_a, which we define as the average absolute deviation between the molecular surfaces of the two models. The linear relation has been established using a test set of seven C6 and C8 hydrocarbons, and it shows a high correlation. The atomistic and coarse-grained molecular surfaces can be calculated as soon as the models are equilibrated in their structural properties. This means that the acceleration factor can be predicted solely from the geometry of the molecules in both resolutions if the observed correlation holds for other systems. Predictiveness is not relevant in the present study of low-molecular-weight liquids, for which the calculation of diffusion coefficients in both resolutions is not an issue. In many systems, however, dynamic quantities can only be calculated at the coarse-grained level, for example, in polymer melts. Here, the atomistic (and thus hopefully "true") mobility remains computationally inaccessible. In such cases, a reliable a priori estimate of the acceleration would make predictions of realistic dynamic properties possible, as dynamic quantities obtained in the coarse-grained simulation would be rescaled to achieve numbers, which can be compared to the experimental values. While being optimistic, we should also point at the untested aspects of our novel method. First, in this first step, it has only been tested on nonpolar small-molecule liquids. Applications to other chemical structures and other molecular sizes need to be tried. Second, we have used only ambient conditions. Recalibration of potential models is a known necessity as one changes the temperature[45] or, particularly, the density.[66]

■ ASSOCIATED CONTENT

Supporting Information

The Supporting Information is available free of charge at https://pubs.acs.org/doi/10.1021/acs.jctc.9b00943.

OPLS-AA bonded parameters of all-atom force field and alternative roughness difference calculations (PDF)

https://dx.doi.org/10.1021/acs.jctc.9b00943
J. Chem. Theory Comput. 2020, 16, 1411−1419

Tabulated coarse-grained potentials (ZIP)

AUTHOR INFORMATION

Corresponding Authors

Melissa K. Meinel − *Eduard-Zintl-Institut für Anorganische und Physikalische Chemie and Profile Area Thermofluids and Interfaces, Technische Universität Darmstadt D-64287 Darmstadt, Germany;* orcid.org/0000-0001-7369-3627; Email: m.meinel@theo.chemie.tu-darmstadt.de

Florian Müller-Plathe − *Eduard-Zintl-Institut für Anorganische und Physikalische Chemie and Profile Area Thermofluids and Interfaces, Technische Universität Darmstadt D-64287 Darmstadt, Germany;* orcid.org/0000-0002-9111-7786; Email: f.mueller-plathe@theo.chemie.tu-darmstadt.de

Complete contact information is available at: https://pubs.acs.org/10.1021/acs.jctc.9b00943

Notes

The authors declare no competing financial interest.

ACKNOWLEDGMENTS

M.K.M. would like to thank Aaron Meinel for his support and critical reading of this manuscript. Support by the Collaborative Research Center 146 "Multiscale Simulation Methods for Soft Matter Systems" is gratefully acknowledged.

REFERENCES

(1) Müller-Plathe, F. Coarse-Graining in Polymer Simulation: From the Atomistic to the Mesoscopic Scale and Back. *ChemPhysChem* **2002**, *3*, 754−769.

(2) Depa, P.; Chen, C.; Maranas, J. K. Why are coarse-grained force fields too fast? A look at dynamics of four coarse-grained polymers. *J. Chem. Phys.* **2011**, *134*, No. 014903.

(3) Izvekov, S.; Voth, G. A. Modeling real dynamics in the coarse-grained representation of condensed phase systems. *J. Chem. Phys.* **2006**, *125*, No. 151101.

(4) Shillcock, J. C.; Lipowsky, R. The computational route from bilayer membranes to vesicle fusion. *J. Phys.: Condens. Matter* **2006**, *18*, S1191−S1219.

(5) Shen, H.; Xia, Z.; Li, G.; Ren, P. A Review of Physics-Based Coarse-Grained Potentials for the Simulations of Protein Structure and Dynamics. *Annu. Rep. Comput. Chem.* **2012**, *8*, 129−148.

(6) Kmiecik, S.; Gront, D.; Kolinski, M.; Wieteska, L.; Dawid, A. E.; Kolinski, A. Coarse-Grained Protein Models and Their Applications. *Chem. Rev.* **2016**, *116*, 7898−7936.

(7) Trément, S.; Schnell, B.; Petitjean, L.; Couty, M.; Rousseau, B. Conservative and dissipative force field for simulation of coarse-grained alkane molecules: A bottom-up approach. *J. Chem. Phys.* **2014**, *140*, No. 134113.

(8) Wagner, J. W.; Dama, J. F.; Durumeric, A. E. P.; Voth, G. A. On the representability problem and the physical meaning of coarse-grained models. *J. Chem. Phys.* **2016**, *145*, No. 044108.

(9) Dunn, N. J. H.; Noid, W. G. Bottom-up coarse-grained models that accurately describe the structure, pressure, and compressibility of molecular liquids. *J. Chem. Phys.* **2015**, *143*, No. 243148.

(10) Rudzinski, J. F.; Noid, W. G. Coarse-graining entropy, forces, and structures. *J. Chem. Phys.* **2011**, *135*, No. 214101.

(11) Hsu, D. D.; Xia, W.; Arturo, S. G.; Keten, S. Thermomechanically Consistent and Temperature Transferable Coarse-Graining of Atactic Polystyrene. *Macromolecules* **2015**, *48*, 3057−3068.

(12) Sokkar, P.; Choi, S. M.; Rhee, Y. M. Simple Method for Simulating the Mixture of Atomistic and Coarse-Grained Molecular Systems. *J. Chem. Theory Comput.* **2013**, *9*, 3728−3739.

(13) Ingólfsson, H. I.; Lopez, C. A.; Uusitalo, J. J.; de Jong, D. H.; Gopal, S. M.; Periole, X.; Marrink, S. J. The power of coarse graining in biomolecular simulations. *Wiley Interdiscip. Rev.: Comput. Mol. Sci.* **2014**, *4*, 225−248.

(14) Shell, M. S. The relative entropy is fundamental to multiscale and inverse thermodynamic problems. *J. Chem. Phys.* **2008**, *129*, No. 144108.

(15) Depa, P. K.; Maranas, J. K. Speed up of dynamic observables in coarse-grained molecular-dynamics simulations of unentangled polymers. *J. Chem. Phys.* **2005**, *123*, No. 094901.

(16) Lyubimov, I.; Guenza, M. G. First-principle approach to rescale the dynamics of simulated coarse-grained macromolecular liquids. *Phys. Rev. E* **2011**, *84*, No. 031801.

(17) Rudzinski, J. F. Recent Progress towards Chemically-Specific Coarse-Grained Simulation Models with Consistent Dynamical Properties. *Computation* **2019**, *7*, 42.

(18) Guenza, M. Thermodynamic consistency and other challenges in coarse-graining models. *Eur. Phys. J.: Spec. Top.* **2015**, *224*, 2177−2191.

(19) Peters, B. L.; Salerno, K. M.; Agrawal, A.; Perahia, D.; Grest, G. S. Coarse-Grained Modeling of Polyethylene Melts: Effect on Dynamics. *J. Chem. Theory Comput.* **2017**, *13*, 2890−2896.

(20) Knoch, F.; Schäfer, K.; Diezemann, G.; Speck, T. Dynamic coarse-graining fills the gap between atomistic simulations and experimental investigations of mechanical unfolding. *J. Chem. Phys.* **2018**, *148*, No. 044109.

(21) Padding, J. T.; Briels, W. J. Time and length scales of polymer melts studied by coarse-grained molecular dynamics simulations. *J. Chem. Phys.* **2002**, *117*, 925−943.

(22) Akkermans, R. L. C.; Briels, W. J. Coarse-grained dynamics of one chain in a polymer melt. *J. Chem. Phys.* **2000**, *113*, 6409−6422.

(23) Hijón, C.; Español, P.; Vanden-Eijnden, E.; Delgado-Buscalioni, R. Mori-Zwanzig formalism as a practical computational tool. *Faraday Discuss.* **2010**, *144*, 301−322.

(24) Qian, H.-J.; Liew, C. C.; Müller-Plathe, F. Effective control of the transport coefficients of a coarse-grained liquid and polymer models using the dissipative particle dynamics and Lowe-Andersen equations of motion. *Phys. Chem. Chem. Phys.* **2009**, *11*, 1962−1969.

(25) Markutsya, S.; Lamm, M. H. A coarse-graining approach for molecular simulation that retains the dynamics of the all-atom reference system by implementing hydrodynamic interactions. *J. Chem. Phys.* **2014**, *141*, No. 174107.

(26) Fu, C.-C.; Kulkarni, P. M.; Shell, M. S.; Leal, L. G. A test of systematic coarse-graining of molecular dynamics simulations: Transport properties. *J. Chem. Phys.* **2013**, *139*, No. 094107.

(27) Lemarchand, C. A.; Couty, M.; Rousseau, B. Coarse-grained simulations of cis- and trans-polybutadiene: A bottom-up approach. *J. Chem. Phys.* **2017**, *146*, No. 074904.

(28) Davtyan, A.; Dama, J. F.; Voth, G. A.; Andersen, H. C. Dynamic force matching: A method for constructing dynamical coarse-grained models with realistic time dependence. *J. Chem. Phys.* **2015**, *142*, No. 154104.

(29) Davtyan, A.; Voth, G. A.; Andersen, H. C. Dynamic force matching: Construction of dynamic coarse-grained models with realistic short time dynamics and accurate long time dynamics. *J. Chem. Phys.* **2016**, *145*, No. 224107.

(30) Dinpajooh, M.; Guenza, M. G. Coarse-graining simulation approaches for polymer melts: the effect of potential range on computational efficiency. *Soft Matter* **2018**, *14*, 7126−7144.

(31) Shell, M. S. Systematic coarse-graining of potential energy landscapes and dynamics in liquids. *J. Chem. Phys.* **2012**, *137*, No. 084503.

(32) Fritz, D.; Koschke, K.; Harmandaris, V. A.; van der Vegt, N. F. A.; Kremer, K. Multiscale modeling of soft matter: scaling of dynamics. *Phys. Chem. Chem. Phys.* **2011**, *13*, 10412−10420.

(33) Song, J.; Hsu, D. D.; Shull, K. R.; Phelan, F. R.; Douglas, J. F.; Xia, W.; Keten, S. Energy Renormalization Method for the Coarse-Graining of Polymer Viscoelasticity. *Macromolecules* **2018**, *51*, 3818−3827.

(34) Xia, W.; Song, J.; Hansoge, N. K.; Phelan, F. R.; Keten, S.; Douglas, J. F. Energy Renormalization for Coarse-Graining the Dynamics of a Model Glass-Forming Liquid. *J. Phys. Chem. B* **2018**, *122*, 2040−2045.

(35) Xia, W.; Hansoge, N. K.; Xu, W.-S.; Phelan, F. R.; Keten, S.; Douglas, J. F. Energy renormalization for coarse-graining polymers having different segmental structures. *Sci. Adv.* **2019**, *5*, No. eaav4683.
(36) Lyubimov, I. Y.; Guenza, M. G. Theoretical reconstruction of realistic dynamics of highly coarse-grained cis-1,4-polybutadiene melts. *J. Chem. Phys.* **2013**, *138*, No. 12A546.
(37) Nielsen, S. O.; Lopez, C. F.; Srinivas, G.; Klein, M. L. Coarse grain models and the computer simulation of soft materials. *J. Phys.: Condens. Matter* **2004**, *16*, R481−R512.
(38) Depa, P. K.; Maranas, J. K. Dynamic evolution in coarse-grained molecular dynamics simulations of polyethylene melts. *J. Chem. Phys.* **2007**, *126*, No. 054903.
(39) Harmandaris, V.; Kremer, K. Dynamics of Polystyrene Melts through Hierarchical Multiscale Simulations. *Macromolecules* **2009**, *42*, 791−801.
(40) Chen, C.; Depa, P.; Maranas, J. K.; Garcia Sakai, V. Comparison of explicit atom, united atom, and coarse-grained simulations of poly(methyl methacrylate). *J. Chem. Phys.* **2008**, *128*, No. 124906.
(41) Fraaije, J. G. E. M.; van Male, J.; Becherer, P.; Serral Gracià, R. Coarse-Grained Models for Automated Fragmentation and Parametrization of Molecular Databases. *J. Chem. Inf. Model.* **2016**, *56*, 2361−2377.
(42) Fraaije, J. G. E. M.; van Male, J.; Becherer, P.; Serral Gracià, R. Calculation of Diffusion Coefficients through Coarse-Grained Simulations Using the Automated-Fragmentation-Parametrization Method and the Recovery of Wilke-Chang Statistical Correlation. *J. Chem. Theory Comput.* **2018**, *14*, 479−485.
(43) Karimi-Varzaneh, H. A.; van der Vegt, N. F. A.; Müller-Plathe, F.; Carbone, P. How Good Are Coarse-Grained Polymer Models? A Comparison for Atactic Polystyrene. *ChemPhysChem* **2012**, *13*, 3428−3439.
(44) Fritz, D.; Herbers, C. R.; Kremer, K.; van der Vegt, N. F. A. Hierarchical modeling of polymer permeation. *Soft Matter* **2009**, *5*, 4556−4563.
(45) Farah, K.; Fogarty, A. C.; Böhm, M. C.; Müller-Plathe, F. Temperature dependence of coarse-grained potentials for liquid hexane. *Phys. Chem. Chem. Phys.* **2011**, *13*, 2894−2902.
(46) Qian, H.-J.; Carbone, P.; Chen, X.; Karimi-Varzaneh, H. A.; Liew, C. C.; Müller-Plathe, F. Temperature-Transferable Coarse-Grained Potentials for Ethylbenzene, Polystyrene, and Their Mixtures. *Macromolecules* **2008**, *41*, 9919−9929.
(47) Carbone, P.; Varzaneh, H. A. K.; Chen, X.; Müller-Plathe, F. Transferability of coarse-grained force fields: The polymer case. *J. Chem. Phys.* **2008**, *128*, No. 064904.
(48) Ghabrial, S. R.; Zaghlool, S. A. The effect of surface roughness on static friction. *Int. J. Math. Tool Des. Res.* **1974**, *14*, 299−309.
(49) Ivković, B.; Djurdjanović, M.; Stamenković, D. The influence of the contact surface roughness on the static friction coefficient. *Tribol. Ind.* **2000**, *22*, 41−44.
(50) Charsetad, H.; Khorsandijou, S. Effect of surface roughness on steel-steel dry friction coefficient. *J. Mech. Res. Appl.* **2012**, *4*, 45−56.
(51) Al-Samarai, R.; Haftirman; Ahmad, K. R.; Al-Douri, Y. The Influence of Roughness on the Wear and Friction Coefficient under dry and lubricated sliding. *Int. J. Sci. Eng. Res.* **2012**, *3*, 1−6.
(52) Funke, R.; Schubert, A. Increase of the Coefficient of Static Friction Using Turn-Milling With an Inclined Milling Spindle. *Procedia CIRP* **2016**, *45*, 83−86.
(53) Liang, G.; Schmauder, S.; Lyu, M.; Schneider, Y.; Zhang, C.; Han, Y. An Investigation of the Influence of Initial Roughness on the Friction and Wear Behavior of Ground Surfaces. *Materials* **2018**, *11*, 237.
(54) Menezes, P. L.; Kishore; Kailas, S. V. Influence of roughness parameters on coefficient of friction under lubricated conditions. *Sadhana* **2008**, *33*, 181−190.
(55) Menezes, P.; Kailas, S. Role of surface texture and roughness parameters on friction and transfer film formation when UHMWPE sliding against steel. *Biosurf. Biotribol.* **2016**, *2*, 1−10.
(56) Parthasarathi, N. L.; Borah, U.; Albert, S. Correlation between coefficient of friction and surface roughness in dry sliding wear of AISI 316 L (N) stainless steel at elevated temperatures. *Comput. Model. New Technol.* **2013**, *17*, 51−63.
(57) Stoudt, M. R.; Hubbard, J. B.; Mates, S. P.; Green, D. E. Evaluating the Relationships Between Surface Roughness and Friction Behavior During Metal Forming. *SAE Tech. Pap.* **2005**, *114*−*115*, 183−190.
(58) Reith, D.; Pütz, M.; Müller-Plathe, F. Deriving effective mesoscale potentials from atomistic simulations. *J. Comput. Chem.* **2003**, *24*, 1624−1636.
(59) Plimpton, S. Fast Parallel Algorithms for Short-Range Molecular Dynamics. *J. Comput. Phys.* **1995**, *117*, 1−19.
(60) Jewett, A. I.; Zhuang, Z.; Shea, J.-E. Moltemplate a Coarse-Grained Model Assembly Tool. *Biophys. J* **2013**, *104*, 169a.
(61) Sun, H. COMPASS: An ab Initio Force-Field Optimized for Condensed-Phase Applications Overview with Details on Alkane and Benzene Compounds. *J. Phys. Chem. B* **1998**, *102*, 7338−7364.
(62) Jorgensen, W. L.; Maxwell, D. S.; Tirado-Rives, J. Development and Testing of the OPLS All-Atom Force Field on Conformational Energetics and Properties of Organic Liquids. *J. Am. Chem. Soc.* **1996**, *118*, 11225−11236.
(63) Swinbank, R.; Purser, J. R. Fibonacci grids: A novel approach to global modelling. *Q. J. R. Meteorol. Soc* **2006**, *132*, 1769−1793.
(64) Yaws, C. L.; Pike, R. W. *Thermophysical Properties of Chemicals and Hydrocarbons*; Yaws, C. L., Ed.; William Andrew Publishing: Norwich, NY, 2009; Chapter 3, pp 106−197.
(65) Karpińska, M.; Domańska, U.; Wlazlo, M. Separation of Ethylbenzene/styrene Systems Using Ionic Liquids in Ternary Lle. *J. Chem. Thermodyn.* **2016**, *103*, 423−431.
(66) Berweger, C. D.; van Gunsteren, W. F.; Müller-Plathe, F. Force field parametrization by weak coupling. Re-engineering SPC water. *Chem. Phys. Lett.* **1995**, *232*, 429−436.

https://dx.doi.org/10.1021/acs.jctc.9b00943
J. Chem. Theory Comput. 2020, 16, 1411−1419

4.2 Roughness Volumes: An Improved RoughMob Concept for Predicting the Increase of Molecular Mobility upon Coarse-Graining

THE JOURNAL OF PHYSICAL CHEMISTRY B
A JOURNAL OF THE AMERICAN CHEMICAL SOCIETY

pubs.acs.org/JPCB

Article

Roughness Volumes: An Improved RoughMob Concept for Predicting the Increase of Molecular Mobility upon Coarse-Graining

Published as part of The Journal of Physical Chemistry virtual special issue "Doros N. Theodorou Festschrift".

Melissa K. Meinel* and Florian Müller-Plathe*

Cite This: *J. Phys. Chem. B* 2022, 126, 3737−3747

Read Online

ACCESS | Metrics & More | Article Recommendations | Supporting Information

ABSTRACT: The reduced number of degrees of freedom in a coarse-grained molecular model compared to its parent atomistic model not only makes it possible to simulate larger systems for longer time scales but also results in an artificial mobility increase. The RoughMob method [Meinel, M. K. and Müller-Plathe, F. *J. Chem. Theory Comput.* **2020**, *16*, 1411.] linked the acceleration factor of the dynamics to the loss of geometric information upon coarse-graining. Our hypothesis is that coarse-graining a multiatom molecule or group into a single spherical bead smooths the molecular surface and, thus, leads to reduced intermolecular friction. A key parameter is the molecular roughness difference, which is calculated via a numerical comparison of the molecular surfaces of both the atomistic and coarse-grained models. Augmenting the RoughMob method, we add the concept of the region where the roughness acts. This information is contained in four so-called roughness volumes. For 17 systems of homogeneous hydrocarbon fluids, simple one-bead coarse-grained models are derived by the structure-based iterative Boltzmann inversion. They include 13 different homogeneous aliphatic and aromatic molecules and two different mapping schemes. We present a simple way to correlate the roughness volumes to the acceleration factor. The resulting relation is able to a priori predict the acceleration factors for an extended size and shape range of hydrocarbon molecules, with different mapping schemes and different densities.

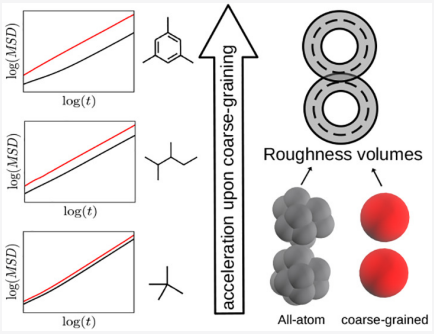

INTRODUCTION

All-atom (AA) molecular dynamics (MD) simulations provide detailed information about different properties such as molecular structures and thermodynamic or transport properties. However, simulations of large systems or on long time scales can be too demanding to be carried out atomistically. Bottom-up coarse-grained models are derived systematically to match certain target properties of the parent all-atom system, often structural properties.[1] Several atoms are thereby coarse-grained into one super atom, in the following called a coarse-grained (CG) bead. The reduced number of degrees of freedom and the smaller number of simulated sites per molecule reduce the computational costs. Compared to its parent atomistic model, the dynamics of a coarse-grained model is usually accelerated: The mobility of the CG beads is higher than that of the chemical groups they represent.[2−7] This acceleration allows the simulation of longer time scales and, thereby, increases the computational efficiency further. However, it precludes the calculation of dynamical and transport quantities. In order to enable predictive calculations of, say, diffusion coefficients or shear viscosities, a time mapping is needed, preferably one which can be determined a priori at the time of coarse-graining and which does not require long atomistic reference simulations. Based on the assumption that different dynamical properties are accelerated by the same factor, we focus in this work on the rescaling of the diffusion coefficient with the scaling or acceleration factor α. It is defined as the ratio of the diffusion coefficients of the CG and the parent AA models.

$$D_{AA} = \frac{1}{\alpha} D_{CG} \tag{1}$$

Common explanations of acceleration are the smoother coarse-grained potential and the elimination of degrees of freedom, which provide the "friction" that restricts the mobility in the atomistic model.[8] While the qualitative reasons behind the acceleration are well understood, the improvement of methods to quantitatively account for the acceleration is still an ongoing issue. A variety of solutions have been proposed to determine the acceleration factor a priori without having to run the expensive all-atom simulation long enough to calculate the dynamics of the all-atom system. These efforts target relative entropy[9,10] or excess entropy scaling[11−13] or derive an

Received: February 8, 2022
Revised: April 24, 2022
Published: May 13, 2022

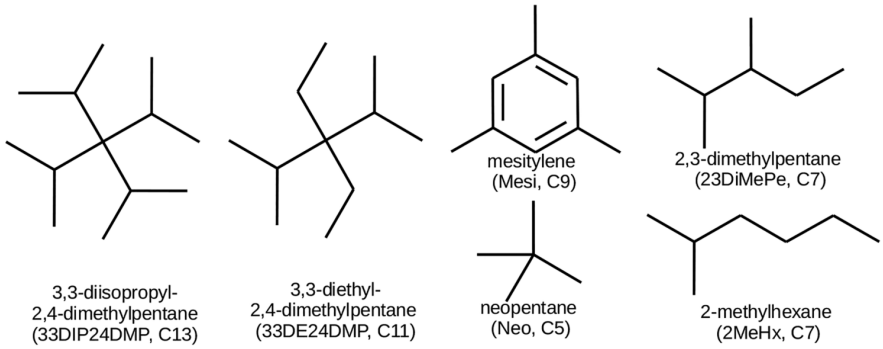

Figure 1. Simulated molecules, their abbreviated name, and the number of carbon atoms.

expression for the monomeric friction coefficient by a first-principle analytical approach starting from the Ornstein–Zernike equation[3,14] or use a biasing potential.[7,15]

As an alternative to rescaling approaches, dynamic properties such as the diffusion coefficients can be included in the set of target properties to be reproduced by the coarse-grained model. This aims at accounting for the physical reasons behind the speed-up and thereby generating a CG model with correct dynamics.[16−23] In our experience, this approach can lead to other structural or thermodynamic properties actually becoming worse, and in some cases, the increase in computational efficiency is diminished or destroyed.

In ref 24, we proposed a method, in the following referred to as the RoughMob method, that connects the change in a molecular surface *roughness* (Rough) to the change in the *mobility* (Mob). The friction is interpreted as an actual mechanical friction that changes upon the change of the molecular surface. The parameter we called *molecular roughness difference* is calculated by a numerical comparison of the hard molecular surfaces (excluded-volumes) of the AA and CG surfaces. The surfaces of both models are represented as numerical grids. The molecular roughness difference is then calculated as the average absolute deviation of the molecular all-atom surface from the molecular coarse-grained surface. It solely exists as a comparative quantity, and no connection between the diffusion coefficient and a roughness of a single system is established. The method has been developed using seven uncharged, apolar, and homogeneous systems of aliphatic and aromatic molecules and has proven capable of estimating the acceleration of spherical hydrocarbons in the range of six (C6) to eight (C8) carbon atoms that are coarse-grained into a single CG bead per molecule. However, the addition of a broader range of hydrocarbons reveals weaknesses, especially when larger molecules are added. Various studies suggest that the acceleration factor is dependent on the molar mass[25] or on the degree of coarse-graining.[26,27] So far, the RoughMob method has been limited to a small size range. In this paper, we investigate hydrocarbons with five (C5) to 13 (C13) carbon atoms and thereby broaden the molecular size and asphericity range of the investigated molecules. We analyze them in terms of four roughness volumes that all depend on the molecular roughness difference. This allows for including not only the change of the molecular roughness itself but also the volume in which this change takes place (*active volumes*) and, even more importantly, where it does not (*passive volume*). The scaling factor also changes between mapping schemes.[28] Therefore, we test two different mapping schemes for four of the original C6 and C8 hydrocarbons.

All systems are simulated under ambient conditions. Recalibration of the CG potentials for different simulated state points is a known requirement,[29−33] although some efforts are directed toward the development of temperature-transferable CG models.[34−37] However, being a geometrical parameter the molecular roughness difference is not expected to change much with the temperature, while the acceleration factor is known to decrease with an increasing temperature.[19,26,38] This provides additional motivation to include not only the value of the molecular roughness difference in the RoughMob method but also differences in its impact, e.g., due to different densities and molecular sizes. With an increasing temperature, the density usually decreases and with it, likely, the impact of the molecular roughness difference, as the molecules are further apart.

Prediction of the acceleration factor will become especially relevant for large or complex systems, such as polymers,[1,8] surfactants,[39] and proteins.[40] In this method development, we focus on low-molecular-weight liquids that are coarse-grained into one bead per molecule in order to distinguish between the impact of active and passive volumes. We do not yet consider the contribution of, for example, overlapping neighboring CG beads in polymer molecules. However, the degree of coarse-graining (5 to 13 C atoms) is chosen with the application of the method to polymer melts in mind, where one monomer is represented by one or two CG beads, which typically fit this number of atoms collected into one CG bead.

SIMULATION DETAILS AND MODELS

The RoughMob method has been developed using a set of seven hydrocarbon liquids, five of them alkanes and two of them aromatic molecules, with six or eight carbon atoms. They are listed in Table 2, together with the newly added liquids. For their structure, see ref 24. Figure 1 shows the structure of the molecules added to the set in this article. 2-Methylhexane and 2,3-dimethylpentane are not symmetrical along the longest chain. Neopentane, mesitylene, 3,3-diethyl-2,4-dimethylpentane, and 3,3-diisopropyl-2,4-dimethylpentane extend the simulated systems to a range of smaller and larger molecules.

Both AA and CG MD simulations are performed with the LAMMPS simulation tool[41] under periodic boundary conditions in three dimensions. To generate the AA configurations, 512 to 1000 molecules are placed in a cubic simulation box with a side length of 100 Å using Moltemplate.[42] The orientations and conformations of the molecules are randomized by Brownian dynamics at 900 K for 0.2 ns, followed by canonical

https://doi.org/10.1021/acs.jpcb.2c00944
J. Phys. Chem. B 2022, 126, 3737−3747

(*NVT*) molecular dynamics for 0.5 ns. Using two simulations of 0.5 ns each under *NPT* conditions, the system is cooled down to 298.15 K at 500 atm, and the pressure is decreased to 1 atm.

Equilibration and production runs are carried out under isothermal−isobaric (*NPT*) conditions at 1 atm and 298.18 K using a velocity-Verlet integrator. Constant temperature and pressure are maintained with both a Nosé−Hoover thermostat (τ_T = 50 fs) and a barostat (τ_p = 500 fs). All systems are equilibrated (self-diffusion coefficients of two successive 2 ns time intervals differ by less than 10%) for 10 ns with a time step of Δt = 0.5 fs, followed by production runs of 10 ns using the same time step.

All-Atom Model. All-atom (AA) interactions are modeled with the fully flexible OPLS-AA force field. The nonbonded parameters are given in Table 1. Nonbonded interactions are treated with a spherical cutoff distance of 11 Å. A scaling factor of 0.5 is applied to nonbonded 1,4-intramolecular interactions, and geometric combination rules are applied for interactions between different species. Standard long-range van der Waals corrections are added to the energy and pressure during the simulations.[43] The bonded force-field parameters are given in the Supporting Information.

Table 1. OPLS-AA Force-Field Nonbonded Energy Parameters[44]

atom type	description	ϵ (kcal mol^{-1})	σ (Å)	q (e)
CT_{CH3}	aliphatic carbon (CH_3)	0.066	3.5	−0.18
CT_{CH2}	aliphatic carbon (CH_2)	0.066	3.5	−0.12
CT_{CH}	aliphatic carbon (CH)	0.066	3.5	−0.06
CT_{CA}	aliphatic carbon bonded to aromatic carbon	0.066	3.5	−0.005
HC	aliphatic hydrogen	0.030	2.5	0.06
CA	aromatic carbon	0.070	3.55	−0.115
HA	aromatic hydrogen	0.030	2.42	0.115

Coarse-Grained Model. In the CG model, each molecule is represented by a single CG bead. Thus, no bonded parameters are needed. The tabulated nonbonded CG potentials are derived by the iterative Boltzmann inversion[1,45] using VOTCA[46] and provided in the Supporting Information. The initial coordinates of the CG systems are generated from a single frame of the AA production run. Two different mapping schemes are used. All systems are coarse-grained with the CG bead positioned at the center of mass of the parent AA molecule ("COM-mapping"). Four systems are additionally simulated with the CG bead positioned on the third carbon atom of the pentane chain (234TriMePe, 3MePe, 23DiMePe, for short-hand notation, see Table 2) or the second carbon atom of the butane chain (23DiMeBu), respectively, which carry a methyl group ("methyl C-mapping"). The initial potential guess is derived by simple Boltzmann inversion. The potential is then updated iteratively until the CG radial distribution function (RDF) matches the RDF of the target AA system. The cutoff radii r_{cut} used for the CG potentials are given in the Supporting Information. The error between the CG-RDF $g^{CG}(r)$ and target RDF $g^{AA}(r)$ (eq 2[19]) is less than 1% for all systems. During the iterative Boltzmann inversion a pressure correction is applied.[45]

$$\delta g = \frac{\int_0^{r_{cut}} |g^{CG}(r) - g^{AA}(r)|\, dr}{\int_0^{r_{cut}} g^{AA}(r)\, dr} \tag{2}$$

Dynamic Properties. The self-diffusion coefficients of the molecules D are determined from their center-of-mass mean square displacement (MSD) using the Einstein relation. The averaged center-of-mass MSD is calculated using every 1000th time step from a 10 ns trajectory, and diffusion coefficients are calculated from the linear fit function of the MSD against the time up to 7.5 ns. The acceleration of dynamics α is

Table 2. Names of the Molecules, Their Abbreviations, and Numbers as Used in the Figure[a]

	molecule name	abbreviation	D_{AA}	D_{CG}	α
		Alkanes, COM-Mapped			
1	*neopentane	Neo	1.64 (0.05)	2.69 (0.12)	1.64 (0.13)
2	2,3-dimethylbutane	23DiMeBu	1.96 (0.04)	5.46 (0.08)	2.78 (0.09)
3	3-methylpentane	3MePe	2.74 (0.18)	11.21 (0.63)	4.10 (0.49)
4	*2,3-dimethylpentane	23DiMePe	2.22 (0.11)	10.56 (0.50)	4.75 (0.46)
5	2,3,4-trimethylpentane	234TriMePe	1.20 (0.05)	7.29 (0.09)	6.09 (0.34)
6	3-ethylhexane	3EtHx	1.72 (0.12)	17.79 (1.01)	10.33 (1.32)
7	*3,3-diethyl-2,4-dimethylpentane	33DE24DMP	0.31 (0.02)	3.54 (0.17)	11.40 (1.21)
8	*2-methylhexane	2MeHx	2.18 (0.02)	25.39 (0.32)	11.66 (0.25)
9	2,5-dimethylhexane	25DiMeHx	1.35 (0.02)	23.82 (1.24)	17.67 (1.23)
10	*3,3-diisopropyl-2,4-dimethylpentane	33DIP24DMP	0.076 (0.01)	1.64 (0.07)	21.67 (3.84)
		Aromatic Molecules, COM-Mapped			
11	benzene	Bz	1.12 (0.08)	3.77 (0.16)	3.37 (0.38)
12	ethylbenzene	EtBz	0.90 (0.03)	9.47 (0.35)	10.49 (0.72)
13	*mesitylene	Mesi	0.52 (0.04)	8.92 (0.31)	17.17 (1.90)
		Alkanes, Methyl C-Mapped			
3c	*3-methylpentane	3MePe	2.74 (0.14)	14.09 (0.57)	5.15 (0.48)
4c	*2,3-dimethylpentane	23DiMePe	2.22 (0.11)	13.75 (0.32)	6.19 (0.45)
2c	*2,3-dimethylbutane	23DiMeBu	1.96 (0.03)	12.50 (0.22)	6.37 (0.20)
5c	*2,3,4-trimethylpentane	234TriMePe	1.20 (0.04)	9.94 (0.21)	8.30 (0.47)

[a]Self-diffusion coefficients are in 10^{-9} m^2 s^{-1}, and the acceleration factor is represented as α; standard deviations between the individual Cartesian components are shown in parentheses. The asterisked molecules with their respective mapping scheme have been added in this contribution; the others were part of the test set of ref 24 previously.

https://doi.org/10.1021/acs.jpcb.2c00944
J. Phys. Chem. B 2022, 126, 3737−3747

characterized as the ratio of diffusion coefficients of the CG and AA models. The diffusion coefficients of the AA models range from 0.076×10^{-9} m^2 s^{-1} (33DIP25DMP) to 2.74×10^{-9} m^2 s^{-1} (3MePe). The scaling factor ranges from 1.64 (Neo) to 21.67 (33DIP25DMP) (Table 2). The methyl C-mapped alkanes show a larger acceleration than their COM-mapped equivalents.

ROUGHMOB METHOD

To determine the molecular roughness difference ΔR, hard molecular surfaces of the AA and the CG molecules are defined based on the nonbonded interactions. For the all-atom system, the radius of an atom is defined as half the size of its Lennard-Jones size parameter σ. The radius of the CG bead is taken from the tabulated CG potentials (Supporting Information) as half the radius where the potential first equals zero, thus as the effective hard sphere radius. A Fibonnaci grid of $n_{grid} = 2501$ rays is superposed on both the AA and the CG molecules. The Fibonacci method provides for an almost uniform distribution of ray directions. The molecular CG surface is thus described by vectors of equal length r_{CG}, and the surface of the AA surface is described by vectors or different length r_{AA}. The molecular roughness difference is then calculated according to eq 3 as the average absolute deviation of the AA surface from the CG surface.[24]

$$\Delta R = \frac{1}{n_{grid}} \sum_{i=1}^{n_{grid}} |r_{AA}^{(i)} - r_{CG}| \tag{3}$$

Figure 2 shows the acceleration of dynamics plotted against the molecular roughness difference for both the seven hydrocarbon systems used originally to develop the RoughMob method[24] and the newly added molecules, broadening the size range from C5 to C13 molecules and including different mapping schemes. 2,3-Dimethylpentane (4), mesitylene (13), and the methyl-C mapped alkanes (2c,3c,4c,5c)—all shown in green—could be predicted with the linear fit function derived in ref 24. The predicted acceleration factor of 2MeHx (*blue*, 8) is too high, and the predicted acceleration factors of Neo (1), 33DE24DMP (7), and 33DIP24DMP (10) are too low. Especially for larger near-spherical molecules like 33DE24DMP and 33DIP24DMP, and under the assumption that the radius of the coarse-grained bead is at least as large as the narrowest part of the AA surface, the value of the molecular roughness difference is mainly limited by the ups and downs on the AA surface caused by H atoms. The molecular roughness difference thus does not properly account for the increasing size of the molecule, while it is known from different studies, that an increasing molar mass or number of atoms that are coarse-grained into one CG bead increases the acceleration of dynamics upon coarse-graining.[25−27] In the following, a means to include the effects of an increasing size or a larger asphericity into the RoughMob method is presented by changing from the molecular roughness difference ΔR as key descriptor to the prediction of the acceleration factor α with volumes that are derived using the molecular roughness difference.

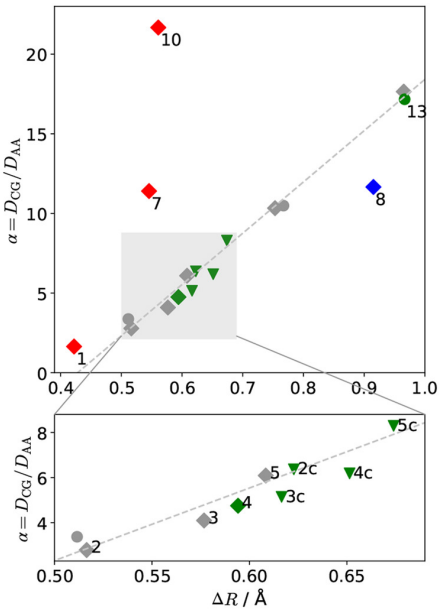

Figure 2. Acceleration factor against molecular roughness difference; *gray*: original seven, *green*: absolute deviation of predicted α equal to or less than 1 from calculated α; *red*: predicted α lower than calculated α; *blue*: predicted α higher than calculated α; *diamond*: *alkane*; circle: aromatic molecule; *triangle*: methyl C-mapped alkane; numbers see Table 2.

Roughness Volumes. The molecular roughness difference is a comparative quantity, which quantifies the deviation between the CG molecular surfaces and the AA molecular surface in absolute terms. The calculation uses vectors, resulting in one length parameter, that carries the information on *how much* the roughness changes upon coarse-graining. In order to extend the method to a broader range of sizes and/or densities, the calculation framework is expanded from rays to volumes. This includes the information on *where* the change in molecular roughness takes place.

The volume is divided in

(i) Active volume, including the shell volume V_{shell} and the overlap volume $V_{overlap}$: The volume in which the change in molecular roughness ΔR takes place. This is a spherical shell whose thickness is defined by ΔR.

(ii) Passive volume, composed of the inner V_{in} and the outer passive volume V_{out}: The volume that is not directly affected by the change in molecular roughness but has an influence on its impact on the acceleration.

The shell volume V_{shell} is described by a spherical shell with the thickness of $2\Delta R$. The change of the molecular roughness happens on the surface of the molecules. To describe this surface and determine the inner and outer radii of the shell, the average radius of the AA model $\overline{r}_{AA}$ is calculated as the arithmetic mean of $r_{AA}^{(i)}$. The spherical shell of the active volume is then defined as

$$V_{shell} = \frac{4}{3}\pi((\overline{r}_{AA} + \Delta R)^3 - (\overline{r}_{AA} - \Delta R)^3) \tag{4}$$

where ΔR is the molecular roughness difference from above (eq 3).

Both an r_{CG} higher and lower than $\overline{r}_{AA}$ can result in the same ΔR and, thus, thickness of the shell of the active volume. This behavior is preserved by making the middle radius of the shell purely dependent on the AA model, while the thickness of the shell is dependent on both the CG model and the AA model. For both the COM and the methyl C-mapping schemes, $\overline{r}_{AA}$ is calculated with the center of the rays being at the center of mass of the molecule. The double of the outer radius of the shell $2(\overline{r}_{AA} + \Delta R)$ is often larger than the average distance between the

https://doi.org/10.1021/acs.jpcb.2c00944
J. Phys. Chem. B 2022, 126, 3737−3747

centers of mass of two molecules. Their shell volumes then overlap. This is quantified in the overlap volume $V_{overlap}$. The RoughMob method is based on the idea that a larger roughness decreases the mobility of the molecules. The shell volume is the volume *in* which the molecular roughness is localized. In the overlap volume, the molecules can be pictured as interlocking gears. A loss in the molecular roughness in this region should be especially dominant for the acceleration of dynamics here. The overlap volume is thus added to the shell volume.

As can be seen in Figure 3, the passive volume is split further into the inner passive volume V_{in} and the outer passive volume

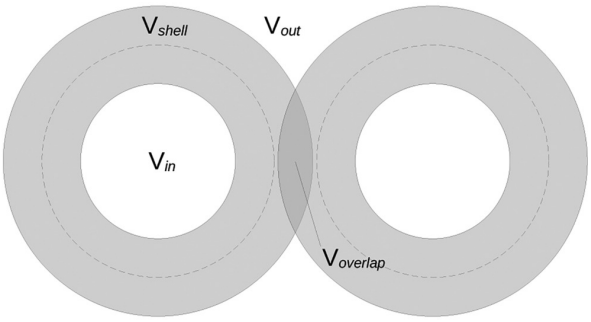

Figure 3. Scheme of two molecules and their shell volume, overlap volume, inner passive volume, and outer passive volume; the dashed line is the average radius of the molecular all-atom surface $\overline{r}_{AA}$; the solid lines are the outer shell radius $\overline{r}_{AA} + \Delta R$ and the inner shell radius $\overline{r}_{AA} - \Delta R$.

V_{out}. Within the RoughMob method, the roughness is interpreted as providing an actual mechanical friction which is reduced as a result of coarse-graining. Staying in the mechanical picture, more space between the molecules should weaken this effect. Thus, a larger outer volume is expected to lower the impact of the change in molecular roughness and the scaling factor of dynamics α. The inner passive volume can be interpreted as the excluded volume that has to be moved geometrically unchanged in both the AA model and CG the model. It provides a means for including the increasing sizes of the molecules that is not covered in a change in the surface. The accelerations are expected to increase with an increasing inner volume. All volumes are calculated on a per-molecule basis. Thus, the different volumes add up to the total volume per molecule, as shown in eq 5.

$$\frac{V}{n_{mol}} = V_{in} + V_{shell} - V_{overlap} + V_{out} \tag{5}$$

All volumes depend on ΔR, which is determined numerically from the molecular geometry and without any simulation. For the calculation of V_{shell}, see eq 4. The inner volume is calculated analytically as

$$V_{in} = \frac{4}{3}\pi(\overline{r}_{AA} - \Delta R)^3 \tag{6}$$

The outer volume is determined numerically using a Monte Carlo algorithm. A mesh of 5000 random points n_{points} is imposed over a $(8\ \text{Å})^3$ cubic cell with at least a 10 Å distance to the simulation box boundaries. For each point, the shortest distance to a nearby center of a molecule is calculated. If the distance is larger than $\overline{r}_{AA} + \Delta R$, the point is associated with V_{out} and counted to n_{out}. The outer volume per molecule can then be calculated from the volume of the simulation box and the number of molecules simulated as shown in eq 7. The calculation is repeated with random points until the average of $\frac{n_{out}}{n_{points}}$ changes by less than 0.001 Å^3 but for at least 10 times.

$$V_{out} = \frac{n_{out}}{n_{points}} \cdot \frac{V_{box}}{n_{mols}} \tag{7}$$

Then, the overlap volume per molecule can be calculated using eq 8.

$$V_{overlap} = \frac{4}{3}\pi(\overline{r}_{AA} + \Delta R)^3 - \left(\frac{V}{n_{mol}} - V_{out}\right) \tag{8}$$

Prediction of the Scaling Factor. Different combinations to predict the scaling factor from the active and passive volumes have been tried. Details on different combinations are included in the Supporting Information. The most suitable proved to be the one shown in eq 9. In this approach, the volumes are separated in an active term $A \cdot (V_{shell} + V_{overlap})$ and a passive term $B \cdot \exp\left(\frac{V_{in}}{V_{out}}\right)$. The passive term resembles the free volume theory,[47−49] where a moving or so-called jumping unit and the free volume are related to the diffusion coefficient. However, like the molecular roughness difference, the passive volume exists purely as a comparative parameter between a CG and a parent model and is thus not correlated to the diffusion coefficient of one of the models but to the acceleration factor.

$$\alpha_{pred} = A \cdot (V_{shell} + V_{overlap}) + B \cdot \exp\left(\frac{V_{in}}{V_{out}}\right) + C \tag{9}$$

The parameters A, B, and C are determined simultaneously via a least-squares fit using the scaling factor α, the shell volume V_{shell}, the overlap volume $V_{overlap}$, the inner passive volume V_{in}, and the outer passive volume V_{out} as calculated from the AA and CG simulations.

RESULTS AND DISCUSSION

Figure 4 shows the predicted scaling factor α_{pred} plotted against the scaling factor α calculated as the ratio of diffusion coefficients from the CG and the AA simulations (eq 1). The dashed line indicates ideal prediction. The acceleration factors α_{pred} are predicted with eq 10, which is determined via a least-squares fit using all the systems presented in this work. All tested sizes and mapping schemes as well as both aliphatic and aromatic molecules are included and reach a good linear correlation with a correlation coefficient of $R^2 = 0.96$. Table 3 shows α and α_{pred} as determined from eq 10, as well as the absolute and the relative error.

$$\alpha_{pred} = \frac{1}{11.51\ \text{Å}^3} \cdot (V_{shell} + V_{overlap}) + 0.837 \cdot \exp\left(\frac{V_{in}}{V_{out}}\right) - 10.61 \tag{10}$$

To understand the contributions of the different roughness volumes, Figures 5−8 show the acceleration factor plotted against different volume terms. Changing from the raw molecular roughness difference to using the active volumes $(V_{shell} + V_{overlap})$ already accounts for some part for the larger size of 33DE24DMP (7) and 33DIP24DMP (10) as can be seen when comparing Figure 2 and Figure 5. The fitting of 2-methylhexane (*blue*, 8), a more asymmetrical molecule, is improved. The alkanes in the C6 to C8 range show a good linear

https://doi.org/10.1021/acs.jpcb.2c00944
J. Phys. Chem. B 2022, 126, 3737−3747

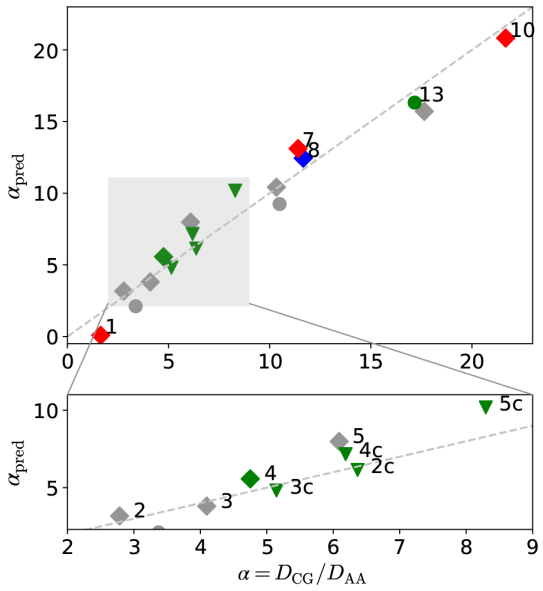

Figure 4. Predicted acceleration factor against simulated acceleration factor; *gray, diamond*: C6 and C8 alkanes; *gray, circle*: C6 and C8 aromatics; *blue*: 2-methylhexane; *green, diamond*: 2,3-dimethylpentane; *green, circle*: mesitylene; *red*: C5, C11, and C13 alkanes; *triangle, green*: methyl C-mapped alkane; *gray, dashed*: scaling factor as calculated from the diffusion coefficients.

Table 3. Acceleration Factor, Predicted Acceleration Factor, and Absolute and Relative Error of Predicted Acceleration Factor

system	α	α_{pred}	abs error	rel error (%)
		alkanes, COM-mapped		
Neo	1.64	0.08	1.56	94.9
23DiMeBu	2.78	3.17	0.38	13.8
3MePe	4.10	3.81	0.29	7.1
23DiMePe	4.75	5.57	0.82	17.2
234TriMePe	6.09	7.98	1.89	31.1
3EtHx	10.33	10.42	0.09	0.8
33DE24DMP	11.40	13.11	1.71	15.0
2MeHx	11.66	12.45	0.79	6.8
25DiMeHx	17.65	15.71	1.94	11.0
33DIP24DMP	21.67	20.82	0.85	3.9
		aromatic molecules, COM-mapped		
Bz	3.37	2.11	1.26	37.4
EtBz	10.49	9.24	1.25	11.9
Mesi	17.17	16.32	0.85	4.9
		alkanes, methyl C-mapped		
3MePe	5.15	4.81	0.33	6.4
23DiMePe	6.19	7.16	0.97	15.7
23DiMeBu	6.37	6.14	0.22	3.5
234TriMePe	8.30	10.18	1.89	22.7

correlation. However, the aromatic molecules (*circles*, 11, 12, 13) are more separated from the alkanes (*diamonds*).

The passive inner volume further increases the contribution of the larger sizes of 33DE24DMP (7) and 33DIP24DMP (10) (Figure 6).

The passive outer volume is especially low for the aromatic molecules (11,12,13), decreasing the effect of the separation of

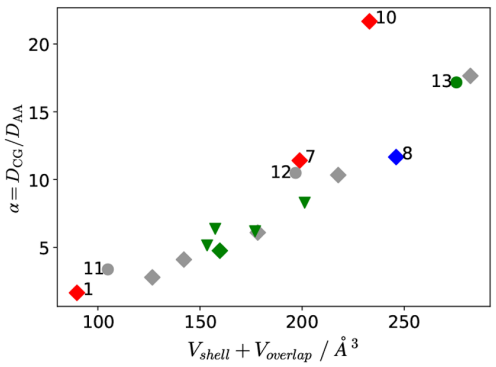

Figure 5. Acceleration factor against active volumes; *gray, diamond*: C6 and C8 alkanes; *gray, circle*: C6 and C8 aromatics; *blue*: 2-methylhexane; *green, diamond*: 2,3-dimethylpentane; *green, circle*: mesitylene; *red*: C5, C11, and C13 alkanes.

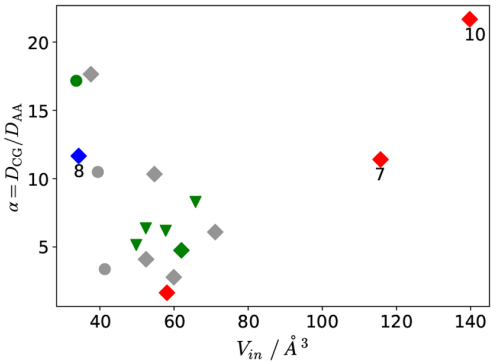

Figure 6. Acceleration factor against inner passive volume; *gray, diamond*: C6 and C8 alkanes; *gray, circle*: C6 and C8 aromatics; *blue*: 2-methylhexane; *green, diamond*: 2,3-dimethylpentane; *green, circle*: mesitylene; *red*: C5, C11, and C13 alkanes.

the two species introduced by the active volume (Figure 7). Its effect is the least systematic.

The differences within the inner passive volume are larger than the ones within the outer passive volume, and they have a larger impact on the passive volume term $B \cdot \exp\left(\frac{V_{in}}{V_{out}}\right)$.

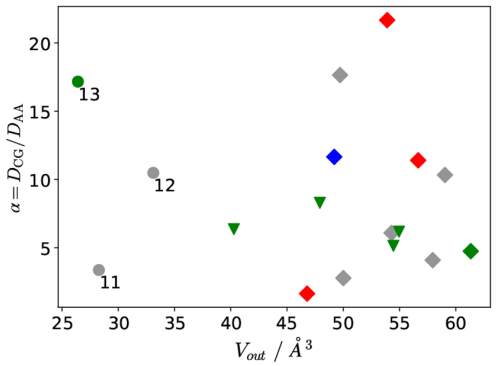

Figure 7. Acceleration factor against outer passive volume; *gray, diamond*: C6 and C8 alkanes; *gray, circle*: C6 and C8 aromatics; *blue*: 2-methylhexane; *green, diamond*: 2,3-dimethylpentane; *green, circle*: mesitylene; *red*: C5, C11, and C13 alkanes.

https://doi.org/10.1021/acs.jpcb.2c00944
J. Phys. Chem. B 2022, 126, 3737−3747

Combining the inner and outer volume keeps the necessary large influence of the size of the molecules (7 and 10) but decreases the loss of precision for the C6 to C8 alkanes that is caused by the introduction of the inner passive volume.

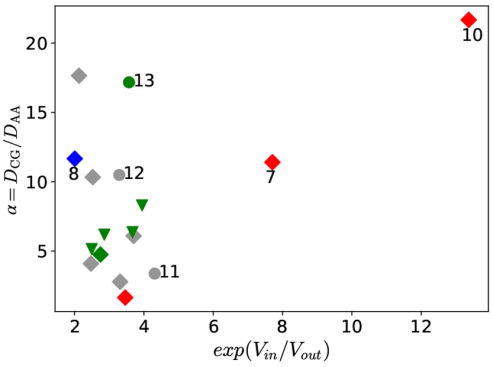

Figure 8. Acceleration factor against the exponential function of the ratio of inner and outer passive volumes; *gray, diamond*: C6 and C8 alkanes; *gray, circle*: C6 and C8 aromatics; *blue*: 2-methylhexane; *green, diamond*: 2,3-dimethylpentane; *green, circle*: mesitylene; *red*: C5, C11, and C13 alkanes.

Table 4 shows the values of the active and passive volumes, as well as the active volume term $A \cdot (V_{shell} + V_{overlap})$ and the passive volume term $B \cdot \exp\left(\frac{V_{in}}{V_{out}}\right)$. The active volume term is at least 1.81 times (33DIP24DMP) up to 13.8 times (25DiMeHx) larger than the passive term, emphasizing the interpretation of the passive volume term as a correction term needed to account for different impacts of the molecular roughness on the acceleration of dynamics upon coarse-graining.

Different Mapping Schemes. Both the predicted scaling factor α_{pred} and the calculated scaling factor α are always higher for the methyl C-mapped model (Table 5). Especially 234TriMePe and 3MePe show very close values for the differences of the acceleration factors. Since $\overline{r}_{AA}$ does not change with a different mapping scheme, all changes in the values of the volumes can be traced back to the difference in the molecular roughness difference ΔR. The increase in ΔR can be caused by a different radius of CG bead r_{CG} and by different placing of its center at the methyl carbon atom and the center of mass of the AA molecule, respectively. The radius of the CG bead is determined from the tabulated CG potential as the effective hard sphere radius. The potential is derived via the iterative Boltzmann inversion where the potential is updated iteratively until the *RDF* of the CG model matches the *RDF* of the parent atomistic model. For different mapping schemes, the *RDF*s differ and thus the radii of the CG beads. However, 23DiMeBu has the lowest change in r_{CG} but the highest change in the scaling factor. This indicates that the change in the acceleration factor is mainly caused by the different centers of the CG bead, thus the distance between the center of mass and the mapped carbon atom, used for the calculation of ΔR. For a given density, both V_{shell} and $V_{overlap}$ increase with ΔR, increasing the total active volume. The inner volume and the outer passive volume both decrease with an increasing ΔR. However, while a smaller V_{out} actually increases the passive volume term, a smaller V_{in} decreases it. The main part of the difference in the acceleration factor is due to the increase in the active volume. The highest increase in both ΔR and α is observed for 23DiMeBu, which has both the smallest scaling factor and the smallest molecular roughness difference in the COM-mapped model (Tables 4 and 2). It is the only molecule (out of the four coarse-grained with two mapping schemes) with a butane chain as the main chain, while the other three systems have a pentane chain as the longest chain. The placement of the CG bead on the second carbon chain atom,

Table 4. Systems, Molecular Roughness Difference, Active Volume Term, Passive Volume Term, Active Roughness Volume, Overlap Volume, Inner Passive Volume, and Outer Passive Volume[a]

system	ΔR	$A(V_{shell} + V_{overlap})$	$B \cdot \exp\left(\frac{V_{in}}{V_{out}}\right)$	V_{shell}	$V_{overlap}$	V_{in}	V_{out}
alkanes, COM-mapped							
Neo	0.42	7.80	2.90	85.3	4.4	58.1	46.8
23DiMeBu	0.52	11.01	2.77	113.7	13.0	59.9	50.0
3MePe	0.58	12.35	2.07	123.4	18.7	52.4	57.9
23DiMePe	0.59	13.88	2.30	140.6	19.1	62.0	61.3
234TriMePe	0.61	15.49	3.10	156.4	21.9	71.1	54.3
3EtHx	0.75	18.92	2.11	186.4	31.2	54.7	59.0
33DE24DMP	0.55	17.28	6.45	176.0	22.8	115.7	56.7
2MeHx	0.92	21.38	1.68	203.9	42.1	34.3	49.2
25DiMeHx	0.97	24.54	1.78	232.1	50.3	37.6	49.7
33DIP24DMP	0.56	20.25	11.19	202.9	30.0	139.8	53.9
aromatic molecules, COM-mapped							
Bz	0.51	9.12	3.61	91.8	13.1	41.3	28.3
EtBz	0.77	17.10	2.75	163.5	33.3	39.4	33.1
Mesi	0.97	23.95	2.99	221.7	53.9	33.6	26.4
alkanes, methyl C-mapped							
3MePe	0.62	13.34	2.09	132.2	21.3	49.8	54.5
23DiMePe	0.65	15.38	2.39	154.5	22.4	57.8	55.0
23DiMeBu	0.62	13.68	3.07	137.7	19.8	52.4	40.3
234TriMePe	0.67	17.49	3.30	173.7	27.6	65.8	47.9

[a]Volumes are in Å^3.

https://doi.org/10.1021/acs.jpcb.2c00944
J. Phys. Chem. B 2022, 126, 3737−3747

Table 5. Differences between the Methyl C-Mapped Minus the COM-Mapped Models of the Calculated and Predicted Acceleration Factor, the Molecular Roughness Difference, the Active Volume Term, the Passive Volume Term, the Center of the Two Mapping Schemes (Bead Center), and the Radius of the Coarse-Grained Bead[a]

system	α	α_{pred}	ΔR	active term	passive term	bead center	r_{CG}
234TriMePe	2.21	2.20	0.066	2.00	0.20	0.55	0.09
23DiMeBu	3.58	2.97	0.106	2.68	0.30	0.84	0.02
23DiMePe	1.44	1.59	0.057	1.50	0.09	0.58	0.24
3MePe	1.05	1.01	0.040	0.99	0.02	0.44	0.10

[a]Distances are in Å.

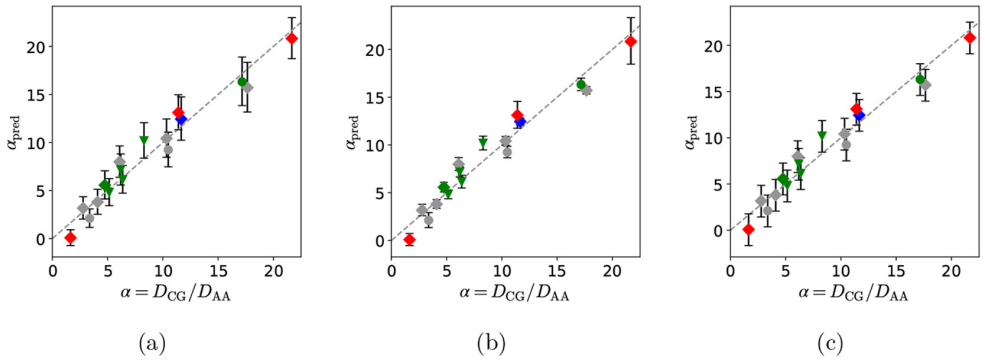

Figure 9. Predicted acceleration factor against the simulated acceleration factor; *gray, diamond*: C6 and C8 alkanes; *gray, circle*: C6 and C8 aromatics; *blue*: 2-methylhexane; *green, diamond*: 2,3-dimethylpentane; *green, circle*: mesitylene; *red*: C5, C11, and C13 alkanes; *triangle, green*: methyl C-mapped alkane; *gray, dashed*: simulated scaling factor; (a) error with $A_{min} = (10.4\ Å^3)^{-1}$ and $A_{max} = (12.9\ Å^3)^{-1}$; (b) error with $B_{min} = 0.66$ and $B_{max} = 1.02$; (c) error with $C_{min} = -12.3$ and $C_{max} = -8.8$.

compared to the third for pentane chains, thus causes a larger deviation from the center of mass.

Testing of Predictiveness. To test the quality of the prediction

(i) the distribution of the regression parameters A, B, and C is estimated with a residuals-resampling bootstrap
(ii) nine out of 17 models are randomly picked to fit the regression model and predict the scaling factors of the remaining eight models
(iii) the 12 models with the smallest acceleration factors are used to predict the scaling factor of the five models with the highest acceleration factor.

To estimate the distribution of the regression parameters A, B, and C, a residuals-resampling bootstrap method is used.[50,51] From the least-squares fit of active volumes and the passive volumes to α according to eq 9, the predicted values α_{pred} and the residuals (R_i) are saved. Then, 5000 sets of synthetic data are generated by adding residuals R_{random} randomly drawn from R_i to the fitted values $\alpha_{boot} = \alpha_{pred} + R_{random}$. The volumes are refitted onto α_{boot} to generate new sets of the regression parameters. From the distributions, for each parameter, a confidence interval is determined as the two values between which the parameter lies with a 90% probability. Figure 9 shows the predicted acceleration factors with the error estimates resulting from the confidence interval of each parameter separately. Both A and B are prefactors within the active and passive terms, respectively, while C is an added constant. For the latter, the absolute error is thus independent of the roughness volumes, thus causing large relative errors for models with a small acceleration such as Neo (Table 3 and Figure 9(c)). The uncertainty caused by the distribution of the prefactors A and B increases with an increasing active volume and an increasing passive volume ratio, respectively. The uncertainty of A mostly causes larger errors in α_{pred} than B. The estimated distribution of B only causes small error bars with the exception of 33DE24DMP and 33DE24DIP, both shown in red, that have the largest passive terms $B \cdot \exp\left(\frac{V_{in}}{V_{out}}\right)$.

In the first test, nine systems are picked randomly and used to predict the acceleration factor of the remaining eight systems. This is repeated 5000 times. Table 6 shows the average absolute deviation of the so predicted α_{pred} from the calculated α, the relative deviation, and the average deviation including the sign of the deviation with a positive sign stating that the predicted acceleration is too high. The highest average absolute deviation can be observed for 33DIP24DMP with 4.84, while the smallest molecule Neo has the highest relative deviation with 123.4%. Here, the average absolute deviation (2.03) is equal to the value of the average deviation (−2.03), meaning, in all samples, the predicted acceleration for Neo is too low. Since the absolute deviation is larger than the calculated α, in many cases, a negative acceleration factor was predicted for Neo. This is physically impossible. The methyl C-mapped 23DiMeBu has the lowest average error (0.40), and 3EtHx has the lowest relative error with 4.8%. Out of the 17 systems, only four, namely Neo, 33DIP24DMP, 25DeMeHx, and 33DE24DMP, do have an average deviation greater than 2. The latter three all have a calculated α larger than 10. The overall average error of all predictions is 1.52, and the overall relative deviation is 22.9%. Out of the 17 systems, six show a deviation larger than 20%, while the remaining 11 are below 20%.

In a second test, the 12 systems with the lowest α, ranging from 1.64 to 10.49, are used to generate the linear fit according to eq 9. The linear fit function with $A = (14.35\ Å^3)^{-1}$, $B = 0.55$, and $C = -7.03$ is then used to predict α_{pred} for the remaining 5 systems which show scaling factors from 11.4 to 21.67 in the

https://doi.org/10.1021/acs.jpcb.2c00944
J. Phys. Chem. B 2022, 126, 3737−3747

Table 6. Average Absolute Deviation, Average Deviation, and Relative Deviation of the Predicted Acceleration Factor α_{pred} from α out of 5000 Samples with Random Test Sets of Nine Systems to Predict the Remaining Eight

system	abs deviation	av deviation	rel deviation (%)
		alkanes, COM-mapped	
Neo	2.03	−2.03	123.4
23DiMeBu	0.61	0.40	21.9
3MePe	0.46	−0.29	11.3
23DiMePe	0.91	0.90	19.2
234TriMePe	1.94	1.94	31.8
3EtHx	0.50	0.02	4.8
33DE24DMP	2.13	1.54	18.7
2MeHx	1.17	0.87	10.0
2SDiMeHx	2.87	−2.87	16.3
33DIP24DMP	4.84	−3.71	22.3
		aromatic molecules, COM-mapped	
Bz	1.71	−1.70	50.7
EtBz	1.45	−1.45	13.8
Mesi	1.55	−1.51	9.0
		alkanes, methyl C-mapped	
3MePe	0.44	−0.33	8.6
23DiMePe	1.04	1.03	16.7
23DiMeBu	0.40	−0.33	6.3
234TriMePe	1.93	1.93	23.3

simulations. As can be seen in Figure 10, the prediction generally underestimates the actual scaling factor by 3 to 24%. The values

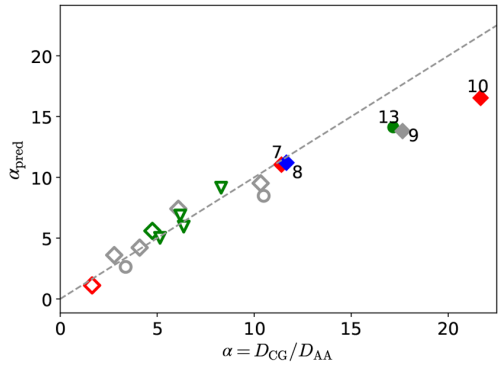

Figure 10. Predicted acceleration factor against the simulated acceleration factor; *gray, diamond*: C6 and C8 alkanes; *gray, circle*: C6 and C8 aromatics; *blue*: 2-methylhexane; *green, diamond*: 2,3-dimethylpentane; *green, circle*: mesitylene; *red*: C5, C11, and C13 alkanes; *triangle, green*: methyl C-mapped alkane; *gray line*: simulated acceleration factor; *unfilled:* systems used for fit of eq 9; *filled*: predicted systems.

of the predicted acceleration factors depend on the model parameters A, B, and C and thus on the set used for the least-squares fit. The low α set used for generating the linear fit neither includes 33DE24DMP (7) nor 33DIP24DMP (10), the molecules providing the motivation to look for a means to include different sizes and density effects. These C11- and C13-molecules are the systems that most strongly differ from a linear behavior of ΔR against α (Figure 2), that also differ from a linear behavior of the active volume against α (Figure 6), and that show the largest difference in the value of the passive term compared to the other systems (Figure 8). Even without including these molecules, the RoughMob method provides a reasonable prediction for a broad range of hydrocarbons with different sizes and shapes. It is also important to note that 2MeHx (8) and 33DE24DMP (10) have very close predicted scaling factors, besides having very different molecular roughness differences and not being included in the set for the least-squares fit.

CONCLUSION

We demonstrated that the RoughMob method, when extended by the concept of the region where roughness actually acts, can be used to get a good estimate of the acceleration factor of dynamics upon coarse-graining for a broad range of hydrocarbons. We are able to describe quantitatively hydrocarbon fluids with 5 to 13 carbon atoms, whose coarse-graining into a single bead results in an artificial mobility increase by factors between 1.64 and 21.7. The absolute average error of the predicted acceleration is 1.00 with a maximum of 1.94 for 2,5-dimethylhexane. The average relative error of the predicted acceleration is 17.9% with a maximum of 94.9% for the molecule with the lowest α neopentane. Due to the large relative error, the method is not recommended for the quantitative determination of diffusion coefficients in a low α_{pred} range.

The prediction of the acceleration factor is done by a numerical comparison of the geometrical information on the all-atom and coarse-grained systems. Once the fluid structure of the atomistic system is equilibrated, the model can be coarse-grained by, e.g., the iterative Boltzmann inversion, and the geometrical information can be derived from a single frame of the atomistic trajectory and the nonbonded potentials of the models. Most information is already derived from single-molecule geometries, i.e., without any simulation. A short simulation run is only needed to determine the outer passive volume. Changing the geometric descriptor, which is correlated with the acceleration upon coarse-graining, from the previous used roughness difference[24] to different parts of the molecular volume, allows us to broaden the range of molecular sizes and shapes. The method now reflects that larger more spherical molecules (for example, 33DE24DMP) and smaller aspherical molecules (for example, 2MeHx) can show the same acceleration factor. While the accuracy of the prediction within the original C6 to C8 range for hydrocarbons is slightly decreased, both aliphatic and aromatic molecules can still be fitted jointly. All systems have been simulated under ambient conditions. The recalibration of CG models for different state points is a known requirement. However, it is to be expected, that the effective (hard-core) radius of a coarse-grained bead will not change significantly, and thus, the shell volume will not change either. In contrast, the acceleration factor is known to decrease at higher temperatures. The lower density will likely increase the outer passive volume and thereby the predicted scaling factor. It has yet to be tested if this accounts for the change in the acceleration factor with temperature at constant pressure. A side result is that most of the difference of the acceleration and its prediction for different mapping schemes is not caused by a change in the size of the coarse-grained bead but by the change of its location within the molecule.

We are optimistic that the simplicity of the RoughMob method allows the application to a broad range of chemical materials as the needed geometrical parameters can be derived independent of the chemical nature. The RoughMob method relies on the comparability of the surfaces of the all-atom and the coarse-grained models. To define the molecular surfaces, we

https://doi.org/10.1021/acs.jpcb.2c00944
J. Phys. Chem. B 2022, 126, 3737−3747

used the effective (hard-core) radii derived from the nonbonded potentials. A consistency between the models provided other definitions of the molecular surfaces based on the potentials or energies are possible and valid or may even be necessary. Of particular interest for future work will be the influence of structural properties beyond the monomeric level, including polar molecules and mixtures of beads with different roughness parameters. Using the iterative Boltzmann inversion with pressure correction for coarse-graining ensures matching distribution functions and densities and thereby matching average distances between the beads and matching coordination numbers. Further investigation is needed to test, if all or only one of these structural characteristics has to be matched to allow the usage of our method. The latter would ease the transferability of the method to other, possibly even not structure based, bottom-up coarse-graining methods.

■ ASSOCIATED CONTENT

Supporting Information

The Supporting Information is available free of charge at https://pubs.acs.org/doi/10.1021/acs.jpcb.2c00944.

Tabulated coarse-grained potentials (ZIP)

OPLS-AA bonded parameters of all-atom force field, cutoff radii for coarse-graining, and alternative calculation routes for predicted acceleration factor (PDF)

■ AUTHOR INFORMATION

Corresponding Authors

Melissa K. Meinel − *Eduard-Zintl-Institut für Anorganische und Physikalische Chemie and Profile Area Thermofluids and Interfaces, Technische Universität Darmstadt, D-64287 Darmstadt, Germany;* orcid.org/0000-0001-7369-3627; Email: m.meinel@theo.chemie.tu-darmstadt.de

Florian Müller-Plathe − *Eduard-Zintl-Institut für Anorganische und Physikalische Chemie and Profile Area Thermofluids and Interfaces, Technische Universität Darmstadt, D-64287 Darmstadt, Germany;* orcid.org/0000-0002-9111-7786; Email: f.mueller-plathe@theo.chemie.tu-darmstadt.de

Complete contact information is available at: https://pubs.acs.org/10.1021/acs.jpcb.2c00944

Notes

The authors declare no competing financial interest.

■ ACKNOWLEDGMENTS

This work has, in part, been supported by the Collaborative Research Center 146 "Multiscale Simulation Methods for Soft Matter Systems" of Deutsche Forschungsgemeinschaft.

■ REFERENCES

(1) Müller-Plathe, F. Coarse-Graining in Polymer Simulation: From the Atomistic to the Mesoscopic Scale and Back. *ChemPhysChem* **2002**, *3*, 754−769.

(2) Deichmann, G.; van der Vegt, N. F. A. Bottom-up approach to represent dynamic properties in coarse-grained molecular simulations. *J. Chem. Phys.* **2018**, *149*, 244114.

(3) Lyubimov, I.; Guenza, M. G. First-principle approach to rescale the dynamics of simulated coarse-grained macromolecular liquids. *Phys. Rev. E* **2011**, *84*, No. 031801.

(4) Harmandaris, V. A.; Reith, D.; van der Vegt, N. F. A.; Kremer, K. Comparison Between Coarse-Graining Models for Polymer Systems: Two Mapping Schemes for Polystyrene. *Macromol. Chem. Phys.* **2007**, *208*, 2109−2120.

(5) Guenza, M. Thermodynamic consistency and other challenges in coarse-graining models. *Eur. Phys. J. Special Topics* **2015**, *224*, 2177−2191.

(6) Rudzinski, J. F. Recent Progress towards Chemically-Specific Coarse-Grained Simulation Models with Consistent Dynamical Properties. *Computation* **2019**, *7*, 42.

(7) Depa, P. K.; Maranas, J. K. Speed up of dynamic observables in coarse-grained molecular-dynamics simulations of unentangled polymers. *J. Chem. Phys.* **2005**, *123*, No. 094901.

(8) Depa, P.; Chen, C.; Maranas, J. K. Why are coarse-grained force fields too fast? A look at dynamics of four coarse-grained polymers. *J. Chem. Phys.* **2011**, *134*, No. 014903.

(9) Shell, M. S. The relative entropy is fundamental to multiscale and inverse thermodynamic problems. *J. Chem. Phys.* **2008**, *129*, 144108.

(10) Shell, M. S. Systematic coarse-graining of potential energy landscapes and dynamics in liquids. *J. Chem. Phys.* **2012**, *137*, No. 084503.

(11) Dyre, J. C. Perspective: Excess-entropy scaling. *J. Chem. Phys.* **2018**, *149*, 210901.

(12) Rondina, G. G.; Böhm, M. C.; Müller-Plathe, F. Predicting the Mobility Increase of Coarse-Grained Polymer Models from Excess Entropy Differences. *J. Chem. Theory Comput.* **2020**, *16*, 1431−1447. PMID: 32031377

(13) Rosenfeld, Y. Relation between the transport coefficients and the internal entropy of simple systems. *Phys. Rev. A* **1977**, *15*, 2545−2549.

(14) Lyubimov, I. Y.; Guenza, M. G. Theoretical reconstruction of realistic dynamics of highly coarse-grained cis-1,4-polybutadiene melts. *J. Chem. Phys.* **2013**, *138*, 12A546.

(15) Fritz, D.; Koschke, K.; Harmandaris, V. A.; van der Vegt, N. F. A.; Kremer, K. Multiscale modeling of soft matter: scaling of dynamics. *Phys. Chem. Chem. Phys.* **2011**, *13*, 10412−10420.

(16) Klippenstein, V.; Tripathy, M.; Jung, G.; Schmid, F.; van der Vegt, N. F. A. Introducing Memory in Coarse-Grained Molecular Simulations. *J. Phys. Chem. B* **2021**, *125*, 4931−4954.

(17) Knoch, F.; Schäfer, K.; Diezemann, G.; Speck, T. Dynamic coarse-graining fills the gap between atomistic simulations and experimental investigations of mechanical unfolding. *J. Chem. Phys.* **2018**, *148*, No. 044109.

(18) Markutsya, S.; Lamm, M. H. A coarse-graining approach for molecular simulation that retains the dynamics of the all-atom reference system by implementing hydrodynamic interactions. *J. Chem. Phys.* **2014**, *141*, 174107.

(19) Fu, C.-C.; Kulkarni, P. M.; Shell, M. S.; Leal, L. G. A test of systematic coarse-graining of molecular dynamics simulations: Transport properties. *J. Chem. Phys.* **2013**, *139*, No. 094107.

(20) Lemarchand, C. A.; Couty, M.; Rousseau, B. Coarse-grained simulations of cis- and trans-polybutadiene: A bottom-up approach. *J. Chem. Phys.* **2017**, *146*, No. 074904.

(21) Akkermans, R. L. C.; Briels, W. J. Coarse-grained dynamics of one chain in a polymer melt. *J. Chem. Phys.* **2000**, *113*, 6409−6422.

(22) Padding, J. T.; Briels, W. J. Time and length scales of polymer melts studied by coarse-grained molecular dynamics simulations. *J. Chem. Phys.* **2002**, *117*, 925−943.

(23) Davtyan, A.; Dama, J. F.; Voth, G. A.; Andersen, H. C. Dynamic force matching: A method for constructing dynamical coarse-grained models with realistic time dependence. *J. Chem. Phys.* **2015**, *142*, 154104.

(24) Meinel, M. K.; Müller-Plathe, F. Loss of Molecular Roughness upon Coarse-Graining Predicts the Artificially Accelerated Mobility of Coarse-Grained Molecular Simulation Models. *J. Chem. Theory Comput.* **2020**, *16*, 1411−1419.

(25) Nielsen, S. O.; Lopez, C. F.; Srinivas, G.; Klein, M. L. Coarse grain models and the computer simulation of soft materials. *J. Phys.: Condens. Matter* **2004**, *16*, R481−R512.

(26) Peters, B. L.; Salerno, K. M.; Agrawal, A.; Perahia, D.; Grest, G. S. Coarse-Grained Modeling of Polyethylene Melts: Effect on Dynamics. *J. Chem. Theory Comput.* **2017**, *13*, 2890−2896.

(27) Depa, P. K.; Maranas, J. K. Dynamic evolution in coarse-grained molecular dynamics simulations of polyethylene melts. *J. Chem. Phys.* **2007**, *126*, No. 054903.
(28) Karimi-Varzaneh, H. A.; van der Vegt, N. F. A.; Müller-Plathe, F.; Carbone, P. How Good Are Coarse-Grained Polymer Models? A Comparison for Atactic Polystyrene. *ChemPhysChem* **2012**, *13*, 3428−3439.
(29) Deichmann, G.; Dallavalle, M.; Rosenberger, D.; van der Vegt, N. F. A. Phase Equilibria Modeling with Systematically Coarse-Grained ModelsA Comparative Study on State Point Transferability. *J. Phys. Chem. B* **2019**, *123*, 504−515.
(30) Farah, K.; Fogarty, A. C.; Böhm, M. C.; Müller-Plathe, F. Temperature dependence of coarse-grained potentials for liquid hexane. *Phys. Chem. Chem. Phys.* **2011**, *13*, 2894−2902.
(31) Berweger, C. D.; van Gunsteren, W. F.; Müller-Plathe, F. Force field parametrization by weak coupling. Re-engineering SPC water. *Chem. Phys. Lett.* **1995**, *232*, 429−436.
(32) Qian, H.-J.; Carbone, P.; Chen, X.; Karimi-Varzaneh, H. A.; Liew, C. C.; Müller-Plathe, F. Temperature-Transferable Coarse-Grained Potentials for Ethylbenzene, Polystyrene, and Their Mixtures. *Macromolecules* **2008**, *41*, 9919−9929.
(33) Carbone, P.; Varzaneh, H. A. K.; Chen, X.; Müller-Plathe, F. Transferability of coarse-grained force fields: The polymer case. *J. Chem. Phys.* **2008**, *128*, No. 064904.
(34) Pretti, E.; Shell, M. S. A microcanonical approach to temperature-transferable coarse-grained models using the relative entropy. *J. Chem. Phys.* **2021**, *155*, No. 094102.
(35) Jin, J.; Yu, A.; Voth, G. A. Temperature and Phase Transferable Bottom-up Coarse-Grained Models. *J. Chem. Theory Comput.* **2020**, *16*, 6823−6842.
(36) Jin, J.; Pak, A. J.; Han, Y.; Voth, G. A. A new one-site coarse-grained model for water: Bottom-up many-body projected water (BUMPer). II. Temperature transferability and structural properties at low temperature. *J. Chem. Phys.* **2021**, *154*, No. 044105.
(37) Xia, W.; Hansoge, N. K.; Xu, W.-S.; Phelan, F. R.; Keten, S.; Douglas, J. F. Energy renormalization for coarse-graining polymers having different segmental structures. *Sci. Adv.* **2019**, *5*, eaav4683.
(38) Fritz, D.; Herbers, C. R.; Kremer, K.; van der Vegt, N. F. A. Hierarchical modeling of polymer permeation. *Soft Matter* **2009**, *5*, 4556−4563.
(39) Izvekov, S.; Voth, G. A. Modeling real dynamics in the coarse-grained representation of condensed phase systems. *J. Chem. Phys.* **2006**, *125*, 151101.
(40) Shillcock, J. C.; Lipowsky, R. The computational route from bilayer membranes to vesicle fusion. *J. Phys.: Condens. Matter* **2006**, *18*, S1191−S1219.
(41) Plimpton, S. Fast Parallel Algorithms for Short-Range Molecular Dynamics. *J. Comput. Phys.* **1995**, *117*, 1−19.
(42) Jewett, A. I.; Zhuang, Z.; Shea, J.-E. Moltemplate a Coarse-Grained Model Assembly Tool. *Biophys. J.* **2013**, *104*, 169a.
(43) Sun, H. COMPASS: An ab Initio Force-Field Optimized for Condensed-Phase Applications Overview with Details on Alkane and Benzene Compounds. *J. Phys. Chem. B* **1998**, *102*, 7338−7364.
(44) Jorgensen, W. L.; Maxwell, D. S.; Tirado-Rives, J. Development and Testing of the OPLS All-Atom Force Field on Conformational Energetics and Properties of Organic Liquids. *J. Am. Chem. Soc.* **1996**, *118*, 11225−11236.
(45) Reith, D.; Pütz, M.; Müller-Plathe, F. Deriving effective mesoscale potentials from atomistic simulations. *J. Comput. Chem.* **2003**, *24*, 1624−1636.
(46) Rühle, V.; Junghans, C.; Lukyanov, A.; Kremer, K.; Andrienko, D. Versatile Object-Oriented Toolkit for Coarse-Graining Applications. *J. Chem. Theory Comput.* **2009**, *5*, 3211−3223.
(47) Ramesh, N.; Davis, P. K.; Zielinski, J. M.; Danner, R. P.; Duda, J. L. Application of free-volume theory to self diffusion of solvents in polymers below the glass transition temperature: A review. *J. Polym. Sci., Part B: Polym. Phys.* **2011**, *49*, 1629−1644.
(48) Vrentas, J. S.; Duda, J. L. Diffusion in polymersolvent systems. I. Reexamination of the free-volume theory. *J. Polym. Sci.: Polymer Physics Edition* **1977**, *15*, 403−416.
(49) Zielinski, J. M.; Duda, J. L. Predicting polymer/solvent diffusion coefficients using free-volume theory. *AIChE J.* **1992**, *38*, 405−415.
(50) Efron, B. Bootstrap Methods: Another Look at the Jackknife. *Annals of Statistics* **1979**, *7*, 1−26.
(51) Freedman, D. A. Bootstrapping Regression Models. *Annals of Statistics* **1981**, *9*, 1218−1228.

https://doi.org/10.1021/acs.jpcb.2c00944
J. Phys. Chem. B 2022, 126, 3737−3747

4.3 Predicting the artificial dynamical acceleration of binary hydrocarbon mixtures upon coarse-graining with roughness volumes and simple averaging rules

Reproduced from Meinel et al., *J. Chem. Phys.* 160, 174108 (2024), with the permission of AIP Publishing.

The Journal of Chemical Physics ARTICLE pubs.aip.org/aip/jcp

Predicting the artificial dynamical acceleration of binary hydrocarbon mixtures upon coarse-graining with roughness volumes and simple averaging rules

Cite as: J. Chem. Phys. **160**, 174108 (2024); doi: 10.1063/5.0200790
Submitted: 29 January 2024 • Accepted: 15 April 2024 •
Published Online: 2 May 2024

Melissa K. Meinel[a] and Florian Müller-Plathe[b]

AFFILIATIONS

Technische Universität Darmstadt, Eduard-Zintl-Institut für Anorganische und Physikalische Chemie and Profile Area Thermofluids and Interfaces, Technische Universität Darmstadt, Peter-Grünberg-Str. 8, D-64287 Darmstadt, Germany

[a]Author to whom correspondence should be addressed: m.meinel@theo.chemie.tu-darmstadt.de
[b]Electronic mail: f.mueller-plathe@theo.chemie.tu-darmstadt.de

ABSTRACT

Coarse-grained (CG) molecular models greatly reduce the computational cost of simulations allowing for longer and larger simulations, but come with an artificially increased acceleration of the dynamics when compared to the parent atomistic (AA) simulation. This impedes their use for the quantitative study of dynamical properties. During coarse-graining, grouping several atoms into one CG bead not only reduces the number of degrees of freedom but also reduces the roughness on the molecular surfaces, leading to the acceleration of dynamics. The RoughMob approach [M. K. Meinel and F. Müller-Plathe, J. Phys. Chem. B **126**(20), 3737–3747 (2022)] quantifies this change in geometry and correlates it to the acceleration by making use of four so-called roughness volumes. This method was developed using simple one-bead CG models of a set of hydrocarbon liquids. Potentials for pure components are derived by the structure-based iterative Boltzmann inversion. In this paper, we find that, for binary mixtures of simple hydrocarbons, it is sufficient to use simple averaging rules to calculate the roughness volumes in mixtures from the roughness volumes of pure components and add a correction term quadratic in the concentration without the need to perform any calculation on AA or CG trajectories of the mixtures themselves. The acceleration factors of binary diffusion coefficients and both self-diffusion coefficients show a large dependence on the overall acceleration of the system and can be predicted *a priori* without the need for any AA simulations within a percentage error margin, which is comparable to routine measurement accuracies. Only if a qualitatively accurate description of the concentration dependence of the binary diffusion coefficient is desired, very few additional simulations of the pure components and the equimolar mixture are required.

I. INTRODUCTION

A. Context

Fluid mixtures are present in industrial and biological processes and in our daily life. They range from mixtures of small molecules, e.g., as solvents/matrix, to polymer solutions and blends or membranes and proteins in a solvent. When experiments are difficult or expensive or simply time-consuming to perform, molecular dynamics (MD) simulations are a powerful and widely used tool to enable or accelerate the study of mixtures.[1–8] However, already a binary mixture of, e.g., hydrocarbons requires a large amount of simulation to test different possible compositions, which increases drastically if there are more different components to choose from. To decrease the computational costs required and thus further quicken the study of mixtures, coarse-grained (CG) simulations can be and already have been widely used for them.[9–20] Molecular mobilities and all ensuing dynamical properties, however, are usually too fast when compared to the reference (atomistic system or experiment).[21–24] This limits the applicability of coarse-grained models since the knowledge of transport properties, such as the diffusion coefficient in fluid mixtures, can be a prerequisite for the design of efficient industrial process plants or the comprehension of biological pro-

cesses, such as transport through membranes.[25–30] Therefore, the role of the dynamical acceleration upon coarse-graining of simple hydrocarbon mixtures is not only of interest for understanding these molecules and systems themselves but also allows us to gain insights and methodologies that can be potentially scaled up and applied to more complex systems. Hydrocarbon mixtures are used as chemical feedstock for industrial processes, as solvents, or in fuel blends,[31,32] and simple hydrocarbons are the basic building blocks of more complex organic compounds, such as polymers. The size of the hydrocarbons coarse-grained into one bead per molecule, as used within this work, reflects the typical size of a polymer bead.

Several methods aimed at coarse-grained models with accurate dynamics have been proposed, such as using data-driven approaches or adding correction terms to the simulation trying to account for the factors behind the artificial acceleration.[33–36] Instead of aiming to include the dynamical properties into the target properties during coarse-graining, which may worsen structural and thermodynamic properties and the computational efficiency, one may try to predict the acceleration and rescale the dynamics (or time) of the coarse-grained simulation to match that of the all-atom simulation or experiment.[22,37–41] One common way to express the change of dynamics is the scaling or acceleration factor α calculated as the ratio of the all-atom (D_{AA}) and coarse-grained (D_{CG}) diffusion coefficients,[22,37,40]

$$\alpha = D_{CG}/D_{AA}. \quad (1)$$

Predicting this acceleration factor *a priori* would make it possible to estimate the atomistic (and thus hopefully "true") diffusion coefficients using only the computationally much more feasible coarse-grained simulation. In our previous work, we have connected the *change* of the mobility of simple hydrocarbons upon coarse-graining an AA model into one CG bead per molecule to the geometrical *change* of the roughness upon coarse-graining. The RoughMob (roughness and mobility) method was originally developed for single component hydrocarbon liquids with 5–13 carbon atoms that were coarse-grained via Iterative Boltzmann Inversion (IBI) into one bead per molecule.[22,42]

This paper extends RoughMob to liquid mixtures and analyzes the acceleration of dynamical properties, specifically of the self-diffusion coefficients and the binary diffusion coefficient, in binary alkane mixtures at varying compositions. It explores the prediction of AA diffusion coefficients from CG simulations, using as few AA simulations, coarse-graining processes, and numerical calculations as possible. Therefore, it is crucial to analyze the behavior of the different alkanes in mixture in both the AA and CG representations.

B. Scope of the present investigation

Iterative Boltzmann inversion is a structure-based coarse-graining approach, where the nonbonded potential is constructed iteratively to match the radial distribution function (RDF) of the CG simulation to the corresponding atomistic reference function. Thus, while some structural properties are preserved (the RDF and ideally the density), on a smaller scale, some geometrical information is lost. The molecular surface of a polyatomic (AA) molecule loses some of its roughness upon coarse-graining. This loss can be expressed as a

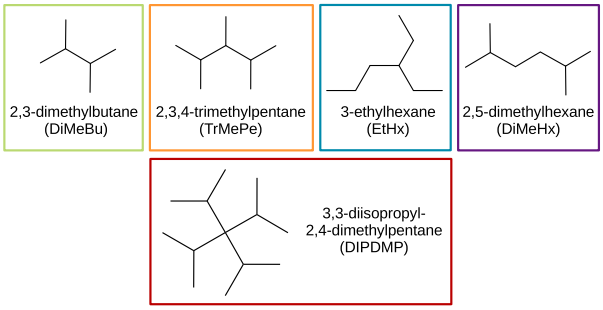

FIG. 1. Simulated molecules, their names, chemical structure, abbreviation, and color; colors from left to right: green, orange, blue, purple, and red; grayscale: from light to dark gray.

numerically determined quantity, which we called *molecular roughness difference* ΔR. For a small size range of spherical hydrocarbons with six (C6) to eight (C8) carbon atoms, the acceleration scaled linear with the *molecular roughness difference* ΔR.[22] Broadening the molecular size and asphericity range required the introduction of four *roughness volumes* that, e.g., account for an increasing size of the molecules, which affect the acceleration of dynamics upon coarse-graining.[42] Details on the definition and purpose of the individual *roughness volumes* are given in Sec. II F 3. The *roughness volumes* are correlated with the acceleration factor by a fitting function, which allows us to predict an estimate of the acceleration α_{pred}. The present study uses five alkanes that have been part of the development process of the *RoughMob* method for pure, apolar liquids. They are illustrated in Fig. 1.

The four alkanes 2,3-dimethylbutane, 2,3,4-trimethylpentane, 3-ethylhexane, and 2,5-dimethylhexane are simulated in every possible binary combination (six combinations) and form mixture group A (see Table I). They cover a size range of six to eight carbon atoms (86.18–114.23 g/mol) with atomistic diffusion coefficients between 1.15 $\times 10^{-9}$ and 1.91 $\times$ 10^{-9} m^2 s^{-1} and acceleration factors α from 2.80 to 17.53 (Table II). We additionally simulate 2,3-dimethylbutane with a heavier version of

TABLE I. Components 1 and 2 of the different mixtures and the total number of molecules in each simulation.

Mixture group A		
DiMeBu	TrMePe	1000 molecules
DiMeBu	EtHx	1000 molecules
DiMeBu	DiMeHx	1000 molecules
TriMePe	EtHx	1000 molecules
TriMePe	DiMeHx	1000 molecules
EtHx	DiMeHx	1000 molecules
Mixture group B		
DiMeBu	DIPDMP	500 molecules
DiMeHx	DIPDMP	500 molecules

TABLE II. Self-diffusion coefficients in 10^{-9} m^2 s^{-1} and the acceleration factor α of the pure components as determined from simulations of Refs. 22 and 42; standard deviations between the individual Cartesian components are shown in parentheses.

System	D_{AA}	D_{CG}	α
DiMeBu	1.91 (0.03)	5.37 (0.05)	2.80 (0.07)
TrMePe	1.15 (0.01)	7.23 (0.09)	6.28 (0.12)
EtHx	1.72 (0.01)	18.43 (0.22)	10.74 (0.22)
DiMeHx	1.37 (0.02)	23.97 (0.31)	17.53 (0.46)
DIPDMP	0.075 (0.004)	1.63 (0.04)	21.83 (1.64)

TABLE III. Lengths of production runs in ns for all-atom and coarse-grained simulations of different compositions (mole fractions x_1).

x_1	AA	CG
0.01 and 0.99	40	100
0.02 and 0.98	40	100
0.05 and 0.95	40	100
0.10 and 0.90	30	50
0.25 and 0.75	20	50
0.50	20	50

3-ethylhexane (210.32 g/mol), where the mass of all C-atoms is doubled. The fifth alkane, 3,3-diisopropyl-2,4-dimethylpentane (DIPDMP), heavily relies on the use of *roughness volumes* to yield a reasonable prediction of α. Compared to the other four molecules, DIPDMP is larger (C13, 184.36 g/mol), its atomistic and coarse-grained diffusion is slower, and the acceleration upon coarse-graining is larger (α = 21.83). It is simulated in mixture with DiMeBu and DiMeHx, the molecules that exhibit the slowest and largest acceleration out of the four small hydrocarbon molecules. All concentrations of these two mixtures form mixture group B.

Nonbonded potentials and roughness volumes of the five pure components have already been determined in Refs. 22 and 42. If binary mixtures are to be simulated at different concentrations, one does not want to reparameterize the mixed potential for each of them, which, in the case of IBI, would require at least a short AA simulation to obtain target RDFs. Ideally, one would either use the potentials of the pure components plus some mixing rules or, at least, minimize the number of AA simulations needed. We therefore first test using a simple combination rule to form the mixed potential for the mixtures. Second, we create *one* mixed potential more expensively by applying IBI to an equimolar mixture, which is then used for *all* other concentrations.

II. METHODS

A. Simulation details

The alkanes 2,3-dimethylbutane, 2,3,4-trimethylpentane, 3-ethylhexane, and 2,5-dimethylhexane are simulated in every possible binary combination (six combinations). Additionally, 3,3-diisopropyl-2,4-dimethylpentane is simulated in mixture with 2,3-dimethylhexane and 2,5-dimethylhexane. Each of the eight combinations is simulated at ambient conditions and in 11 different compositions with mole fractions between x = 0.01 and x = 0.99 (Table III). Thus, 92 (88 mixtures, 5 pure) systems are simulated, each composed of 1000 (500 for mixtures with DIPDMP) molecules in total.

Molecular dynamics simulations (AA and CG) are performed with the Large-scale Atomic/Molecular Massively Parallel Simulator (LAMMPS).[43,44] To generate the initial AA configurations, the molecules are distributed in a cubic simulation box (side length = 100 Å) using Moltemplate.[45] After an energy-minimization with a conjugated gradient algorithm, the molecular conformations and orientations are randomized by Brownian dynamics at 900 K for 0.2 ns and with *NVT* dynamics with a Nosé–Hoover thermostat for 0.5 ns (coupling time τ_t = 50 fs). The system is cooled down to 298.18 K at 500 atm for 0.5 ns with *NPT* dynamics using a Nosé–Hoover thermostat (τ_t = 50 fs) and Nosé–Hoover barostat (τ_p = 500 fs). The pressure is decreased to 1 atm using the same thermostat and barostat conditions for 0.5 ns.

Production and equilibration runs for both AA-MD and CG-MD systems are carried out under isothermal–isobaric (*NPT*) conditions at 1 atm and 298.18 K with both the Nosé–Hoover thermostat (τ_t = 50 fs) and barostat (τ_p = 500 fs). Some CG-MD simulations are additionally performed under *NVT*-conditions. Integration is accomplished with a velocity-Verlet algorithm with time steps of 0.5 fs for both AA and CG simulations.

Periodic boundary conditions are applied in all three dimensions. All systems are equilibrated for 10 ns with a time step of Δt = 0.5 fs, followed by production runs of at least 20 ns using the same time step. The lengths of the production runs for the AA and CG simulation and different compositions can be found in Table III.

B. All-atom model

The fully flexible OPLS-AA force field is used to model AA interactions.[46] Nonbonded and bonded parameters are given in the supplementary material. Both the atomistic nonbonded size σ and nonbonded energy ε parameters are obtained by geometric combination rules for interactions between unlike atoms. During the simulations, energy and pressure are corrected by adding standard long-range van der Waals corrections. Intramolecular nonbonded interactions are evaluated for atoms separated by more than two bonds. The potential is scaled down by 0.5 for the 1,4-intramolecular interactions. Nonbonded interactions are calculated up to a cut-off radius of 11 Å. The atomistic models contain no electrostatic terms.

C. Coarse-grained model

Each molecule is mapped into one single CG bead positioned at the center of mass of the AA molecule. The tabulated potentials of the pure components have been derived by Iterative Boltzmann Inversion (IBI) as part of the work in Refs. 22 and 42. They are tabulated in the supplementary material. To simulate binary mixtures of various compositions without the need to re-coarse-grain each concentration via IBI, two approaches are tested. In the first, the mixed potentials of all mixtures in mixture group A are modeled by arithmetic combination rules [Eq. (2)] with the fitting parameter c ranging from 0.1 to 0.9 in steps of 0.1 for each composition,[47]

$$U_{A-B} = c \cdot U_{A-A} + (1-c) \cdot U_{B-B}. \quad (2)$$

In the second approach, the mixed potential is directly derived via IBI using VOTCA[48] from an AA simulation of a 1:1 mixture, i.e., 500 (250) molecules of either type. This potential is then used for every concentration. The second potential overall matches the densities and radial distribution functions of all mixtures better compared to the first (see Sec. III A and the supplementary material). Consequently, we used the IBI approach in this work and recommend its adoption for similar studies. This approach, while slightly more expensive than the first, remains efficient, requiring only a short AA simulation of a single composition to yield improved results across all concentrations. Some additional information on the effects of different potentials on the dynamics is provided in the supplementary material, adding insights into the potential magnitude of error when other potentials are used. All mixtures in mixture group A (i.e., not containing DIPDMP) with x_1 equal to 0.25, 0.5, and 0.75 are additionally simulated under NVT conditions using the mixed potentials generated with the combination rules. The CG potentials of the neat alkanes and their mixed potentials for two combinations of mixture group A are shown in Fig. 2, and the others are shown in the supplementary material. During IBI, a simple pressure correction is applied,[49] with an exception of the generation of the mixed DiMeHx–DIPDMP, where correcting the pressure worsened the mixing ability. The pure potentials and IBI generated potentials of mixture group B are displayed in Fig. 3.

D. Dynamical properties

The dynamics of the individual species are characterized using self-diffusion coefficients D_1 and D_2 (also referred to as tracer or *intra*diffusion coefficient) according to Einstein's equation from the mean squared displacement (MSD) of the centers of mass of the molecules. Minority components with low mole fractions suffer

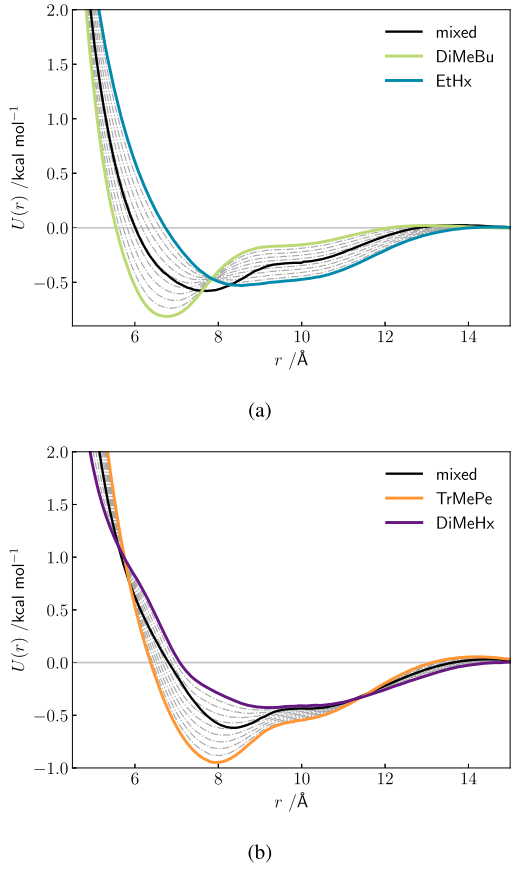

FIG. 2. Coarse-grained potentials for (a) pure 2,3-dimethylbutane (*green line*), pure 3-ethylhexane (*blue line*), and their mixed potentials (*black line*) and (b) pure 2,3,4-trimethylpentane (*orange line*), pure 2,5-dimethylhexane (*purple line*), and their mixed potentials (*black line*); mixed potentials generated by iterative Boltzmann inversion for a 1:1 mixture *solid* and via combination rules according to Eq. (2) with c ranging from 0.1 to 0.9 (*dashed-dotted curves*).

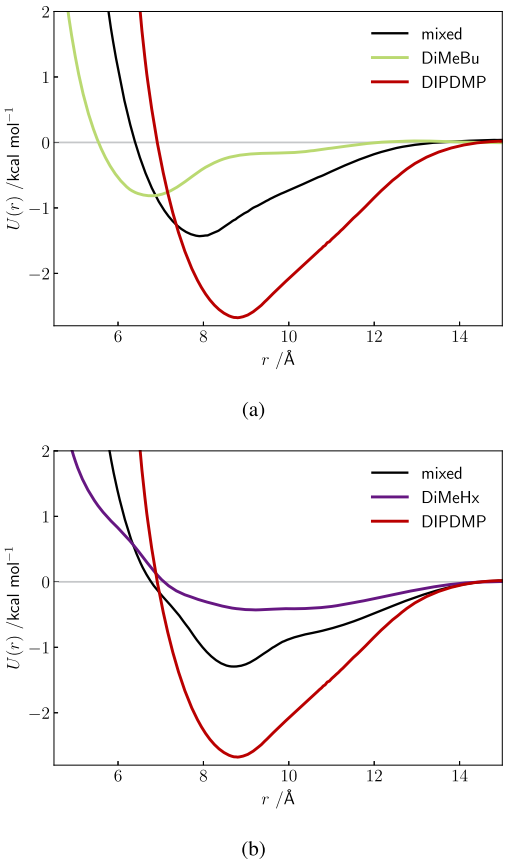

FIG. 3. Coarse-grained potentials for (a) pure 2,3-dimethylbutane (*green line*), pure 3,3-diisopropyl-2,4-dimethylpentane (*red line*), and their mixed potentials (*black line*) and (b) pure 2,5-dimethylhexane (*purple line*), pure 3,3-diisopropyl-2,4-dimethylpentane (*red line*), and their mixed potentials (*black line*); mixed potentials generated by iterative Boltzmann inversion for a 1:1 mixture.

from poor sampling as, e.g., for the 1:99 mixtures only ten molecules (five molecules for mixtures with DIPDMP) of one component are present. Therefore, the MSDs are calculated over the whole production run, but the self-diffusion coefficients are only calculated from the linear fit of the MSD against the time between 50 and 150 ps for AA simulations and 100 and 300 ps for CG simulations.

In addition to the two self-diffusion coefficients of the components, the mixtures can be characterized by a single system-specific so-called binary diffusion coefficient D_{12} (also referred to as mutual diffusion coefficient or *inter*diffusion coefficient). For binary mixtures, it can easily be calculated from MD simulations with Eq. (3) using the mean squared displacement of the center of mass of *all* molecules of one species r_i^{com}. The binary diffusion coefficient as calculated from species i requires an additional prefactor,

$$D_{12}^{i} = \lim_{t\to\infty} (x_i M_i)^2 \left(\frac{1}{x_1 M_1} + \frac{1}{x_2 M_2}\right)^2 \frac{N x_1 x_2}{6t} \left\langle \left(\Delta r_i^{com}\right)^2 \right\rangle, \quad (3)$$

with the total number of molecules N and the molecular weights M_1 and M_2.[50] The so-calculated diffusion coefficients are Maxwell–Stefan diffusion coefficients. Fick diffusion coefficients can be calculated from MS diffusion coefficients using the thermodynamic factor. Details on the calculation of the binary (MS) diffusion coefficient in MD simulations can be found in the supplementary material. As momentum is conserved, calculations for species 1 and 2 yield the same binary diffusion coefficient $D_{12}^1 = D_{12}^2 = D_{12}$. For the calculation of D_{12}, each time step only provides one r^{com}. The collective MSD can thus only be averaged over multiple time origins but not over molecules, leading to a larger statistical uncertainty. The binary diffusion coefficients are calculated in the range of 10–50 ps (AA, 75–125 ps for mixture group B) or 20–100 ps (CG), respectively. For AA simulations, the long production run is supplemented by 15 runs of 2 ns with different random start velocities, while for the CG simulations, four different production runs of 50 ns and 10 runs of 10 ns are used. The center of mass position of the entire system is subtracted in each time step to allow the linear fit in this short time regime with only small MSD of the center of mass of the whole set of molecules of one type.

The self-diffusion coefficient describes the motion of one molecule of a specific type among all other molecules, including the molecules of the same type. The binary diffusion coefficient describes the collective motion of one type of molecules vs that of the other species. At infinite dilution, when one molecule is surrounded only by the other species, the self-diffusion coefficient of this molecule and the binary diffusion coefficient are identical. Acceleration factors may be determined from both the self-diffusion coefficients, $\alpha_{self,1} = D_1^{CG}/D_1^{AA}$, and the binary diffusion coefficients, $\alpha_{binary} = D_{12}^{CG}/D_{12}^{AA}$.

E. Structural properties

The potentials of the pure components have been generated using IBI, a structure-based coarse-graining method, that iteratively matches the radial distribution function (RDF or g) of the CG model to the target distribution of the AA model. Thus, structural properties, the RDF and the density or volume per molecule, are used to determine the quality of a CG model. For a comparison between the CG model and the AA model, the radial distribution function of the centers of mass is used. An error function[51] is calculated using the following equation:

$$\delta g = \frac{\int_0^{r_{cut}} \left| g^{\mathrm{CG}}(r) - g^{\mathrm{AA}}(r) \right| dr}{\int_0^{r_{cut}} g^{\mathrm{AA}}(r)\, dr}. \quad (4)$$

We use $r_{\mathrm{cut}} = 10$ Å for all systems. This value always includes the first solvation shell of the RDF, but is below the maximum position of the second shell to emphasize the importance of the direct neighbors within the RoughMob method. Including the second shell usually lowers the error of the RDF. For binary mixtures, three different δg can be calculated—two same species errors δg_{11} and δg_{22} and one mixed species error δg_{12}. To enable the simple comparison of the systems regarding the quality of the structural properties, we define a total error of RDF δg_{total} as the average of the three δg weighted based on the mole fraction present in the mixture,

$$\delta g_{total} = \frac{x_1^2\, \delta g_{11} + x_1 x_2\, \delta g_{12} + x_2^2\, \delta g_{22}}{x_1^2 + x_1 x_2 + x_2^2}. \quad (5)$$

TABLE IV. All-atom radii and effective hard-sphere radii of CG beads in Å.

Atom/bead name	Radius
C	1.75
H	1.25
DiMeBu	2.77
TrMePe	3.19
EtHx	3.37
DiMeHx	3.54
DIPDMP	3.46

F. RoughMob method

1. Basics

The RoughMob method connects the *change* in the molecular surface roughness ("Rough") to the *change* in the mobility ("Mob") upon coarse-graining. The geometries of the molecules are defined by the positions of the atoms or beads and their radii. We define the radius of an atom as half its nonbonded size parameter $r_{AA} = 0.5\sigma_{ii}$ and the radius of a CG bead as half of the distance where the tabulated CG potential first is equal to or below zero and thus the effective hard-sphere radius. The values are listed in Table IV.

2. Molecular roughness difference

The molecular roughness difference ΔR is a comparative quantity that is defined as the deviation between the molecular surface of the all atom molecule and the molecular surface of the coarse-grained molecule. The molecular surfaces are represented as spherical numerical grids with the same number of points n_{grid} of a Fibonacci grid that is superposed on both the AA and the CG surface. When the center of mass of the molecule is placed at the origin of a spherical coordinate system, ΔR can be calculated according to

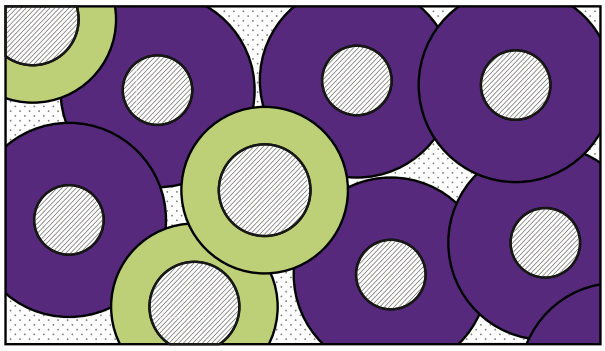

FIG. 4. Illustration of all shell volumes (part of active volumes) in a binary mixture; different molecule types are represented by different colors.

Eq. (6) with $r_{\mathrm{AA}}^{(i)}$ and $r_{\mathrm{CG}}^{(i)}$ being the radial distance of the AA surface points. Details of the calculation can be found in Refs. 22 and 42,

$$\Delta R = \frac{1}{n_{grid}} \sum_{i=1}^{n_{grid}} \left| r_{\mathrm{AA}}^{(i)} - r_{\mathrm{CG}}^{(i)} \right|. \tag{6}$$

The radial distance $r_{\mathrm{CG}}^{(i)}$ is always equal to the radius of the spherical CG bead r_{CG}. From the radial distances of the AA surface, an average radius of the AA molecule $\bar{r}_{\mathrm{AA}}$ can be calculated.

3. Roughness volumes

Using the molecular roughness difference, we defined active and passive volumes. All volumes of the model are illustrated in Figs. 4–7. Active volumes are volumes in which the difference between the molecular surfaces in the two resolutions manifests itself. Based on the spherical structure of the CG beads, the main part of the active volume is called shell volume V_{shell}. The shell volume has a thickness of twice the molecular roughness difference [Eq. (6)] and is illustrated in Fig. 4. As highlighted in Fig. 5, the shell volumes can overlap. The active volume is thus expanded by adding the overlap volume $V_{overlap}$ to V_{shell}. In this region, the change of the roughness should be especially noticeable, increasing the impact on the acceleration of dynamics.

The passive volumes are those volumes within the simulation box that are not affected by the difference of the molecular surfaces between the atomistic and the coarse-grained model. They are divided into the inner and outer passive volume. The inner volume V_{in} lies within the molecule as illustrated in Fig. 6. It accounts for the basic size of the beads, which is not sufficiently represented in the shell volume. A larger inner volume increases the acceleration of dynamics. The opposite is the case for the outer volume V_{out}, the passive volume outside of the molecule, or, more precisely, outside of V_{shell} (see Fig. 7). A large outer volume should decrease the acceleration of dynamics as the molecules are less able to feel the change of the roughness on the surface of the surrounding molecules. Details on the numerical calculations of the molecular roughness difference and the roughness volumes can be found in Refs. 22 and 42. Example calculations can be found on GitHub.

Equation (7) emerged as useful for predicting the acceleration factor α_{pred}. Given a training set of acceleration factors α and roughness volumes, the fitting parameters A, B, and C are determined simultaneously via a least squares fit,

$$\begin{aligned} \alpha_{pred} &= A \cdot \left(V_{shell} + V_{overlap}\right) + B \cdot \exp\left(\frac{V_{in}}{V_{out}}\right) + C, \\ \text{with} \quad A &= \frac{1}{11.51\ \text{Å}^3} \\ \text{and} \quad B &= 0.837 \\ \text{and} \quad C &= -10.61. \end{aligned} \tag{7}$$

The above equation can then be used to predict the acceleration factor of other molecules. In Ref. 42, we used 17 systems of pure hydrocarbons for the least squares fit resulting in the given parameters. The five molecules of interest in this work were part of the training set used to determine this fitting equation. The roughness volumes of the pure components as determined in our previous work are listed in Table V. The summand containing the active volumes is also referred to as active volume term $(A(V_{shell} + V_{overlap}))$, and the summand containing the passive volumes is also referred to as passive volume term $(B \exp\left(\frac{V_{in}}{V_{out}}\right))$.

In a mixture, one can not only look at the roughness volumes present in the whole system but also differentiate between the different species. Figure 8 already shows two possible ways to look at the local contribution of the shell volume for a single molecule. It is unknown whether the acceleration of the molecule is purely connected to the loss of roughness of the molecule itself (a) or only results from the interaction of the molecule with its direct neighbors that likewise suffer from a smoothened molecular surface (b). Similar considerations can be made for all roughness volumes of the different species as well as their possible interaction with the surroundings. The equations presented in Sec. III C are phenomenological descriptions of the observed behavior that allow for a future adjustment or refinement. All data (dynamical and geometrical properties) are provided in the supplementary material. Codes for the calculation of the roughness volumes and examples for fitting procedures can be found on GitHub.

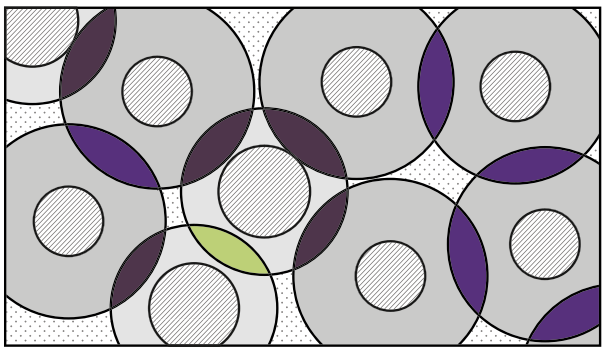

FIG. 5. Illustration of all overlap volumes (part of active volumes) in a binary mixture.

TABLE V. Systems (pure components), molecular roughness difference, active volume term, passive volume term, shell volume, overlap volume, inner passive volume, and outer passive volume as determined in Refs. 22 and 42; molecular roughness difference is in Å; volumes are in Å^3.

System	ΔR	$A(V_{shell}+V_{overlap})$	$B\exp\left(\frac{V_{in}}{V_{out}}\right)$	V_{shell}	$V_{overlap}$	V_{in}	V_{out}	V_{mol}
DiMeBu	0.52	11.01	2.77	113.7	13.0	59.9	50.0	210.6
TrMePe	0.61	15.49	3.10	156.4	21.9	71.1	54.3	259.8
EtHx	0.75	18.92	2.11	186.4	31.2	54.7	59.0	268.9
DiMeHx	0.97	24.54	1.78	232.1	50.3	37.6	49.7	269.1
DIPDMP	0.56	20.25	11.19	202.9	30.0	139.8	53.9	366.6

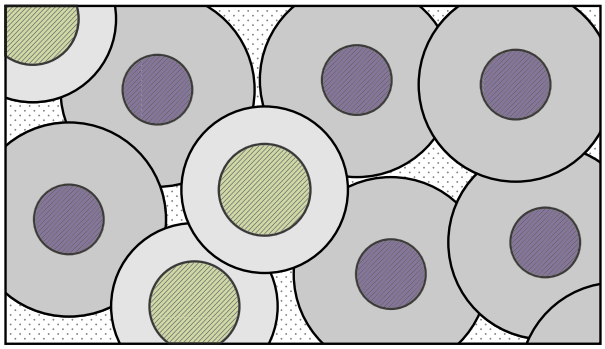

FIG. 6. Illustration of inner passive volumes in a binary mixture.

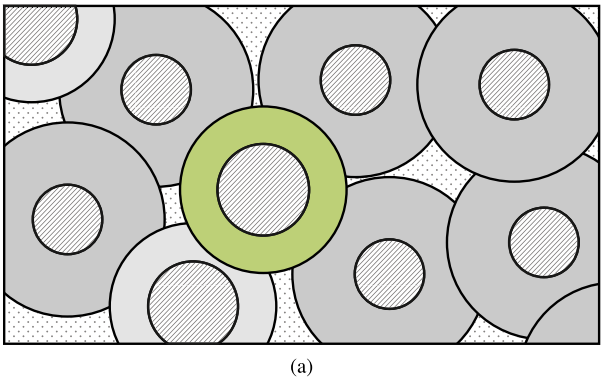

(a)

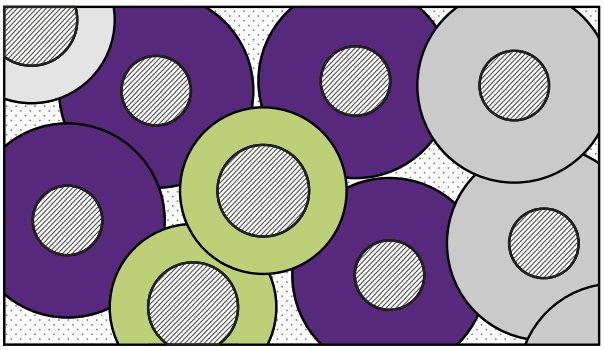

(b)

FIG. 8. Illustration of shell volume for a specific molecule in a binary mixture; (a) excluding and (b) including a possible influence of the neighboring molecules.

III. RESULTS AND DISCUSSION

A. Change of the structural properties upon mixing and coarse-graining

The AA densities of the pure components range from 0.680 g mol^{-1} for DiMeBu over 0.705 for both EtHx and DiMeHx and 0.73 for TrMePe to 0.835 g mol^{-1} for DIPDMP. The densities of the mixtures are between those of the pure components, e.g., the density of the DiMeBu–TrMePe mixtures increases when more TrMePe is present. Alternatively, one can look at the molecular volume, which ranges from 211 Å^3 for DiMeBu over 260 Å^3 for TrMePe and 269 Å^3 for both EtHx and DiMeHx to 366 Å^3 for DIPDMP. Mixing a component with a low molecular volume with a second component with a higher molecular volume increases the molecular volume of the system. All values are provided in the supplementary material. All AA simulations exhibit a close to linear relation with the mole fraction so that $V_{mol} = x_1 V_{mol,1} + x_2 V_{mol,2}$ as they should for ideal

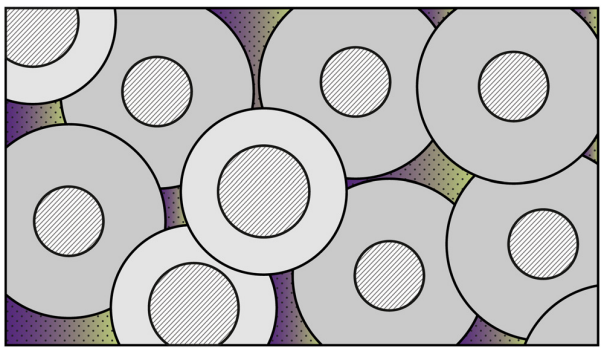

FIG. 7. Illustration of outer passive volume in a binary mixture.

mixtures.[52] The deviation between so-calculated V_{mol} and simulated $V_{mol,AA}$ is always equal to or less than 0.4% and on average only 0.05%. Mixtures of group A and the DiMeBu–DIPDMP mixtures from group B show a good match between the CG densities calculated from simulations with the IBI generated mixed potentials with an averaged deviation of only 0.29%. During IBI of the equimolar DiMeHx–DIPDMP mixture, pressure correction could not be achieved resulting in large differences in the densities between AA and CG simulations under NPT conditions for most compositions of this mixture. As the RoughMob method required matching densities, all DiMeHx–DIPDMP coarse-grained models are simulated under NVT conditions. Mixtures simulated (CG) under NVT conditions use a volume that is calculated from the molecular volumes of the pure components. This is done instead of using $V_{mol,AA}$, as ideally there should be no need for any AA simulations with the different compositions. Using combination rules for the generation of the mixed IBI potential overall worsened the structural properties, while sometimes yielding similar structural and dynamical results to the mixed IBI potential. A short discussion on the influence of CG potentials with their different densities (and RDFs) on the dynamical results can be found in the supplementary material.

As an example, Fig. 9 shows the radial distribution functions of a TrMePe–DiMeHx mixture and DiMeBu–EtHx mixture with $x_1 = 0.1$ for AA and CG simulations with IBI generated potential from equimolar mixtures. For the mixtures, the lesser component exhibits poor structural matching, while the majority component matches well. While the RDF error for same species contacts can get up to 42% (for DiMeBu with $x_1 = 0.01$ in DiMeHx), the total RDF error δg_{total} [Eq. (5)] of mixture group A remains below a maximum of 9% with an average of 1.8%. Group B suffers from poor matching of the RDFs especially for $x_1 = 0.25, 0.5$, and 0.75 with high total RDF errors of up to 22%. The average δg_{total} for the DiMeBu–DIPDMP and DiMeHx–DIPDMP mixtures is 6.9% and 8.1%, respectively. All values of the RDF errors and plots of the RDFs for the different compositions can be found in the supplementary material. For most mixtures, the RDF varies little when the mole fraction is small. Exceptions are the CG simulations of mixtures in group B and the RDF of DiMeBu in the AA simulations of DiMeBu–DIPDMP mixtures. Here, the height of the first peak significantly changes with the mole fraction.

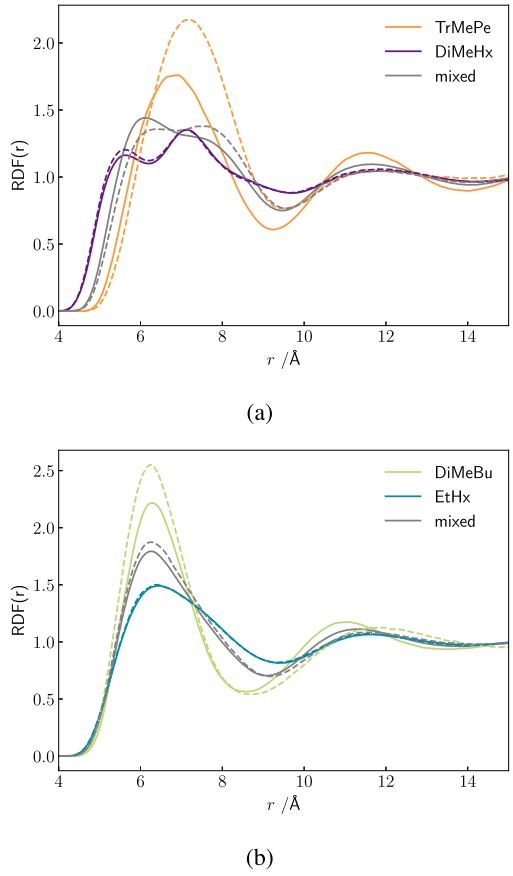

FIG. 9. Radial distribution functions of the atomistic (solid) and coarse-grained (dashed) simulations with $x_1 = 0.1$ for (a) TrMePe in DiMeBx and (b) DiMeBu in EtHx.

B. Change of molecular mobility upon mixing

Figures 10 and 11 display the self-diffusion coefficients and single-species acceleration factors $\alpha_{self,1}$ of one component in different mixtures plotted against the mole fraction of the second component for the first component being DiMeBu (a) and DiMeHx (b). The plots for EtHx, TrMePe, and DIPDMP are shown in the supplementary material. The color indicates the second component

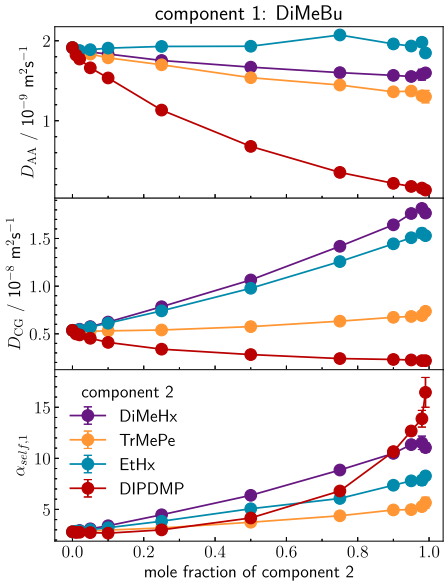

FIG. 10. Self-diffusion coefficients and acceleration factors of 2,3-dimethylbutane in binary mixtures against the mole fraction of the second component according to color; the error bars of diffusion coefficients are standard deviations between the independent Cartesian components.

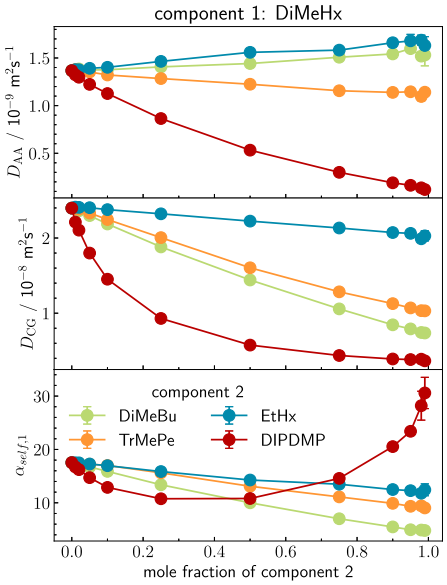

FIG. 11. Self-diffusion coefficients and acceleration factors of 2,5-dimethylhexane in binary mixtures against the mole fraction of the second component according to color; the error bars of diffusion coefficients are standard deviations between the independent Cartesian components.

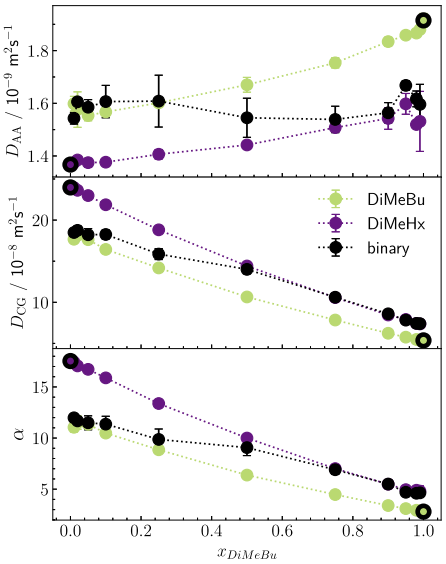

FIG. 12. Self- and binary-diffusion coefficients and acceleration factors in a 2,3-dimethylbutane and 2,5-dimethlyhexane mixture against the mole fraction; the error bars of diffusion coefficients are standard deviations between the independent Cartesian components.

the primary component is mixed with. Mixtures with low mole fractions of one component suffer from a poorer sampling as, e.g., for the 1:99 mixtures only ten molecules (5 for mixtures with DIPDMP) of component 1 are present. This shows up in the larger errors, which are calculated as standard deviations between independent Cartesian components of the diffusion coefficients. When a slow component is mixed with a faster second component, its self-diffusion coefficient increases and vice versa. For example, the blue markers in Fig. 10 (middle) represent D_{CG} of DiMeBu (component 1) mixed with EtHx (component 2). The self-diffusion coefficient of DiMeBu increases with the amount of EtHx as D_{CG} of a pure DiMeBu is lower than D_{CG} of EtHx. The opposite is the case for the CG simulations (Fig. 11, middle, blue curve) of DiMeHx mixed with EtHx. Here, D_{CG} of DiMeHx decreases with an increasing amount of EtHx. While the self-diffusion coefficients are known to depend on the mass of the molecules, the acceleration factor of DiMeBu and EtHx in the mixture did not change when a heavier version of EtHx was used [e.g., $\alpha_{self,\mathrm{DiMeBu}} = 5.07$ vs 5.12 (heavier EtHx) and $\alpha_{self,\mathrm{EtHx}} = 7.19$ vs 7.18 (heavier EtHx) in a 1:1 mixture]. It is interesting to see that the concentration dependence of a self-diffusion coefficient can be reversed between atomistic and coarse-grained models. An example is DiMeBu in mixture with DiMeHx (Fig. 10, top and bottom, purple curve), and a counter-example is DiMeHx in mixture with TrMePe (Fig. 11, top and bottom, orange curve). For mixture group A, overall, the trend of the self-diffusion coefficients and acceleration factors appears to be close to linear in the mole fraction. However, mixture group B (red curves, the second component is DIPDMP) clearly differs from a linear trend. For all AA and CG simulations, the self-diffusion coefficient of DiMeBu or DiMeHx, respectively, decreases with an increasing amount of DIPDMP. The acceleration factor of DiMeBu in DIPDMP, however, increases with an increasing amount of DIPDMP as the decrease of the diffusion

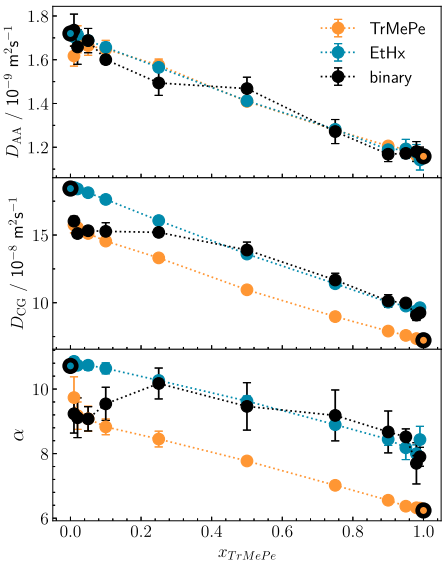

FIG. 13. Self- and binary-diffusion coefficients and acceleration factors in a 2,3,4-trimethylpentane and 3-ethylhexane mixture against the mole fraction; the error bars of diffusion coefficients are standard deviations between the independent Cartesian components.

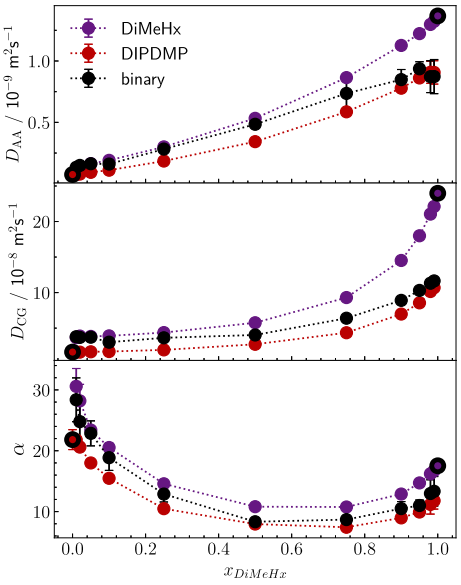

FIG. 14. Self- and binary-diffusion coefficients and acceleration factors in a 2,5-dimethylhexane and 3,3-diisopropyl-2,4-dimethylpentane mixture against the mole fraction; the error bars of diffusion coefficients are standard deviations between the independent Cartesian components.

coefficient is less pronounced in the CG simulation. For DiMeHx, this even results in a minimum of the acceleration factor (Fig. 11, bottom, red) around $x_{DIPDMP} \approx 0.25$. The acceleration factor $\alpha_{self,1}$ is highly dependent on the other component. While $\alpha_{self,1}$ of DiMeBu only gets up to around 5.3 in a DiMeBu–TrMePe mixture with $x_1 = 0.01$, it gets up to around 12 in a DiMeBu–DiMeHx mixture. The acceleration of the individual components is thus strongly affected by the overall acceleration of the system.

Figures 12–14 show how both the self- and the binary-diffusion coefficients and acceleration factors within one mixture change with the mole fraction. They further illustrate the variance in the dynamical behavior of different mixtures when AA and CG simulations are compared. In a DiMeBu–DiMeHx mixture, the all-atom self-diffusion coefficients increase with x_{DiMeHx} but decrease with x_{DiMeHx} in the CG representation (Fig. 12). For a TrMePe–EtHx mixture, the AA self-diffusion coefficients are almost identical, but they differ by a factor of around 0.8 in all CG simulations (Fig. 13). The diffusion coefficients of the DiMeHx–DIPDMP mixture increase with x_{DiMeHx} in both AA and CG simulations, while the acceleration factor initially decreases with an increasing x_{DiMeHx} (Fig. 14). Interestingly, even though DiMeHx has a lower acceleration factor than DIPDMP (as a pure component), the acceleration of DiMeHx in the mixture is in fact larger than the acceleration of DIPDMP. The acceleration factors of the remaining mixtures are shown in Figs. 15 and 16.

Within one mixture, the ratio $\alpha_{self,2}/\alpha_{self,1}$ stays approximately constant with the highest value for the DiMeBu–DiMeHx mixture (Fig. 12, around 1.55) and the lowest value for the DiMeHx–DIPDMP mixture (Fig. 14, around 0.72). The largest

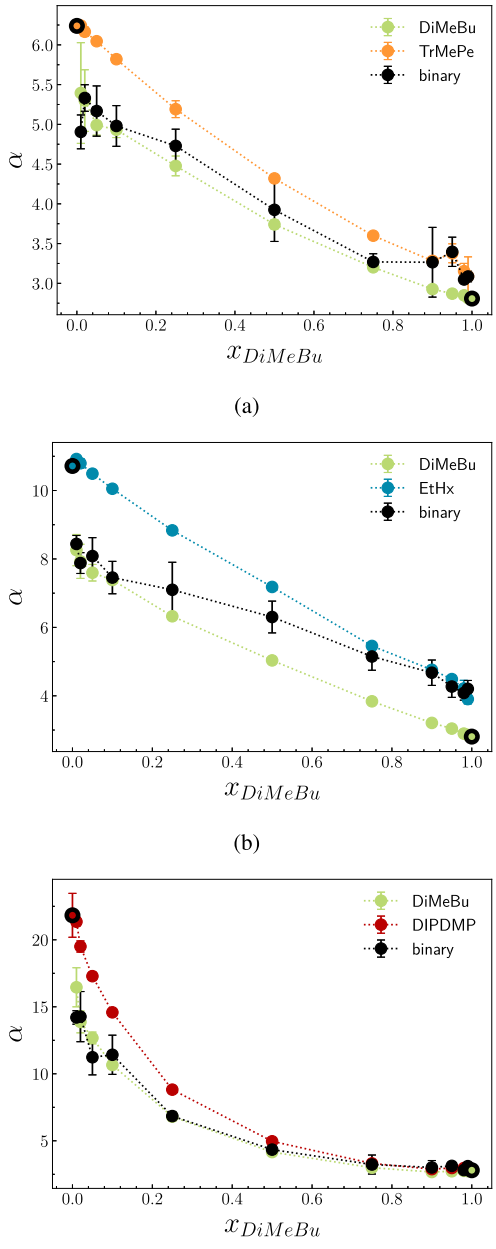

FIG. 15. Acceleration factor of the self-diffusion coefficients and binary diffusion coefficient in a (a) DiMeBu–TrMePe, (b) DiMeBu–EtHx, and (c) DiMeBu–DIPDMP mixture.

variation is found for DiMeBu–DIPDMP (Fig. 15) where the ratio changes between 1.06 (for $x_{\mathrm{DiMeBu}} = 0.01$) to 1.53 ($x_{\mathrm{DiMeBu}} = 0.99$). For an easy discussion, we use the convention that component 1 always refers to the component that has the lower acceleration

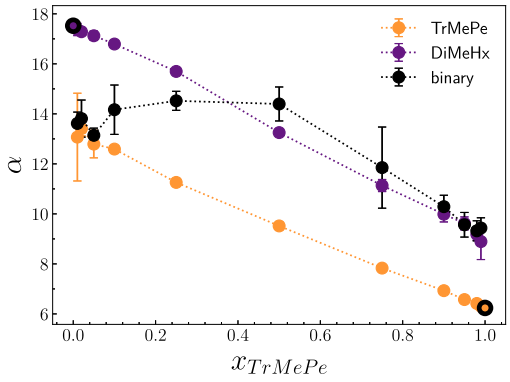

(a)

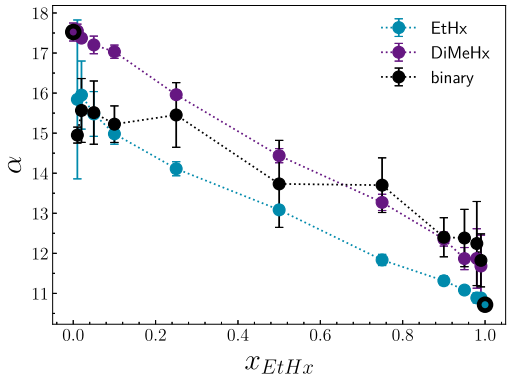

(b)

FIG. 16. Acceleration factor of the self-diffusion coefficients and binary diffusion coefficient in a (a) TrMePe–DiMeHx and (b) EtHx–DiMeHx mixture.

factor as a pure liquid. The acceleration factors of the binary diffusion coefficients have larger error bars than those of self-diffusion coefficients due to poorer sampling (see above). Furthermore, while the acceleration factor of the binary diffusion coefficient is always close to the acceleration factor of the self-diffusion coefficient of the minority component for mole fraction of or below $x = 0.05$, the behavior of α_{binary} differs greatly in the x range between 0.25 and 0.75 between different mixtures. The binary diffusion acceleration factor of the 1:1 DiMeBu–TrMePe mixture is close to the acceleration factor of the self-diffusion coefficient of DiMeBu [Fig. 15(a)], while it is close to α_i of DiMeHx in a 1:1 DiMeBu–DiMeHx mixture (Fig. 12, bottom). What causes the different behavior is as yet unknown.

C. RoughMob method

1. Prediction of the overall acceleration

Each binary mixture has three acceleration factors of interest: the acceleration of self-diffusion coefficients of both components ($\alpha_{self,1}$ and $\alpha_{self,2}$) and the binary acceleration factor (α_{binary}). The observation that the acceleration of the individual components is strongly affected by the overall acceleration in a mixture leads us to the definition of an auxiliary acceleration factor that represents this overall acceleration and can be calculated from the simulations using the following equation:

$$\alpha_{mix} = x_1 \cdot \alpha_{self,1} + x_2 \cdot \alpha_{self,2}. \tag{8}$$

In order to reduce the discussion, we analyze how this overall acceleration α_{mix} can be predicted in the this section and proceed to use the findings to the prediction of the acceleration of the self-diffusion coefficients (Sec. III C 2) and the acceleration of the binary diffusion coefficients (Sec. III C 3).

In mixtures, the different roughness volumes must be assembled into "mixed" variants. Ideally, one could simply use the arithmetic mixing rules for calculating average roughness volumes, for example,

$$V_{shell,mix} = x_1 \cdot V_{shell,1} + x_2 \cdot V_{shell,2}, \tag{9}$$

and analogous for the other volumes and use the same fitting parameters as determined for the single component systems to predict the acceleration present in the mixture. We thus define the prediction of an "ideal" or arithmetic mixing acceleration factor according to

$$\alpha^*_{mix,pred} = \frac{1}{11.51\ \text{Å}^3}\left(V_{shell,mix} + V_{overlap,mix}\right) + 0.837 \cdot \exp\left(\frac{V_{in,mix}}{V_{out,mix}}\right) - 10.61. \tag{10}$$

Note that the numerical coefficients [cf. Eq. (7)] are those determined previously for neat fluid hydrocarbons and that no reparameterization for mixtures has been done up to this point. Figure 17 shows the prediction of this arithmetic acceleration factor [$\alpha^*_{mix,pred}$, Eq. (10)], as calculated with averaged roughness volumes, plotted against the "true" overall acceleration factor (α_{mix}) determined from the actual simulations according to Eq. (8). The agreement for mixture group A (all markers except squares) is overall good, while group B (squares) deviates significantly.

To understand the nature of this difference in the behavior between the two groups, we distinguish between the active volume term ($A\left(V_{shell,mix} + V_{overlap,mix}\right)$) and the passive volume term ($B \cdot \exp\left(\frac{V_{in,mix}}{V_{out,mix}}\right)$). This differentiation allows for a more nuanced understanding of their respective impacts within the studied system. Figure 18 displays how the active volume term (dashed lines) and the passive volume term (dotted lines) of the acceleration change in the mixtures with the mole fraction of component 1. Component 1 is always the component with the lower pure component acceleration factor.

As in the case of single component systems (Table V), the active term always exceeds the passive term. The active volume term greatly differs between the mixtures, and it changes almost linear with the concentration. Linearity ("ideality") is evident for both mixture groups, despite the inherently different slopes. The active volume term does, therefore, not allow for a distinction between mixture group A and mixture group B that explains the difference in the behavior between the two groups. Mixture groups A and B, however, differ widely and qualitatively in the composition dependence

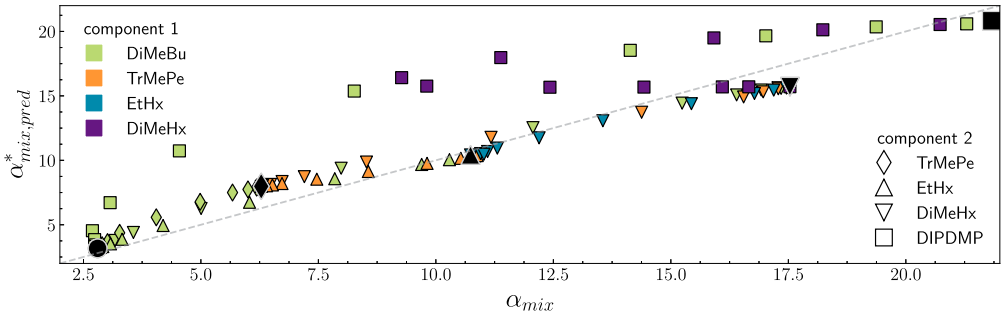

FIG. 17. "Ideal" arithmetic mixing prediction of the overall acceleration [Eq. (10)] against the "true" overall acceleration as calculated from the simulations [Eq. (8)]; marker colors represent component 1, markers represent component 2; *black markers* represent pure components; and the *gray dashed line* represents $\alpha^*_{mix,pred} = \alpha_{mix}$.

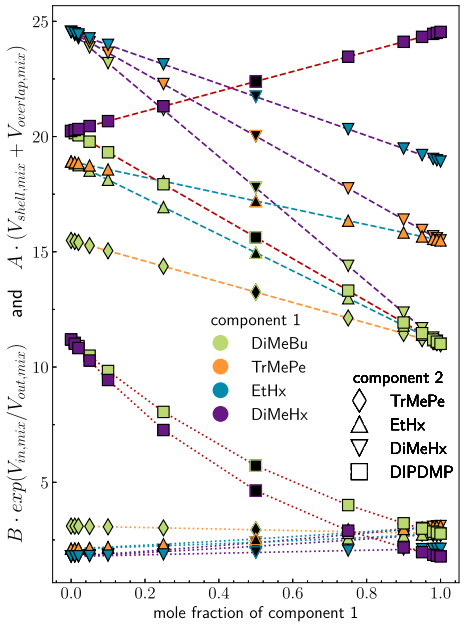

FIG. 18. Active volume term (dashed lines) and passive volume term (dotted lines) of the mixture against the mole fraction of component 1; marker colors represent component 1, markers represent component 2; and black markers represent active $\mathscr{A}$ and passive $\mathscr{P}$ correction terms (passive correction term scaled by $1/\omega$).

of the passive volume terms. The variations of the passive volume terms of mixture group A are almost negligible regarding both the differences between different mixtures within that group and the change of the passive volume term with the concentrations. Mixture group B, however, behaves significantly different. The passive term reaches higher absolute values; it shows a larger variation with the concentration, and the variations are non-linear. Based on these observations, we propose a methodology wherein a correction term is added to the arithmetically predicted acceleration factor of the mixture ($\alpha^*_{mix,pred}$) that utilizes the passive volumes as an indicator to ascertain the necessity of incorporating a correction term,

$$\alpha_{mix,pred} = \alpha^*_{mix,pred} + x_1 x_2 (1 - \mathscr{P}) \mathscr{A}, \tag{11}$$

with $\mathscr{P}$ being the passive correction term calculated from the passive volumes in a mixture at $x_1 = 0.5$ in the form of Eq. (12) and $\mathscr{A}$ being the active correction term calculated from active volumes [Eq. (13)] in an equimolar mixture. The prefactor $x_1 x_2$ arises from the phenomenon that the deviation of $\alpha^*_{mix,pred}$ from α_{mix} is higher for mole fractions that are close to an equimolar distribution and lower for low mole fractions of one component,

$$\begin{aligned} \mathscr{P} &= \omega B \exp\left(\frac{0.5 \cdot V_{in,1} + 0.5 \cdot V_{in,2}}{V_{out,mix}}\right) \\ &= \omega B \sqrt{\exp\left(\frac{V_{in,1}}{V_{out,mix}}\right) \cdot \exp\left(\frac{V_{in,2}}{V_{out,mix}}\right)}, \end{aligned} \tag{12}$$

$$\begin{aligned} \mathscr{A} &= A(0.5(V_{shell,1} + V_{shell,2}) + 0.5(V_{overlap,1} + V_{overlap,2})) \\ &= 0.5 \cdot A(V_{shell,1} + V_{overlap,1}) + 0.5 \cdot A(V_{shell,2} + V_{overlap,2}), \end{aligned} \tag{13}$$

with $A = \frac{1}{11.51\ \text{Å}^3}$ and $B = 0.837$ as in Eq. (7). Note that all roughness volumes are single-component quantities determined previously; $V_{out,mix}$ is assembled from pure-component volumes, too [Eq. (9)]. For mixtures in group A, the term $(1 - \mathscr{P})$ should be close to zero as only little to no correction is required. Thus, $\mathscr{P}$ should be close to one. Since the passive volume term of mixture group A ranges from 1.78 to 3.10, a weighting factor ω is needed. Equation (12) shows that taking the passive contribution to the correction at $x_1 = 0.5$ also allows for the interpretation as a geometric average of the contributions of the individual molecules. While the inner passive volume of the individual molecules does not change upon mixing, the outer passive volume only exists as a system property of the mixture (Fig. 7). Similarly, the active contribution to the correction is equal to the arithmetic mean of the active volume terms for the individual molecules.

We tested both fitting ω individually for the different mixtures and fixing ω at 0.5. The results of the fitting are shown in Table VI.

TABLE VI. System and, for Eq. (11), fitted ω using roughness volumes and simulated α_{mix} as training sets.

System	ω
DiMeBu–TrMePe	0.55
DiMeBu–EtHx	0.50
DiMeBu–DiMeHx	0.56
TrMePe–EtHx	0.47
TrMePe–DiMeHx	0.45
EtHx–DiMeHx	0.39
DiMeBu–DIPDMP	0.48
DiMeHx–DIPDMP	0.53

When ω is derived from fitting $\alpha_{mix,pred}$, the values predominantly converge around 0.5. The lower ω value observed in the EtHx–DiMeHx mixture may stem from the prediction error in the pure components. Both EtHx and DiMeHx show a slight underprediction of the acceleration of the pure components (3% for EtHx and 10% for DiMeHx). This lower ω value, and consequently a higher value of $(1 - \mathscr{P})$, might compensate for an inadequately low passive or active volume term of the pure components (and consequently their volume terms in a mixture). The average error of $\alpha_{mix,pred}$ only slightly increases from 10.3% to 10.5% when $\omega = 0.5$ is used instead of the fitted value. Figure 19 shows good agreement between $\alpha_{mix,pred}$ and α_{mix}. When the passive volume terms of the pure components are low—as it is the case for all components in mixture group A, predicting the overall acceleration purely based on an "ideal" arithmetic mixing of the roughness volumes yields good results. Adding a component with a passive volume term that significantly influences the acceleration of the pure component (as it is the case for DIPDMP) to the mixture requires the addition of an correction term. Incorporating the magnitude of the passive volume into the correction term allows for the usage of the same prediction formula for all mixtures. The overall acceleration in a mixture can thus be predicted purely based on the roughness volumes as calculated from the pure components using simple averaging rules omitting the need for any additional fitting.

2. Prediction of the acceleration of the individual self-diffusion coefficients

The acceleration of the self-diffusion coefficient of the minor component is always strongly affected by the acceleration of the self-diffusion coefficient of the major component. We therefore aim to define the acceleration of self-diffusion coefficients in relation to the overall acceleration present in the system. The overall acceleration can be predicted purely based on the roughness volumes of the pure components. This requires the introduction of an auxiliary quantity F_1, which we define as the ratio of the two acceleration factors of the self-diffusion coefficients $\alpha_{self,2}/\alpha_{self,1}$. This quantity can thereby be interpreted as a measurement for the distribution of acceleration between the individual components. Component 2 refers thereby to the component that has a higher pure-component acceleration factor. Using this ratio and the definition of the overall acceleration [Eq. (8)], the acceleration factor of component 1 is expressed as

$$\alpha_{self,1} = \frac{\alpha_{mix}}{x_1 + x_2 F_1}. \tag{14}$$

The ratio of self-diffusion acceleration factors F_1 can technically be determined individually for each composition. However, using the observation that the ratio is approximately constant (Figs. 15 and 16), F_1 is treated as a system specific constant within this work. Furthermore, to *predict* $\alpha_{self,1,pred}$ for all compositions, the need to actually calculate the acceleration factors from simulations in both representations has to be avoided. Hence, an estimation of F_1 is required. The mixture of DiMeHx and DIPDMP is a unique case as it exhibits an F_1 value below 1 because the self-diffusion acceleration factor of the component with a lower pure acceleration factor is actually higher in mixture when compared to the second component. This phenomenon coupled with the observation that in this specific mixture the active volume term is lower for the component with a higher acceleration factor leads to the hypothesis that the distribution of acceleration among different components is linked to

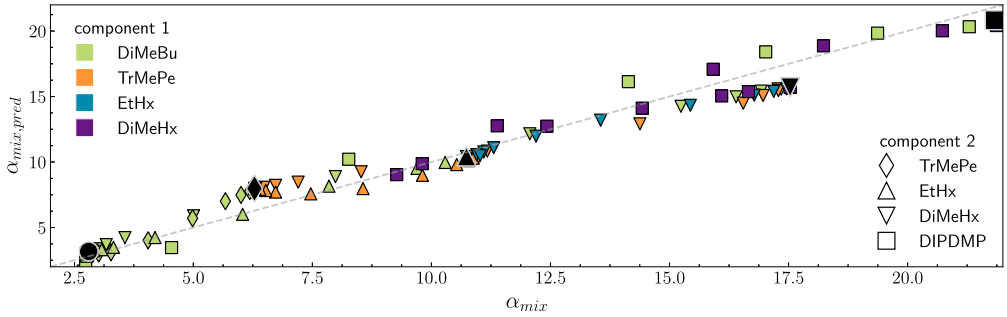

FIG. 19. Plot of the predicted overall acceleration factor with Eq. (11) and $\omega = 0.5$ against the overall acceleration in the mixture as calculated from the simulations [Eq. (8)]; marker colors represent component 1, markers represent component 2; *black markers* represent pure components; and the *gray dashed line* represents $\alpha_{mix,pred} = \alpha_{mix}$.

TABLE VII. System, ratio of the self-diffusion acceleration of the different components as calculated from simulations (averaged over all concentration and for equimolar mixtures) and estimated via Eq. (15) using shell and molecular volumes.

System	$\frac{\alpha_{self,2}}{\alpha_{self,1}}$ (av.)	$\frac{\alpha_{self,2}}{\alpha_{self,1}}$ (1:1)	Estimate of F_1
DiMeBu–TrMePe	1.15	1.17	1.20
DiMeBu–EtHx	1.39	1.42	1.39
DiMeBu–DiMeHx	1.57	1.57	1.73
TrMePe–EtHx	1.25	1.24	1.17
TrMePe–DiMeHx	1.39	1.37	1.45
EtHx–DiMeHx	1.11	1.11	1.24
DiMeBu–DIPDMP	1.21	1.19	1.23
DiMeHx–DIPDMP	0.72	0.74	0.71

their active volumes. In other words, a higher active volume (or more precisely, shell volume) of one component appears to augment the acceleration of this component relative to the second component. The approximation of F_1 we found most suitable is shown in the following equation:

$$F_1 \approx \frac{V_{shell,2}}{V_{shell,1}} \cdot \left(\frac{V_{mol,1}}{V_{mol,2}}\right)^{2/3}. \tag{15}$$

The sole use of shell volumes did not allow for a reasonable prediction; we therefore set the shell volume in relation to the molecular volume. This means that a higher shell volume relative to the volume it occupies in the mixture (expressed through V_{mol}) increases the acceleration of this component relative to the second component. The exponent of $\frac{2}{3}$ found empirically might be a consequence of the different scaling of V_{shell} and V_{mol} with an increasing size of the molecules. While V_{shell} roughly scales with r^2, V_{mol} roughly scales with r^3. The actual (averaged) ratio of self-diffusion coefficients and the estimates via Eq. (15) are listed in Table VII. The results of the predicted self-diffusion acceleration factors with F_1 estimated according to Eq. (15) are plotted in Fig. 20. Table VIII shows the average absolute and relative error of the predicted values for the individual components. For the averages, absolute values are used, omitting the information whether the prediction is too high or too low, as, e.g., $\alpha_{self,pred}$ of DiMeHx in DiMeBu can be too high for low concentrations of DiMeHx and too low for high mole fractions of DiMeHx. Detailed tables of all prediction errors, including the direction of the deviation, can be found in the supplementary material. Despite the approximation of F_1 as a constant value that is estimated from the shell and molar volumes of the pure components, the overall agreement of the prediction of self-diffusion acceleration factors in mixture is good. The average absolute and relative errors of 1.00% and 11.5%, respectively, are within the range of the errors that were already present in the prediction of the acceleration of pure components.

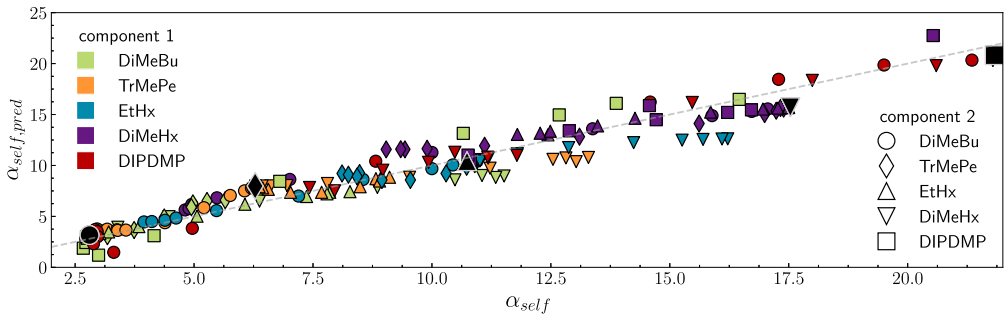

FIG. 20. Predicted self-diffusion acceleration factor with Eq. (14) and a F_1 parameter estimated according to Eq. (15) against the "true" self-diffusion acceleration as calculated from the simulations; marker colors represent component 1, markers represent component 2; *black markers* represent pure components; and the *gray dashed line* represents $\alpha_{self,pred} = \alpha_{self}$.

TABLE VIII. Overall concentration averaged errors of the absolute values and relative errors (in brackets and %) of the predicted acceleration factors of self-diffusion coefficients of component 1 $\alpha_{self,1,pred}$; rows are component 1 and columns represent component 2.

	In DiMeBu	In TrMePe	In EtHx	In DiMeHx	In DIPDMP
DiMeBu	0.37 (13.08)	0.55 (12.20)	0.35 (7.10)	1.13 (14.85)	1.18 (20.08)
TrMePe	0.78 (15.87)	1.70 (27.01)	0.71 (10.36)	1.59 (16.75)	⋯
EtHx	0.32 (4.95)	0.76 (8.11)	0.32 (2.97)	1.70 (11.62)	⋯
DiMeHx	1.19 (14.14)	1.69 (14.02)	1.06 (7.04)	1.82 (10.40)	1.08 (5.63)
DIPDMP	0.97 (17.06)	⋯	⋯	0.65 (5.10)	1.00 (4.60)

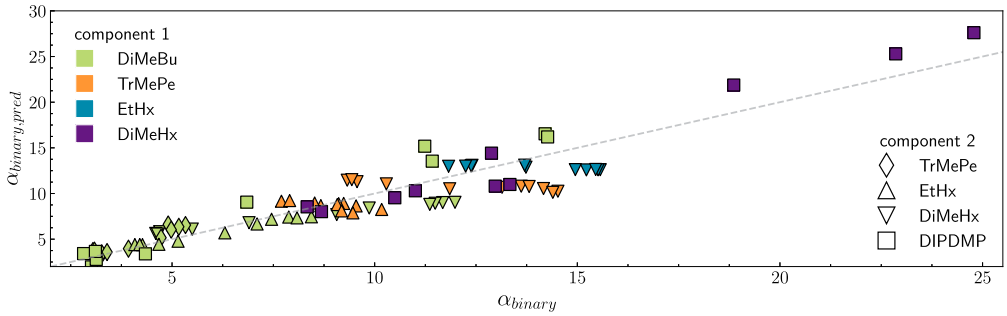

FIG. 21. Binary diffusion acceleration factor predicted with Eq. (16) and a F_1 parameter estimated according to Eq. (15) against the actual binary diffusion acceleration as calculated from the simulations; marker colors represent component 1, markers represent component 2; and the *gray dashed line* represents $\alpha_{binary,pred} = \alpha_{binary}$.

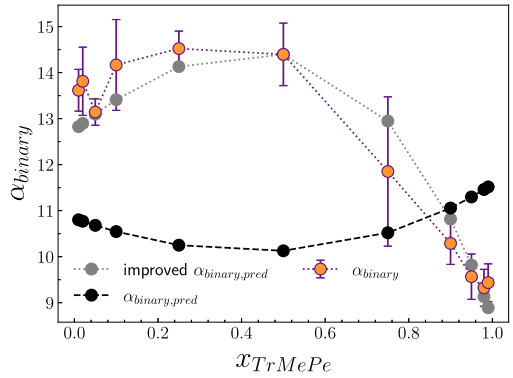

(a)

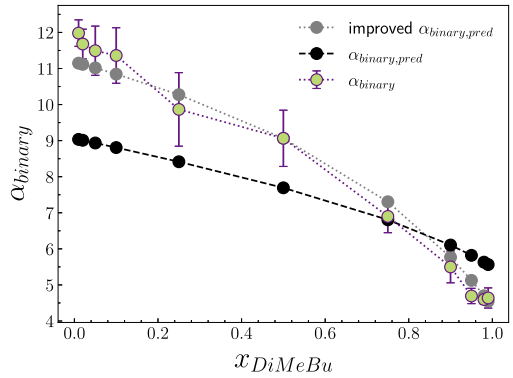

(b)

FIG. 22. Simulated binary acceleration factors, predicted binary acceleration as calculated with $\omega = 0.5$ and F_1 estimated via Eq. (15) (*black dashed line*), and improved predicted binary acceleration from equimolar simulation as calculated with ω and F_1 as listed in Tables IX and VII and with overall acceleration according to Eq. (17) (*gray dotted line*); in TrMePe–DiMeHx (a) and DiMeBu–DiMeHx (b) mixtures.

3. Prediction of the acceleration of binary-diffusion coefficients

To estimate the binary-diffusion acceleration factor, we use the fact that the binary diffusion coefficient (and thus the acceleration factor) converges to the self-diffusion coefficient of the minority component at infinite dilution. This means for a very low mole fraction of component 1, $\alpha_{self,1} = \alpha_{binary}$. This limitary behavior is met by the following equation that uses the same parameters as used for the prediction of the self-diffusion acceleration and the overall acceleration:

$$\alpha_{binary,pred} = \frac{\alpha^*_{mix,pred} + x_1 x_2 \cdot (1 - \mathscr{P})\mathscr{A}}{x_2 F_1 + x_1 \frac{1}{F_1}}. \quad (16)$$

While the deviation averaged over all mixtures of $\alpha_{binary,pred}$ from α_{binary} seems acceptable with 14.8%, Fig. 21 shows difficulties in accurately predicting the binary acceleration for different compositions. For example, the binary acceleration of the TrMePe–DiMeHx mixture (orange triangles down) appears to be systematically underpredicted at many compositions. In comparison, $\alpha_{mix,pred}$ has an average deviation of 18.8% from α_{binary}.

This means that Eq. (16) predicts the order of α_{binary} quite well. It does, however, not capture all details of its concentration dependence (Fig. 22, black markers). With default settings of $\omega = 0.5$

TABLE IX. System from equimolar simulations calculated ω parameters for binary acceleration factors with a predicted overall acceleration according to Eq. (17).

System	Calculated ω
DiMeBu–TrMePe	0.399
DiMeBu–EtHx	0.426
DiMeBu–DiMeHx	0.467
TrMePe–EtHx	0.286
TrMePe–DiMeHx	0.150
EtHx–DiMeHx	0.543
DiMeBu–DIPDMP	0.529
DiMeHx–DIPDMP	0.638

and F_1 estimated with Eq. (15), it deviates from the true binary acceleration by up to 68%. The larger discrepancy observed in the predicted binary diffusion acceleration (when compared to self-diffusion acceleration) could be attributed to two primary factors. First, $\alpha_{binary,pred}$ may exhibit an enhanced sensitivity to pre-existing deviations in the pure components. Second, it is conceivable that, despite the general suitability of the functional form in describing the behavior of binary diffusion acceleration, the passive and active correction terms may have to be adjusted for a more accurate representation of binary diffusion. Both factors can be addressed with additional simulations of the pure AA systems and AA systems at equimolar concentration. The extraction of AA diffusion coefficients of neat hydrocarbon liquids is cost-effective, when compared to the expensive calculation of binary diffusion coefficients due to their worse statistics (see above). The "ideal" overall acceleration factor $\alpha^*_{mix,pred}$ is then predicted from the actual self-diffusion acceleration factor of the pure components [Eq. (17)] instead of using arithmetic means of the roughness volumes [Eq. (10)].

$$\alpha^*_{mix,pred} = x_1 \cdot \alpha_{self,1,pure} + x_2 \cdot \alpha_{self,2,pure}. \quad (17)$$

Simulations of equimolar mixtures are used to calculate F_1 from the self-diffusion acceleration factors (Table VII) and ω from Eqs. (16) and (12) solved for ω (Table IX). The agreement between predicted binary acceleration factor and the actual binary acceleration factor over all concentration improves drastically to an average deviation of 6.6%, and it manages to capture the details of the concentration dependence (Fig. 22).

IV. CONCLUSION

This paper extends the RoughMob method[22,42] for the prediction of the artificial acceleration, when the description of a system is changed from atomistic to coarse-grained, from pure (single-component) molecular liquids to their binary mixtures. Acceleration is measured for the two self-diffusion coefficients $\alpha_{self,1}$ and $\alpha_{self,2}$, as well as for the binary diffusion (interdiffusion, mutual diffusion) coefficient α_{binary}. As all diffusion coefficients are concentration-dependent, so are these acceleration factors. In particular, the ansatz of roughness volumes has been followed here. The roughness volumes are parameters that are derived *a priori* from the geometries of the constituting molecules, i.e., almost entirely without doing simulations. The only exception is the so-called outer passive volume, which is akin to a free volume and must be sampled from a short simulation. The molecular dynamics calculations that are needed anyway in the iterative-Boltzmann-inversion coarse-graining process can be re-used for this purpose. The different roughness volumes enter a predictive equation for the acceleration factor. Predicting the acceleration factor for neat liquids has been very successful.[42]

The chosen strategy for the generalization to liquid mixtures has been to keep the formalism, the prediction equation, and its parameterization [Eqs. (7) and (10)], but to find ways of estimating the roughness volumes for mixtures, which then enter the prediction equation. It turns out that the roughness volumes for the binary mixtures can be obtained as number-weighted averages of those of the two separate components [Eq. (9)]. In addition, the mixtures require a cross-term quadratic in the concentration [Eq. (11)], whose coefficients, however, can be assembled from roughness volumes already known [Eqs. (13), (12), and (15)] so that no extra simulations are needed at this point either. With this simple approach, acceleration factors for the self-diffusion coefficients $\alpha_{self,1}$ and $\alpha_{self,2}$ are predicted that are on average within ±1 (absolute) and 11.9% (relative) of the actual acceleration factors obtained as references by direct molecular-dynamics simulations. The largest deviation found has been 60% (DiMeBu) and 55% (DIPDMP) relative for a DiMeBu–DIPDMP mixture with $x_{\mathrm{DiMeBu}} = 0.75$ with all other below 30% and 3.6 absolute for EtHx in a mixture with DiMeHx with $x_{\mathrm{DiMeBu}} = 0.01$. It should be noted that the acceleration of self-diffusion in our set of binary mixtures spans a range from 2.7 to 30.6. Therefore, this paper shows that it is quite possible to calculate self-diffusion coefficients of binary fluid mixtures using inexpensive coarse-grained models and then rescaling them using the acceleration factors predicted by the RoughMob approach. The rescaling should bring them close to the diffusion coefficients of the parent atomistic model, which in turn should be close to the experimental ones. The average error introduced by the RoughMob procedure is of the same order as that of the typical disagreement between the more costly atomistic simulations and the experiment. The usefulness of this approach is commented below.

The situation changes to some degree when the acceleration of the binary diffusion coefficient α_{binary} is investigated. While being of the same order as the self-diffusion coefficients, the binary diffusion coefficient is notorious for having a much lower accuracy in molecular-dynamics simulations. Its order is well predicted by the approach outlined above (on average 14.8%); however, the details of its concentration-dependence are not predicted always. For some systems and at some compositions, the deviation of the predicted acceleration from the MD-simulated value can be as large as 68%. If one is willing to perform an extra set of simulations for the neat components and at x = 0.5 and use it to calculate, rather than predict, two parameters [$F_1 = \alpha_{self,2}/\alpha_{self,1}$ and the weight of the passive-volume term ω, Eq. (12)], the deviation of α_{binary} can be pushed down to an average of 6.6% for all systems at all concentrations.

We have shown in this paper that the RoughMob method in the roughness volumes formalism can be extended from neat molecular liquids to their mixtures. In its simple form, all auxiliary quantities needed to predict the artificial acceleration upon coarse graining can be calculated *a priori* for the individual molecules. Accelerations in the mixtures can then be predicted from the single-species quantities. The CG model development requires only short AA trajectories of the pure components and of the 1:1 mixture to generate the same and mixed species radial distribution functions and thus the CG potentials via Iterative Boltzmann Inversion (IBI). The mixed potential can then be used for all concentrations. Using mixed potentials generated via IBI from equimolar mixtures instead of combination rules improves the agreement between the AA and CG densities or molecular volumes and radial distribution functions (RDFs) at all compositions and is therefore advised as the safe approach for the applicability of the RoughMob method. With this approach, the mobility of individual molecules, i.e., the self-diffusion, can be estimated from coarse-grained simulations with an error that is smaller than the typical deviation between atomistic and experimental diffusion coefficients (20%) or among different experimental values (10%–50%). If a different marker of acceleration is selected, namely, binary diffusion, and not only the same accuracy but also the cap-

turing of mixture-specific details of the concentration dependencies is required, one may have to supplement the approach by one more calculation of one mixed system and simulations of the neat components to gauge the auxiliary quantities for the mixtures. The scalability of the approach to mixtures with more than two components will be of interest in future works. First tests indicate a similar behavior of the ratios of the self-diffusion acceleration factors F_1 as observed in the binary mixtures and a need to adjust the cross-correction-terms.

Is this useful? Not for a few mixtures of molecular liquids. While coarse-grained simulations of a large variety of mixtures at several concentrations and combinations certainly quicken the study, they can generally be simulated long enough at the full atomistic level, and they have been in this contribution to provide the "true" reference values of the acceleration. The situation is, however, very different for polymers and other soft matter, for which atomistic simulations are often prohibitive, and for which coarse-grained simulations produce mobilities accelerated by an unpredictable factor. This practically precludes the use of coarse-grained models for quantitative dynamical and transport properties. The calculation on fluid mixtures presented here is a necessary stepping stone toward the application of RoughMob to polymers. The coarse-grained polymer models obtained by, say, iterative Boltzmann inversion typically collect about 5–10 carbon atoms into one bead. The beads have, thus, the same size and the same level of coarse graining as the molecules studied here. It is expected that the smoothing of their surfaces by coarse-graining produces similar artificial accelerations and that a rescaling of the coarse-grained dynamics with an acceleration factor estimated *a priori* from the loss of monomer roughness can reproduce the true bead mobility. This expectation is supported by the fact that dynamical properties of polymers can often be formulated like $D = C \cdot L^{\nu}$, i.e., a universal power-law scaling with the polymer length L, multiplied with a prefactor C, which contains the system-specific monomeric friction and which would be the target of the RoughMob scheme. The extension from single-component systems to binary systems has been motivated not only by an interest in polymer solutions or polymer mixtures but also especially because many coarse-grained polymer models simultaneously contain two or more different beads to map different chemical moieties. The success of the RoughMob for binary systems, as well as for neat liquids, is therefore encouraging for the development of coarse-grained models for polymers, which can ultimately, by way of rescaling, predict transport properties, such as melt viscosities.

SUPPLEMENTARY MATERIAL

A supplementary material is available as PDF containing the OPLS-AA bonded parameters of the all-atom force-field, additional figures as referred to throughout the text and tables (with errors) of RDFs, densities, molecular volumes, and predicted acceleration factors for all simulations. Furthermore, the PDF includes additional explanations on the mutual/binary Maxwell–Stefan diffusion coefficient and on the relation between coarse-grained potential, structure, and mobility. Coarse-grained potentials via IBI for all pure components and mixtures are available and tabulated. Dynamical and geometrical properties are provided as ASCII tables.

ACKNOWLEDGMENTS

M.K.M. thanks Maxim Abrossimow for support with the realization of graphical designs.

AUTHOR DECLARATIONS

Conflict of Interest

The authors have no conflicts to disclose.

Author Contributions

Melissa K. Meinel: Investigation (lead); Methodology (lead); Writing – original draft (lead). **Florian Müller-Plathe**: Conceptualization (lead); Writing – review & editing (equal).

DATA AVAILABILITY

The data that support the findings of this study are available within the article and its supplementary material and on GitHub (https://github.com/MKMeinel/RoughMob).

REFERENCES

[1] D. J. L. Prak, B. H. Morrow, S. Maskey, J. A. Harrison, J. S. Cowart, and P. C. Trulove, "Densities, speeds of sound, and viscosities of binary mixtures of an *n*-alkylcyclohexane (*n*-propyl-, *n*-pentyl-, *n*-hexyl-, *n*-heptyl, *n*-octyl-, *n*-nonyl-, *n*-decyl-, and *n*-dodecyl-) with *n*-hexadecane," J. Chem. Eng. Data **63**, 4632–4648 (2018).

[2] B. H. Morrow, S. Maskey, M. Z. Gustafson, D. J. Luning Prak, and J. A. Harrison, "Impact of molecular structure on properties of *n*-hexadecane and alkylbenzene binary mixtures," J. Phys. Chem. B **122**, 6595–6603 (2018).

[3] D. J. Luning Prak, B. H. Morrow, J. S. Cowart, P. C. Trulove, and J. A. Harrison, "Thermophysical properties of binary mixtures of *n*-dodecane with *n*-alkylcyclohexanes: Experimental measurements and molecular dynamics simulations," J. Chem. Eng. Data **64**, 1550–1568 (2019).

[4] K. D. Papavasileiou, L. D. Peristeras, A. Bick, and I. G. Economou, "Molecular dynamics simulation of pure *n*-alkanes and their mixtures at elevated temperatures using atomistic and coarse-grained force fields," J. Phys. Chem. B **123**, 6229–6243 (2019).

[5] G. Yatsenko, E. J. Sambriski, and M. G. Guenza, "Coarse-grained description of polymer blends as interacting soft-colloidal particles," J. Chem. Phys. **122**, 054907 (2005).

[6] Z. A. Makrodimitri, A. Heller, T. M. Koller, M. H. Rausch, M. S. Fleys, A. R. Bos, G. P. van der Laan, A. P. Fröba, and I. G. Economou, "Viscosity of heavy *n*-alkanes and diffusion of gases therein based on molecular dynamics simulations and empirical correlations," J. Chem. Thermodyn. **91**, 101–107 (2015).

[7] V. K. Michalis, O. A. Moultos, I. N. Tsimpanogiannis, and I. G. Economou, "Molecular dynamics simulations of the diffusion coefficients of light *n*-alkanes in water over a wide range of temperature and pressure," Fluid Phase Equilib. **407**, 236–242 (2016).

[8] G. Milano and F. Müller-Plathe, "Cyclohexane–benzene mixtures: Thermodynamics and structure from atomistic simulations," J. Phys. Chem. B **108**, 7415 (2004).

[9] L. Baran, "Coarse-grained modeling of on-surface self-assembly of mixtures comprising di-substituted polyphenyl-like compounds and metal atoms of different sizes," ACS Omega **6**, 25193–25200 (2021).

[10] C. Herdes, T. S. Totton, and E. A. Müller, "Coarse grained force field for the molecular simulation of natural gases and condensates," Fluid Phase Equilib. **406**, 91–100 (2015).

[11] N. Chennamsetty, H. Bock, and K. E. Gubbins, "Coarse-grained potentials from Widom's particle insertion method," Mol. Phys. **103**, 3185–3193 (2005).
[12] T. Ohkuma and K. Kremer, "A composition transferable and time-scale consistent coarse-grained model for cis-polyisoprene and vinyl-polybutadiene oligomeric blends," J. Phys.: Mater. **3**, 034007 (2020).
[13] J. Zhong, R. Zhao, W. Ouyang, and S. Xu, "Molecular dynamics simulation of the Soret effect on two binary liquid solutions with equimolar *n*-alkane mixtures," ACS Omega **7**, 518–527 (2022).
[14] A.-T. Kuo, S. Urata, K. Nakabayashi, H. Watabe, and S. Honmura, "Coarse-grained molecular dynamics simulation of perfluorosulfonic acid polymer in water–ethanol mixtures," Macromolecules **54**, 609–620 (2021).
[15] P. Gao, X. Yang, and A. M. Tartakovsky, "Learning coarse-grained potentials for binary fluids," J. Chem. Inf. Model. **60**, 3731–3745 (2020).
[16] G. Yatsenko, E. J. Sambriski, M. A. Nemirovskaya, and M. Guenza, "Analytical soft-core potentials for macromolecular fluids and mixtures," Phys. Rev. Lett. **93**, 257803 (2004).
[17] J. McCarty, I. Y. Lyubimov, and M. G. Guenza, "Effective soft-core potentials and mesoscopic simulations of binary polymer mixtures," Macromolecules **43**, 3964–3979 (2010).
[18] A. Kopf, B. Dünweg, and W. Paul, "Dynamics of polymer 'isotope' mixtures: Molecular dynamics simulation and Rouse model analysis," J. Chem. Phys. **107**, 6945–6955 (1997).
[19] P. Sokkar, S. M. Choi, and Y. M. Rhee, "Simple method for simulating the mixture of atomistic and coarse-grained molecular systems," J. Chem. Theory Comput. **9**, 3728–3739 (2013).
[20] N. J. H. Dunn and W. G. Noid, "Bottom-up coarse-grained models with predictive accuracy and transferability for both structural and thermodynamic properties of heptane-toluene mixtures," J. Chem. Phys. **144**, 204124 (2016).
[21] P. Depa, C. Chen, and J. K. Maranas, "Why are coarse-grained force fields too fast? A look at dynamics of four coarse-grained polymers," J. Chem. Phys. **134**, 014903 (2011).
[22] M. K. Meinel and F. Müller-Plathe, "Loss of molecular roughness upon coarse-graining predicts the artificially accelerated mobility of coarse-grained molecular simulation models," J. Chem. Theory Comput. **16**, 1411–1419 (2020).
[23] M. Guenza, "Thermodynamic consistency and other challenges in coarse-graining models," Eur. Phys. J.: Spec. Top. **224**, 2177–2191 (2015).
[24] J. F. Rudzinski, "Recent progress towards chemically-specific coarse-grained simulation models with consistent dynamical properties," Computation **7**, 42 (2019).
[25] L. Wolff, S. H. Jamali, T. M. Becker, O. A. Moultos, T. J. H. Vlugt, and A. Bardow, "Prediction of composition-dependent self-diffusion coefficients in binary liquid mixtures: The missing link for Darken-based models," Ind. Eng. Chem. Res. **57**, 14784–14794 (2018).
[26] G. Guevara-Carrion, R. Fingerhut, and J. Vrabec, "Diffusion in multicomponent aqueous alcoholic mixtures," Sci. Rep. **11**, 12319 (2021).
[27] R. Taylor and R. Krishna, *Multicomponent Mass Transfer* (Wiley, New York, 1993).
[28] E. L. Cussler, in *Diffusion Mass Transfer in Fluid Systems*, 3rd ed. (Cambridge University Press, Cambridge, 2009).
[29] X. Liu, T. J. H. Vlugt, and A. Bardow, "Maxwell–Stefan diffusivities in binary mixtures of ionic liquids with dimethyl sulfoxide (DMSO) and H_2O," J. Phys. Chem. B **115**, 8506–8517 (2011).
[30] U. A. Higgoda, C. J. Kankanamge, R. Hellmann, T. M. Koller, and A. P. Fröba, "Fick diffusion coefficients of binary fluid mixtures consisting of methane, carbon dioxide, and propane via molecular dynamics simulations based on simplified pair-specific *ab initio*-derived force fields," Fluid Phase Equilib. **502**, 112257 (2019).
[31] Y. A. Aljeshi, M. B. M. Taib, and J. P. M. Trusler, "Modelling the diffusion coefficients of dilute gaseous solutes in hydrocarbon liquids," Int. J. Thermophys. **42**, 140 (2021).
[32] A. Heller, M. H. Rausch, P. S. Schulz, P. Wasserscheid, and A. P. Fröba, "Binary diffusion coefficients of the liquid organic hydrogen carrier system dibenzyltoluene/perhydrodibenzyltoluene," J. Chem. Eng. Data **61**, 504–511 (2016).
[33] V. Klippenstein and N. F. A. van der Vegt, "Bottom-up informed and iteratively optimized coarse-grained non-Markovian water models with accurate dynamics," J. Chem. Theory Comput. **19**, 1099–1110 (2023).
[34] S. Bag, M. K. Meinel, and F. Müller-Plathe, "Toward a mobility-preserving coarse-grained model: A data-driven approach," J. Chem. Theory Comput. **18**, 7108–7120 (2022).
[35] A. Davtyan, J. F. Dama, G. A. Voth, and H. C. Andersen, "Dynamic force matching: A method for constructing dynamical coarse-grained models with realistic time dependence," J. Chem. Phys. **142**, 154104 (2015).
[36] A. Davtyan, G. A. Voth, and H. C. Andersen, "Dynamic force matching: Construction of dynamic coarse-grained models with realistic short time dynamics and accurate long time dynamics," J. Chem. Phys. **145**, 224107 (2016).
[37] D. Fritz, K. Koschke, V. A. Harmandaris, N. F. A. van der Vegt, and K. Kremer, "Multiscale modeling of soft matter: Scaling of dynamics," Phys. Chem. Chem. Phys. **13**, 10412–10420 (2011).
[38] I. Lyubimov and M. G. Guenza, "First-principle approach to rescale the dynamics of simulated coarse-grained macromolecular liquids," Phys. Rev. E **84**, 031801 (2011).
[39] I. Y. Lyubimov and M. G. Guenza, "Theoretical reconstruction of realistic dynamics of highly coarse-grained *cis*-1,4-polybutadiene melts," J. Chem. Phys. **138**, 12A546 (2013).
[40] G. G. Rondina, M. C. Böhm, and F. Müller-Plathe, "Predicting the mobility increase of coarse-grained polymer models from excess entropy differences," J. Chem. Theory Comput. **16**, 1431–1447 (2020).
[41] J. Jin, K. S. Schweizer, and G. A. Voth, "Understanding dynamics in coarse-grained models. I. Universal excess entropy scaling relationship," J. Chem. Phys. **158**, 034103 (2023).
[42] M. K. Meinel and F. Müller-Plathe, "Roughness volumes: An improved RoughMob concept for predicting the increase of molecular mobility upon coarse-graining," J. Phys. Chem. B **126**(20), 3737–3747 (2022).
[43] S. Plimpton, "Fast parallel algorithms for short-range molecular dynamics," J. Comput. Phys. **117**, 1–19 (1995).
[44] A. P. Thompson, H. M. Aktulga, R. Berger, D. S. Bolintineanu, W. M. Brown, P. S. Crozier, P. J. in't Veld, A. Kohlmeyer, S. G. Moore, T. D. Nguyen, R. Shan, M. J. Stevens, J. Tranchida, C. Trott, and S. J. Plimpton, "LAMMPS - A flexible simulation tool for particle-based materials modeling at the atomic, meso, and continuum scales," Comput. Phys. Commun. **271**, 108171 (2022).
[45] A. I. Jewett, Z. Zhuang, and J.-E. Shea, "Moltemplate a coarse-grained model assembly tool," Biophys. J. **104**, 169a (2013).
[46] W. L. Jorgensen, D. S. Maxwell, and J. Tirado-Rives, "Development and testing of the OPLS all-atom force field on conformational energetics and properties of organic liquids," J. Am. Chem. Soc. **118**, 11225–11236 (1996).
[47] H.-J. Qian, P. Carbone, X. Chen, H. A. Karimi-Varzaneh, C. C. Liew, and F. Müller-Plathe, "Temperature-transferable coarse-grained potentials for ethylbenzene, polystyrene, and their mixtures," Macromolecules **41**, 9919–9929 (2008).
[48] V. Rühle, C. Junghans, A. Lukyanov, K. Kremer, and D. Andrienko, "Versatile object-oriented toolkit for coarse-graining applications," J. Chem. Theory Comput. **5**, 3211–3223 (2009).
[49] D. Reith, M. Pütz, and F. Müller-Plathe, "Deriving effective mesoscale potentials from atomistic simulations," J. Comput. Chem. **24**, 1624–1636 (2003).
[50] H. Schmitz, R. Faller, and F. Müller-Plathe, "Molecular mobility in cyclic hydrocarbons: A simulation study," J. Phys. Chem. B **103**, 9731–9737 (1999).
[51] C.-C. Fu, P. M. Kulkarni, M. S. Shell, and L. G. Leal, "A test of systematic coarse-graining of molecular dynamics simulations: Transport properties," J. Chem. Phys. **139**, 094107 (2013).
[52] M. Chakraborty, S. Barik, A. Mahapatra, and M. Sarkar, "Binary mixtures of ionic liquids: Ideal, non-ideal, or quasi-ideal?," J. Chem. Phys. **154**, 224507 (2021).

5 Conclusion and Outlook

This work presents the development of a new approach to predict the acceleration of dynamics upon coarse-graining. The RoughMob method connects the *change* of a molecular surface roughness to the *change* in mobility. It has been tested on and applied to single component systems and binary mixtures of aliphatic and aromatic molecules in a size range between five to 13 carbon atoms that where coarse-grained into one bead per molecule. The acceleration factor, measured as ratio between the self-diffusion coefficients in the all-atom (AA) and coarse-grained (CG) simulation, spans a range from 1.6 to 30.6. Only short AA simulation runs of the neat components, and in case of the binary mixture, of the 1:1 mixtures, are needed to equilibrate the structural properties. Then, the coarse-grained (CG) model can be derived by the iterative Boltzmann inversion. No additional simulation is needed to extract any geometrical information used to calculate the changes of molecular roughness. Detailed results were presented in the previous chapter and are briefly summarized here.

1. The acceleration of dynamics can directly be correlated with the *molecular roughness difference* for simple hydrocarbon liquids, both aliphatic and aromatic systems, of similar size and shape with six to eight carbon atoms per molecule. The *molecular roughness difference* shows a remarkably good linear correlation with the acceleration factor (R^2=0.996). This even holds up when a different mapping scheme is added.

2. The concept of four so-called *roughness volumes* separates the system into regions that take part in the change of roughness (active volumes) and regions that do not take part (passive volumes). This enables the prediction of acceleration factors for pure liquids in the size range between five and 13 carbon atoms. The prediction uses a fit function with three fitting parameters that are derived via a least squared fit. The absolute average error of the predicted acceleration factor is 1.0 and the average relative error is 17.9 %. Molecules with a smaller acceleration factor tend to have a higher relative error.

3. Binary liquid mixtures can use the same *roughness volumes* and fit parameters as derived for neat liquids. Some mixtures require the addition of a cross-term quadratic in the concentration to account for deviations from a prediction based on an arithmetic mixing of the volumes. The need for this cross-term is determined by the passive volumes, the size of the cross-term by the active volumes. The distribution of acceleration between the self-diffusion coefficients can be estimated with the ratio of shell volumes and molecular volumes of the two components. This allows the prediction of both self-diffusion coefficients with an average accuracy of 1.0 (absolute) and 11.9 % (relative).

The outcomes presented here are promising and allow for an optimistic outlook on the method's potential for expansion. The easy to use framework for an a priori prediction of the acceleration factor enables the use of computationally significantly less expensive CG simulations for the calculation of dynamical properties that can then be scaled back to the atomistic and thus hopefully true values. However, the study is still in its infancy. While quickening the study of various simple systems is beneficial, the ultimate aim is to enable quantitative dynamical analysis of complex systems, such as polymer melts, which are currently beyond the reach of molecular dynamics simulations. Therefore, a brief outline of future work is provided below.

Different state points Our own experiences and other studies [85, 86] show, that the pressure is of minor importance for the acceleration factor of a system. In contrast, the acceleration factor is highly dependent on the temperature. While usually self-diffusion coefficients increase with an increasing temperature in both all-atom and coarse-grained representation, the acceleration factor is known to decrease. [39, 42, 74, 85] Even though the CG potentials are known to require recalibaration for different state points, it is to expect, that the effective hard-sphere radius (used as the size of the CG bead) will not change significantly, and thus, neither will the *molecular roughness difference* nor the shell volume. The outer passive volume and overlap volume are, however, dependent on the density. With an increasing temperature at constant pressure, the density decreases, increasing the separation between molecules. Consequently, the importance of roughness changes for the dynamics should decrease, as wider separations between molecules diminish the influence of surface roughness on their interactions. This is reflected in an increasing outer passive volume and a decreasing overlap volume — both factors that decrease the predicted acceleration factor. However, first tests show, that this does not fully account for the change in the acceleration factor with the temperature at constant pressure. Possible approaches include e.g. modeling of one or more of the fitting parameters of the prediction equation as temperature dependent parameters. Another option is to consider a temperature dependent definition of the particle sizes. As of now, the radii are defined as half the value where the nonbonded interaction potential first takes the value of zero. Instead of using zero, one could change the definition to $k_B T$. This would lead to smaller particles with an increasing temperature which could amplify the changes in the *roughness volumes*.

Polar molecules and ionic liquids Polar molecules add some electrostatic forces and are locally more ordered than nonpolar molecules. The basic assumption would be, that the nature of the forces is irrelevant as long as the structural properties (radial distribution function and density) are maintained. However, the increased ordering among polar molecules could alter how the importance of roughness changes is distributed across the molecular surface. For nonpolar molecules (coarse-grained into a single bead), roughness contributions are uniform across the surface. For polar molecules, this uniformity may need adjustment, e.g. in form of a weighted distribution of the roughness contributions. High viscosities and structuring processes at long length and time scales can make ionic liquids expensive to simulate atomistically [87, 88] and thus an interesting target for the application of the RoughMob method. Here, the ratio of diffusion of the anionic and cationic moieties relative to each other can be of special importance. [71] The RoughMob method has proven capable to distinguish between self-diffusion coefficients of different components in a binary fluid mixture. This is

a first promising step towards the application for anions and cations. However, both anions and cations are often represented by several beads. Together with the complexity added through present charges and thus additional structuring, this is an application range that should be targeted after the framework has been expanded to multiple CG beads per molecule.

Multiple coarse-grained beads Developing the RoughMob method is strongly motivated by the limitations of molecular dynamics simulations in accurately quantifying the dynamical properties of polymer melts and other soft matter systems. Studies have shown that the acceleration factor for polymers remains constant regardless of chain length once the polymer exceeds a certain chain length, typically between 50 to 90 monomers. [25, 59, 85] This suggests that it may be feasible to determine an acceleration factor specific to a monomer or CG bead rather than for the entire polymer chain. However, adapting the RoughMob method to such complex systems entails addressing several challenges:

1. Geometric complexity in multi-bead models: When the reference geometry within the RoughMob framework shifts from a simple sphere to configurations involving multiple intersecting spheres, the technical aspects of calculating relevant quantities become more difficult. Particularly, the ray-based method used to calculate the *molecular roughness difference* encounters difficulties because not every point on a coarse-grained surface has a direct counterpart on the all-atom surface. A potential solution is to adopt a Monte Carlo algorithm that can concurrently evaluate the space that is:
    - Not occupied by either the AA or CG models.
    - Occupied by both the AA and CG models.
    - Exclusively occupied by the AA model.
    - Exclusively occupied by the CG model.
2. Region specific importance of roughness changes: Determining which changes in roughness significantly affect the dynamics poses another challenge. For instance, are the grooves formed at the intersections of two spheres more critical to dynamics than other areas? One argument might be that these grooves are not fully accessible to surrounding nonbonded beads, rendering them less crucial. Conversely, since a configuration of intersecting spheres could introduce its own form of roughness, this area might require special consideration.
3. Complexity of motion: In more complex CG models, different types of molecular motion may interact, such as diffusion processes overlapping with bond relaxations. [16, 89] Each type of motion might require a distinct treatment due to their inherent differences in dynamics and influence on the system's overall behavior.

The challenges outlined above can be systematically addressed by initially focusing on nonpolar liquids that are coarse-grained into two beads per molecule. This enables first adjustments to the RoughMob framework to calculations on multiple beads, while keeping the bonded interactions limited to one bond in the CG representation. Progressing to models with three sequential beads allows for distinguishing between end and

middle beads, establishing the basis for longer chains. The two CG bead molecules can also be used as a basis for introducing polarities. Using polar molecules with similar structures facilitates a direct analysis of the additional effects added by the stronger interactions and increased order.

Bibliography

[1] D. Frenkel, B. Smit, *Understanding Molecular Simulation: From Algorithms to Applications (Second Edition)*, Academic Press, San Diego, **2002**.

[2] A. Rahman, "Correlations in the Motion of Atoms in Liquid Argon", *Physical Review* **1964**, *136*, A405–A411.

[3] G. D. Harp, B. J. Berne, "Time-Correlation Functions, Memory Functions, and Molecular Dynamics", *Physical Review A* **1970**, *2*, 975–996.

[4] M. Bishop, M. H. Kalos, H. L. Frisch, "Molecular dynamics of polymeric systems", *The Journal of Chemical Physics* **1979**, *70*, 1299–1304.

[5] S. A. Hollingsworth, R. O. Dror, "Molecular Dynamics Simulation for All", *Neuron* **2018**, *99*, 1129–1143.

[6] M. Karplus, J. A. McCammon, "Molecular dynamics simulations of biomolecules", *Nature Structural Biology* **2002**, *9*, 646–652.

[7] O. M. H. Salo-Ahen, I. Alanko, R. Bhadane, A. M. J. J. Bonvin, R. V. Honorato, S. Hossain, A. H. Juffer, A. Kabedev, M. Lahtela-Kakkonen, A. S. Larsen, E. Lescrinier, P. Marimuthu, M. U. Mirza, G. Mustafa, A. Nunes-Alves, T. Pantsar, A. Saadabadi, K. Singaravelu, M. Vanmeert, "Molecular Dynamics Simulations in Drug Discovery and Pharmaceutical Development", *Processes* **2021**, *9*, 71.

[8] D. J. L. Prak, B. H. Morrow, S. Maskey, J. A. Harrison, J. S. Cowart, P. C. Trulove, "Densities, Speeds of Sound, and Viscosities of Binary Mixtures of an n-Alkylcyclohexane (n-Propyl-, n-Pentyl-, n-Hexyl-, n-Heptyl, n-Octyl-, n-Nonyl-, n-Decyl-, and n-Dodecyl-) with n-Hexadecane", *Journal of Chemical & Engineering Data* **2018**, *63*, 4632–4648.

[9] B. H. Morrow, S. Maskey, M. Z. Gustafson, D. J. Luning Prak, J. A. Harrison, "Impact of Molecular Structure on Properties of n-Hexadecane and Alkylbenzene Binary Mixtures", *The Journal of Physical Chemistry B* **2018**, *122*, 6595–6603.

[10] C. E. Leiserson, N. C. Thompson, J. S. Emer, B. C. Kuszmaul, D. S. Butler W. Lampson, T. B. Schardl, "There's plenty of room at the Top: What will drive computer performance after Moore's law?", *Science* **2020**, *368*, eaam9744.

[11] T. E. I. Gartner, A. Jayaraman, "Modeling and Simulations of Polymers: A Roadmap", *Macromolecules* **2019**, *52*, 755–786.

[12] C. Peter, K. Kremer, "Multiscale simulation of soft matter systems – from the atomistic to the coarse-grained level and back", *Soft Matter* **2009**, *5*, 4357–4366.

[13] W. G. Noid, "Perspective: Coarse-grained models for biomolecular systems", *The Journal of Chemical Physics* **2013**, *139*, 090901.

[14] E. Brini, E. A. Algaer, P. Ganguly, C. Li, F. Rodríguez-Ropero, N. F. A. van der Vegt, "Systematic coarse-graining methods for soft matter simulations – a review", *Soft Matter* **2013**, *9*, 2108–2119.

[15] M. Feig, Y. Sugita, "Whole-Cell Models and Simulations in Molecular Detail", *Annual Review of Cell and Developmental Biology* **2019**, *35*, 191–211.

[16] V. A. Harmandaris, N. P. Adhikari, N. F. A. van der Vegt, K. Kremer, "Hierarchical Modeling of Polystyrene: From Atomistic to Coarse-Grained Simulations", *Macromolecules* **2006**, *39*, 6708–6719.

[17] C. Peter, K. Kremer, "Multiscale simulation of soft matter systems", *Faraday Discuss.* **2010**, *144*, 9–24.

[18] T. Murtola, A. Bunker, I. Vattulainen, M. Deserno, M. Karttunen, "Multiscale modeling of emergent materials: biological and soft matter", *Physical Chemistry Chemical Physics* **2009**, *11*, 1869–1892.

[19] J. A. Armstrong, C. Chakravarty, P. Ballone, "Statistical mechanics of coarse graining: Estimating dynamical speedups from excess entropies", *The Journal of Chemical Physics* **2012**, *136*, 124503.

[20] K. R. Hadley, C. McCabe, "On the Investigation of Coarse-Grained Models for Water: Balancing Computational Efficiency and the Retention of Structural Properties", *The Journal of Physical Chemistry B* **2010**, *114*, 4590–4599.

[21] S. Riniker, W. F. van Gunsteren, "Mixing coarse-grained and fine-grained water in molecular dynamics simulations of a single system", *The Journal of Chemical Physics* **2012**, *137*, 044120.

[22] M. Dinpajooh, M. G. Guenza, "Coarse-Graining Simulation Approaches for Polymer Melts: the Effect of Potential Range on Computational Efficiency", *Soft Matter* **2018**, *14*, 7126–7144.

[23] C. Chen, P. Depa, J. K. Maranas, V. G. Sakai, "Comparison of Explicit Atom, United Atom, and Coarse-Grained Simulations of poly(methyl methacrylate)", *The Journal of Chemical Physics* **2008**, *128*, 124906.

[24] P. K. Depa, J. K. Maranas, "Speed Up of Dynamic Observables in Coarse-Grained Molecular-Dynamics Simulations of Unentangled Polymers", *The Journal of Chemical Physics* **2005**, *123*, 094901.

[25] P. K. Depa, J. K. Maranas, "Dynamic Evolution in Coarse-Grained Molecular Dynamics Simulations of Polyethylene Melts", *The Journal of Chemical Physics* **2007**, *126*, 054903.

[26] P. Depa, C. Chen, J. K. Maranas, "Why Are Coarse-Grained Force Fields Too Fast? a Look At Dynamics of Four Coarse-Grained Polymers", *The Journal of Chemical Physics* **2011**, *134*, 014903.

[27] R. Potestio, C. Peter, K. Kremer, "Computer Simulations of Soft Matter: Linking the Scales", *Entropy* **2014**, *16*, 4199–4245.

[28] F. Müller-Plathe, "Coarse-Graining in Polymer Simulation: From the Atomistic to the Mesoscopic Scale and Back", *Chemphyschem* **2002**, *3*, 755–69.

[29] W. G. Noid, J.-W. Chu, G. S. Ayton, V. Krishna, S. Izvekov, G. A. Voth, A. Das, H. C. Andersen, "The Multiscale Coarse-Graining Method. I. a Rigorous Bridge Between Atomistic and Coarse-Grained Models", *The Journal of Chemical Physics* **2008**, *128*, 244114.

[30] S. Trément, B. Schnell, L. Petitjean, M. Couty, B. Rousseau, "Conservative and Dissipative Force Field for Simulation of Coarse-Grained Alkane Molecules: a Bottom-Up Approach", *The Journal of Chemical Physics* **2014**, *140*, 134113.

[31] S. T. John, G. Csányi, "Many-Body Coarse-Grained Interactions Using Gaussian Approximation Potentials", *The Journal of Physical Chemistry B* **2017**, *121*, 10934–10949.

[32] S. J. Marrink, H. J. Risselada, S. Yefimov, D. P. Tieleman, A. H. de Vries, "The MARTINI Force Field: Coarse Grained Model for Biomolecular Simulations", *The Journal of Physical Chemistry B* **2007**, *111*, 7812–7824.

[33] M. S. Shell, "The relative entropy is fundamental to multiscale and inverse thermodynamic problems", *The Journal of Chemical Physics* **2008**, *129*, 144108.

[34] D. Reith, H. Meyer, F. Müller-Plathe, "Mapping Atomistic to Coarse-Grained Polymer Models Using Automatic Simplex Optimization To Fit Structural Properties", *Macromolecules* **2001**, *34*, 2335–2345.

[35] D. Reith, M. Pütz, F. Müller-Plathe, "Deriving effective mesoscale potentials from atomistic simulations", *Journal of Computational Chemistry* **2003**, *24*, 1624–1636.

[36] N. J. H. Dunn, W. G. Noid, "Bottom-up coarse-grained models that accurately describe the structure, pressure, and compressibility of molecular liquids", *The Journal of Chemical Physics* **2015**, *143*, 243148.

[37] P. Ganguly, N. F. A. van der Vegt, "Representability and Transferability of Kirkwood–Buff Iterative Boltzmann Inversion Models for Multicomponent Aqueous Systems", *Journal of Chemical Theory and Computation* **2013**, *9*, 5247–5256.

[38] D. Fritz, K. Koschke, V. A. Harmandaris, N. F. A. van der Vegt, K. Kremer, "Multiscale Modeling of Soft Matter: Scaling of Dynamics", *Physical Chemistry Chemical Physics* **2011**, *13*, 10412.

[39] C.-C. Fu, P. M. Kulkarni, M. S. Shell, L. G. Leal, "A test of systematic coarse-graining of molecular dynamics simulations: Transport properties", *The Journal of Chemical Physics* **2013**, *139*, 094107.

[40] M. Guenza, "Thermodynamic consistency and other challenges in coarse-graining models", *The European Physical Journal Special Topics* **2015**, *224*, 2177–2191.

[41] M. K. Meinel, F. Müller-Plathe, "Loss of Molecular Roughness upon Coarse-Graining Predicts the Artificially Accelerated Mobility of Coarse-Grained Molecular Simulation Models", *Journal of Chemical Theory and Computation* **2020**, *16*, 1411–1419.

[42] D. Fritz, C. R. Herbers, K. Kremer, N. F. A. van der Vegt, "Hierarchical modeling of polymer permeation", *Soft Matter* **2009**, *5*, 4556–4563.

[43] S. O. Nielsen, C. F. Lopez, G. Srinivas, M. L. Klein, "Coarse Grain Models and the Computer Simulation of Soft Materials", *Journal of Physics: Condensed Matter* **2004**, *16*, R481–R512.

[44] Z. Wu, F. Müller-Plathe, "Slip-Spring Hybrid Particle-Field Molecular Dynamics for Coarse-Graining Branched Polymer Melts: Polystyrene Melts as an Example", *Journal of Chemical Theory and Computation* **2022**, *18*, 3814–3828.

[45] V. Klippenstein, N. F. A. van der Vegt, "Bottom-Up Informed and Iteratively Optimized Coarse-Grained Non-Markovian Water Models with Accurate Dynamics", *Journal of Chemical Theory and Computation* **2023**, *19*, 1099–1110.

[46] S. Bag, M. K. Meinel, F. Müller-Plathe, "Toward a Mobility-Preserving Coarse-Grained Model: A Data-Driven Approach", *Journal of Chemical Theory and Computation* **2022**, *18*, 7108–7120.

[47] S. Bag, M. K. Meinel, F. Müller-Plathe, "Synthetic Force-Field Database for Training Machine Learning Models to Predict Mobility-Preserving Coarse-Grained Molecular-Simulation Potentials", *Journal of Chemical Theory and Computation* **2024**, *20*, 3046–3060.

[48] A. Davtyan, J. F. Dama, G. A. Voth, H. C. Andersen, "Dynamic force matching: A method for constructing dynamical coarse-grained models with realistic time dependence", *The Journal of Chemical Physics* **2015**, *142*, 154104.

[49] A. Davtyan, G. A. Voth, H. C. Andersen, "Dynamic force matching: Construction of dynamic coarse-grained models with realistic short time dynamics and accurate long time dynamics", *The Journal of Chemical Physics* **2016**, *145*, 224107.

[50] M. Tripathy, V. Klippenstein, N. F. A. van der Vegt, "Dynamical coarse-grained models of molecular liquids and their ideal and non-ideal mixtures", *The Journal of Chemical Physics* **2023**, *159*, 094904.

[51] F. Knoch, K. Schäfer, G. Diezemann, T. Speck, "Dynamic coarse-graining fills the gap between atomistic simulations and experimental investigations of mechanical unfolding", *The Journal of Chemical Physics* **2018**, *148*, 044109.

[52] J. T. Padding, W. J. Briels, "Time and Length Scales of Polymer Melts Studied By Coarse-Grained Molecular Dynamics Simulations", *The Journal of Chemical Physics* **2002**, *117*, 925–943.

[53] R. L. C. Akkermans, W. J. Briels, "Coarse-grained dynamics of one chain in a polymer melt", *The Journal of Chemical Physics* **2000**, *113*, 6409–6422.

[54] S. Izvekov, G. A. Voth, "Modeling real dynamics in the coarse-grained representation of condensed phase systems", *The Journal of Chemical Physics* **2006**, *125*, 151101.

[55] S. Markutsya, M. H. Lamm, "A Coarse-Graining Approach for Molecular Simulation That Retains the Dynamics of the All-Atom Reference System By Implementing Hydrodynamic Interactions", *The Journal of Chemical Physics* **2014**, *141*, 174107.

[56] H.-J. Qian, C. C. Liew, F. Müller-Plathe, "Effective control of the transport coefficients of a coarse-grained liquid and polymer models using the dissipative particle dynamics and Lowe-Andersen equations of motion", *Physical Chemistry Chemical Physics* **2009**, *11*, 1962–1969.

[57] C. A. Lemarchand, M. Couty, B. Rousseau, "Coarse-Grained Simulations of Cis- and Trans-Polybutadiene: a Bottom-Up Approach", *The Journal of Chemical Physics* **2017**, *146*, 074904.

[58] M. Palma Banos, A. V. Popov, R. Hernandez, “Representability and Dynamical Consistency in Coarse-Grained Models”, *The Journal of Physical Chemistry B* **2024**, *128*, 1506–1514.

[59] V. A. Harmandaris, K. Kremer, “Predicting polymer dynamics at multiple length and time scales”, *Soft Matter* **2009**, *5*, 3920–3926.

[60] J. B. Accary, V. Teboul, “Time versus temperature rescaling for coarse grain molecular dynamics simulations”, *The Journal of Chemical Physics* **2012**, *136*, 094502.

[61] J. Jin, K. S. Schweizer, G. A. Voth, “Understanding dynamics in coarse-grained models. I. Universal excess entropy scaling relationship”, *Chemical Physics* **2023**, *158*, 034103.

[62] A. F. Behbahani, L. Schneider, A. Rissanou, A. Chazirakis, P. Bačová, P. K. Jana, W. Li, M. Doxastakis, P. Polińska, C. Burkhart, M. Müller, V. A. Harmandaris, “Dynamics and Rheology of Polymer Melts via Hierarchical Atomistic, Coarse-Grained, and Slip-Spring Simulations”, *Macromolecules* **2021**, *54*, 2740–2762.

[63] G. Milano, F. Müller-Plathe, “Mapping Atomistic Simulations to Mesoscopic Models: A Systematic Coarse-Graining Procedure for Vinyl Polymer Chains”, *The Journal of Physical Chemistry B* **2005**, *109*, 18609–18619.

[64] V. A. Harmandaris, K. Kremer, “Dynamics of Polystyrene Melts through Hierarchical Multiscale Simulations”, *Macromolecules* **2009**, *42*, 791–802.

[65] M. S. Shell, “Systematic coarse-graining of potential energy landscapes and dynamics in liquids”, *The Journal of Chemical Physics* **2012**, *137*, 084503.

[66] G. G. Rondina, M. C. Böhm, F. Müller-Plathe, “Predicting the Mobility Increase of Coarse-Grained Polymer Models from Excess Entropy Differences”, *Journal of Chemical Theory and Computation* **2020**, *16*, 1431–1447.

[67] A. Chaimovich, M. S. Shell, “Coarse-graining errors and numerical optimization using a relative entropy framework”, *The Journal of Chemical Physics* **2011**, *134*, 094112.

[68] I. Lyubimov, M. G. Guenza, “First-principle approach to rescale the dynamics of simulated coarse-grained macromolecular liquids”, *Physical Review E* **2011**, *84*, 031801.

[69] I. Y. Lyubimov, M. G. Guenza, “Theoretical reconstruction of realistic dynamics of highly coarse-grained cis-1,4-polybutadiene melts”, *The Journal of Chemical Physics.* **2013**, *138*, 12A546.

[70] J. G. E. M. Fraaije, J. van Male, P. Becherer, R. S. Gracià, “Calculation of Diffusion Coefficients Through Coarse-Grained Simulations Using the Automated-Fragmentation-Parametrization Method and the Recovery of Wilke-Chang Statistical Correlation”, *Journal of Chemical Theory and Computation* **2018**, *14*, 479–485.

[71] J. F. Rudzinski, S. Kloth, S. Wörner, T. Pal, K. Kremer, T. Bereau, M. Vogel, “Dynamical properties across different coarse-grained models for ionic liquids”, *Journal of Physics: Condensed Matter* **2021**, *33*, 224001.

[72] M. K. Meinel, F. Müller-Plathe, “Roughness Volumes: An Improved RoughMob Concept for Predicting the Increase of Molecular Mobility upon Coarse-Graining”, *The Journal of Physical Chemistry B* **2022**, *126*, 3737–3747.

[73] M. K. Meinel, F. Müller-Plathe, “Predicting the artificial dynamical acceleration of binary hydrocarbon mixtures upon coarse-graining with roughness volumes and simple averaging rules”, *The Journal of Chemical Physics* **2024**, *160*, 174108.

[74] P. Carbone, H. A. K. Varzaneh, X. Chen, F. Müller-Plathe, “Transferability of coarse-grained force fields: The polymer case”, *The Journal of Chemical Physics* **2008**, *128*, 064904.

[75] B. J. Alder, T. E. Wainwright, “Studies in Molecular Dynamics. I. General Method”, *The Journal of Chemical Physics* **1959**, *31*, 459–466.

[76] L. Verlet, “Computer "Experiments" on Classical Fluids. I. Thermodynamical Properties of Lennard-Jones Molecules”, *Physical Review* **1967**, *159*, 98–103.

[77] M. S. Shell, *Thermodynamics and Statistical Mechanics: An Integrated Approach*, Cambridge University Press, **2015**.

[78] A. P. Sutton, J. Chen, “Long-range Finnis–Sinclair potentials”, *Philosophical Magazine Letters* **1990**, *61*, 139–146.

[79] Y. Mishin, D. Farkas, M. J. Mehl, D. A. Papaconstantopoulos, “Interatomic potentials for monoatomic metals from experimental data and ab initio calculations”, *Physical Review B* **1999**, *59*, 3393–3407.

[80] J. Tersoff, “Modeling solid-state chemistry: Interatomic potentials for multicomponent systems”, *Physical Review B* **1989**, *39*, 5566–5568.

[81] W. L. Jorgensen, D. S. Maxwell, J. Tirado-Rives, “Development and Testing of the OPLS All-Atom Force Field on Conformational Energetics and Properties of Organic Liquids”, *Journal of the American Chemical Society* **1996**, *118*, 11225–11236.

[82] J. F. Rudzinski, W. G. Noid, “Coarse-Graining Entropy, Forces, and Structures”, *The Journal of Chemical Physics* **2011**, *135*, 214101.

[83] J. W. Wagner, J. F. Dama, A. E. P. Durumeric, G. A. Voth, “On the Representability Problem and the Physical Meaning of Coarse-Grained Models”, *The Journal of Chemical Physics* **2016**, *145*, 044108.

[84] M. P. Allen, D. J. Tildesley, *Computer Simulation of Liquids*, Oxford University Press, **2017**.

[85] B. L. Peters, K. M. Salerno, A. Agrawal, D. Perahia, G. S. Grest, “Coarse-Grained Modeling of Polyethylene Melts: Effect on Dynamics”, *Journal of Chemical Theory and Computation* **2017**, *13*, 2890–2896.

[86] V. K. Michalis, O. A. Moultos, I. N. Tsimpanogiannis, I. G. Economou, “Molecular dynamics simulations of the diffusion coefficients of light n-alkanes in water over a wide range of temperature and pressure”, *Fluid Phase Equilibria* **2016**, *407*, 236–242.

[87] Y.-L. Wang, B. Li, A. Laaksonen, “Coarse-grained simulations of ionic liquid materials: from monomeric ionic liquids to ionic liquid crystals and polymeric ionic liquids”, *Physical Chemistry Chemical Physics* **2021**, *23*, 19435–19456.

[88] T. D. Stoffel, J. B. Haskins, J. W. Lawson, S. Markutsya, “Coarse-Grained Dynamically Accurate Simulations of Ionic Liquids: [pyr14][TFSI] and [EMIM][BF4]”, *The Journal of Physical Chemistry B* **2022**, *126*, 1819–1829.

[89] F. Schmid, “Understanding and Modeling Polymers: The Challenge of Multiple Scales”, *ACS Polymers Au* **2023**, *3*, 28–58.

Supporting Information: Loss of molecular roughness upon coarse-graining predicts the artificially accelerated mobility of coarse-grained molecular simulation models

Melissa K. Meinel* and Florian Müller-Plathe*

Eduard-Zintl-Institut für Anorganische und Physikalische Chemie and Profile Area Thermofluids and Interfaces, Technische Universität Darmstadt, Alarich-Weiss-Strasse 8, D-64287 Darmstadt, Germany

E-mail: m.meinel@theo.chemie.tu-darmstadt.de; f.mueller-plathe@theo.chemie.tu-darmstadt.de

All-atom potentials

Table 1: Atomistic Force Field Potential Energy Bonded Parameters with sp^3 aliphatic carbon atoms (CT), aliphatic hydrogen atoms (HC), aromatic carbon atoms (CA) and aromatic hydrogen atoms (HA).

bonds	$E_{\text{bond}} = K_r(r - r_{\text{eq}})^2$	
type	K_r /kcal mol^{-1}Å^{-2}	r_{eq} /Å
CT–CT[d]	268	1.529
CT–HC[d]	340	1.090
CT–CA[a]	317	1.510
CA–CA[a]	469	1.400
CA–HA[a]	367	1.080
angles	$E_{\text{angle}} = K_\theta(\theta - \theta_{\text{eq}})^2$	
type	K_θ /kcal mol^{-1}rad^{-2}	θ_{eq} /deg
CT–CT–CT[d]	58.35	112.7
CT–CT–HC[d]	37.5	110.7
HC–CT–HC[d]	33	107.8
CT–CT–CA[a]	63	114
CT–CA–CA[a]	70	120
HC–CT–CA	35	109.5
CA–CA–CA[a]	63	120
CA–CA–HA[a]	35	120
dihedrals	$E_{\text{torsion}} = \frac{1}{2}[V_1(1+\cos(\varphi)) + V_2(1-\cos(2\varphi)) + V_3(1+\cos(3\varphi))]$	
type	V_1/kcal mol^{-1}	V_2/kcal mol^{-1}	V_3/kcal mol^{-1}
CT–CT–CT–CT[c]	1.3	-0.05	0.2
CT–CT–CT–HC[c]	0.0	0.0	0.3
HC–CT–CT–HC[c]	0.0	0.0	0.3
CT–CT–CA–CA[b]	0.0	0.0	0.0
CT–CA–CA–CA[d]	0.0	7.25	0.0
CT–CA–CA–HA[d]	0.0	7.25	0.0
HC–CT–CT–CA[b]	0.0	0.0	0.462
HC–CT–CA–CA[b]	0.0	0.0	0.0
CA–CA–CA–CA[d]	0.0	7.25	0.0
CA–CA–CA–HA[d]	0.0	7.25	0.0
HA–CA–CA–HA[d]	0.0	7.25	0.0

[a] Values from Ref. 1 ; [b] values from Ref. 2 ; [c] values from Ref. 3 ; [d] values from Ref. 4 .

Reference surfaces

Two alternative ways of defining the reference surface for the molecular roughness calculation have been tested. Both arise purely from the geometry of the all-atom molecule, assuming that the roughness of the CG bead is zero, and yield lower correlations with the acceleration factor.

Average atomistic surface radius

A sphere with the average radius of the AA surface grid $\mathcal{R}_{\mathrm{AA}}$ is used as reference geometry. The radii $\overline{r}_{\mathrm{AA}}$ of the spheres, (thus, the equivalent to r_{CG}) can be found in Table 2.

$$\overline{r}_{\mathrm{AA}} \;=\; \frac{1}{n_{grid}} \sum_{(\theta,\varphi,r_{\mathrm{AA}})\in\mathcal{R}_{\mathrm{AA}}} r_{\mathrm{AA}} \tag{1}$$

$$\mathcal{R}_{\mathrm{ref}} \;=\; \overline{r}_{\mathrm{AA}} \cdot \mathcal{R}_{\mathrm{dir}} \tag{2}$$

Table 2: Molecular roughness difference, skewness and kurtosis averaged over 200 molecules for each system.

	ΔR_a /Å	$\overline{r}_{\mathrm{AA}}$ /Å	R_{sk}	R_{ku}
23DiMeBu	0.495	2.94	-0.28	2.37
Bz	0.461	2.66	-0.37	2.61
3MePe	0.576	2.90	0.15	2.41
234TriMePe	0.608	3.18	-0.16	2.31
3EtHx	0.708	3.10	0.42	2.56
EtBz	0.695	2.88	0.2	2.3
25DiMeHx	0.847	3.04	0.43	2.07

The correlation coefficient of the linear relation between α and ΔR_a is $R^2 = 0.97$.

$$\alpha \;=\; 39\ \text{Å}^{-1}(\Delta R_a \;-\; 0.43\ \text{Å})$$

Convex hull

Instead of using a sphere as reference surface, the reference surface follows the shape of the convex hull of the AA molecule and is scaled so that the average radius equals the average atomistic surface radius. The surface of the AA molecule is generated numerically using the Shrake-Rupley Algorithm[5] with a probe radius of 0. The convex hull of a point cloud is the smallest convex set that contains all its points which means that every line segment connecting two points lies completely within the hull. The convex hull of this point grid is described by a triangulated surface with T_i being the i^{th} triangle. $\mathcal{R}_{\mathrm{cH}}$ is the set of ray-triangle intersection points of all rays $\mathcal{R}_{\mathrm{dir}}$ and all triangles of the convex hull.

$$\mathcal{R}_{\mathrm{cH}} = \left\{ p \in T_i \cap r \cdot \mathcal{R}_{\mathrm{dir}} | i = 1, ..., n_{triangles}; r \in \mathbb{R}^+ \right\} \tag{3}$$

$$\overline{r}_{\mathrm{cH}} = \frac{1}{n_{grid}} \sum_{(\theta,\varphi,r_{\mathrm{cH}}) \in \mathcal{R}_{\mathrm{cH}}} r_{\mathrm{cH}} \tag{4}$$

The radius component of each point in $\mathcal{R}_{\mathrm{cH}}$ is scaled so that the average radius equals the average atomistic surface radius $\overline{r}_{\mathrm{AA}}$.

$$\mathcal{R}_{\mathrm{ref}} = \frac{\overline{r}_{\mathrm{AA}}}{\overline{r}_{\mathrm{cH}}} \cdot \mathcal{R}_{\mathrm{cH}} \tag{5}$$

Table 3: Molecular roughness difference, skewness and kurtosis averaged over 200 molecules for each system.

	ΔR_a /Å	$\overline{r}_{\mathrm{AA}}$ /Å	R_{sk}	R_{ku}
23DiMeBu	0.291	3.24	-1.14	3.61
Bz	0.114	2.76	-1.29	4.18
3MePe	0.315	3.23	-0.96	3.14
234TriMePe	0.352	3.55	-1.05	3.36
3EtHx	0.393	3.56	-0.72	2.79
EtBz	0.297	3.19	-1.03	3.36
25DiMeHx	0.439	3.56	-0.45	2.28

References

(1) Cornell, W. D.; Cieplak, P.; Bayly, C. I.; Gould, I. R.; Merz, K. M.; Ferguson, D. M.; Spellmeyer, D. C.; Fox, T.; Caldwell, J. W.; Kollman, P. A. A Second Generation Force Field for the Simulation of Proteins, Nucleic Acids, and Organic Molecules. *J. Am. Chem. Soc.* **1995**, *117*, 5179–5197.

(2) Jorgensen, W. L.; Maxwell, D. S.; Tirado-Rives, J. Development and Testing of the OPLS All-Atom Force Field on Conformational Energetics and Properties of Organic Liquids. *J. Am. Chem. Soc.* **1996**, *118*, 11225–11236.

(3) Price, M. L. P.; Ostrovsky, D.; Jorgensen, W. L. Gas-phase and liquid-state properties of esters, nitriles, and nitro compounds with the OPLS-AA force field. *J. Comput. Chem.* **2001**, *22*, 1340–1352.

(4) Rizzo, R. C.; Jorgensen, W. L. OPLS All-Atom Model for Amines: Resolution of the Amine Hydration Problem. *J. Am. Chem. Soc.* **1999**, *121*, 4827–4836.

(5) Shrake, A.; Rupley, J. Environment and exposure to solvent of protein atoms. Lysozyme and insulin. *J. Mol. Biol.* **1973**, *79*, 351–371.

Supporting Information: Roughness volumes: An improved RoughMob concept for predicting the increase of molecular mobility upon coarse-graining

Melissa K. Meinel* and Florian Müller-Plathe*

Eduard-Zintl-Institut für Anorganische und Physikalische Chemie and Profile Area Thermofluids and Interfaces, Technische Universität Darmstadt, Alarich-Weiss-Strasse 8, D-64287 Darmstadt, Germany

E-mail: m.meinel@theo.chemie.tu-darmstadt.de; f.mueller-plathe@theo.chemie.tu-darmstadt.de

All-atom potentials

Table S1: Atomistic Force Field Potential Energy Bonded Parameters with sp^3 aliphatic carbon atoms (CT), aliphatic hydrogen atoms (HC), aromatic carbon atoms (CA) and aromatic hydrogen atoms (HA).

bonds	$E_{\text{bond}} = K_r(r - r_{\text{eq}})^2$	
type	K_r /kcal mol^{-1}Å^{-2}	r_{eq} /Å
CT–CT[d]	268	1.529
CT–HC[d]	340	1.090
CT–CA[a]	317	1.510
CA–CA[a]	469	1.400
CA–HA[a]	367	1.080
angles	$E_{\text{angle}} = K_\theta(\theta - \theta_{\text{eq}})^2$	
type	K_θ /kcal mol^{-1}rad^{-2}	θ_{eq} /deg
CT–CT–CT[d]	58.35	112.7
CT–CT–HC[d]	37.5	110.7
HC–CT–HC[d]	33	107.8
CT–CT–CA[a]	63	114
CT–CA–CA[a]	70	120
HC–CT–CA	35	109.5
CA–CA–CA[a]	63	120
CA–CA–HA[a]	35	120
dihedrals	$E_{\text{torsion}} = \frac{1}{2}[V_1(1+\cos(\varphi)) + V_2(1-\cos(2\varphi)) + V_3(1+\cos(3\varphi))]$	
type	V_1/kcal mol^{-1}	V_2/kcal mol^{-1}	V_3/kcal mol^{-1}
CT–CT–CT–CT[c]	1.3	-0.05	0.2
CT–CT–CT–HC[c]	0.0	0.0	0.3
HC–CT–CT–HC[c]	0.0	0.0	0.3
CT–CT–CA–CA[b]	0.0	0.0	0.0
CT–CA–CA–CA[d]	0.0	7.25	0.0
CT–CA–CA–HA[d]	0.0	7.25	0.0
HC–CT–CT–CA[b]	0.0	0.0	0.462
HC–CT–CA–CA[b]	0.0	0.0	0.0
CA–CA–CA–CA[d]	0.0	7.25	0.0
CA–CA–CA–HA[d]	0.0	7.25	0.0
HA–CA–CA–HA[d]	0.0	7.25	0.0

[a] Values from Ref. 1 ; [b] values from Ref. 2 ; [c] values from Ref. 3 ; [d] values from Ref. 4 .

Cut off-radii for Iterative Boltzmann Inversion

Table S2: Cut of-radii used for coarse-graining via Iterative Boltzmann Inversion in Å.

system	r_{cut}
alkanes, COM-mapped	
Neo	14.9
23DiMeBu	15.5
3MePe	15.3
23DiMePe	15.95
234TriMePe	16.5
3EtHx	15.1
33DE24DMP	15.5
2MeHx	14.9
25DiMeHx	15.2
33DIP24DMP	16.1
aromatic molecules, COM-mapped	
Bz	14.3
EtBz	14.9
Mesi	15.35
alkanes, methyl C-mapped	
3MePe	15.3
23DiMePe	16.0
23DiMeBu	15.5
234TriMePe	16.6

Predicted acceleration factor

Instead of using

$$\alpha_{pred} = A \cdot (V_{shell} + V_{overlap}) + B \cdot \exp\left(\frac{V_{in}}{V_{out}}\right) + C \quad (1)$$

as fitted equation to predict the scaling factor, other combinations of the roughness volumes have been tested. Some of them are shown here. Figure S1 and S2 show the fits for two alternative ways of defining the passive volume term (equations above the figures). Figure S3 and S4 show fits with active volume terms without adding the overlap volume or with

subtracting it (to use only the volumes summing up to the molecular volume). Generally, the fit with all systems results in acceptable agreements between the predicted acceleration and the calculated acceleration factor (Figures (a)), while the prediction of higher acceleration factors from lower acceleration factors (Figures (b)) worsens. Adding different factors, such as the coordination number C_N or the ratio of the molecular surfaces to the fitted parameter has been tested as well (see Figure S5). However, since no significant improvements were reached, they were left out for simplicity.

$$\alpha_{pred} = A \cdot (V_{shell} + V_{overlap}) + B \cdot (V_{in} - V_{out}) + C \tag{2}$$

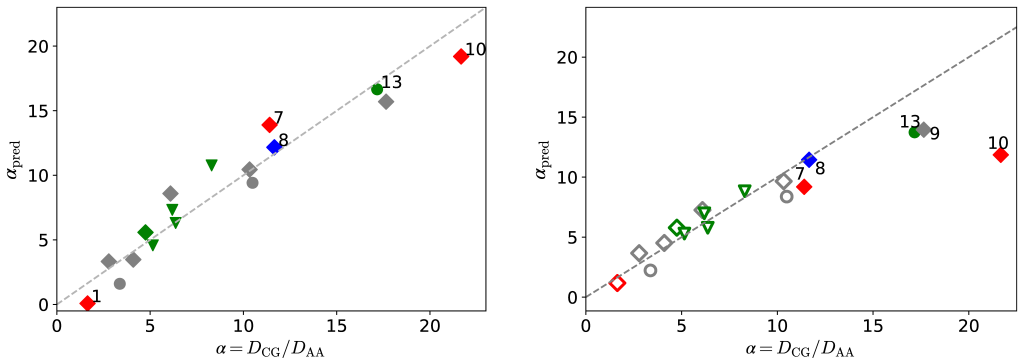

(a) (b)

Figure S1: Predicted acceleration factor against simulated acceleration factor; *gray, diamond*: C6 and C8 alkane; *gray, circle*: C6 and C8 aromatic; *blue*: 2-methylhexane; *green, diamond*: 2,3-dimethylpentane; *green, circle*: mesitylene; *red*: C5, C11 and C13 alkane; *triangle, green*: methyl C-mapped alkane; *gray, dashed*: simulated scaling factor; (a) all systems used for fit of Eq. 2; (b) *unfilled*: systems used for fit; *filled*: predicted systems

$$\alpha_{pred} = A \cdot (V_{shell} + V_{overlap}) + B \cdot \left(\frac{V_{in}}{V_{out}}\right) + C \tag{3}$$

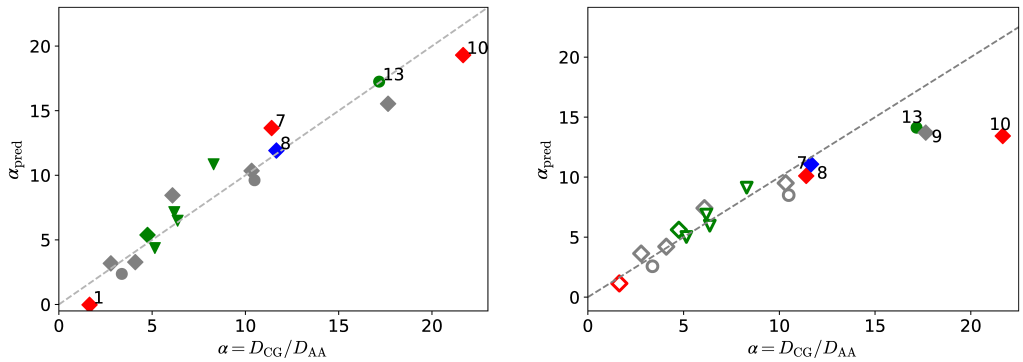

(a) (b)

Figure S2: Predicted acceleration factor against simulated acceleration factor; *gray, diamond*: C6 and C8 alkane; *gray, circle*: C6 and C8 aromatic; *blue*: 2-methylhexane; *green, diamond*: 2,3-dimethylpentane; *green, circle*: mesitylene; *red*: C5, C11 and C13 alkane; *triangle, green*: methyl C-mapped alkane; *gray, dashed*: simulated scaling factor; (a) all systems used for fit of Eq. 3; (b) *unfilled*: systems used for fit; *filled*: predicted systems

$$\alpha_{pred} = A \cdot (V_{shell}) + B \cdot \exp\left(\frac{V_{in}}{V_{out}}\right) + C \tag{4}$$

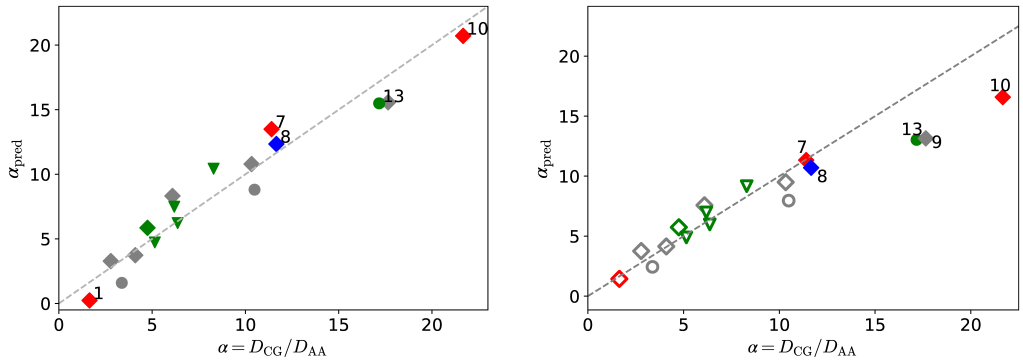

(a) (b)

Figure S3: Predicted acceleration factor against simulated acceleration factor; *gray, diamond*: C6 and C8 alkane; *gray, circle*: C6 and C8 aromatic; *blue*: 2-methylhexane; *green, diamond*: 2,3-dimethylpentane; *green, circle*: mesitylene; *red*: C5, C11 and C13 alkane; *triangle, green*: methyl C-mapped alkane; *gray, dashed*: simulated scaling factor; (a) all systems used for fit of Eq. 4; (b) *unfilled*: systems used for fit; *filled*: predicted systems

$$\alpha_{pred} = A \cdot (V_{shell} - V_{overlap}) + B \cdot \exp\left(\frac{V_{in}}{V_{out}}\right) + C \tag{5}$$

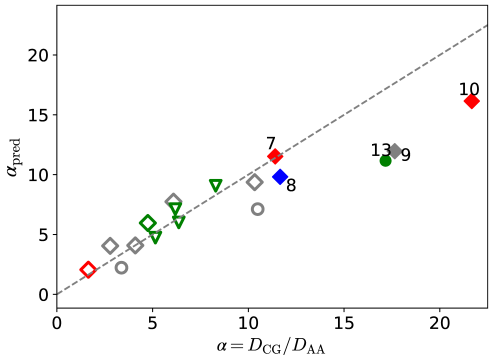

(a) (b)

Figure S4: Predicted acceleration factor against simulated acceleration factor; *gray, diamond*: C6 and C8 alkane; *gray, circle*: C6 and C8 aromatic; *blue*: 2-methylhexane; *green, diamond*: 2,3-dimethylpentane; *green, circle*: mesitylene; *red*: C5, C11 and C13 alkane; *triangle, green*: methyl C-mapped alkane; *gray, dashed*: simulated scaling factor; (a) all systems used for fit of Eq. 5; (b) *unfilled*: systems used for fit; *filled*: predicted systems

While not adding the overlap volume provides comparable results to the ones presented in the paper, subtracting it (to use only the volumes summing up to the molecular volume) significantly worsens it.

$$\alpha_{pred} = A \cdot C_N \cdot (V_{shell} - V_{overlap}) + B \cdot \exp\left(\frac{V_{in}}{V_{out}}\right) + C \tag{6}$$

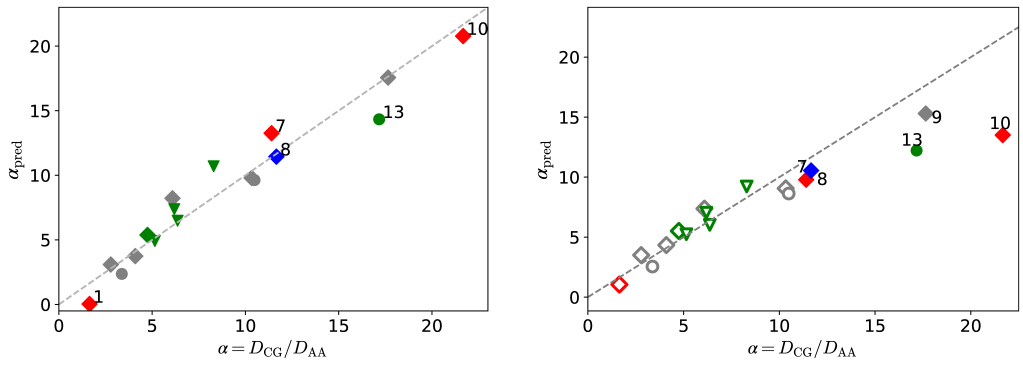

(a) (b)

Figure S5: Predicted acceleration factor against simulated acceleration factor; *gray, diamond*: C6 and C8 alkane; *gray, circle*: C6 and C8 aromatic; *blue*: 2-methylhexane; *green, diamond*: 2,3-dimethylpentane; *green, circle*: mesitylene; *red*: C5, C11 and C13 alkane; *triangle, green*: methyl C-mapped alkane; *gray, dashed*: simulated scaling factor; (a) all systems used for fit Eq. 6; (b) *unfilled*: systems used for fit; *filled*: predicted systems

References

(1) Cornell, W. D.; Cieplak, P.; Bayly, C. I.; Gould, I. R.; Merz, K. M.; Ferguson, D. M.; Spellmeyer, D. C.; Fox, T.; Caldwell, J. W.; Kollman, P. A. A Second Generation Force Field for the Simulation of Proteins, Nucleic Acids, and Organic Molecules. *J. Am. Chem. Soc.* **1995**, *117*, 5179–5197.

(2) Jorgensen, W. L.; Maxwell, D. S.; Tirado-Rives, J. Development and Testing of the OPLS All-Atom Force Field on Conformational Energetics and Properties of Organic Liquids. *J. Am. Chem. Soc.* **1996**, *118*, 11225–11236.

(3) Price, M. L. P.; Ostrovsky, D.; Jorgensen, W. L. Gas-phase and liquid-state properties of esters, nitriles, and nitro compounds with the OPLS-AA force field. *J. Comput. Chem.* **2001**, *22*, 1340–1352.

(4) Rizzo, R. C.; Jorgensen, W. L. OPLS All-Atom Model for Amines: Resolution of the Amine Hydration Problem. *J. Am. Chem. Soc.* **1999**, *121*, 4827–4836.

Supplementary Material: Predicting the artificial dynamical acceleration of binary hydrocarbon mixtures upon coarse-graining with roughness volumes and simple averaging rules

Melissa K. Meinel* and Florian Müller-Plathe*

Eduard-Zintl-Institut für Anorganische und Physikalische Chemie and Profile Area Thermofluids and Interfaces, Technische Universität Darmstadt, Peter-Grünberg-Strasse 8, D-64287 Darmstadt, Germany

E-mail: m.meinel@theo.chemie.tu-darmstadt.de; f.mueller-plathe@theo.chemie.tu-darmstadt.de

All-atom potentials

Table S1: Atomistic Force Field Potential Energy Bonded Parameters with sp^3 aliphatic carbon atoms (CT), aliphatic hydrogen atoms (HC), aromatic carbon atoms (CA) and aromatic hydrogen atoms (HA).

bonds	$E_{\text{bond}} = K_r(r - r_{\text{eq}})^2$	
type	K_r /kcal mol^{-1}Å^{-2}	r_{eq} /Å
CT–CT[d]	268	1.529
CT–HC[d]	340	1.090
CT–CA[a]	317	1.510
CA–CA[a]	469	1.400
CA–HA[a]	367	1.080
angles	$E_{\text{angle}} = K_\theta(\theta - \theta_{\text{eq}})^2$	
type	K_θ /kcal mol^{-1}rad^{-2}	θ_{eq} /deg
CT–CT–CT[d]	58.35	112.7
CT–CT–HC[d]	37.5	110.7
HC–CT–HC[d]	33	107.8
CT–CT–CA[a]	63	114
CT–CA–CA[a]	70	120
HC–CT–CA	35	109.5
CA–CA–CA[a]	63	120
CA–CA–HA[a]	35	120
dihedrals	$E_{\text{torsion}} = \frac{1}{2}[V_1(1+\cos(\varphi)) + V_2(1-\cos(2\varphi)) + V_3(1+\cos(3\varphi))]$	
type	V_1/kcal mol^{-1}	V_2/kcal mol^{-1}	V_3/kcal mol^{-1}
CT–CT–CT–CT[c]	1.3	-0.05	0.2
CT–CT–CT–HC[c]	0.0	0.0	0.3
HC–CT–CT–HC[c]	0.0	0.0	0.3
CT–CT–CA–CA[b]	0.0	0.0	0.0
CT–CA–CA–CA[d]	0.0	7.25	0.0
CT–CA–CA–HA[d]	0.0	7.25	0.0
HC–CT–CT–CA[b]	0.0	0.0	0.462
HC–CT–CA–CA[b]	0.0	0.0	0.0
CA–CA–CA–CA[d]	0.0	7.25	0.0
CA–CA–CA–HA[d]	0.0	7.25	0.0
HA–CA–CA–HA[d]	0.0	7.25	0.0

[a] Values from Ref. 1 ; [b] values from Ref. 2 ; [c] values from Ref. 3 ; [d] values from Ref. 4 .

Coarse-grained potentials

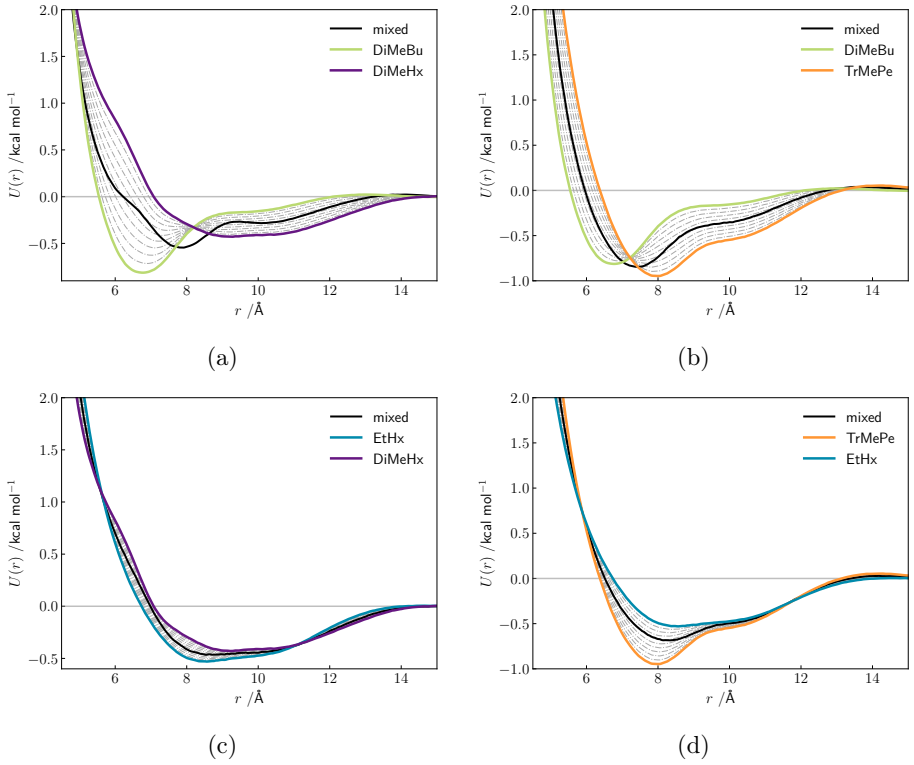

Figure S1: Coarse-grained potentials for (a) pure 2,3-dimethylbutane (*green*), pure 2,5-dimehthylhexane (*purple*) and their mixed potentials (*black*); (b) pure 2,3-dimethylbutane (*green*), pure 2,3,4-trimethylpentane (*orange*) and their mixed potentials (*black*);(c) pure 3-ethylhexane (*blue*), pure 2,5-dimehthylhexane (*purple*) and their mixed potentials (*black*) and (d) pure 3-ethylhexane (*blue*), pure 2,3,4-trimethylpentane (*orange*) and their mixed potentials (*black*); mixed potential generated by Iterative Boltzmann Inversion for a 1:1 mixture *solid* and via combination rules with c ranging from 0.1 to 0.9 *dashed-dotted*.

Structural properties

RDFs

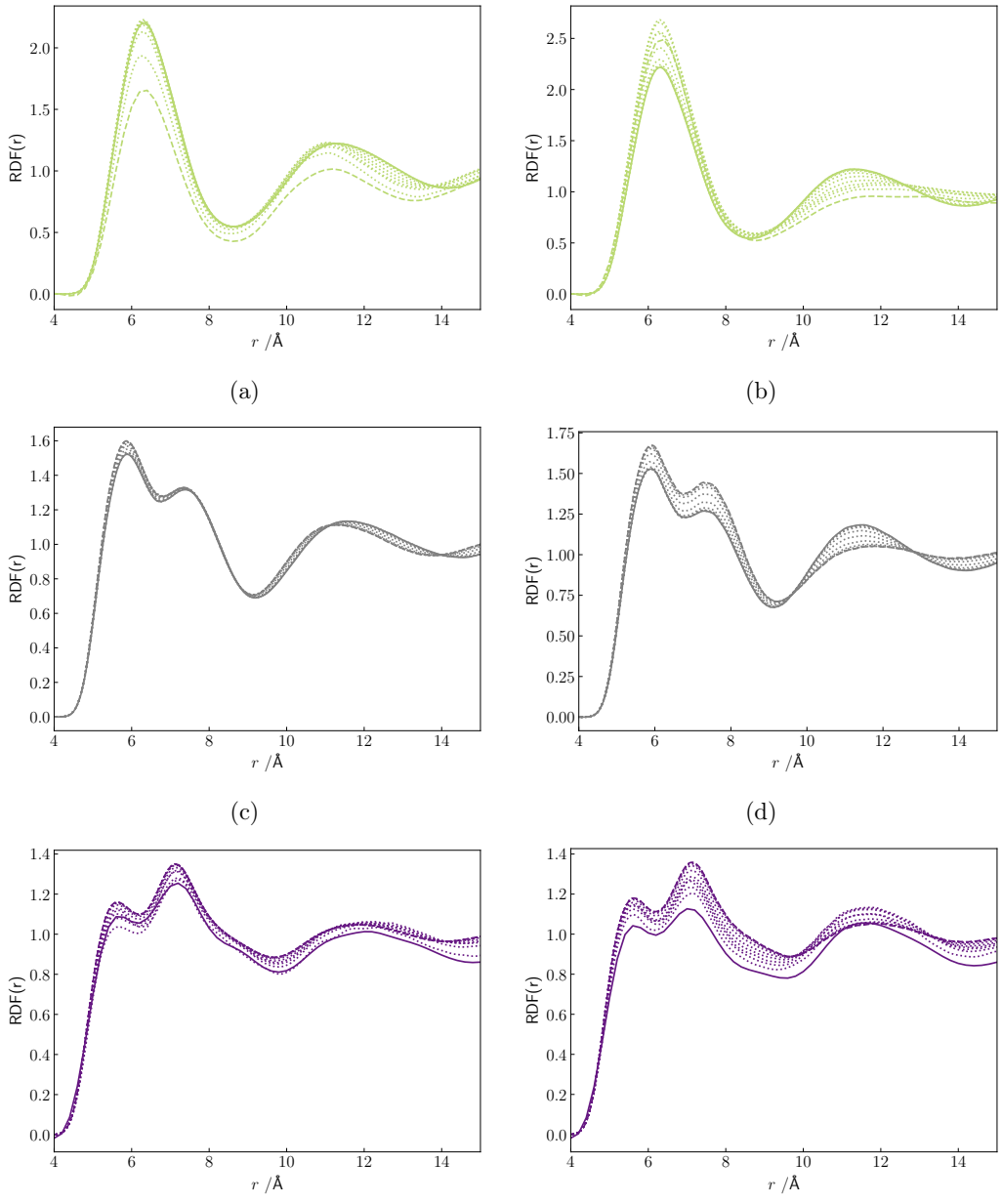

Figure S2: Radial distribution function of 2,3-dimethylbutane (*green*) and 2,5-dimethylhexane (*purple*) and their mixed species interaction (*gray*); *left*: all-atom; *right*: coarse-grained; *solid:* x_{DiMeBu}=0.01; *dashed:* x_{DiMeHx}=0.01.

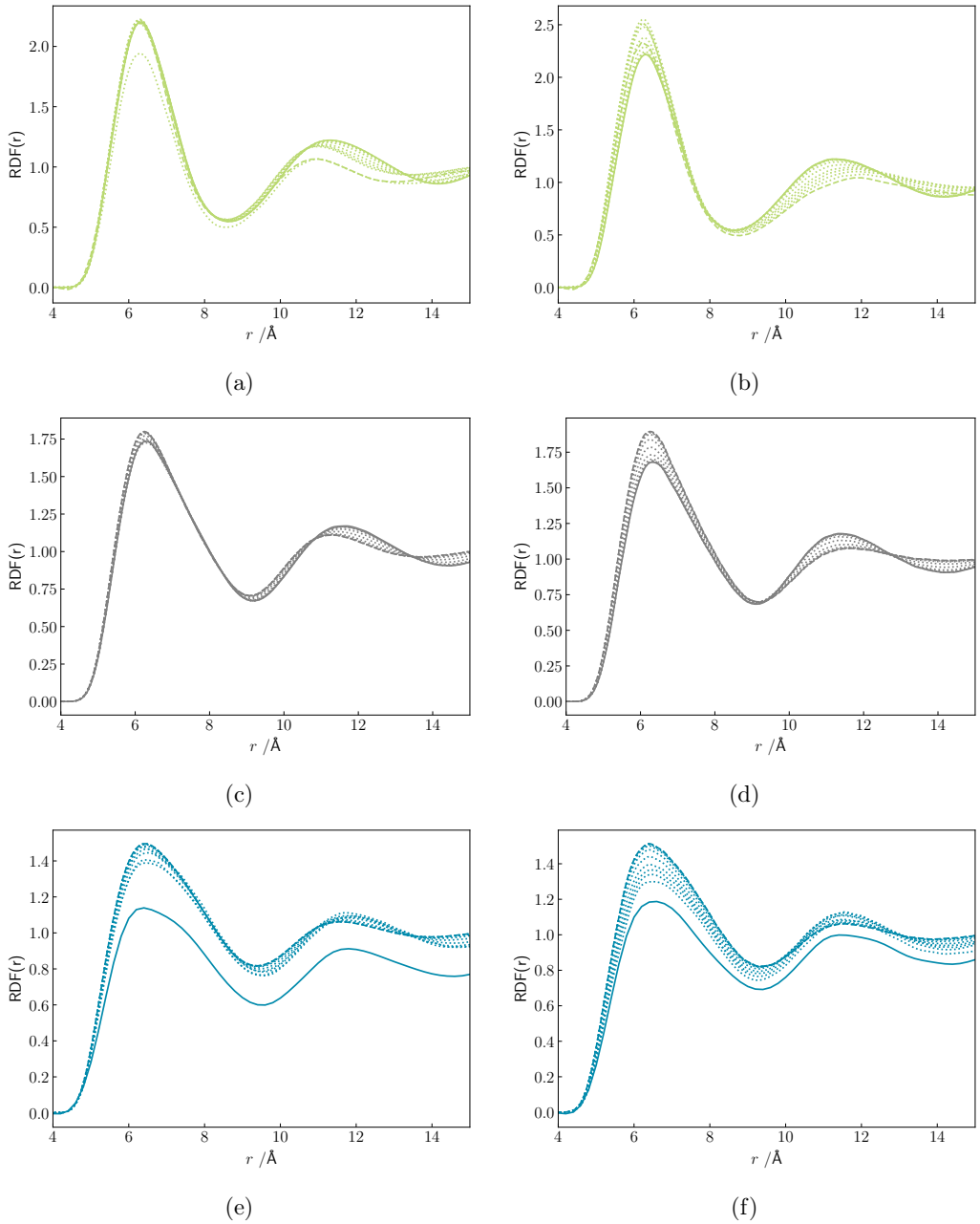

Figure S3: Radial distribution function of 2,3-dimethylbutane (*green*) and 3-ethylhexane (*blue*) and their mixed species interaction (*gray*); *left*: all-atom; *right*: coarse-grained; *solid:* x_{DiMeBu}=0.01; *dashed:* x_{EtHx}=0.01.

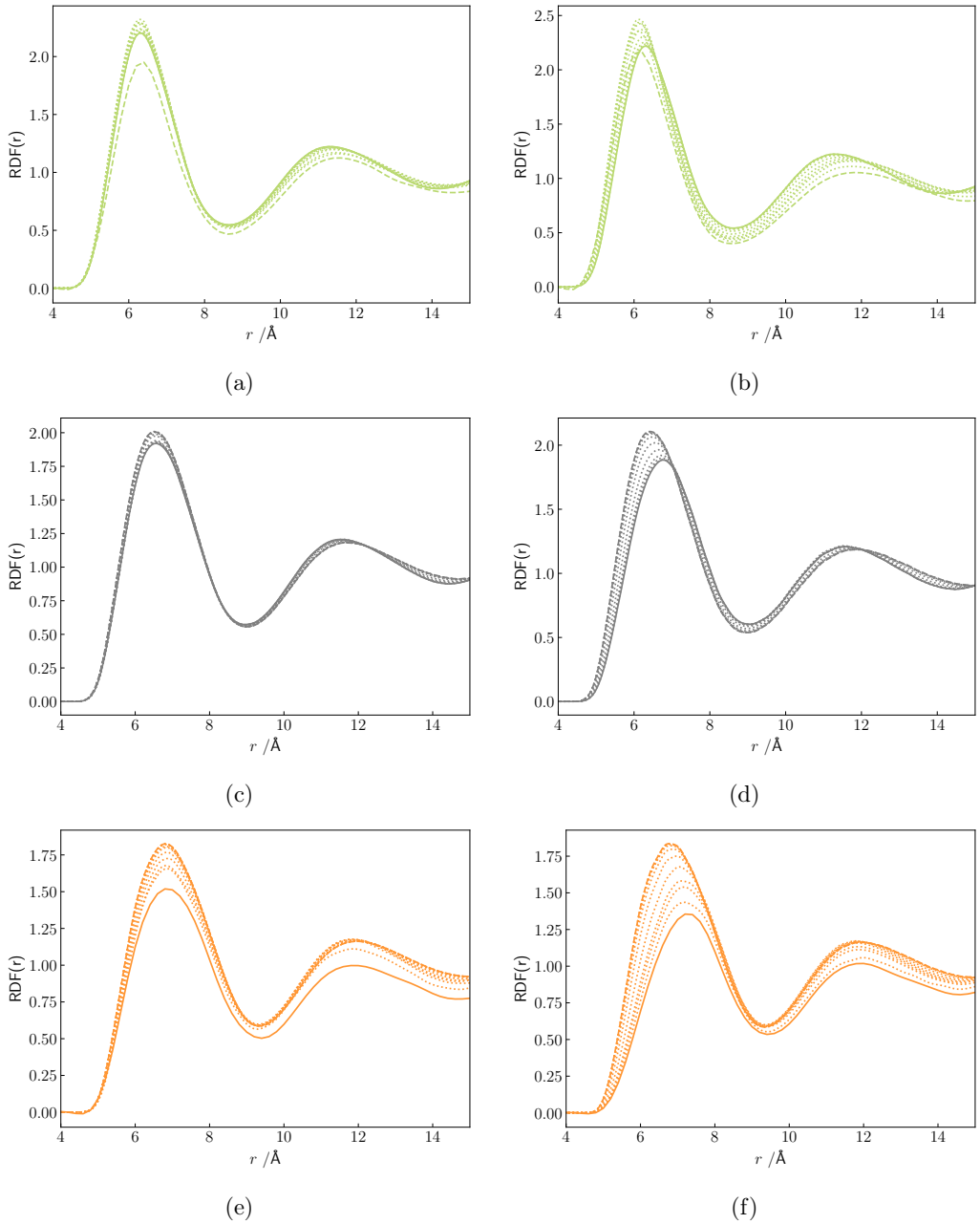

Figure S4: Radial distribution function of 2,3-dimethylbutane (*green*) and 2,3,4-trimethylpentane (*orange*) and their mixed species interaction (*gray*); *left*: all-atom; *right*: coarse-grained; *solid:* x_{DiMeBu}=0.01; *dashed:* x_{TrMePe}=0.01.

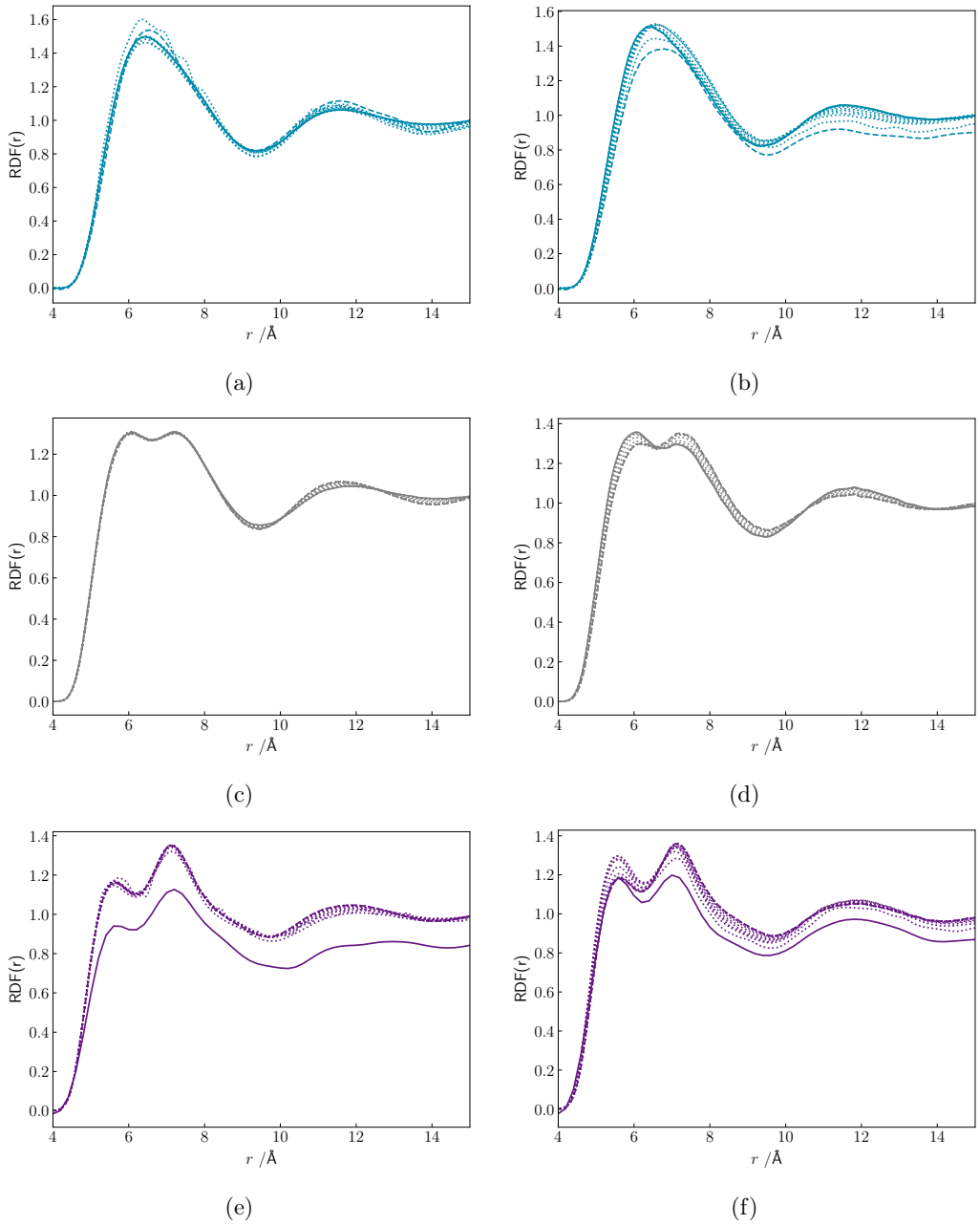

Figure S5: Radial distribution function of 3-ethylhexane (*blue*) and 2,5-dimethylhexane (*purple*) and their mixed species interaction (*gray*); *left*: all-atom; *right*: coarse-grained; *solid:* x_{EtHx}=0.01; *dashed:* x_{DiMeHx}=0.01.

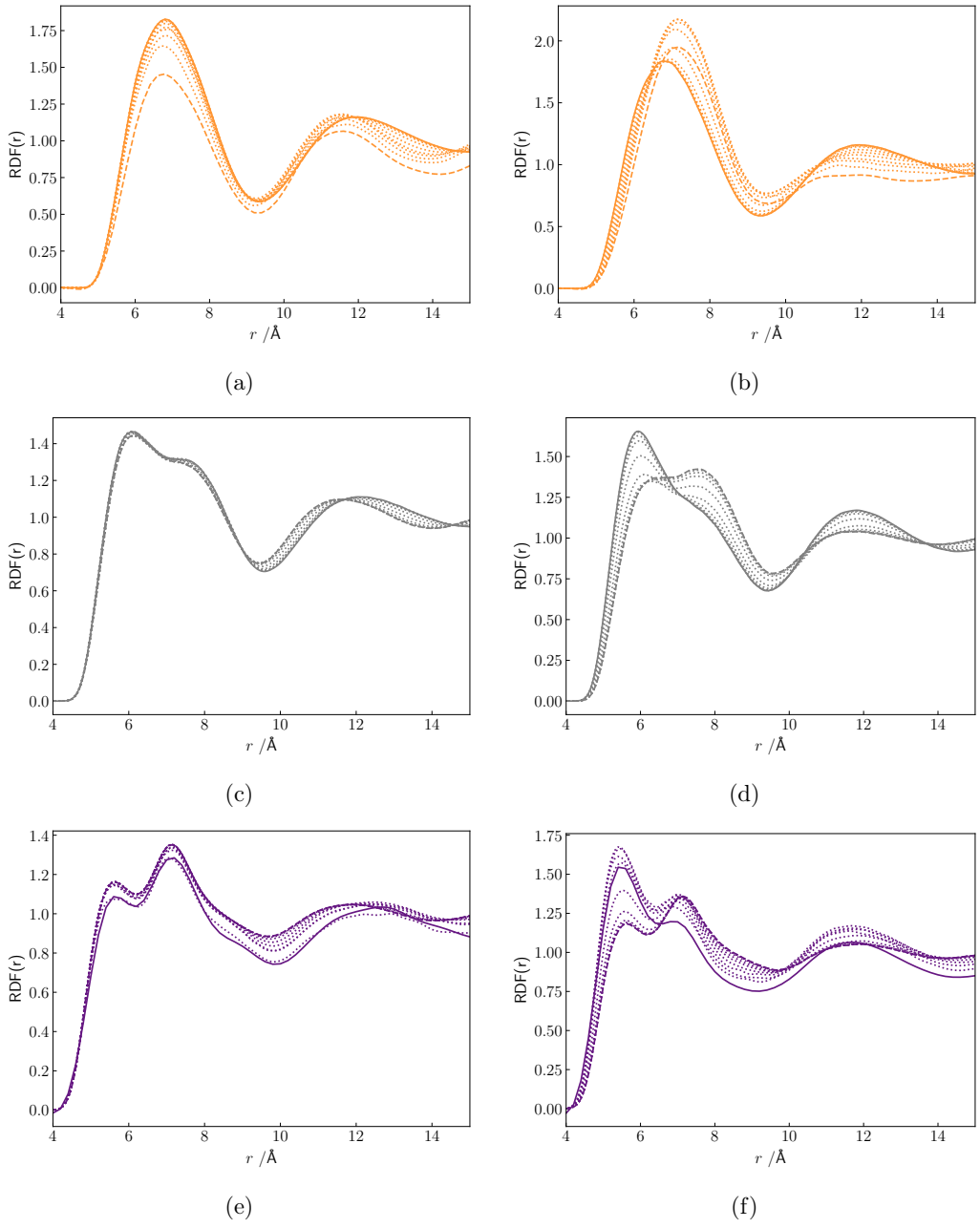

Figure S6: Radial distribution function of 2,3,4-trimethylpentane (*orange*) and 2,5-dimethylhexane (*purple*) and their mixed species interaction (*gray*); *left*: all-atom; *right*: coarse-grained; *solid:* x_{TrMePe}=0.01; *dashed:* x_{DiMeHx}=0.01.

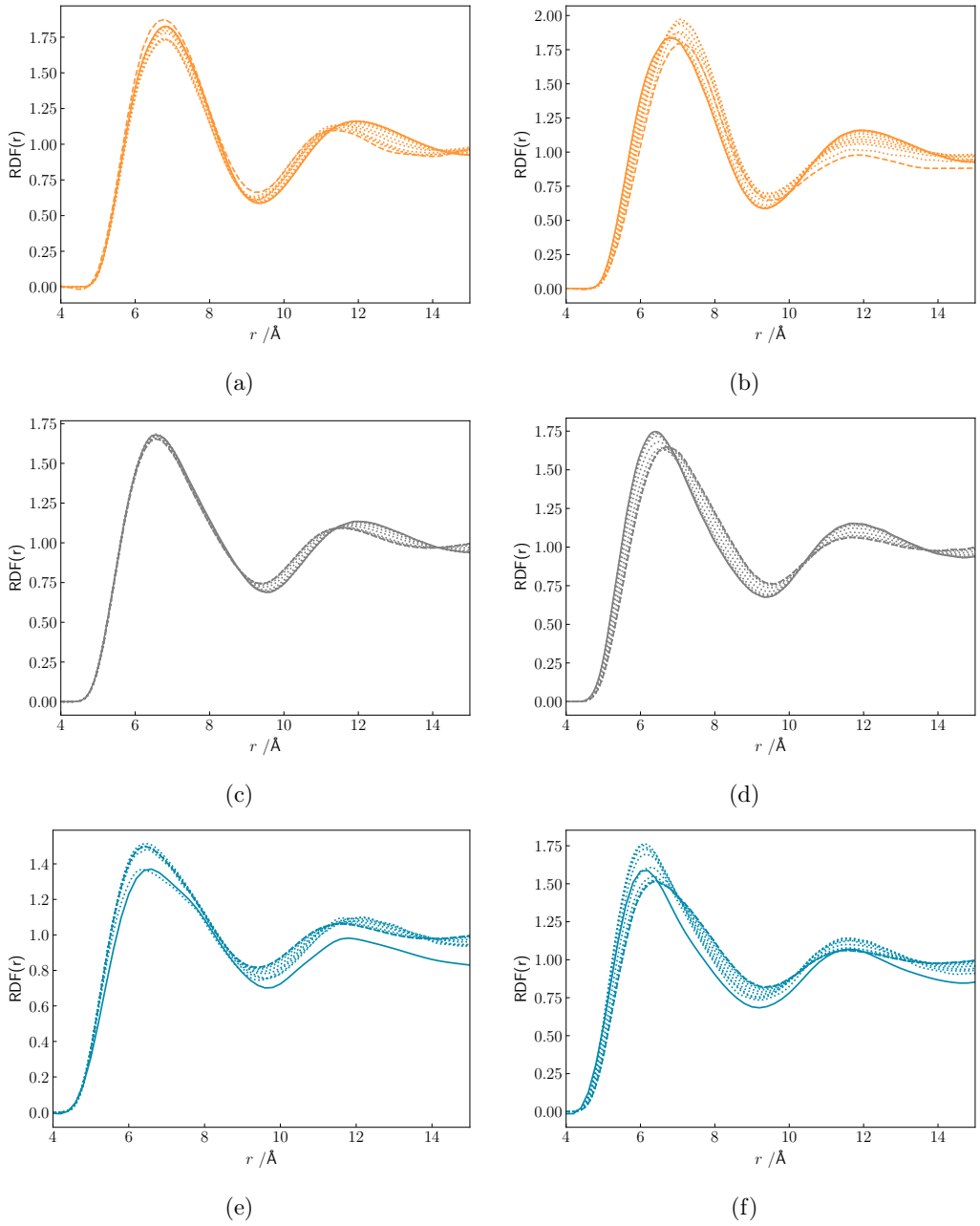

Figure S7: Radial distribution function of 2,3,4-trimethylpentane (*orange*) and 3-ethylhexane (*blue*) and their mixed species interaction (*gray*); *left*: all-atom; *right*: coarse-grained; *solid:* x_{TrMePe}=0.01; *dashed:* x_{EtHx}=0.01.

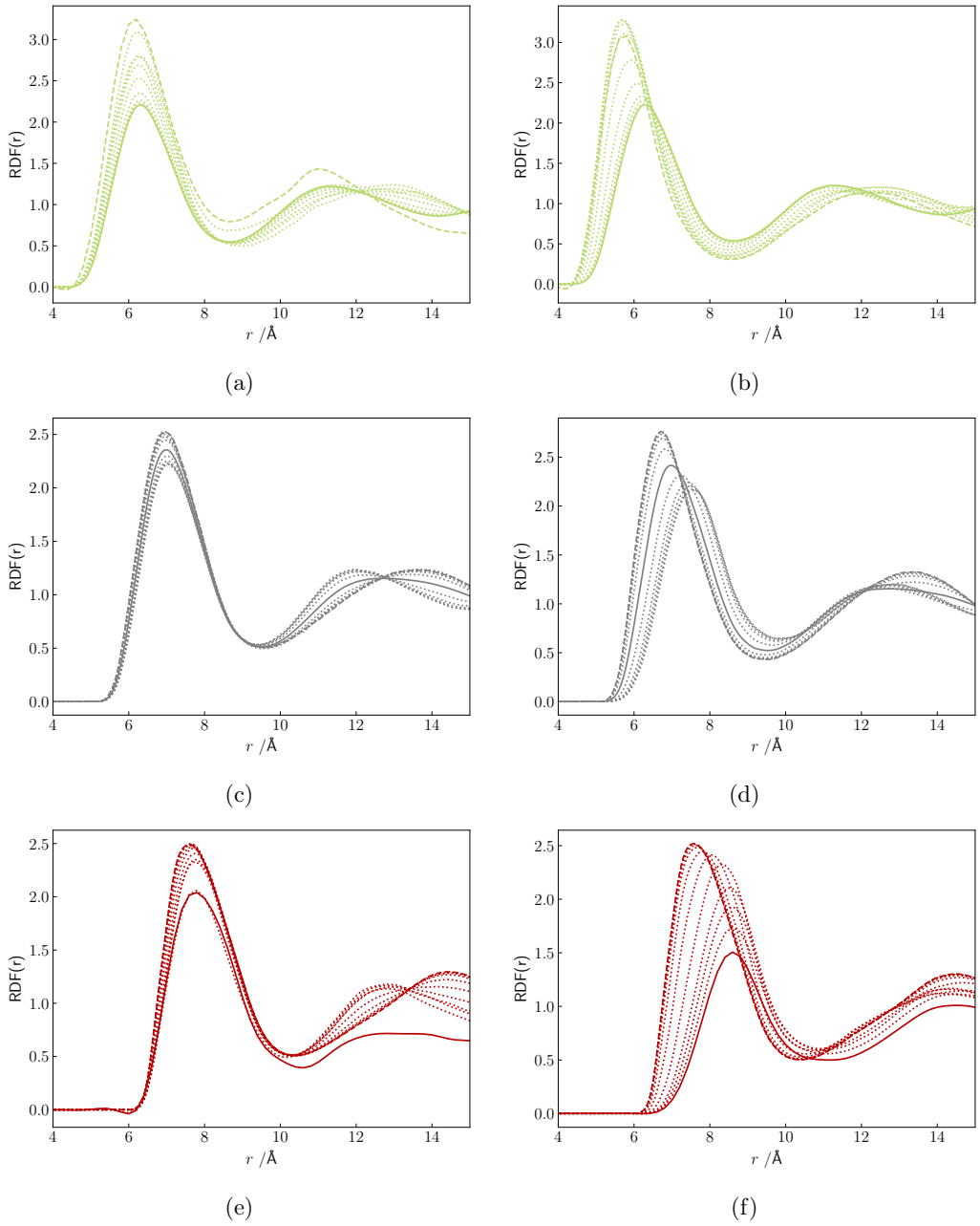

Figure S8: Radial distribution function of 2,3-dimethylbutane (*green*) and 3,3-diisopropyl-2,4-dimethylpentane (*red*) and their mixed species interaction (*gray*); *left*: all-atom; *right*: coarse-grained; *solid:* x_{DiMeBu}=0.01; *dashed:* x_{DIPDMP}=0.01.

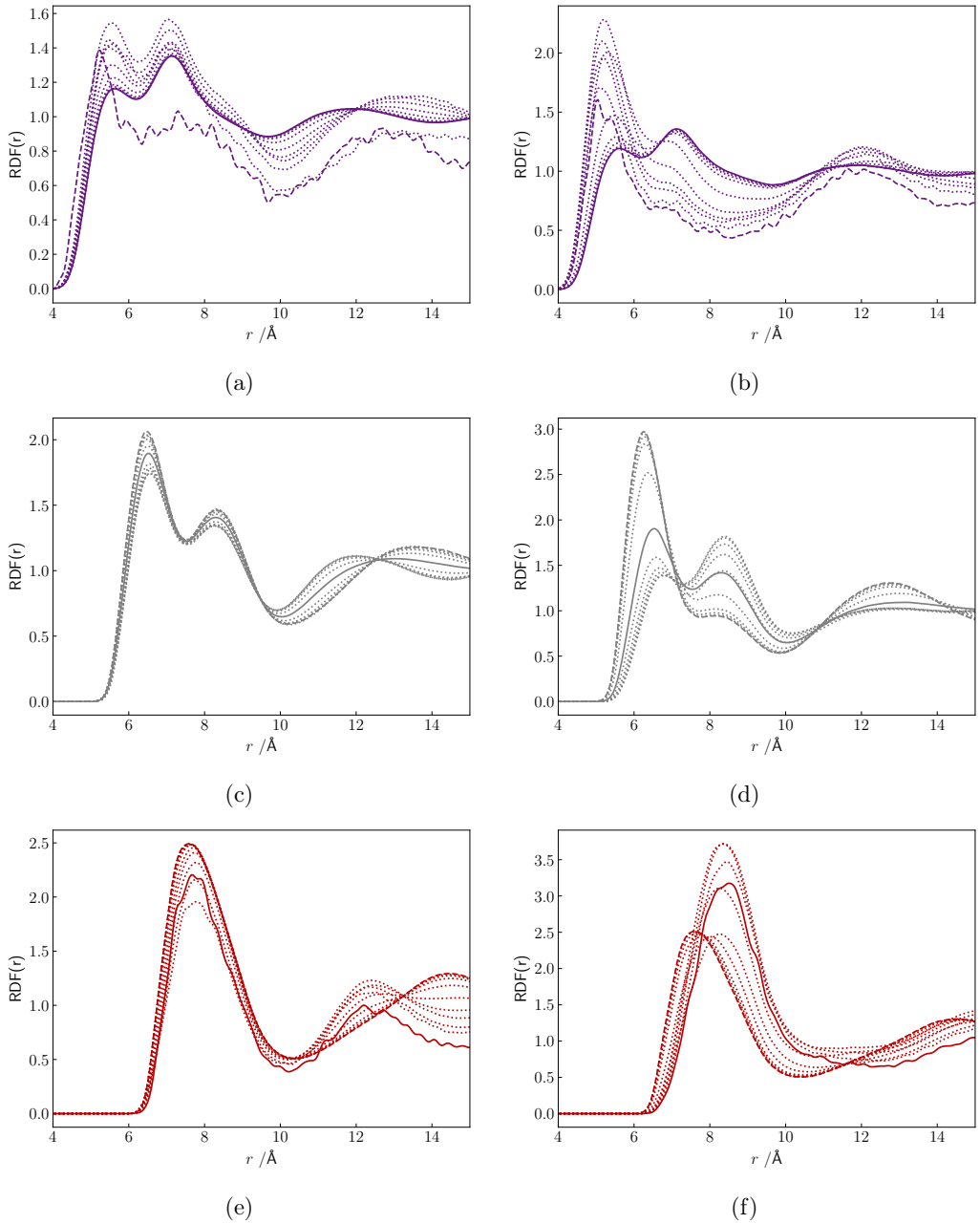

Figure S9: Radial distribution function of 2,5-dimethylhexane (*purple*) and 3,3-diisopropyl-2,4-dimethylpentane (*red*) and their mixed species interaction (*gray*); *left*: all-atom; *right*: coarse-grained; *solid:* x_{DiMeBu}=0.01; *dashed:* x_{DIPDMP}=0.01.

RDF errors

$$\delta g_{total} = \frac{x_1^2\ \delta g_{11}\ +\ x_1 x_2\ \delta g_{12} +\ x_2^2\ \delta g_{22}}{x_1^2 + x_1 x_2 + x_2^2} \tag{1}$$

$$\delta g_1 = x_1^2\ \delta g_{11}\ +\ x_1 x_2\ \delta g_{12} \tag{2}$$

$$\delta g_2 = x_2^2\ \delta g_{22}\ +\ x_1 x_2\ \delta g_{12} \tag{3}$$

Table S2: RDF errors of all simulations with IBI generated mixed potentials in %, x_1 refers to component first in the mixture name

DiMeBu-DiMeHx-mixture						
x_1	δg_{11}	δg_{22}	δg_{12}	δg_1	δg_2	δg_{total}
0.01	41.82	0.96	5.69	6.05	1.01	1.01
0.02	27.21	0.91	5.6	6.04	1.01	1.02
0.05	22.21	0.78	5.15	6.0	1.0	1.05
0.1	18.63	0.98	4.52	5.93	1.33	1.52
0.25	13.36	1.85	2.68	5.35	2.06	2.93
0.5	7.84	2.99	0.38	4.11	1.68	3.74
0.75	3.46	3.71	1.82	3.05	2.29	3.1
0.9	1.42	4.78	2.16	1.5	2.42	1.53
0.95	0.9	5.67	2.39	0.98	2.55	0.99
0.98	0.74	4.36	2.36	0.77	2.4	0.77
0.99	0.73	7.83	2.46	0.75	2.52	0.75
DiMeBu-TrMePe-mixture						
x_1	δg_{11}	δg_{22}	δg_{12}	δg_1	δg_2	δg_{total}
0.01	17.7	0.53	5.61	5.73	0.58	0.58

0.02	15.6	0.49	5.59	5.79	0.59	0.6
0.05	14.73	0.41	5.36	5.83	0.66	0.69
0.1	14.51	0.46	4.96	5.91	0.91	1.06
0.25	12.94	1.58	3.69	6.0	2.11	2.94
0.5	9.45	4.69	2.01	5.73	3.35	5.38
0.75	5.86	8.78	3.94	5.38	5.15	5.64
0.9	2.93	12.67	6.66	3.3	7.26	3.41
0.95	1.86	13.21	7.68	2.15	7.96	2.18
0.98	1.21	15.38	8.41	1.35	8.55	1.36
0.99	0.96	17.11	8.74	1.04	8.82	1.04

TrMePe-DiMeHx-mixture

x_1	δg_{11}	δg_{22}	δg_{12}	δg_1	δg_2	δg_{total}
0.01	33.57	1.0	9.48	9.72	1.08	1.09
0.02	32.69	0.99	9.08	9.55	1.15	1.16
0.05	29.26	1.03	8.6	9.64	1.41	1.48
0.1	25.89	1.55	7.48	9.33	2.14	2.4
0.25	21.25	3.76	4.86	8.96	4.03	5.36
0.5	12.27	8.47	4.33	8.3	6.4	8.35
0.75	5.62	14.75	5.52	5.59	7.83	6.3
0.9	2.22	18.31	8.71	2.87	9.67	3.04
0.95	1.1	18.58	9.89	1.54	10.33	1.59
0.98	0.62	19.41	10.57	0.82	10.75	0.83
0.99	0.58	20.06	10.81	0.68	10.9	0.68

DiMeBu-EtHx-mixture

x_1	δg_{11}	δg_{22}	δg_{12}	δg_1	δg_2	δg_{total}

0.01	8.32	0.91	5.05	5.08	0.95	0.96
0.02	22.77	0.87	4.77	5.13	0.95	0.96
0.05	13.6	0.73	4.6	5.05	0.93	0.96
0.1	13.0	0.71	4.09	4.98	1.05	1.18
0.25	10.07	1.23	2.7	4.54	1.6	2.25
0.5	6.28	2.11	0.8	3.54	1.46	3.07
0.75	3.2	3.59	1.26	2.71	1.84	2.78
0.9	1.65	3.42	2.41	1.73	2.51	1.74
0.95	1.17	4.87	2.61	1.24	2.73	1.25
0.98	0.9	10.69	2.72	0.93	2.88	0.94
0.99	0.81	5.6	2.99	0.83	3.01	0.83

EtHx-DiMeHx-mixture

x_1	δg_{11}	δg_{22}	δg_{12}	δg_1	δg_2	δg_{total}
0.01	6.08	1.01	3.31	3.34	1.03	1.03
0.02	6.44	0.99	3.42	4.64	1.04	1.07
0.05	6.61	0.98	3.07	3.25	1.08	1.09
0.1	6.66	0.99	2.67	3.06	1.16	1.22
0.25	4.62	1.71	1.91	2.58	1.76	1.98
0.5	3.21	3.17	0.51	1.86	1.84	2.29
0.75	1.7	4.85	1.44	1.63	2.29	1.88
0.9	1.13	5.99	2.34	1.25	2.71	1.3
0.95	1.03	5.74	2.79	1.12	2.94	1.13
0.98	0.99	52.2	2.97	1.03	3.96	1.05
0.99	0.98	11.02	3.09	1.0	3.17	1.0

DiMeBu-DIPDMP-mixture

x_1	δg_{11}	δg_{22}	δg_{12}	δg_1	δg_2	δg_{total}
0.01	44.13	0.74	19.04	19.29	0.92	0.93
0.02	49.12	0.6	18.14	18.76	0.95	0.97
0.05	44.48	1.17	17.81	19.15	2.0	2.11
0.1	41.17	2.44	16.42	18.89	3.83	4.24
0.25	37.8	8.07	11.03	17.73	8.81	11.04
0.5	28.55	20.04	2.55	15.55	11.29	17.05
0.75	17.38	35.65	14.72	16.71	19.95	18.17
0.9	8.36	44.85	25.92	10.12	27.81	10.5
0.95	4.78	47.63	29.94	6.04	30.82	6.15
0.98	2.4	51.43	32.1	3.0	32.48	3.02
0.99	1.6	50.23	33.02	1.91	33.19	1.92

DiMeHx-DIPDMP-mixture

x_1	δg_{11}	δg_{22}	δg_{12}	δg_1	δg_2	δg_{total}
0.01	25.86	0.86	36.14	36.03	1.22	1.22
0.02	38.95	1.47	36.21	36.26	2.16	2.18
0.05	38.15	3.87	34.5	34.68	5.4	5.49
0.1	38.61	8.02	31.73	32.42	10.39	10.7
0.25	38.28	20.68	20.78	25.15	20.71	22.06
0.5	26.64	35.71	0.66	13.65	18.18	21.0
0.75	10.12	48.62	7.79	9.54	18.0	12.54
0.9	4.63	74.79	16.69	5.83	22.5	6.59
0.95	2.57	87.14	22.02	3.55	25.27	3.77
0.98	1.28	88.87	25.52	1.77	26.79	1.8
0.99	0.98	74.26	26.29	1.23	26.77	1.24

Table S3: Total RDF error in % for all simulations with combination rule generated CG potentials with c=0.1 to 0.9, x_1 refers to component first in the mixture name

DiMeBu-DiMeHx-mixture									
x_1	0.1	0.2	0.3	0.4	0.5	0.6	0.7	0.8	0.9
0.01	1.04	0.94	0.89	0.88	0.90	0.92	0.94	0.96	1.02
0.02	1.49	1.31	1.18	1.10	1.10	1.10	1.16	1.24	1.30
0.05	3.58	2.88	2.37	1.99	1.81	1.75	1.79	1.96	2.18
0.10	7.53	6.43	5.05	4.05	3.33	2.93	2.91	3.23	3.90
0.25	20.24	18.21	14.64	11.39	8.42	6.27	6.41	8.89	11.33
0.50	28.32	28.32	23.97	18.56	13.09	8.90	10.36	15.05	19.30
0.75	19.96	18.99	15.66	12.04	8.64	6.19	6.27	8.90	11.43
0.90	7.63	7.08	5.54	4.32	3.39	2.88	2.78	3.05	3.69
0.95	3.92	3.19	2.57	2.10	1.83	1.71	1.71	1.85	2.04
0.98	1.61	1.40	1.24	1.13	1.10	1.08	1.13	1.19	1.24
0.99	1.08	0.98	0.92	0.90	0.91	0.92	0.93	0.94	1.00
DiMeBu-TrMePe-mixture									
x_1	0.1	0.2	0.3	0.4	0.5	0.6	0.7	0.8	0.9
0.01	1.34	1.23	1.11	1.06	1.05	1.02	0.99	0.98	0.97
0.02	2.04	1.80	1.57	1.44	1.38	1.34	1.31	1.27	1.23
0.05	4.17	3.49	2.85	2.46	2.26	2.14	2.06	2.05	2.04
0.10	7.89	6.50	5.20	4.16	3.69	3.40	3.34	3.45	3.63
0.25	18.29	15.20	12.08	8.98	7.12	6.19	6.33	7.75	9.77
0.50	26.35	22.17	17.83	13.34	8.72	6.85	7.43	12.27	18.18
0.75	19.56	16.44	13.27	10.05	6.97	4.77	4.89	6.57	8.94
0.90	8.98	7.59	6.25	4.90	3.64	2.63	2.40	2.57	2.87

0.95	4.85	4.17	3.50	2.86	2.25	1.76	1.55	1.57	1.62
0.98	2.36	2.11	1.86	1.61	1.39	1.20	1.09	1.06	1.05
0.99	1.52	1.41	1.27	1.16	1.06	0.96	0.89	0.89	0.89

TrMePe-DiMeHx-mixture

x_1	0.1	0.2	0.3	0.4	0.5	0.6	0.7	0.8	0.9
0.01	0.70	0.68	0.69	0.71	0.74	0.77	0.82	0.86	0.90
0.02	0.88	0.83	0.82	0.87	0.93	0.99	1.07	1.16	1.30
0.05	1.73	1.47	1.31	1.34	1.43	1.57	1.80	2.13	2.53
0.10	4.08	3.05	2.47	2.18	2.15	2.44	2.95	3.78	4.66
0.25	13.97	9.50	6.41	4.76	3.99	4.16	5.68	7.86	10.07
0.50	23.78	16.00	10.29	6.90	5.17	4.59	7.09	10.36	13.63
0.75	14.04	9.92	6.85	4.82	3.58	3.73	5.19	7.30	9.46
0.90	4.70	3.57	2.76	2.12	1.78	2.02	2.51	3.30	4.17
0.95	2.14	1.75	1.44	1.26	1.17	1.28	1.51	1.83	2.22
0.98	1.05	0.94	0.87	0.82	0.81	0.85	0.93	1.02	1.16
0.99	0.79	0.74	0.71	0.69	0.68	0.70	0.75	0.79	0.83

DiMeBu-EtHx-mixture

x_1	0.1	0.2	0.3	0.4	0.5	0.6	0.7	0.8	0.9
0.01	1.02	0.95	0.89	0.86	0.88	0.90	0.90	0.91	0.95
0.02	1.47	1.28	1.13	1.06	1.06	1.08	1.11	1.14	1.19
0.05	3.10	2.50	1.99	1.70	1.61	1.58	1.62	1.73	1.86
0.10	6.47	5.25	3.96	2.99	2.59	2.41	2.44	2.75	3.13
0.25	17.30	14.62	11.46	8.05	5.62	4.49	4.54	6.93	9.24
0.50	26.10	22.88	18.80	13.76	8.53	5.89	7.18	12.46	16.97
0.75	18.01	15.44	12.43	9.16	5.76	4.01	4.25	6.92	9.43

0.90	7.13	5.95	4.71	3.55	2.58	2.13	2.16	2.48	2.86
0.95	3.47	2.91	2.37	1.91	1.57	1.45	1.46	1.56	1.67
0.98	1.63	1.42	1.26	1.11	1.05	1.03	1.04	1.06	1.11
0.99	1.11	1.02	0.95	0.89	0.88	0.88	0.87	0.88	0.91

TrMePe-EtHx-mixture

x_1	0.1	0.2	0.3	0.4	0.5	0.6	0.7	0.8	0.9
0.01	0.63	0.61	0.61	0.63	0.66	0.69	0.73	0.77	0.82
0.02	0.71	0.70	0.69	0.72	0.78	0.86	0.95	1.05	1.19
0.05	1.20	0.97	0.88	0.96	1.05	1.25	1.56	1.87	2.23
0.10	2.60	1.86	1.38	1.27	1.44	1.80	2.40	3.10	3.85
0.25	8.12	5.60	3.57	2.20	1.98	2.69	4.19	5.83	7.44
0.50	14.36	9.90	6.83	4.37	2.82	2.67	4.80	6.98	9.20
0.75	8.91	6.66	4.78	3.25	2.49	2.80	4.02	5.47	6.96
0.90	3.41	2.67	2.06	1.66	1.45	1.58	2.03	2.64	3.33
0.95	1.66	1.38	1.19	1.09	0.99	1.06	1.28	1.55	1.89
0.98	0.91	0.86	0.81	0.76	0.73	0.77	0.81	0.90	1.02
0.99	0.73	0.70	0.67	0.65	0.64	0.64	0.67	0.70	0.74

EtHx-DiMeHx-mixture

x_1	0.1	0.2	0.3	0.4	0.5	0.6	0.7	0.8	0.9
0.01	1.10	1.13	1.17	1.20	1.25	1.30	1.35	1.43	1.53
0.02	1.25	1.32	1.41	1.55	1.75	1.94	2.13	2.37	2.58
0.05	1.68	2.02	2.50	3.02	3.56	4.12	4.68	5.27	5.84
0.10	2.60	3.50	4.54	5.58	6.64	7.66	8.74	9.81	10.86
0.25	4.61	3.85	3.18	2.66	2.43	2.38	2.55	2.82	3.22
0.50	7.36	5.97	4.70	3.70	3.11	2.92	3.01	3.65	4.70

0.75	4.86	4.00	3.24	2.57	2.10	1.98	2.06	2.27	2.65
0.90	2.37	3.31	4.35	5.39	6.46	7.48	8.57	9.64	10.70
0.95	1.54	1.90	2.37	2.90	3.44	4.00	4.57	5.15	5.73
0.98	1.19	1.26	1.35	1.50	1.69	1.89	2.08	2.31	2.52
0.99	1.08	1.12	1.16	1.19	1.23	1.28	1.34	1.41	1.52

Densities and volumes

Table S4: Densities and volumes (in $Å^3$) per molecule of all simulations with IBI generated mixed potentials

DiMeBu-DiMeHx-mixture						
x_1	ρ_{AA}	ρ_{CG}	rel. ρ error	$V_{mol,\mathrm{AA}}$	$V_{mol,\mathrm{CG}}$	rel. V_{mol} error
0.01	0.705	0.704	0.13 %	268.5	269.0	0.19 %
0.02	0.705	0.704	0.08 %	267.9	268.3	0.14 %
0.05	0.704	0.704	0.04 %	266.2	266.2	0.01 %
0.10	0.703	0.704	0.18 %	263.1	262.8	0.13 %
0.25	0.700	0.703	0.37 %	254.3	253.4	0.33 %
0.50	0.695	0.695	0.07 %	239.5	239.4	0.04 %
0.75	0.688	0.686	0.36 %	224.9	225.7	0.38 %
0.90	0.683	0.679	0.57 %	216.2	217.5	0.58 %
0.95	0.682	0.677	0.65 %	213.4	214.8	0.67 %
0.98	0.680	0.676	0.71 %	211.7	213.2	0.73 %
0.99	0.680	0.675	0.72 %	211.1	212.7	0.73 %
DiMeBu-TrMePe-mixture						
x_1	ρ_{AA}	ρ_{CG}	rel. ρ error	$V_{mol,\mathrm{AA}}$	$V_{mol,\mathrm{CG}}$	rel. V_{mol} error

0.01	0.730	0.730	0.06 %	259.3	259.2	0.04 %
0.02	0.729	0.730	0.09 %	258.9	258.7	0.07 %
0.05	0.728	0.729	0.16 %	257.3	257.0	0.14 %
0.10	0.726	0.728	0.25 %	254.8	254.2	0.24 %
0.25	0.720	0.723	0.45 %	247.4	246.4	0.43 %
0.50	0.710	0.710	0.06 %	234.4	234.3	0.05 %
0.75	0.695	0.694	0.05 %	222.8	223.0	0.07 %
0.90	0.686	0.683	0.47 %	215.4	216.4	0.49 %
0.95	0.683	0.679	0.61 %	212.9	214.3	0.62 %
0.98	0.681	0.676	0.67 %	211.6	213.0	0.69 %
0.99	0.680	0.676	0.72 %	211.0	212.6	0.74 %

TrMePe-DiMeHx-mixture

x_1	ρ_{AA}	ρ_{CG}	rel. ρ error	$V_{mol,\mathrm{AA}}$	$V_{mol,\mathrm{CG}}$	rel. V_{mol} error
0.01	0.705	0.703	0.26 %	269.0	269.9	0.32 %
0.02	0.706	0.703	0.33 %	268.8	269.9	0.39 %
0.05	0.706	0.703	0.47 %	268.5	269.9	0.52 %
0.10	0.708	0.704	0.59 %	268.0	269.7	0.65 %
0.25	0.712	0.708	0.57 %	266.3	268.0	0.61 %
0.50	0.719	0.719	0.06 %	263.9	263.8	0.03 %
0.75	0.725	0.728	0.48 %	261.7	260.5	0.45 %
0.90	0.728	0.731	0.36 %	260.6	259.7	0.34 %
0.95	0.729	0.731	0.21 %	260.2	259.7	0.20 %
0.98	0.730	0.730	0.09 %	259.9	259.8	0.07 %
0.99	0.730	0.730	0.08 %	259.9	259.8	0.07 %

DiMeBu-EtHx-mixture

x_1	ρ_{AA}	ρ_{CG}	rel. ρ error	$V_{mol,\mathrm{AA}}$	$V_{mol,\mathrm{CG}}$	rel. V_{mol} error
0.01	0.705	0.704	0.16 %	268.3	268.8	0.20 %
0.02	0.705	0.704	0.11 %	267.8	268.2	0.15 %
0.05	0.704	0.704	0.05 %	266.0	266.3	0.09 %
0.10	0.703	0.703	0.02 %	263.1	263.2	0.02 %
0.25	0.700	0.701	0.12 %	254.5	254.2	0.09 %
0.50	0.693	0.693	0.07 %	240.0	240.2	0.09 %
0.75	0.687	0.684	0.49 %	225.3	226.4	0.51 %
0.90	0.682	0.678	0.63 %	216.5	218.0	0.65 %
0.95	0.681	0.676	0.72 %	213.5	215.1	0.74 %
0.98	0.680	0.675	0.74 %	211.7	213.3	0.76 %
0.99	0.680	0.675	0.75 %	211.1	212.7	0.77 %

TrMePe-EtHx-mixture

x_1	ρ_{AA}	ρ_{CG}	rel. ρ error	$V_{mol,\mathrm{AA}}$	$V_{mol,\mathrm{CG}}$	rel. V_{mol} error
0.01	0.706	0.704	0.20 %	268.8	269.4	0.24 %
0.02	0.706	0.705	0.21 %	268.7	269.3	0.25 %
0.05	0.707	0.705	0.24 %	268.4	269.2	0.28 %
0.10	0.708	0.706	0.28 %	268.0	268.8	0.32 %
0.25	0.712	0.709	0.32 %	266.6	267.5	0.35 %
0.50	0.718	0.717	0.12 %	264.3	264.7	0.15 %
0.75	0.724	0.724	0.05 %	262.0	261.9	0.03 %
0.90	0.728	0.728	0.07 %	260.7	260.5	0.05 %
0.95	0.729	0.729	0.09 %	260.3	260.1	0.08 %
0.98	0.730	0.730	0.05 %	260.0	259.9	0.03 %
0.99	0.730	0.730	0.04 %	259.9	259.9	0.02 %

EtHx-DiMeHx-mixture

x_1	ρ_{AA}	ρ_{CG}	rel. ρ error	$V_{mol,\mathrm{AA}}$	$V_{mol,\mathrm{CG}}$	rel. V_{mol} error
0.01	0.705	0.703	0.21 %	269.1	269.8	0.27 %
0.02	0.705	0.703	0.19 %	269.1	269.8	0.25 %
0.05	0.705	0.703	0.19 %	269.1	269.8	0.25 %
0.10	0.705	0.703	0.21 %	269.1	269.8	0.26 %
0.25	0.705	0.704	0.21 %	269.1	269.8	0.26 %
0.50	0.705	0.704	0.15 %	269.1	269.6	0.20 %
0.75	0.705	0.704	0.15 %	269.0	269.5	0.20 %
0.90	0.705	0.704	0.18 %	268.9	269.5	0.22 %
0.95	0.705	0.704	0.15 %	268.9	269.4	0.19 %
0.98	0.705	0.704	0.18 %	268.9	269.5	0.22 %
0.99	0.705	0.704	0.18 %	268.9	269.5	0.22 %

Table S5: The deviation of CG densities from AA densities for all simulations with combination rule generated CG potentials with c=0.1 to 0.9

DiMeBu-DiMeHx-mixture

x_1	0.1	0.2	0.3	0.4	0.5	0.6	0.7	0.8	0.9
0.01	0.29 %	0.23 %	0.16 %	0.16 %	0.01 %	0.07 %	0.18 %	0.29 %	0.36 %
0.02	0.34 %	0.28 %	0.18 %	0.05 %	0.19 %	0.37 %	0.49 %	0.70 %	0.87 %
0.05	0.04 %	0.08 %	0.05 %	0.22 %	0.56 %	1.00 %	1.45 %	1.92 %	2.41 %
0.10	1.53 %	0.70 %	0.36 %	0.52 %	1.03 %	1.82 %	2.63 %	3.61 %	4.66 %
0.25	5.20 %	2.88 %	1.39 %	0.96 %	1.52 %	2.88 %	4.69 %	6.90 %	9.34 %
0.50	4.17 %	2.10 %	0.63 %	0.06 %	0.67 %	2.38 %	4.74 %	7.33 %	9.70 %
0.75	0.57 %	1.15 %	1.39 %	1.15 %	0.38 %	0.98 %	2.54 %	4.02 %	5.34 %

0.90	2.18 %	1.98 %	1.70 %	1.22 %	0.66 %	0.00 %	0.63 %	1.17 %	1.68 %
0.95	1.92 %	1.69 %	1.37 %	1.05 %	0.70 %	0.37 %	0.08 %	0.20 %	0.42 %
0.98	1.35 %	1.21 %	1.04 %	0.88 %	0.73 %	0.60 %	0.50 %	0.36 %	0.29 %
0.99	1.07 %	0.99 %	0.88 %	0.80 %	0.72 %	0.65 %	0.60 %	0.55 %	0.50 %

DiMeBu-TrMePe-mixture

x_1	0.1	0.2	0.3	0.4	0.5	0.6	0.7	0.8	0.9
0.01	0.01 %	0.03 %	0.06 %	0.08 %	0.10 %	0.09 %	0.12 %	0.12 %	0.15 %
0.02	0.02 %	0.06 %	0.11 %	0.16 %	0.19 %	0.21 %	0.21 %	0.25 %	0.24 %
0.05	0.12 %	0.15 %	0.21 %	0.26 %	0.34 %	0.42 %	0.48 %	0.54 %	0.62 %
0.10	0.45 %	0.41 %	0.45 %	0.51 %	0.62 %	0.78 %	0.93 %	1.09 %	1.21 %
0.25	1.88 %	1.41 %	1.12 %	1.06 %	1.19 %	1.53 %	2.11 %	2.77 %	3.52 %
0.50	2.04 %	1.38 %	0.96 %	0.77 %	0.93 %	1.59 %	2.74 %	4.39 %	6.39 %
0.75	0.26 %	0.08 %	0.03 %	0.13 %	0.49 %	1.10 %	2.07 %	3.34 %	4.84 %
0.90	1.10 %	0.97 %	0.80 %	0.57 %	0.27 %	0.08 %	0.53 %	0.99 %	1.45 %
0.95	1.14 %	1.03 %	0.88 %	0.72 %	0.52 %	0.30 %	0.10 %	0.12 %	0.31 %
0.98	0.95 %	0.87 %	0.79 %	0.73 %	0.63 %	0.54 %	0.44 %	0.38 %	0.31 %
0.99	0.90 %	0.84 %	0.80 %	0.75 %	0.69 %	0.65 %	0.62 %	0.59 %	0.54 %

TrMePe-DiMeHx-mixture

x_1	0.1	0.2	0.3	0.4	0.5	0.6	0.7	0.8	0.9
0.01	0.13 %	0.00 %	0.12 %	0.30 %	0.53 %	0.73 %	1.04 %	1.24 %	1.54 %
0.02	0.11 %	0.08 %	0.38 %	0.71 %	1.15 %	1.61 %	2.07 %	2.62 %	3.13 %
0.05	0.16 %	0.59 %	1.26 %	1.98 %	2.95 %	3.88 %	4.96 %	6.11 %	7.25 %
0.10	0.79 %	1.44 %	2.45 %	3.64 %	5.11 %	6.72 %	8.38 %	10.18 %	12.11 %
0.25	2.75 %	3.42 %	4.51 %	6.13 %	8.00 %	10.03 %	12.20 %	14.53 %	16.87 %
0.50	4.00 %	4.28 %	4.94 %	5.85 %	7.02 %	8.34 %	9.84 %	11.40 %	13.13 %

0.75	3.28 %	3.07 %	3.12 %	3.31 %	3.67 %	4.14 %	4.75 %	5.46 %	6.25 %
0.90	1.82 %	1.57 %	1.40 %	1.40 %	1.47 %	1.59 %	1.81 %	2.06 %	2.35 %
0.95	1.00 %	0.84 %	0.74 %	0.72 %	0.76 %	0.79 %	0.91 %	1.01 %	1.15 %
0.98	0.42 %	0.33 %	0.32 %	0.28 %	0.30 %	0.31 %	0.35 %	0.40 %	0.47 %
0.99	0.26 %	0.19 %	0.17 %	0.19 %	0.18 %	0.18 %	0.20 %	0.22 %	0.25 %

DiMeBu-EtHx-mixture

x_1	0.1	0.2	0.3	0.4	0.5	0.6	0.7	0.8	0.9
0.01	0.30 %	0.23 %	0.17 %	0.08 %	0.09 %	0.01 %	0.05 %	0.07 %	0.12 %
0.02	0.33 %	0.26 %	0.11 %	0.03 %	0.07 %	0.20 %	0.28 %	0.34 %	0.42 %
0.05	0.34 %	0.19 %	0.04 %	0.20 %	0.40 %	0.65 %	0.85 %	1.07 %	1.28 %
0.10	0.12 %	0.06 %	0.20 %	0.47 %	0.84 %	1.28 %	1.74 %	2.20 %	2.70 %
0.25	2.22 %	1.40 %	1.03 %	1.06 %	1.68 %	2.61 %	3.70 %	5.00 %	6.38 %
0.50	2.35 %	1.41 %	0.85 %	0.86 %	1.51 %	2.85 %	4.70 %	6.81 %	8.86 %
0.75	0.74 %	0.83 %	0.76 %	0.31 %	0.50 %	1.62 %	3.03 %	4.51 %	5.87 %
0.90	1.93 %	1.64 %	1.25 %	0.78 %	0.23 %	0.33 %	0.95 %	1.51 %	1.98 %
0.95	1.77 %	1.47 %	1.16 %	0.84 %	0.48 %	0.19 %	0.10 %	0.37 %	0.56 %
0.98	1.30 %	1.14 %	0.95 %	0.80 %	0.67 %	0.53 %	0.41 %	0.32 %	0.22 %
0.99	1.06 %	0.98 %	0.87 %	0.79 %	0.73 %	0.63 %	0.60 %	0.56 %	0.49 %

TrMePe-EtHx-mixture

x_1	0.1	0.2	0.3	0.4	0.5	0.6	0.7	0.8	0.9
0.01	0.14 %	0.08 %	0.03 %	0.12 %	0.22 %	0.36 %	0.44 %	0.56 %	0.67 %
0.02	0.08 %	0.06 %	0.23 %	0.42 %	0.61 %	0.82 %	1.05 %	1.26 %	1.50 %
0.05	0.08 %	0.44 %	0.86 %	1.24 %	1.74 %	2.17 %	2.63 %	3.14 %	3.69 %
0.10	0.37 %	1.01 %	1.70 %	2.41 %	3.19 %	4.00 %	4.84 %	5.69 %	6.54 %
0.25	1.26 %	2.32 %	3.49 %	4.71 %	5.92 %	7.18 %	8.39 %	9.62 %	10.84 %

0.50	2.10 %	3.16 %	4.20 %	5.26 %	6.31 %	7.34 %	8.38 %	9.41 %	10.45 %
0.75	1.84 %	2.33 %	2.81 %	3.30 %	3.83 %	4.40 %	4.94 %	5.54 %	6.11 %
0.90	0.99 %	1.10 %	1.28 %	1.46 %	1.67 %	1.89 %	2.11 %	2.37 %	2.66 %
0.95	0.57 %	0.63 %	0.70 %	0.80 %	0.88 %	0.99 %	1.12 %	1.25 %	1.39 %
0.98	0.23 %	0.28 %	0.30 %	0.32 %	0.36 %	0.43 %	0.45 %	0.50 %	0.59 %
0.99	0.14 %	0.15 %	0.17 %	0.18 %	0.21 %	0.21 %	0.25 %	0.28 %	0.31 %

EtHx-DiMeHx-mixture

x_1	0.1	0.2	0.3	0.4	0.5	0.6	0.7	0.8	0.9
0.01	0.13 %	0.27 %	0.47 %	0.69 %	0.88 %	1.15 %	1.38 %	1.57 %	1.83 %
0.02	0.40 %	0.77 %	1.12 %	1.54 %	1.97 %	2.37 %	2.81 %	3.25 %	3.69 %
0.05	1.12 %	1.99 %	2.87 %	3.75 %	4.71 %	5.69 %	6.64 %	7.62 %	8.63 %
0.10	2.14 %	3.65 %	5.14 %	6.71 %	8.30 %	9.90 %	11.42 %	13.08 %	14.72 %
0.25	0.79 %	0.94 %	0.96 %	0.90 %	0.71 %	0.44 %	0.08 %	0.36 %	0.86 %
0.50	0.43 %	0.74 %	0.89 %	0.92 %	0.80 %	0.58 %	0.27 %	0.14 %	0.62 %
0.75	0.11 %	0.37 %	0.52 %	0.63 %	0.61 %	0.55 %	0.42 %	0.24 %	0.02 %
0.90	0.60 %	1.37 %	2.18 %	2.99 %	3.85 %	4.74 %	5.65 %	6.61 %	7.54 %
0.95	0.21 %	0.59 %	1.02 %	1.50 %	1.96 %	2.45 %	2.95 %	3.47 %	4.00 %
0.98	0.03 %	0.15 %	0.31 %	0.51 %	0.70 %	0.92 %	1.11 %	1.34 %	1.55 %
0.99	0.12 %	0.01 %	0.10 %	0.18 %	0.28 %	0.36 %	0.47 %	0.60 %	0.71 %

Dynamics

Maxwell-Stefan-Diffusion Coefficient in MD Simulations

In the Maxwell-Stefan formalism, the driving force for diffusion is the chemical potential gradient which is balanced by friction forces expressed as the inversion friction coefficient or

MS-diffusion coefficient D_{ij}^{MS}

$$-\frac{1}{RT} \bigtriangledown \mu_i \;=\; \sum_{j=1, j\neq i}^{n} \frac{x_j(\nu_i - \nu_j)}{D_{ij}^{MS}} \tag{4}$$

with the difference between the average velocities $(\nu_i - \nu_j)$.

Onsager relations between diffusive Fluxes J_i and the gradients of the chemical potentials μ_j [5] are given by

$$J_i \;=\; -\sum_{j=1}^{n} \Lambda_{ij} \bigtriangledown \mu_j \tag{5}$$

with the Onsager coefficients Λ_{ij}. For a binary mixture, the Maxwell-Stefan diffusion coefficient can be expressed from the three Onsager coefficients.[6,7]

$$D_{12}^{MS} \;=\; \frac{x_2}{x_1}\Lambda_{11} \;+\; \frac{x_1}{x_2}\Lambda_{22} \;-\; 2\Lambda_{12} \tag{6}$$

To calculate the Onsager coefficients the temporally correlated net velocity or collective displacements of all individual molecules are analyzed.[8,9]

$$\Lambda_{ij} \;=\; \lim_{t\to\infty} \frac{1}{6Nt} \left\langle \left(\sum_{k=1}^{N_i} (r_{k,i}(t) - r_{k,i}(0)) \right) \times \left(\sum_{l=1}^{N_j} (r_{l,j}(t) - r_{l,j}(0)) \right) \right\rangle \tag{7}$$

using COM instead yields Eq. 8 or for $i = j$ Eq. 9

$$\Lambda_{ij} \;=\; \lim_{t\to\infty} \frac{x_i x_j N}{6t} \left\langle (r_i^{com}(t) - r_i^{com}(0)) \times \left(r_j^{com}(t) - r_j^{com}(0) \right) \right\rangle \tag{8}$$

$$\Lambda_{ii} \;=\; \lim_{t\to\infty} \frac{x_i^2 N}{6t} \left\langle (\Delta r_i^{com})^2 \right\rangle \tag{9}$$

The Onsager coefficients are symmetric ($\Lambda_{ij} \;=\; \Lambda_{ji}$) and they are defined in a reference frame, where the velocities of the center of mass is zero ($\sum_{i=1}^{n} \omega_i \nu_i = 0$) and all mass fluxes sum to zero. This leads to the constrain $\sum_{i=1}^{n} M_i \Lambda_{ij} = 0$.[6,10,11]

For a binary system this results in

$$0 = M_1\Lambda_{12} + M_2\Lambda_{22} \qquad \rightarrow \qquad \Lambda_{12} = -\frac{M_2}{M_1}\Lambda_{22} \tag{10}$$

$$0 = M_1\Lambda_{11} + M_2\Lambda_{21} \qquad \rightarrow \qquad \Lambda_{21} = -\frac{M_1}{M_2}\Lambda_{11} \tag{11}$$

$$\text{with} \qquad \Lambda_{ij} = \Lambda_{ji} \qquad \rightarrow \qquad \Lambda_{22} = \left(\frac{M_1}{M_2}\right)^2 \Lambda_{11} \tag{12}$$

The combination of 10 and 12 with equation 6

$$\begin{aligned} D_{12}^{MS} = \frac{x_2}{x_2}\Lambda_{11} + \frac{x_1}{x_2}\frac{M_1^2}{M_2^2}\Lambda_{11} + 2\frac{M_1}{M_2}\Lambda_{11} &= \Lambda_{11}\left(\frac{x_2^2M_2^2 + x_1^2M_1^2 + 2x_1x_2M_1M_2}{x_1x_2M_2^2}\right) \\ &= \Lambda_{11}\frac{(x_1M_1 + x_2M_2)^2}{x_1x_2M_2^2} \end{aligned} \tag{13}$$

Replacing Λ_{11} with Eq. 9 yields the Equation for D_{12} as used within this work and shown in Ref.[12]

$$\begin{aligned} D_{12} &= \lim_{t\to\infty}\frac{1}{6t}x_1^2N\frac{(x_1M_1 + x_2M_2)^2}{x_1x_2M_2^2} \\ &= \lim_{t\to\infty}\frac{1}{6t}x_1x_2N(x_1M_1)^2\frac{(x_1M_1 + x_2M_2)^2}{(x_1x_2M_1M_2)^2} \\ &= \lim_{t\to\infty}\frac{1}{6t}\left(\frac{1}{x_1M_1} + \frac{1}{x_2M_2}\right)^2(x_1M_1)^2N\ x_1x_2 \end{aligned} \tag{14}$$

While the MS diffusion coefficient is easily accessible via simulations, experimentally, usually Fick diffusion coefficients are measured. They are related via a thermodynamic factor Γ which can be obtained form experiments and simulations.[13]

$$D^{Fick} = \Gamma D^{MS} \tag{15}$$

Acceleration factor and self diffusion coefficients

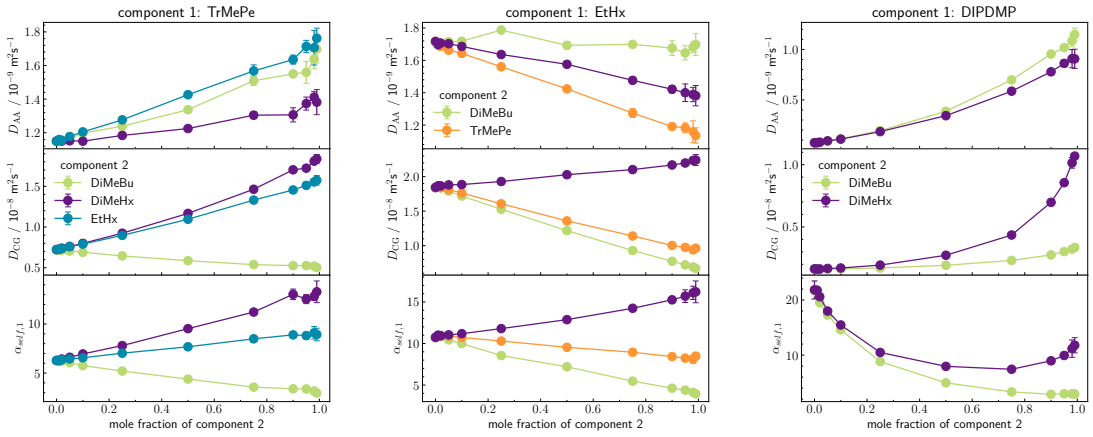

(a) (b) (c)

Figure S10: Self diffusion coefficients and acceleration factor of (a) 2,3,4-trimethylpentane (b) 3-ethylhexane and (c) 3,3-diisopropyl-2,4-dimethylpentane in binary mixtures against the mole fraction of the second component; second component according to color: *green:* DiMeBu, *orange:* TrMePe,*blue:* EtHx,*purple:* DiMeHx. The error bars of diffusion coefficients are standard deviations between the three individual cartesian components.

Relation between coarse-grained potential, structure and mobility

This section analyzes the effect of different mixed-bead coarse-grained potentials on the CG dynamics and thereby on the usage within the RoughMob framework. The dynamics are characterized by the diffusion coefficients D_{CG}. The structure is characterized by the molecular volume of the CG simulations $V_{mol,\mathrm{CG}}$ and RDF. As quantities to characterize the mixed potentials we use the "mixed hard sphere radius" and both the value and the position of the minimal potential ε_{mix}. The "mixed hard sphere radius" r_{mix} is calculated similar to the CG bead radius as half the value where the CG potential first reaches zero. The minimal potential is taken as positive value, so that a large value means a deeper potential. Since these three characteristics strongly simplify the classification of the CG potentials and their influences on the dynamics is always an interaction of all characteristic, they allow an easy comparison of the CG potentials. The RoughMob method was developed using IBI

for coarse-graining, which ensures matching RDFs for the pure components. Using IBI with a pressure correction additionally ensures matching densities. Furthermore, by definition, V_{out} can only be calculated for systems that have the same density in both the AA and the CG representation. These requirements are met for all CG simulation with IBI generated mixed potentials of Mixture Group A (i.e. *not* containing DIPDMP). We thus use the CG simulations of Mixture Group A with the IBI generated mixed potentials as reference points that represent the CG simulations working within the RoughMob framework. All quantities that are calculated from the simulations with IBI generated potentials are named with IBI as subscript, e.g. $D_{\mathrm{CG,IBI}}$ and $\varepsilon_{mix,IBI}$.

The quality of the dynamics for CG simulations with potentials generated from mixing rules is characterized as the *ratio* of the diffusion coefficients $D_{\mathrm{CG}}/D_{\mathrm{CG,IBI}}$. We investigate first whether there is a correlation between the error in dynamics of the mixing rule based potential and their errors in structural quantities. The quality of the description of structure is characterized by the (absolute) deviation of the molecular volume $\delta V_{mol} = V_{mol,\mathrm{CG}} - V_{mol,\mathrm{CG,IBI}}$ (as the RoughMob method generally relies on volumes) and by the total error of the RDF (Eq. 1) with the RDF from the IBI-CG simulation as reference. For NVT simulations, additionally, the absolute deviation of the pressure from 1 bar is calculated. The plots of the quality of the dynamics against the different structural errors are shown in Figure S11. As to expect, the diffusion coefficient is correlated to the molecular volume (Fig. S11 (a)). A lower molecular volume (negative value of δV_{mol}) decreases the diffusion coefficient, as the molecules are closer to each other in the system. While for smaller absolute values of δV_{mol}, between a range of around -3 and 12 Å^3, there are many simulations with a diffusion coefficient ratio between 0.9 and 1.1, for a larger deviation with -20 [3] or more, the ratio of diffusion coefficients is always below 0.9. Figure S11 (c) shows that a high error of the RDF does not necessarily increase the deviation from $D_{\mathrm{CG,IBI}}$. The size of the markers indicated the error of the molecular volume. There is a clear regime with values of δg_{total} of up to 25 where the ratio of diffusion coefficients remains between around 0.9 and 1.1. The

diffusion coefficients that strongly correlate with the error of RDF generally have a high error of the molecular volume. Using NVT simulations (Fig. S11 (b) and (d)) overall improves the average deviation from $D_{\mathrm{CG,IBI}}$, while for individual cases the deviation can worsen. The error of the pressure is indicated by the size of the markers. The relative deviation of the diffusion coefficients still reaches values up to -45 % (ratio of diffusion coefficients of 0.55) and using NVT conditions might worsen other properties of the simulation such as the pressure as shown in Fig. S11 (b). While a high difference in the density or molecular volume always results in a large dynamical deviation, larger deviations in the RDF or a high error of the pressure can still result in a reasonable representation of the dynamics as it is the case for DiMeBu-TrMePe mixtures (green-orange markers). We note an overall tendency of the diffusion coefficient falling below the IBI reference.

The influence of the value and position difference of ε on the dynamics is shown in Fig. S12. A shallower potential (when compared to the IBI generated potential; negative value of $\varepsilon_{mix} - \varepsilon_{mix,\mathrm{IBI}}$) can result in both faster and slower dynamics, while a deeper potential (positive value of $\varepsilon_{mix} - \varepsilon_{mix,\mathrm{IBI}}$) in all cases slowed down the dynamics. However, potential depths close to $\varepsilon_{mix,\mathrm{IBI}}$ can already have large deviations in the dynamics.

Small differences in both the position of ε_{mix} (Fig. S12 (b)) and in the mixed hard sphere radii r_{mix} (Fig. S13) show only small deviations from $D_{\mathrm{CG,IBI}}$.

The plot of the dynamical deviation against the difference between the mixed hard sphere radius r_{mix} from the combination-rule-generated potentials and from the IBI-generated potential $r_{mix,\mathrm{IBI}}$ shows that the smallest deviation from $D_{\mathrm{CG,IBI}}$ is reached when r_{mix} is close to or little larger than $r_{mix,\mathrm{IBI}}$. However, ideally one does not want to actually perform IBI in order to calculate $r_{mix,\mathrm{IBI}}$ as a reference to check other potentials against. The all-atom force-field used for the simulations uses geometric combination rules to calculate the non-bonded interactions between particles of different types. Similarly, the "ideal" mixed hard sphere radius can be estimated using geometric combination rules. As can be seen in Table S6, $r_{mix,\mathrm{IBI}}$ and r_{12} are close to each other.

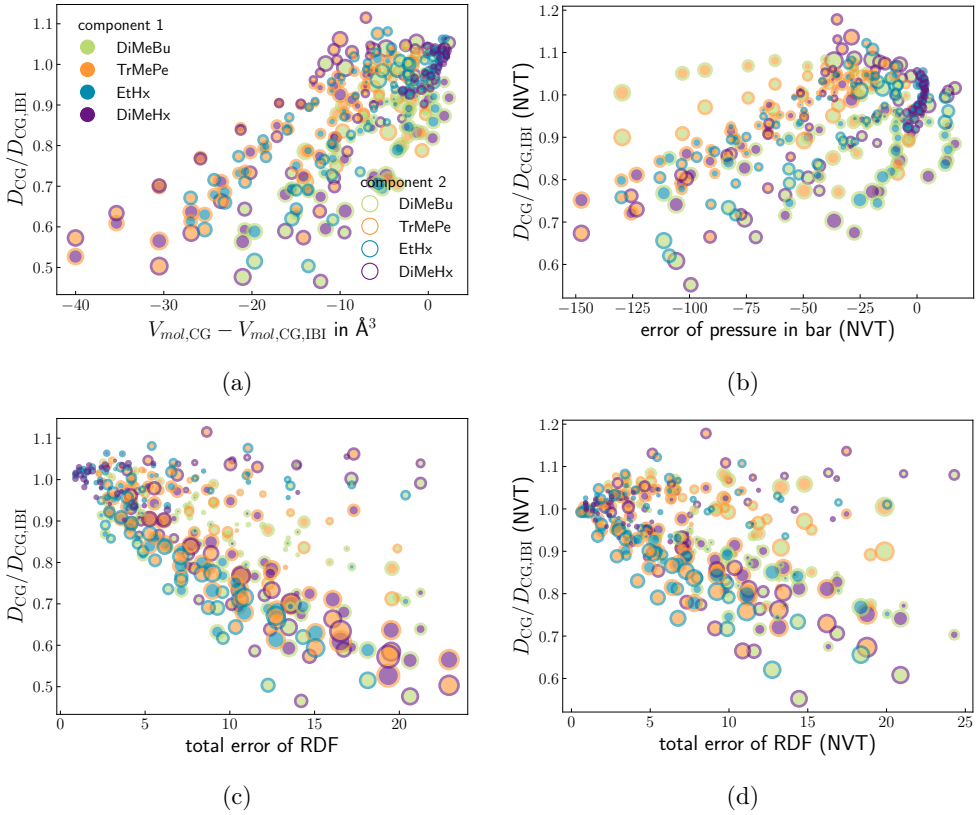

Figure S11: Ratio between coarse-grained self-diffusion coefficient determined with combination rule generated CG potentials from diffusion coefficient of simulation with the IBI generated mixed potential plotted against the error of the molecular volume (a) the radial distribution function (b) and (c) the latter using NVT simulations (otherwise NpT); size (area) of markers indicates error of radial distribution function (a) molecular volume (b) and pressure (c).

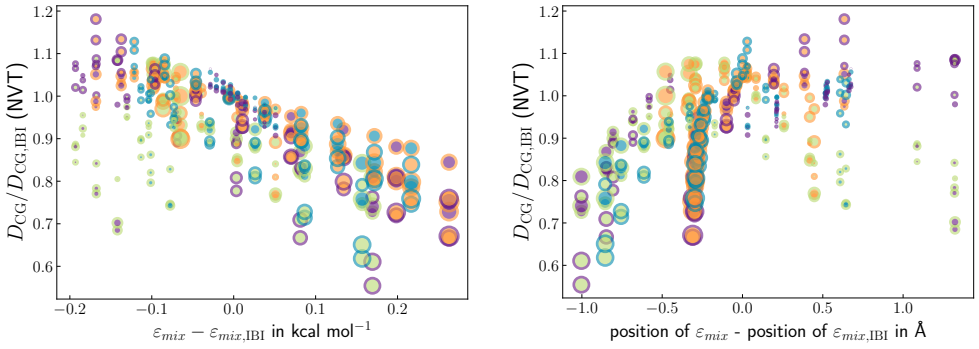

(a) (b)

Figure S12: Deviation of self-diffusion coefficients from $D_{CG,\mathrm{IBI}}$ as determined with the IBI generated mixed potential plotted against the difference between the value (a) and the position (b) of the minimal potential; *green:* 2,3-dimethylbutane; *orange:* 2,3,4-trimethylpentane; *blue:* 3-ethylhexane and *purple:* 2,5-dimethylhexane; size (area) of markers indicates error of pressure.

If both the error of the RDF and of V_{mol} (or the pressure) are small, as it is the case for the simulations with IBI generated mixed potentials, the determination of $\alpha_{self,1}$ and $\alpha_{self,2}$ works well within the RoughMob method. While a larger error of V_{mol} always impedes the applicability of the method, simulations with a larger δg_1 and δg_{total} may still yield good dynamical results. The simple comparison of different CG potentials via their mixed hard sphere radius appears to be an easy tool to gauge the predictive capability of the potential. Choosing only CG potentials with mixed hard sphere radii that are close to or little larger than an "ideal" radius should allow for the determination of reasonable CG dynamics despite some deviations in the pressure and RDFs. Such a consistent size logic between the AA and the CG simulation fits well to the geometrical approach of the RoughMob method.

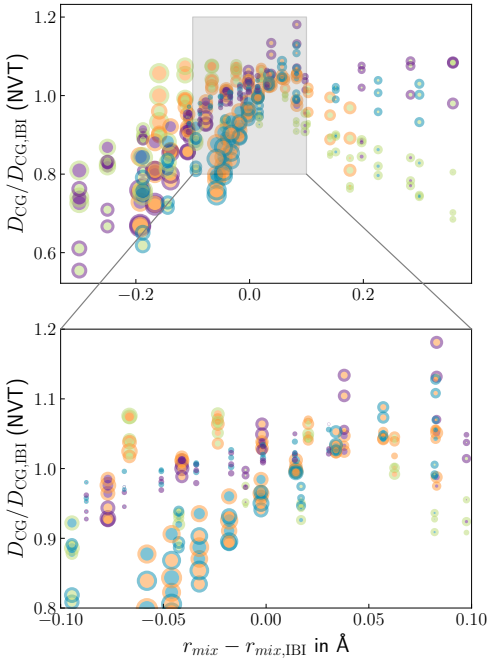

Figure S13: Deviation of self-diffusion coefficients from $D_{CG,\mathrm{IBI}}$ as determined with the IBI generated mixed potential plotted against the difference between the mixed hard sphere radii; *green:* 2,3-dimethylbutane; *orange:* 2,3,4-trimethylpentane; *blue:* 3-ethylhexane and *purple:* 2,5-dimethylhexane; size (area) of markers indicates error of pressure.

Table S6: Mixed hard sphere radius and minimal potential as calculated from the IBI generated potentials $r_{mix,\mathrm{IBI}}$ and $\varepsilon_{mix,\mathrm{IBI}}$ and as ideal radius from geometric combination rules of the potentials of pure components r_{12} and ε_{12} in Å and kcal mol^{-1}.

	$r_{mix,\mathrm{IBI}}$	r_{12}	$\varepsilon_{mix,\mathrm{IBI}}$	ε_{12}
DiMeBu-TrMePe	2.98	2.97	0.85	0.88
DiMeBu-EtHx	3.00	3.06	0.58	0.66
DiMeBu-DiMeHx	3.11	3.13	0.55	0.59
TrMePe-EtHx	3.26	3.28	0.69	0.71
TrMePe-DiMeHx	3.40	3.36	0.62	0.64
EtHx-DiMeHx	3.49	3.45	0.46	0.48
DiMeBu-DIPDMP	3.20	3.10	1.43	1.48
DiMeHx-DIPDMP	3.39	3.50	1.29	1.07

Mixture Group B generally suffered from poorer matching of the RDFs. However, for DiMeBu-DIPDMP, the molecular volumes show a very good agreement and $r_{mix,\mathrm{IBI}}$ is little higher than r_{12}. This constellation should therefore yield a good results within the RoughMob

framework. A deeper potential, as for DiMeHx-DIPDMP, when $\varepsilon_{mix,\mathrm{IBI}}$ is compared to ε_{12} will likely result in a lower (negative) pressure for NVT simulations and might decreases the dynamics. The total error of RDF exceeds 10 % for $x_{DiMeHx} = 0.1$, 0.25, 0.5 and 0.75 to a maximum of 22 %. Paired with an $r_{mix,\mathrm{IBI}}$ that is lower than r_{12} by 0.11 Å, this means that the CG diffusion coefficients of those compositions may be lowered by up to 30 %. This is, however, a pessimistic approximation. Using the same functions for Group A and B with no need to adjust for a lower pressure worked fine for the given mixtures as shown in the paper.

Error of prediction of acceleration factors

Table S7: Absolute and relative (in percent and brackets) error of prediction for acceleration factors of both self-diffusion coefficients, the binary diffusion coefficient and the overall averaged system acceleration ($\alpha_{mix,pred}$)

DiMeBu-DiMeHx-mixture				
x_1	comp 1	comp 2	overall	binary
0.01	0.7 (6.31)	-1.81 (-10.37)	-1.78 (-10.28)	-0.37 (-3.12)
0.02	0.1 (0.91)	-1.53 (-8.99)	-1.51 (-8.91)	-0.12 (-1.01)
0.05	-0.1 (-0.89)	-1.48 (-8.85)	-1.42 (-8.66)	-0.08 (-0.67)
0.1	0.13 (1.27)	-1.12 (-7.08)	-0.98 (-6.44)	-0.19 (-1.68)
0.25	0.0 (0.02)	-0.12 (-0.9)	0.1 (0.8)	0.51 (5.15)
0.5	-0.06 (-0.95)	0.51 (5.07)	0.9 (11.31)	-0.24 (-2.66)
0.75	-0.1 (-2.26)	0.4 (5.7)	0.88 (17.67)	-0.03 (-0.43)
0.9	0.15 (4.47)	-0.11 (-2.09)	0.66 (18.5)	-0.09 (-1.59)
0.95	0.24 (7.86)	-0.3 (-6.08)	0.52 (16.37)	0.17 (3.57)
0.98	0.3 (10.14)	-0.68 (-13.96)	0.41 (13.83)	-0.08 (-1.83)
0.99	0.35 (12.09)	-0.75 (-15.55)	0.4 (14.01)	-0.25 (-5.29)

DiMeBu-TrMePe-mixture

x_1	comp 1	comp 2	overall	binary
0.01	-0.42 (-7.39)	1.63 (26.21)	1.65 (26.44)	0.97 (19.79)
0.02	-0.08 (-1.43)	1.54 (24.87)	1.58 (25.49)	0.48 (9.0)
0.05	0.1 (2.02)	1.35 (22.29)	1.44 (24.06)	0.45 (8.78)
0.1	-0.06 (-1.25)	1.11 (19.35)	1.27 (22.34)	0.34 (6.74)
0.25	-0.03 (-0.69)	0.26 (5.0)	0.63 (12.61)	-0.23 (-4.95)
0.5	-0.12 (-3.1)	-0.55 (-12.45)	-0.03 (-0.73)	-0.39 (-9.91)
0.75	0.02 (0.55)	-0.35 (-9.92)	-0.06 (-1.98)	0.04 (1.22)
0.9	0.15 (5.01)	-0.03 (-0.76)	0.08 (2.59)	0.43 (13.17)
0.95	0.26 (9.05)	0.14 (4.04)	0.22 (7.46)	0.54 (16.03)
0.98	0.31 (11.04)	0.45 (14.33)	0.3 (10.47)	1.07 (35.22)
0.99	0.33 (11.59)	0.71 (23.86)	0.32 (11.37)	1.1 (35.73)

TrMePe-DiMeHx-mixture

x_1	comp 1	comp 2	overall	binary
0.01	0.39 (2.92)	-1.61 (-9.32)	-1.69 (-9.76)	0.18 (1.31)
0.02	0.73 (5.73)	-1.68 (-9.66)	-1.81 (-10.47)	0.02 (0.16)
0.05	0.63 (5.04)	-1.53 (-8.9)	-1.83 (-10.8)	0.8 (6.08)
0.1	-0.45 (-3.47)	-1.34 (-7.88)	-1.97 (-11.93)	-0.07 (-0.5)
0.25	-0.24 (-2.13)	-0.33 (-2.09)	-1.36 (-9.44)	-0.19 (-1.3)
0.5	-0.52 (-5.44)	0.81 (6.21)	-0.34 (-3.04)	-0.49 (-3.41)
0.75	0.17 (2.23)	0.46 (4.12)	0.63 (7.4)	0.41 (3.44)
0.9	0.9 (12.91)	-0.22 (-2.21)	1.19 (16.5)	0.29 (2.77)
0.95	1.28 (19.35)	-0.37 (-4.0)	1.45 (21.51)	0.32 (3.3)
0.98	1.51 (23.47)	-0.91 (-9.61)	1.58 (24.32)	0.11 (1.16)

0.99	1.67 (26.52)	-0.66 (-7.35)	1.7 (26.99)	-0.16 (-1.7)

DiMeBu-EtHx-mixture

x_1	comp 1	comp 2	overall	binary
0.01	-0.26 (-3.14)	-0.51 (-4.67)	-0.51 (-4.75)	-0.44 (-5.21)
0.02	0.09 (1.13)	-0.54 (-5.03)	-0.55 (-5.09)	0.08 (1.07)
0.05	-0.08 (-1.01)	-0.36 (-3.41)	-0.38 (-3.71)	-0.22 (-2.77)
0.1	-0.02 (-0.23)	-0.25 (-2.48)	-0.29 (-2.94)	0.23 (3.08)
0.25	0.25 (4.06)	0.21 (2.42)	0.17 (2.16)	0.05 (0.72)
0.5	-0.21 (-4.13)	-0.06 (-0.87)	-0.03 (-0.47)	-0.09 (-1.4)
0.75	-0.07 (-1.7)	0.08 (1.48)	0.19 (4.59)	0.06 (1.2)
0.9	0.14 (4.48)	0.01 (0.3)	0.28 (8.57)	-0.11 (-2.37)
0.95	0.23 (7.55)	-0.05 (-1.2)	0.3 (9.89)	0.07 (1.62)
0.98	0.31 (10.55)	0.04 (1.08)	0.34 (11.63)	0.12 (2.95)
0.99	0.33 (11.48)	0.15 (3.79)	0.35 (12.07)	-0.05 (-1.11)

TrMePe-EtHx-mixture

x_1	comp 1	comp 2	overall	binary
0.01	0.54 (6.09)	-0.48 (-4.39)	-0.53 (-4.86)	0.4 (4.33)
0.02	0.3 (3.27)	-0.5 (-4.58)	-0.6 (-5.55)	0.53 (5.79)
0.05	0.37 (4.2)	-0.49 (-4.5)	-0.72 (-6.69)	0.57 (6.33)
0.1	-0.04 (-0.44)	-0.34 (-3.17)	-0.8 (-7.56)	0.13 (1.32)
0.25	-0.46 (-5.47)	-0.04 (-0.43)	-0.92 (-9.39)	-0.5 (-4.9)
0.5	-0.46 (-6.02)	0.23 (2.43)	-0.59 (-6.91)	0.07 (0.77)
0.75	0.15 (2.2)	0.05 (0.61)	0.2 (2.67)	0.01 (0.13)
0.9	1.0 (15.21)	-0.03 (-0.35)	1.05 (15.67)	0.22 (2.49)
0.95	1.31 (20.33)	-0.07 (-0.88)	1.35 (20.64)	0.25 (2.9)

0.98	1.52 (23.82)	-0.08 (-0.99)	1.53 (23.97)	0.99 (12.86)
0.99	1.66 (26.42)	-0.5 (-5.85)	1.66 (26.42)	0.76 (9.63)

EtHx-DiMeHx-mixture

x_1	comp 1	comp 2	overall	binary
0.01	-0.42 (-2.61)	-1.78 (-10.16)	-1.82 (-10.43)	-0.15 (-0.98)
0.02	-0.36 (-2.25)	-1.76 (-10.05)	-1.85 (-10.57)	-0.73 (-4.72)
0.05	-0.14 (-0.88)	-1.51 (-8.77)	-1.72 (-10.0)	-0.61 (-3.9)
0.1	0.01 (0.06)	-1.18 (-6.95)	-1.55 (-9.25)	-0.22 (-1.42)
0.25	0.17 (1.17)	-0.17 (-1.05)	-0.95 (-6.17)	-0.33 (-2.11)
0.5	0.14 (1.12)	0.75 (5.26)	-0.36 (-2.65)	0.95 (6.91)
0.75	-0.11 (-0.91)	0.16 (1.18)	-0.36 (-2.94)	-0.34 (-2.5)
0.9	-0.26 (-2.36)	-0.03 (-0.27)	-0.31 (-2.78)	-0.29 (-2.34)
0.95	-0.37 (-3.38)	-0.28 (-2.28)	-0.39 (-3.54)	-0.77 (-6.19)
0.98	-0.42 (-3.81)	-0.09 (-0.78)	-0.42 (-3.81)	-0.95 (-7.74)
0.99	-0.54 (-4.91)	-0.83 (-6.71)	-0.55 (-4.95)	-0.64 (-5.38)

DiMeBu-DIPDMP-mixture

x_1	comp 1	comp 2	overall	binary
0.01	-3.58 (-21.73)	-1.26 (-5.89)	-0.99 (-4.67)	-1.68 (-11.85)
0.02	-1.23 (-8.84)	-0.1 (-0.53)	0.41 (2.14)	-1.96 (-13.73)
0.05	-0.72 (-5.64)	0.22 (1.29)	1.26 (7.39)	0.45 (3.96)
0.1	0.2 (1.84)	0.31 (2.13)	1.78 (12.59)	-0.76 (-6.64)
0.25	1.07 (15.71)	0.79 (9.01)	1.66 (20.07)	0.99 (14.53)
0.5	-0.02 (-0.52)	-0.02 (-0.36)	-1.08 (-23.72)	-0.2 (-4.65)
0.75	-0.66 (-21.91)	-0.87 (-26.34)	-1.8 (-58.79)	-0.75 (-23.09)
0.9	-0.21 (-8.0)	-1.46 (-50.47)	-0.77 (-28.57)	0.28 (9.3)
0.95	0.02 (0.61)	-1.83 (-61.44)	-0.27 (-9.96)	0.93 (29.78)

0.98	0.22 (8.08)	-1.98 (-66.74)	0.11 (3.84)	1.87 (66.36)
0.99	0.33 (12.17)	-1.99 (-68.06)	0.27 (10.03)	1.82 (58.47)

DiMeHx-DIPDMP-mixture

x_1	comp 1	comp 2	overall	binary
0.01	-5.11 (-16.69)	-1.51 (-6.91)	-1.48 (-6.76)	-3.1 (-10.93)
0.02	-3.31 (-11.73)	-0.84 (-4.08)	-0.77 (-3.72)	-0.22 (-0.88)
0.05	-0.19 (-0.8)	0.27 (1.48)	0.49 (2.7)	-0.3 (-1.29)
0.1	0.14 (0.68)	0.55 (3.58)	0.92 (5.81)	0.72 (3.81)
0.25	0.29 (1.97)	0.54 (5.14)	1.06 (9.29)	0.1 (0.74)
0.5	-0.5 (-4.6)	-0.77 (-9.67)	-0.23 (-2.53)	-0.28 (-3.42)
0.75	0.19 (1.79)	0.02 (0.31)	0.42 (4.26)	-0.21 (-2.47)
0.9	0.48 (3.74)	0.1 (1.08)	0.59 (4.72)	0.08 (0.74)
0.95	-0.24 (-1.66)	-0.13 (-1.3)	-0.15 (-1.02)	0.52 (4.72)
0.98	-1.02 (-6.28)	-0.89 (-7.95)	-0.98 (-6.07)	-0.83 (-6.38)
0.99	-1.26 (-7.57)	-1.33 (-11.31)	-1.25 (-7.48)	-0.98 (-7.31)

References

(1) Cornell, W. D.; Cieplak, P.; Bayly, C. I.; Gould, I. R.; Merz, K. M.; Ferguson, D. M.; Spellmeyer, D. C.; Fox, T.; Caldwell, J. W.; Kollman, P. A. A Second Generation Force Field for the Simulation of Proteins, Nucleic Acids, and Organic Molecules. *J. Am. Chem. Soc.* **1995**, *117*, 5179–5197.

(2) Jorgensen, W. L.; Maxwell, D. S.; Tirado-Rives, J. Development and Testing of the OPLS All-Atom Force Field on Conformational Energetics and Properties of Organic Liquids. *J. Am. Chem. Soc.* **1996**, *118*, 11225–11236.

(3) Price, M. L. P.; Ostrovsky, D.; Jorgensen, W. L. Gas-phase and liquid-state properties of esters, nitriles, and nitro compounds with the OPLS-AA force field. *J. Comput. Chem.* **2001**, *22*, 1340–1352.

(4) Rizzo, R. C.; Jorgensen, W. L. OPLS All-Atom Model for Amines: Resolution of the Amine Hydration Problem. *J. Am. Chem. Soc.* **1999**, *121*, 4827–4836.

(5) Hartmann, M. A.; Weinkamer, R.; Fratzl, P.; Svoboda, J.; Fischer, F. D. Onsager's coefficients and diffusion laws—a Monte Carlo study. *Philosophical Magazine* **2005**, *85*, 1243–1260.

(6) Krishna, R.; van Baten, J. M. The Darken Relation for Multicomponent Diffusion in Liquid Mixtures of Linear Alkanes: An Investigation Using Molecular Dynamics (MD) Simulations. *Industrial & Engineering Chemistry Research* **2005**, *44*, 6939–6947.

(7) Van de Ven-Lucassen, I. M. J. J.; Vlugt, T. J. H.; Van der Zanden, A. J. J.; Kerkhof, P. J. A. M. Using molecular dynamics to obtain Maxwell-Stefan diffusion coefficients in liquid systems. *Molecular Physics* **1998**, *94*, 495–503.

(8) Klein, T.; Wu, W.; Rausch, M. H.; Giraudet, C.; Koller, T. M.; Fröba, A. P. Influence of Liquid Structure on Fickian Diffusion in Binary Mixtures of n-Hexane and Carbon Dioxide Probed by Dynamic Light Scattering, Raman Spectroscopy, and Molecular Dynamics Simulations. *J. Phys. Chem. B* **2018**, *122*, 7122–7133.

(9) Higgoda, U. A.; Kankanamge, C. J.; Hellmann, R.; Koller, T. M.; Fröba, A. P. Fick diffusion coefficients of binary fluid mixtures consisting of methane, carbon dioxide, and propane via molecular dynamics simulations based on simplified pair-specific ab initio-derived force fields. *Fluid Phase Equilibria* **2019**, *502*, 112257.

(10) Fong, K. D.; Self, J.; McCloskey, B. D.; Persson, K. A. Ion Correlations and Their Impact on Transport in Polymer-Based Electrolytes. *Macromolecules* **2021**, *54*, 2575–2591.

(11) Jamali, S. H.; Wolff, L.; Becker, T. M.; Bardow, A.; Vlugt, T. J. H.; Moultos, O. A. Finite-Size Effects of Binary Mutual Diffusion Coefficients from Molecular Dynamics. *Journal of Chemical Theory and Computation* **2018**, *14*, 2667–2677.

(12) Schmitz, H.; Faller, R.; Müller-Plathe, F. Molecular Mobility in Cyclic Hydrocarbons A Simulation Study. *J. Phys. Chem. B* **1999**, *103*, 9731–9737.

(13) Yang, H.; Zhang, J.; Müller-Plathe, F.; Yang, Y. A reverse nonequilibrium molecular dynamics method for calculating the mutual diffusion coefficient for binary fluids. *Chemical Engineering Science* **2015**, *130*, 1–7.

Erklärung zur Begutachtung der Veröffentlichungen

Weder Referent Prof. Dr. Florian Müller-Plathe noch Koreferent Prof. Dr. Nico van der Vegt der vorliegenden kumulativen Doktorarbeit waren an der Begutachtung nachstehender Veröffentlichungen beteiligt.

1. M. K. Meinel, F. Müller-Plathe, *Loss of Molecular Roughness upon Coarse-Graining Predicts the Artificially Accelerated Mobility of Coarse-Grained Molecular Simulation Models*, J. Chem. Theory Comput. **16**, 1411-1419 (2020)
2. M. K. Meinel, F. Müller-Plathe, *Roughness volumes: An improved RoughMob concept for predicting the increase of molecular mobility upon coarse-graining*, J. Phys. Chem. B **126**, 3737-3747 (2022)
3. M. K. Meinel, F. Müller-Plathe, *Predicting the artificial dynamical acceleration of binary hydrocarbon mixtures upon coarse-graining with roughness volumes and simple averaging rules*, Accepted for publication in the Journal of Chemical Physics on 15th of April 2024

Datum

Referent
Prof. Dr. Florian Müller-Plathe

Koreferent
Prof. Dr. Nico van der Vegt

Erklärung zum Eigenanteil an den Veröffentlichungen

Im Folgenden ist aufgelistet, mit welchem Anteil ich an den Veröffentlichungen beteiligt war.

1. Mein Anteil an der folgenden Veröffentlichung beträgt 90 %:
   M. K. Meinel, F. Müller-Plathe, *Loss of Molecular Roughness upon Coarse-Graining Predicts the Artificially Accelerated Mobility of Coarse-Grained Molecular Simulation Models*, J. Chem. Theory Comput. **16**, 1411-1419 (2020)
2. Mein Anteil an der folgenden Veröffentlichung beträgt 95 %:
   M. K. Meinel, F. Müller-Plathe, *Roughness volumes: An improved RoughMob concept for predicting the increase of molecular mobility upon coarse-graining*, J. Phys. Chem. B **126**, 3737-3747 (2022)
3. Mein Anteil an der folgenden Veröffentlichung beträgt 90 %:
   M. K. Meinel, F. Müller-Plathe, *Predicting the artificial dynamical acceleration of binary hydrocarbon mixtures upon coarse-graining with roughness volumes and simple averaging rules*, Accepted for publication in Journal of Chemical Physics on 15th of April 2024

Datum

Melissa K. Meinel